The University Of Sheffield.

An Ultrasonic Method to Measure Thin Surface Coatings and Films Using A Superimposed Standing Wave

Joseph Kanja

April 2021

A thesis submitted in partial fulfilment of the requirements for the degree of Doctor of Philosophy

The University of Sheffield
Faculty of Engineering
Department of Mechanical Engineering

Supervisor: Professor Rob Dwyer-Joyce

Summary

The thickness of a protective surface coating that is left on a substrate after a wear process is an indicator of how much 'life' is left in terms of the surface coating functionality. Monitoring and quantifying the surface coating thickness is crucial in the evaluation of the risk of failure and maintenance to acceptable risk levels.

Ultrasound methods can be used to measure a coating/film layer thickness that is out of direct reach. Most pulse-echo ultrasonic methods use a time-of-flight through the layer to determine its thickness. As the layer becomes thinner, the reflected echoes overlap, and deconvolution and resonance methods are used to resolve this in most cases. However, the deconvolution methods are generally complex and time consuming whereas the resonance methods are usually limited by a narrow transducer usable bandwidth in common practice. In this work, the use of an ultrasonic continuously repeated chirp longitudinal wave within a solid was proposed to extend the usable transducer bandwidth and to amplify the effect of a coating. The multiple reflections interfere within the solid to form a superimposed standing wave whose amplitude spectrum is highly sensitive to a coating thickness at the interface of interest.

Epoxy coatings in the thickness range 70μm to 350μm were successfully measured using a standing wave method and showed a good agreement with standalone profilometer measurements. The standing wave measurements showed minimum and maximum percentage change accuracies of 1.04% and 10%, respectively. The epoxy resonances obtained from the standing wave method showed a greater reduction in the resonant mode magnitude than those obtained from a pulse-echo method, signifying increased sensitivity due to the multiple reflections.

A standing wave was then modelled from single frequency wave interference principles to simulate the frequency response of a coating on aluminium substrate using ultrasound propagation equations. The experimental data and mathematical model results showed a strong correlation indicating that the model can be applied to simulate or to compare real coating frequency responses. The model can also be used to optimise the standing wave method.

The thickness of a single epoxy layer bonded on a steel substrate was measured at different temperatures using a standing wave method. A good correlation was observed between experimental results and a linear thermal expansion model for data in the temperature range 24°C to 40°C. Beyond this range up to 70°C the difference between the experimental data and model results increased. Identification of epoxy resonant frequencies became difficult beyond 70°C due to the onset of a glass transition state.

A standing wave method was then applied to investigate the lowest measurable polyimide layer thickness that was bonded on a steel substrate using a standing wave method. The highest and lowest thicknesses measured were 530μm and 42.49μm, respectively. The lowest measurable thickness was limited by the upper bandwidth limit. There was no upper limit on the highest thickness measurable by a standing wave method although for much thicker layers it is more convenient to use a time-of-flight method. The results between the polyimide thickness measured using a standing wave and pulsed wave methods showed a strong agreement. Moreover, the standing wave measurements showed greatest sensitivity in terms of the resonant mode magnitudes when compared with conventional pulsed wave methods. This is practically useful in

improving the identification of the coating/film resonant modes. The standing wave method was simpler because it had fewer processing steps involved. The hardware to be used was also relatively cheap.

Finally, a measurement concept was developed that ultrasonically measured both viscosity and film thickness of lubricants and solvents spreading on a surface. Ultrasonic viscometry was performed using shear sensors and an acoustic matching layer that increased the viscosity measurement sensitivity. A standing wave method was used to measure the film thickness. Results showed that the liquid viscosity was proportional to the film thickness measured at the end of the experiment with the least viscous sample having the least film thickness and vice versa. The solvent viscosity was directly proportional to the carbon chain length of the constituents in the mixture. The results also showed a relatively rapid step-change reduction in the film thickness at certain points occurring particularly for solvents that were volatile. This indicated evaporation of the lighter constituents in the mixture. The proposed measurement concept could be optimised to further investigate the performance properties of lubricants and volatile solvents in real engineering components.

Acknowledgements

I would like to begin by thanking my supervisor Professor Rob Dwyer-Joyce for his continued encouragement and unwavering support throughout the entire PhD process. I could not have got to this stage without his help and guidance. I have learnt a lot from him, and I am very grateful for this rare opportunity. My countless interactions with him have always been very productive, refreshing, and rewarding and I could not have asked for a better supervisor to work with and to have as a mentor.

Secondly, I would like to thank the entire iT-CDT academic staff for their trust in me from the very start, the iT-CDT Centre Manager Mrs Kimberly Hyde who is always there to offer a helping hand and support at any time, my colleagues in the iT-CDT and the tribology researchers that I have interacted with in the Leonardo Laboratory. I have immensely appreciated the various conversations and engagements that we have had and your readiness to help me at every turn in my PhD process has not gone unnoticed. To Dr Xiangwei, Mr Tomos, Dr Georgios , Mr Sushil, and Dr Olivia, thank you for the productive, and more often than not, impromptu conversations and discussions that have always led to new insights. To Dave Butcher and Luke Callaghan, thank you for the technical support. I must also thank Dr Robin Mills for his encouragement with the project from the start. Thank you for giving me the chance to pick your brain!

I cannot forget to thank my family and friends, scattered across the UK and abroad, for their encouragement, patience and understanding during the entire PhD process. I whole heartedly appreciate the support.

Lastly, to Beth Mamicha, you have been there every step of the way and you have been my anchor and a voice of reason, and for that I appreciate you more than words can say. Thank you for the endless patience and support you have provided me.

Table of Contents

List of Figures

List of Tables

Nomenclature

Symbol	Chapter	Description	Units
A	2	Surface area of determining measurement area	cm^2
A	3	Wave equation constant	-
A	3,5,6,9	Wave amplitude	V
A_0	3,6	Initial wave amplitude	V
A	9	Wetted surface area	m^2
B	3	Liquid bulk modulus	Pa
B	3	Wave equation constant	-
c	2	Projected half-width	μm
c	2,3,4,5,6,7,8	Speed of sound wave	m/s
C	7	Speed of sound wave in component	m/s
C	2	Capacitance	F
d	2	Coating thickness	μm
d	2	Twice the coating thickness	μm
d	7	Distance	m
D	3	Effective dimension of the piezo element	m
D_c	2	Coating thickness	μm
E	3	Young's modulus of elasticity	Pa
f	3	Fundamental frequency	Hz
f	3,7	Wave frequency	Hz
f_d	3	Driving frequency	Hz
f_m	3	Resonant frequency	Hz
f_n	4,6,7	Harmonic frequency	Hz
f_0	3	Fundamental frequency	Hz
f_s	7	Coherent resonant frequency	Hz
Δf_s	7	Change in coherent resonant frequency	Hz
F	9	Shear force	N
G	3	Shear modulus	Pa
G'	9	Storage modulus	Pa
G''	9	Loss modulus	Pa
h	3,4,7,9	Film thickness	μm
I	2	Current	Amp
k	3	Wave number ($k=2\pi/\lambda$)	Hz.s/m
K	3,4	Stiffness	N/m
l	7	Material length	m
L	3,5,6,7,8	Material length	m
m	2	Combined mass	g
m	3	Resonant frequency mode number	-
m_0	2	Substrate mass	g
n	3,4,6,7	Resonant frequency mode number	-

n	6	Number of reflections	-
N_f	3	Frequency constant	Hz.m
P	3	Wave pressure	Pa
R	3,4,5,8,9	Reflection coefficient	-
R	6	Reflection coefficient at the interface of interest	-
R'	6	Reflection coefficient at the transducer interface	-
S	5,6,7,8,9	Standing wave reflection coefficient	-
S_{layer}	4	Signal from trapped layer	-
$S_{m,ref}$	4	Reference signal	-
S_{ref}	4	Measurement signal	-
t_d	2	Dry film thickness	cm
t_w	2	Wet film thickness	cm
T	3	Transmission coefficient	-
t	3	Coating thickness	μm
t	3,5,6,8	Time	s
T	7	Temperature	℃
Δt	2	Time separation between electromagnetic reflections	ps
Δt	2,8	Time interval between reflections	ms
ToF	4	Time-of-flight	μs
u	3,9	Velocity	m/s
U	2	Voltage	V
υ	3	Poisson's ratio	-
ν	9	Kinematic viscosity	cP
z	3,4,9	Acoustic impedance	Rayl (Pa.s/m)
α	2	Cut angle	degrees
α	3,6	Attenuation	Nepers/m
α	7	Coefficient of linear thermal expansion	μm/m˚C
δ	9	Penetration depth	m
ε	2	Coating dielectric constant	-
η	2	Coating refractive index	-
η	9	Dynamic viscosity	Pa.s
ϕ	2	Magnetic flux	Wb
$\dot{\gamma}$	9	Shear rate	s^{-1}
λ	3,7	Wavelength	m
ω	3,4,6	Angular frequency ($\omega=kc$)	Hz
ρ	2,9	Liquid density	g/cm^3
ρ	3,4,9	Material density	g/cm^3
ρ_0	2	Dry coating density	g/cm^3
τ	9	Shear stress	Pa
Ø	6	Phase at the interface of interest	Radians
Ø'	6	Phase at the transducer interface	Radians

1 Introduction

Surface coatings primarily protect the substrate on which they are adhered to from damage from the immediate environment. Additionally, they have decorative purposes. There has been significant growth in research and development of coating technologies in recent years and this has led to a commercialisation of specialized coatings that have novel functionalities over the more traditional protective and decorative functions. These coatings, otherwise referred to as functional coatings, provide an extra-added value in three main areas namely: at the coating-air interface, at the bulk of the coating, and the substrate-coating interface.

A surface coating within the context of this research work was used to describe a solid layer of material that is bonded on a substrate. Classification of functional surface coatings by application type according to the American Coatings Association (ACA) and the United States (US) Census Bureau is visualised in Figure 1-1.

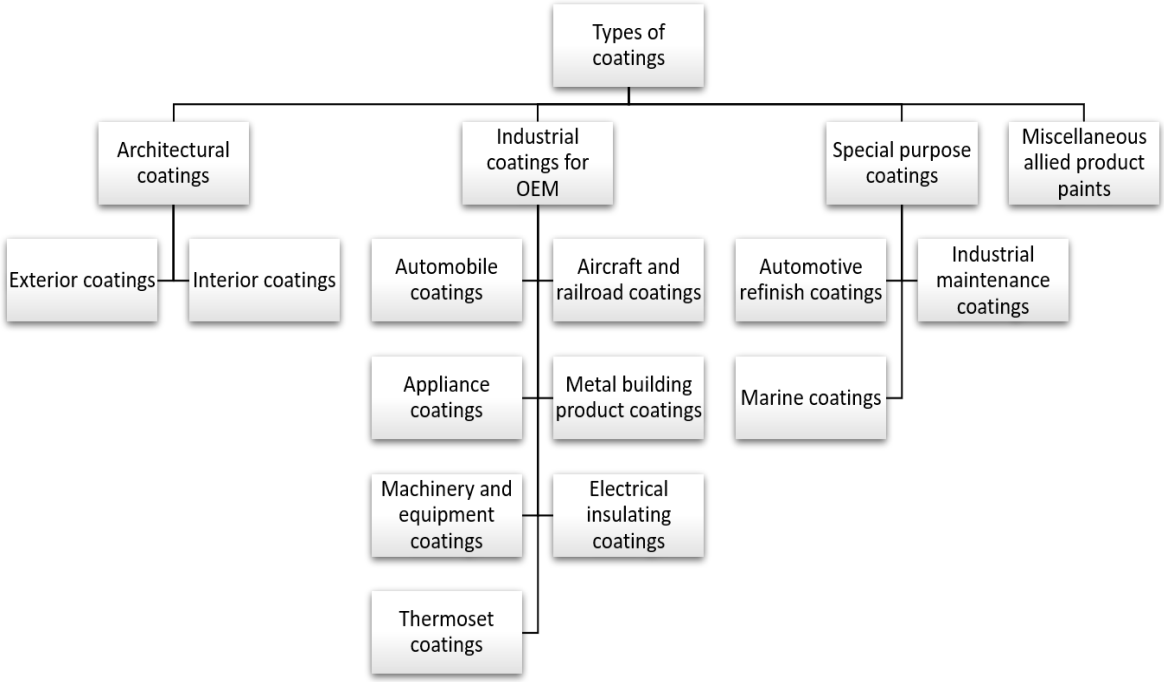

Figure 1-1. A classification of coating types adapted from ACA and US Census Bureau Current Industrial Report MA 325F [source www. https://www.census.gov/].

This list is not entirely exhaustive, but it helps to imply the vastness of the modern surface coatings industry. Functional surface coating thicknesses usually range from a few nanometres to a couple of centimetres, depending on the application. A majority of the coatings are found on easily accessible surfaces therefore measuring and quantifying them can be done with ease. However, a few are found on difficult-to-reach surfaces and some examples of this are the corrosion-protection layer inside oil-carrying pipelines and the fibre-reinforced plastics in chemical storage tanks. For the coatings to serve their primary function, the optimum thickness has to lie within specified limits. Over time, this thickness reduces depending on the immediate environmental conditions.

Surface coatings can also be formed as a result of fouling. For example, sedimentation inside heat exchangers and pipelines, varnish and sludge build-up inside internal combustion engines, and coking deposit inside a turbocharger housing. They harm the operational efficiency of the engineering component and over time, their increasing thicknesses reduces the overall efficiency.

A thin surface film within the context of this research work was used to refer to a liquid layer in contact with a substrate. Thin surface films, on metal substrates in particular, occur often in industrial applications and the thickness ranges from 5μm to above 8mm. An example is a thin film that is formed along the wall of a transporting tube of an air-oil lubrication system where the constitution and distribution of the thin lubricating film are essential for the efficiency of the lubricant [1], [2]. Another example is the oil that forms ahead of an approaching piston head in an internal combustion engine.

Monitoring and quantifying thin surface coating and film thickness is crucial in the evaluation of the risk of failure and maintenance to acceptable risk levels.

Thin surface coating and film thickness measurement techniques can be broadly categorised into either destructive or non-destructive. Destructive technique examples include cross-sectioning, inspection gauges and surface profilometry. Non-destructive examples include X-ray fluorescence, electromagnetism, beta-backscatter, photothermal, magnetic induction, white-light interferometry, capacitance, weight gain, and ultrasonic techniques. The main difference between destructive and non-destructive techniques is that destructive techniques involve either destroying or changing the coating material in such a way that after the thickness measurement has been performed, the material cannot resume normal operation whereas non-destructive techniques do not damage the material. Non-destructive techniques have an added advantage of reduced downtime in terms of inspection times and less have manual steps involved.

According to a recent film thickness measurement market report [3], as of 2016, the annual worldwide surface film thickness measurement market was valued at 370.6 million American dollars. It is predicted to increase at a compound annual growth rate of 4.9% from 391.8 million American dollars in the year 2017 and estimated to reach a valuation of 521.9 million American dollars by 2023. A total of 239.6 thousand units were estimated to be shipped in the year 2016 and this is likely to increase by 127 thousand units by the year 2023 after taking into consideration a compound annual growth rate of 6.1%. These statistics show that there is an increased requirement for technology miniaturisation, huge market demand for optimizing costs across the multiple industrial applications and a sharp rise in meeting quality standards. These factors serve to drive and direct the demand for innovative thin surface coating and film thickness measurement solutions.

1.1 Problem Statement

Measuring the thickness of surface coatings and films in-situ that are located inside closed assemblies becomes difficult when using most thickness measurement techniques because of the requirement of a direct access to the surface coating and film. However, ultrasound technique can be used to measure surface coating and film thickness indirectly. Ultrasound waves are able to penetrate a substrate from the back face and the reflections that bounce off the boundary between the front face and the surface coating carry information that can be used to quantify the surface

coating and film thickness. In essence, sound can be used to 'see' inaccessible surfaces, has the potential of reducing downtime, and can be used non-invasively, in-situ and in real time.

The most common and well understood ultrasonic coating thickness measurement technique is the time-of-flight or round-trip time method where the time it takes for an ultrasound wave to travel through a coating is directly related to the coating/ film thickness, provided the speed of sound in the material is known. The time value is extracted from the difference between discrete echoes from the substrate and the coating/film interfaces in the time domain, provided that the coating/film layer is sufficiently thick [4]–[7]. As the coating/film layer thickness reduces, the reflected echoes overlap, and it becomes difficult to distinguish between the discrete echoes. Nevertheless, measurement of thin coating and surface film thicknesses in the range 1-100μm is still possible with this technique and would usually require a broadband transducer with relatively high centre frequencies. However, higher frequencies experience higher attenuation and this method becomes impractical.

A resonance method is usually applied where the echoes overlap [8], [9]. By comparing the frequency spectra before and after the layer is applied (this ratio is otherwise known as the reflection coefficient *R*), the proportion of the reflected wave can then be used to extract the resonant frequency thus deducing the layer thickness. In most practical cases, the frequency that will cause the coating to resonate is usually not known in advance and it may also lie outside of the usable transducer bandwidth (-6dB or -12dB for most practical applications).

In this work, an alternative approach was proposed that utilised an ultrasonic continuously repeated chirp longitudinal wave to amplify the effect of the surface film. Multiple reflections interfered within the solid to form a superimposed standing wave whose amplitude spectrum was highly sensitive to the surface film thickness. The chirp wave was set to be sufficiently long enough to maximise the bandwidth of the transducer and the signal amplitude, therefore, allowing extraction of resonant frequencies that would otherwise not be detected by conventional means, and also increased the signal-to-noise ratio.

1.2 Research Aims and Objectives

This research aimed to develop a new method to non-invasively measure a thin surface coating and film thickness using a superimposed standing wave that is formed within a metal substrate by sending continuously repeating longitudinal chirp ultrasound waves. This technique has four main advantages namely:

1. **Increased sensitivity**. Because of the multiple reflections occurring within the substrate, the effect at the front-face is significantly improved.
2. **Faster response time**. Where the traditional ultrasound techniques rely on the pulse repetition rate between successive measurements, the peaks formed using the continuous method become measurement points.
3. **Low instrumentation costs involved**. This eliminates the need for a conventional ultrasonic pulsing system.
4. **Less processing times involved**. The standing wave method does not require the isolation of the first echo that is usually followed by zero-padding signal processing procedures that are normally involved with the conventional pulse-echo technique.

The objectives of this research were:

A. To describe an experimental approach for the formation of a superimposed standing wave within a metal substrate and to correlate a standing wave reflection coefficient to coating thickness determined using an independent surface profilometry measurement.
B. To describe a mathematical model for the formation of a superimposed standing wave within a metal substrate.
C. To investigate the factors that influence a coating thickness measurement using the standing wave method.
D. To compare and correlate experimental data and mathematical model results.
E. To investigate the lowest measurable coating using the standing wave method and to compare with conventional pulse-echo methods.
F. To investigate the performance properties of penetrants and solvents using a standing wave method by monitoring the liquid film thickness and correlation with the liquid viscosity.

1.3 Thesis Layout

This thesis is divided into ten chapters. This section reports a summary of each.

Chapter 1: Introduction

Chapter 2: Background on Surface Coating and Film Thickness Measurement This chapter aims to provide the reader with various surface coating/film thickness measurement techniques currently in use. A suggestion for ultrasound use as a non-invasive, in-situ measurement technique is presented.

Chapter 3: Background on Ultrasound The fundamental ultrasound principles are discussed.

Chapter 4: Literature Review This chapter covers some of the current and relevant ultrasonic techniques for a surface coating/film thickness measurement. The ultrasonic techniques are discussed thematically. This chapter then concludes by identifying a potential research gap in ultrasonic coating/film thickness measurement, and that is on the use of a superimposed standing wave for thickness measurement of thin surface coatings and films on metal substrates.

Chapter 5: Standing Wave Experimental Approach This chapter reports on the instrumentation of an aluminium substrate with piezoelectric sensors on the back face and the subsequent thickness measurement of an epoxy coating that is bonded on the front side by a superimposed standing wave method.

Chapter 6: Mathematical Modelling A mathematical description of the superimposed standing wave is presented in this chapter. The components of the model and the factors influencing the mathematical model are discussed. Experimental results from the previous chapter are compared with the model here.

Chapter 7: Thermal Effects on Standing Wave Measurement This chapter reports on the capability of the standing wave method to measure a solid epoxy thickness on a metal substrate as the temperature varies.

Chapter 8: Polyimide Thickness Measurement This chapter reports on the instrumentation of a metal testing component with piezoelectric transducers bonded on the back face and a

sufficiently thick solid polyimide layer bonded on the front face. The polyimide layer was machined to a range of thicknesses to investigate the lowest measurable thickness and a comparison between the superimposed standing wave and the conventional pulsed methods for the polyimide layer thickness measurement sensitivity will be discussed.

Chapter 9: Case Study on Penetrant Spreading This chapter reports the instrumentation of a testing component with sensors on the back face and a polyimide 'acoustic matching layer' on the front surface for the investigation of performance properties of penetrants and solvents under spreading conditions on the front face. Longitudinal sensors were used to measure liquid film thickness whereas shear sensors were used to measure the liquid viscosity. The measurement concept will be analysed by discussing the lubricant film thickness and viscosity measurements.

Chapter 10: Conclusions and Future Work This chapter provides a summary of the key findings arising from this research work. The advantages and disadvantages of the superimposed standing wave method are discussed, followed by a consideration of its practical implications. Recommendations for future work are also outlined.

2 Background on Surface Coating and Film Thickness Measurement

This chapter presents an overview of surface coatings and films thickness measurement techniques. An in-depth review of all possible measurement techniques is extensive and lies outside the scope of this research work and therefore only the working principles of the most commonly used measurement techniques will be discussed and assessed and a rationale for the use of ultrasound technology as a non-invasive, in-situ thin surface coating and film thickness measurement technique.

As surface coating technology gains momentum in modern-day applications, so is an increased demand for technology miniaturisation and optimisation to be able to perform innovative thickness measurement. Portable hand-held devices have been developed such as the Elcometer 456 Coating Thickness Gauge that uses magnetism and eddy current technologies to measure surface coatings on metal substrates [10]. It incorporates Universal Serial Bus (USB) and Bluetooth connectivity to allow data transfer to a PC or a mobile device as well as being compatible with bespoke smartphone software that allow instant data review especially when out in the field. Another example of a hand-held device is the PosiTector® 200 that uses ultrasound technology to measure coating thickness on non-metal substrates [11]. It also has USB, Wi-Fi, and Bluetooth connectivity to PC and smartphone software. This innovation drive is also synchronous with the necessity to monitor unwanted surface coatings and films inside engineering components. The thickness of a coating is important because it allows for the control of wear resistance, corrosion protection among other key properties [12]. On the other hand, the build-up of unwanted coatings/films inside an engineering component reduces its overall performance. Therefore, it is vital to be able to measure surface coating and film thicknesses to assess their functionality.

A coating/film layer thickness can be defined as the distance between the substrate-layer interface and the layer-air interface. The thickness can be broadly categorised into dry (solid coating) and wet (liquid film) thickness. The dry and wet thickness can be measured both destructively and non-destructively. Destructive techniques usually involve damaging the material in such a way that it cannot resume normal operation after the thickness measurement has been performed. Non-destructive techniques, as the name would suggest, do not damage the material, and usually have fewer steps involved. A family tree illustrating the destructive and non-destructive thickness measurement techniques is shown in Figure 2-1.

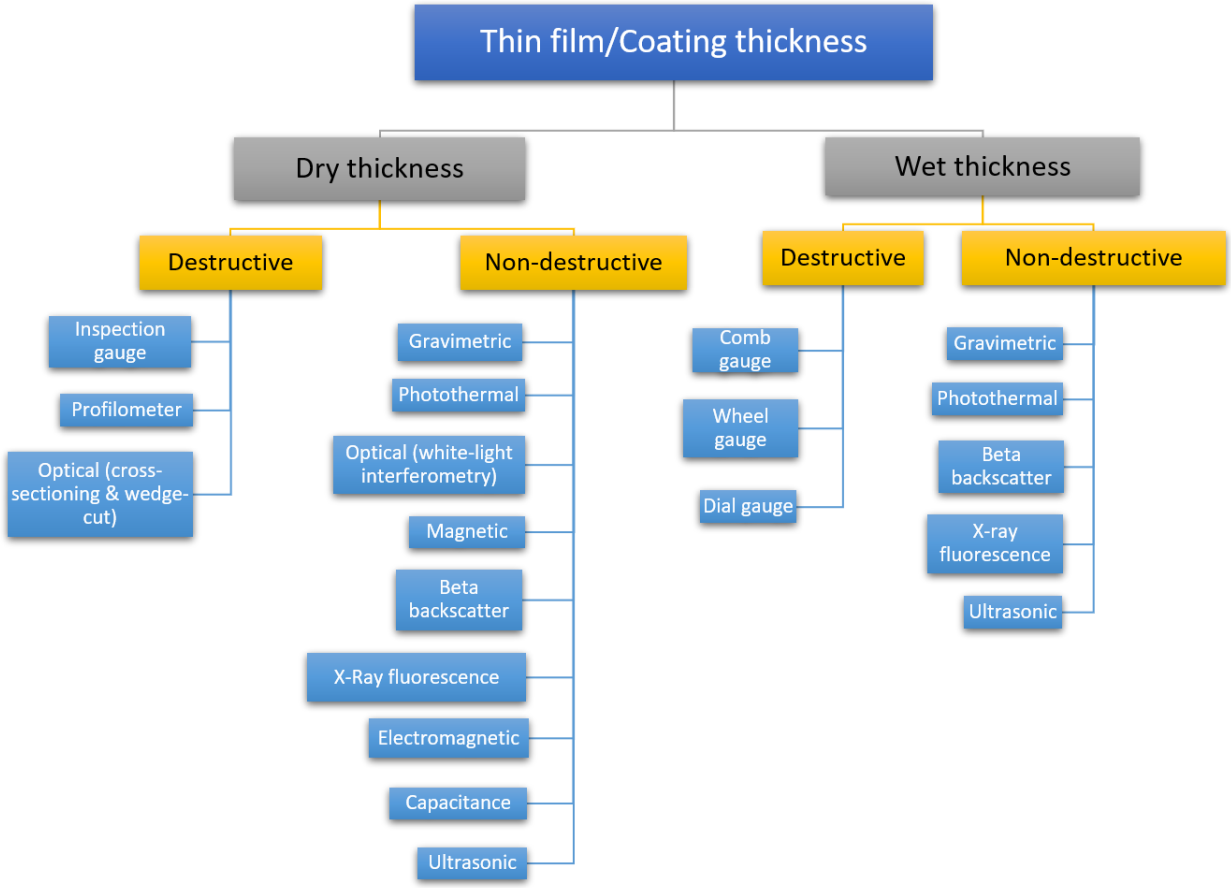

Figure 2-1. Thin film/coating thickness measurement techniques, reproduced from literature [13], [14].

The principles behind these techniques will be discussed in the sections that follow.

2.1 Inspection Gauge

Examples of inspection gauges are an external micrometer screw gauge and a micrometer depth screw gauge (Figure 2-2).

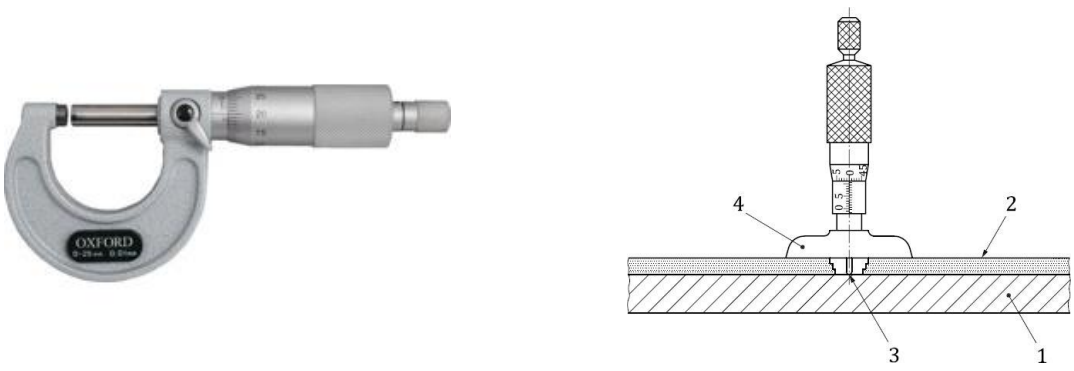

Figure 2-2. (Left) A photograph of a 0-25mm external micrometer [15]. (Right) A schematic of a micrometer depth gauge [Key: 1- substrate, 2 – coating, 3 – contacting element, 4 – foot].

These are generally inexpensive and can be readily bought from retailers. A 0-25mm external micrometer gauge costs roughly £107 (2021 pricing from [15]). Normally, measurements are performed to the nearest 1µm. An external micrometer screw gauge is used to measure the coating

difference between the combined thickness (substrate + coating) and the substrate. Destructively speaking, the combined thickness is first measured, and the coating is removed. The substrate thickness is then measured, and the difference gives the coating thickness. Non-destructively, the substrate thickness is measured first and then the combined thickness is measured after coating is applied. When using a micrometer screw gauge, the spindle is moved until the ratchet is activated. A depth gauge is used to measure the coating thickness by first zeroing on a reference plate. The coating is removed from the measurement area. The foot of the depth gauge is placed on the coating such that the spindle is located perpendicularly above the exposed measurement area. The spindle is then moved until the tip has touched the bare substrate and the ratchet is now activated. ASTM D1005-95 is the current industry standard that is used for the measurement of dry-film thickness using micrometers [16].

2.2 Profile Scanning

A profilometer is an example of a profile scanner. It is made up of a traversing stylus that is located at the end of a retractable arm that acts as a lever. The arm is then connected to amplifying and recording equipment. A schematic of a profilometer is shown in Figure 2-3.

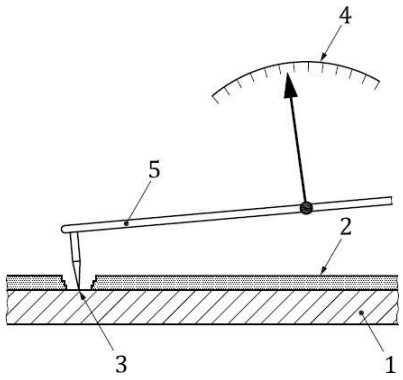

Figure 2-3. A schematic of a profilometer [Key: 1- substrate, 2 – coating, 3 – stylus tip, 4 – scale (located in a piece of recording equipment), 5 – lever].

During coating thickness measurement, the thickness value can be obtained destructively or non-destructively. Destructively, the profilometer is used to record the shoulder-profile that is formed between the substrate and the coating by removing part of the coating. Non-destructively, the coating thickness value is obtained by recording the step-change that occurs when the stylus moves from the substrate to the coating when traversing (Figure 2-4).

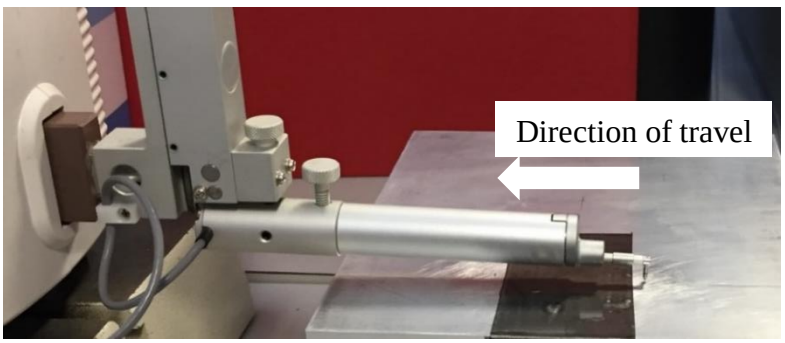

Figure 2-4. A photograph of a Mitutoyo™ profilometer stylus contacting a coated substrate (Photograph taken by author).

Stylus profilometers are capable of measuring thicknesses ranging from 10 nanometres to a few millimetres. DIN 50933 is an industry-standard currently used to measure coating thickness using stylus instruments [17].

A three-dimensional (3D) optical profilometer such as the InfiniteFocusSL™ from Alicona Imaging GmbH can utilise light instead of a stylus probe. A photograph of the Alicona optical profilometer is shown in Figure 2-5a illustrating the measurement of an epoxy layer on a steel substrate. A 3D colour profile measurement of the scanned area in Figure 2-5a is shown in Figure 2-5b.

(a)

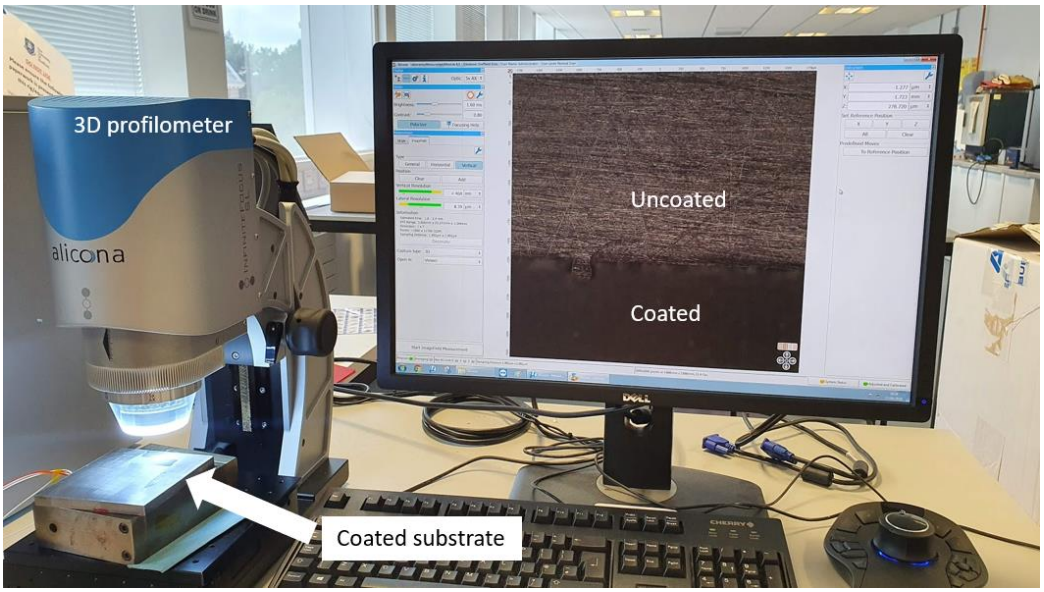

(b)

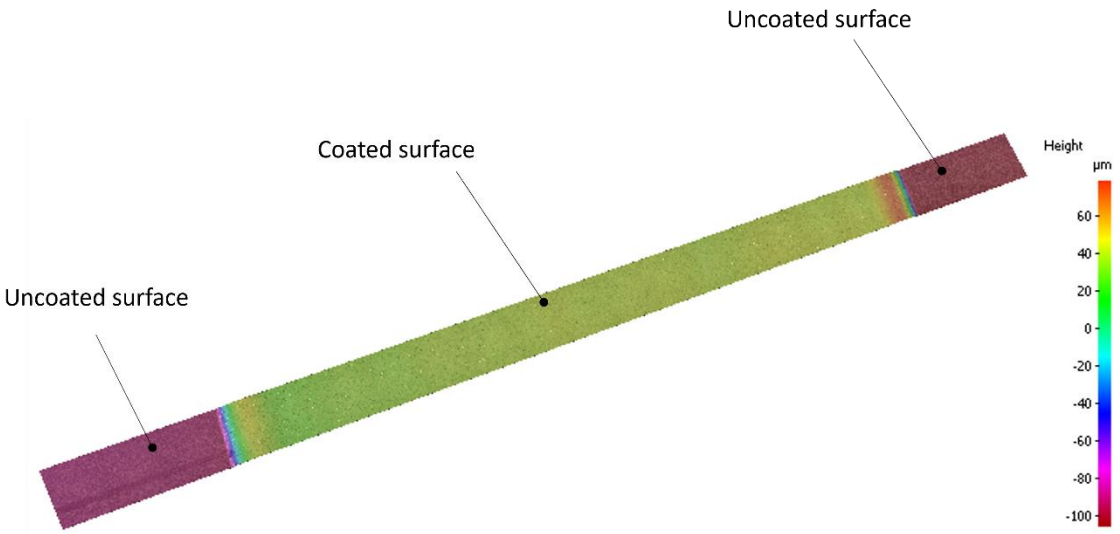

Figure 2-5. (a) A photograph showing a scanned area on a PC monitor of an epoxy coating on a steel substrate that was acquired using Alicona InfiniteFocusSL (Photograph taken by author). (b) A 3D colour profile measurement showing the coated and uncoated surfaces.

The coating thickness is calculated by measuring the vertical height of the coated surface from the uncoated surface from the 3D profile measurement.

The Alicona InfiniteFocusSL is capable of a vertical resolution of 100 nanometres allowing coating thickness measurement from a few microns to a few millimetres. A three-dimensional profile of the examined section thereby allows for further types of surface analyses. Contact and optical profilometers are expensive and cost anywhere between £2,000 to tens of thousands. The maintenance and upkeep costs are also expensive and require trained personnel.

2.3 Optical

Another way to optically measure a coating thickness is to perform a cross-section. The specimen is cut along a plane that is perpendicular to the coating and the substrate as illustrated in Figure 2-6.

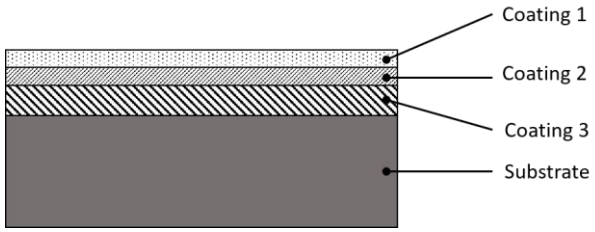

Figure 2-6. A schematic to show a cross-sectioned specimen.

The cross-sectioned specimen can now be inspected directly using an optical microscope to determine the coating thickness. This process produces precise thickness measurements, is widely used in industry, and follows ISO 1463 industry standard [18].

A wedge-cut of known dimensions can be made in the coating material using a tool at a specified angle to the substrate. A schematic of a wedge-cut is shown in Figure 2-7. The reader is directed to ISO 19399 standard that has more details on this [19].

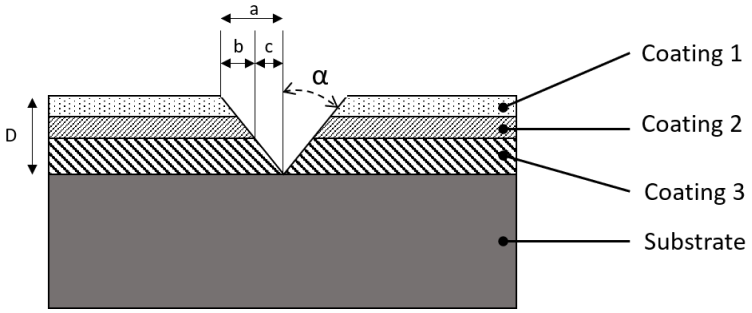

Figure 2-7. A schematic to show a symmetrical wedge-cut.

For coating 3, the thickness D_c is calculated using:

$$D_c = c \times tan\alpha \qquad \text{Equation 2-1}$$

where:

- c is the projected half-width of the wedge-cut which is determined using a microscope.
- α is the cut angle [standard cut angles are in the range α =5.7° to α=45°].

It is worth noting that cross-sectioning requires care to avoid damaging the coating otherwise the true coating thickness would not be measured. This requires dedicated tooling machines which are costly and involve trained personnel.

The coating thickness can also be measured using white-light interferometry. The coating material needs to be optically transparent for this technique to work. A beam of white light is directed at the coating as illustrated in Figure 2-8 and the measured interferences are then to be compared with set values which have been measured on coatings of known thicknesses through an established standard, such as ISO 25178-604 [20]. The equipment required is expensive and requires trained personnel.

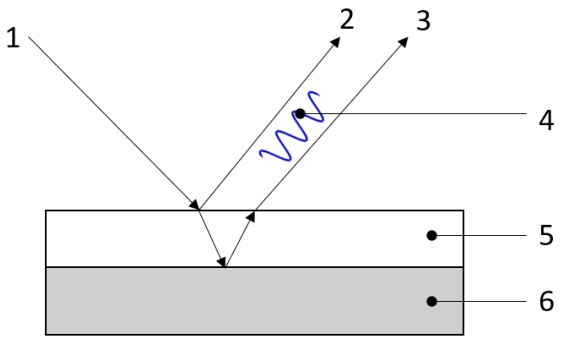

Figure 2-8. A schematic of a white-light interferometry beam path [Key: 1-incident beam, 2-partial reflected beam 1, 3-partial reflected beam 2, 4-interference, 5-coating, 6-substrate].

2.4 Comb Gauge

A comb gauge is normally flat. It is inexpensive and made of material that does not corrode. It has protrusions along its edges that are each assigned value (see Figure 2-9).

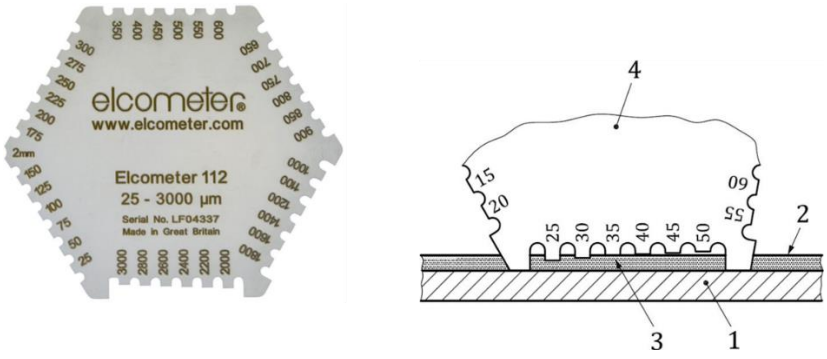

Figure 2-9. (Left) A photograph of a hexagonal wet film thickness comb gauge with 25µm to 3000µm scale [21]. (Right) A schematic of a wet film thickness comb gauge [Key: 1-substrate, 2-coating, 3-wetting contact, 4-comb gauge].

The corners of the comb gauge serve as a reference to provide a baseline and the protrusions are arranged as a series of graduated gaps. To measure the wet film thickness, the comb is pressed firmly onto the wet surface such that the longest protrusions are contacting the surface of the substrate. The gauge is then pulled away and the longest protrusion with liquid and the adjacent protrusion without are noted. The wet film thickness lies between these two readings. The comb gauge usually has an accuracy of ±5% of marked value or 3µm, whichever is the greater. Industry-

standard ASTM D4414 - 95 provides an in-depth guideline on how to measure wet films using a comb gauge [22].

2.5 Wheel Gauge

A wheel gauge is fabricated from corrosion-resistant steel that is hardened. It has three projecting rims such that two of them have the same diameter and are concentric to the axle. The third rim of a smaller diameter is eccentric (see Figure 2-10 and Figure 2-11).

Figure 2-10. An example of a wheel gauge [23].

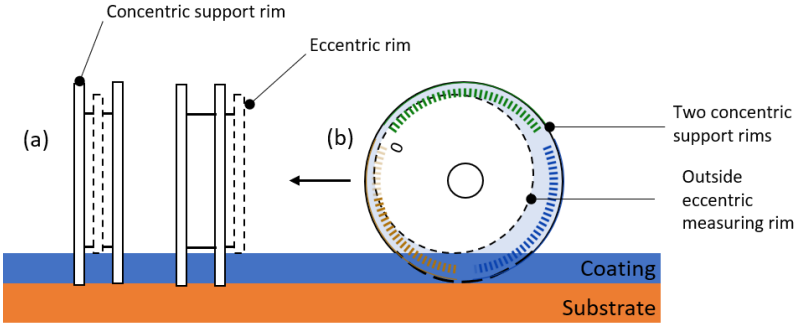

Figure 2-11. (a) A simplified view to show the positioning of the concentric and eccentric circles in two versions of wheel gauges. (b) An exaggerated view of a wheel gauge showing the eccentric rim relative to the concentric rims.

One outer rim has a scale from which the protrusion of the concentric rims from the eccentric rim is read. There are two versions of wheel gauges namely:

i. The eccentric rim is located between the concentric rims.
ii. The eccentric rim is located outside the concentric rims and adjacent to one.

To measure a wet film thickness, the gauge is placed at a thickness greater than what is expected, and the gauge is rolled to a thickness less than expected. The gauge is then lifted, and examination of the outside eccentric rim will show the thickness value where the wet film coating has been picked up. The resolution varies from 1µm to 20µm depending on the size of the wheel gauge used. ASTM D1212 - 91 provides a guideline on how to measure wet films using wheel gauges [24].

2.6 Dial Gauge

A dial gauge has two contacting pins that are equidistant and in a straight line from a plunger. The plunger is controlled by an adjusting screw. Traditional analogue dial gauges conform to ISO 463 [25]. Schematics to illustrate a digital and analogue dial gauge are shown in Figure 2-12.

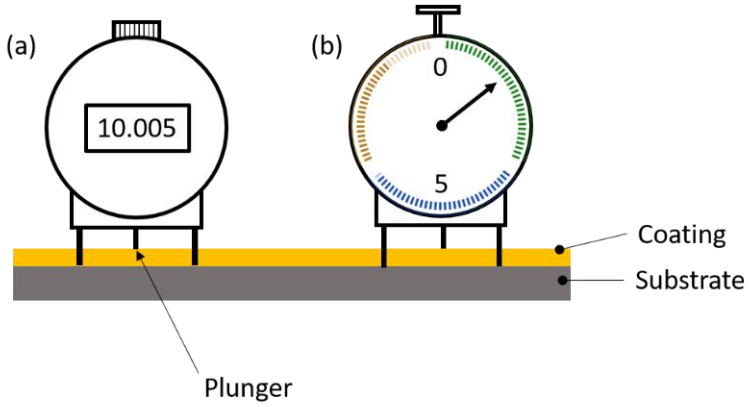

Figure 2-12. A schematic of an (a) digital dial gauge and (b) analogue dial gauge.

To measure the wet film thickness, the dial gauge is zeroed on a reference plate such that the plunger is just touching the reference plate. The plunger is then screwed back from the zero position. The contacting pins are then placed on the substrate and the plunger is lowered down until the tip is just touching the surface of the wet film. The wet film thickness is then read directly from the gauge. The resolution is dictated by the dial gauge graduation and the most common ones have a 5μm resolution. Errors are prone to arise when lowering the tip to touch the surface of the wet film.

2.7 Gravimetric

The principle behind the gravimetric technique is to calculate the differential between the combined mass (that of the substrate and the coating) and the substrate mass. For wet film thickness:

$$t_w = \frac{m - m_0}{A \times \rho} \qquad \text{Equation 2-2}$$

where t_w is the wet film thickness (cm), m is the combined mass (grams), m_0 is the mass of the substrate (grams), A is the surface area of the determining measurement area (cm^2), and ρ is the liquid density (g/cm^3). This technique is only applicable where the volatile substance contained in the liquid is low. The thickness measured is assumed to be the mean over the entire coated surface area.

For dry film thickness:

$$t_d = \frac{m - m_0}{A \times \rho_0} \qquad \text{Equation 2-3}$$

where t_d is the dry film thickness (cm), m is the combined mass (grams), m_0 is the mass of the substrate (grams), A is the surface area of the determining measurement area (cm^2), and ρ is the dry coating density (g/cm^3). This conforms to ISO 3892 [26].

2.8 Photothermal

The photothermal technique is a non-contact heat propagation method that operates on the principle that the coating thermal conductivity is different from that of the substrate and that the coating is optically accessible. The thickness measurement is performed by first emitting thermal

radiation from a source e.g. light-emitting diodes and laser sources, which excites the coating. A schematic of a photothermal set-up is shown in Figure 2-13.

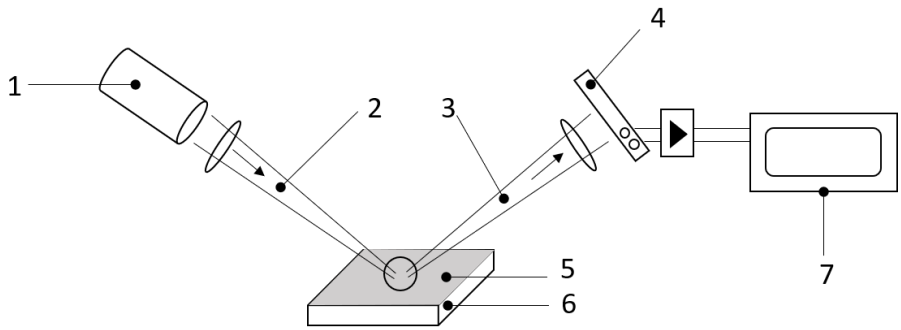

Figure 2-13. A schematic of photothermal material testing [Key: 1-excitation source, 2-emitted radiation, 3-re-emitted radiation, 4-detector, 5-coating, 6-substrate, 7-measured value processed and compared with calibrated data].

The interaction of thermal radiation with the coating leads to a series of effects that can be used to measure the coating properties directly or indirectly. These effects include heat radiation and acoustic waves. The photothermal equipment is normally calibrated with reference materials that have different absorption properties at different thicknesses. The thermal effects induced at the heated location are detected by various methods and the time it takes for a thermal wave to be radiated towards the coating and to be re-emitted is compared to coatings of known thickness [27]. This technique is only cost-effective for high-tech applications due to the complexity and costs involved in operating photothermal equipment.

2.9 Magnetic

The coating thickness can be determined from the interaction between a metallic substrate and the magnetic force field [28]. For a magnetic pull-off gauge, the coating thickness is determined from the force that is required to dislodge a magnet from the coating as illustrated in Figure 2-14.

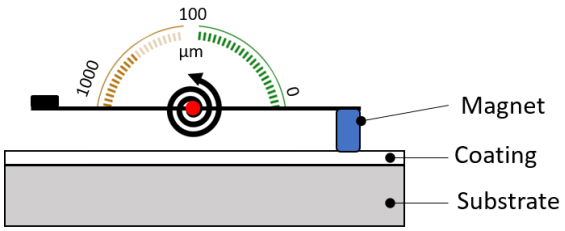

Figure 2-14. A schematic of a magnetic pull-off gauge.

The thicker the coating the less force is required and vice versa.

For a magnetic-flux gauge (Figure 2-15), the coating thickness is determined from the change in the magnetic flux density that is caused by the metallic substrate (Hall sensor principle).

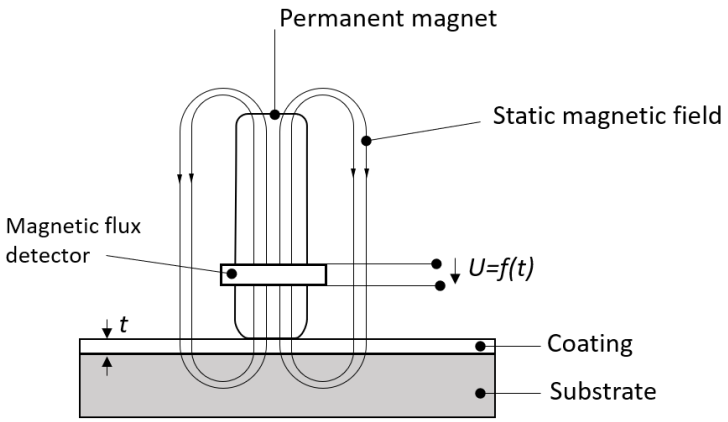

Figure 2-15. A schematic of a magnetic-flux detector gauge.

The magnetic flux density increases if the relative fraction of the coating is less in comparison to the magnetic substrate. The relationship between the coating thickness and the magnetic flux detector output U is nonlinear and is dependent on the metallic substrate permeability. This instrument needs to be first calibrated with known coating thicknesses on metallic substrates.

For a magnetic-induction gauge, the coating thickness is determined from the change that is produced when current, I, passes through the coil of an electromagnet to generate magnetic flux, ϕ. This results in the generation of voltage, U. A schematic of a magnetic-inductive gauge is shown in Figure 2-16.

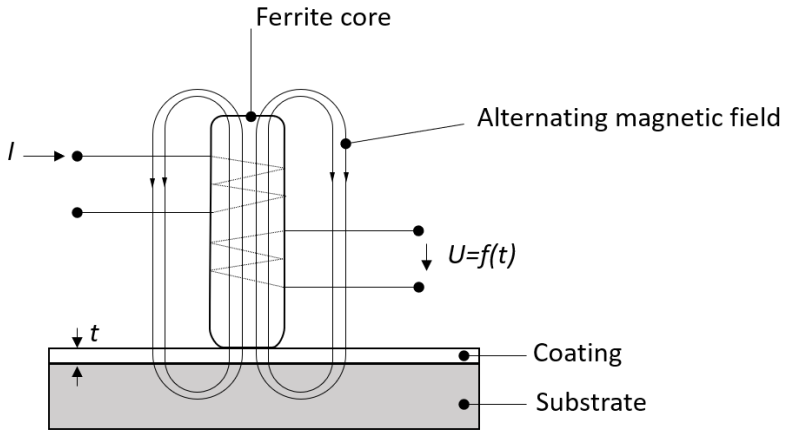

Figure 2-16. A schematic of a magnetic-inductive coating thickness gauge.

The coating thickness affects ϕ in the electromagnet which is observed in the measured U. The measured voltage is then compared to calibration values.

For the eddy current measurement technique, an exciting current, I, is passed through the coils on a ferrite core to produce an electromagnetic field (Figure 2-17).

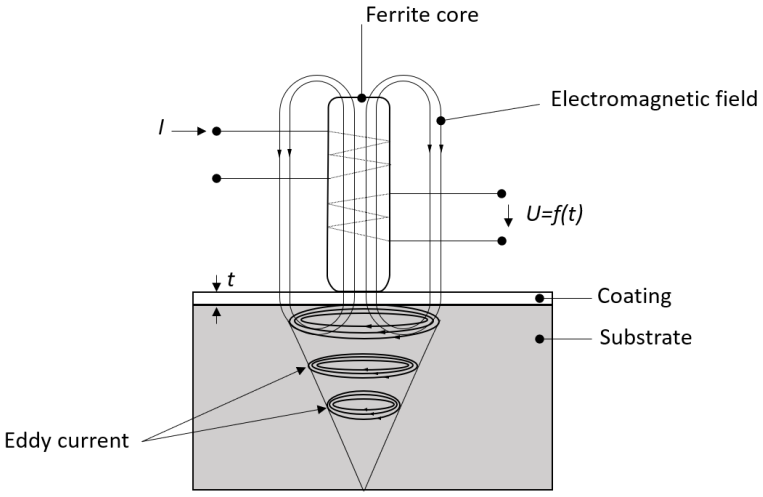

Figure 2-17. A schematic of the eddy-current method.

This creates eddy currents in the metallic substrate underneath the coating material. Depending on the coating thickness, these currents produce a change in the electromagnetic field that surrounds the core coil therefore changing the impedance of the core coil. The impedance values are then compared with calibrated coating thickness reference standards [29].

Magnetic techniques require that the substrate be ferrous whereas eddy current techniques require non-ferrous substrates. Some modern portable handheld devices are designed to incorporate both magnetic and eddy-current techniques into one device. They are readily available and relatively inexpensive. An example is the Extech™ Coating Thickness tester CG204 costing £210 (2021 pricing [30]). A photograph of this device is shown in Figure 2-18.

Figure 2-18. A photograph of the Extech™ Coating Thickness tester CG204 device showing calibration with a 99µm standard (Photograph taken by author).

Devices such as the Extech™ CG204 usually come with precision (or reference) standards, calibration substrate (iron and aluminium) and a USB cable for PC interface. The device is calibrated using the precision standards on the appropriate substrate (illustrated in Figure 2-18) before performing any coating thickness measurement on real components. The thickness measurement ranges from 0µm to 1250µm with an accuracy of ±5% for both magnetic induction and eddy current. The device is limited to minimum substrate thicknesses of 0.5mm and 0.3mm for ferrous and non-ferrous substrates, respectively.

2.10 Beta Backscatter

When beta particles are directed towards a coating material, a fraction of the particles are backscattered and detected using a Geiger counter. The number of backscattered particles depends on the difference in the atomic numbers of the coating material and the substrate. A schematic of a beta backscatter method is shown in Figure 2-19.

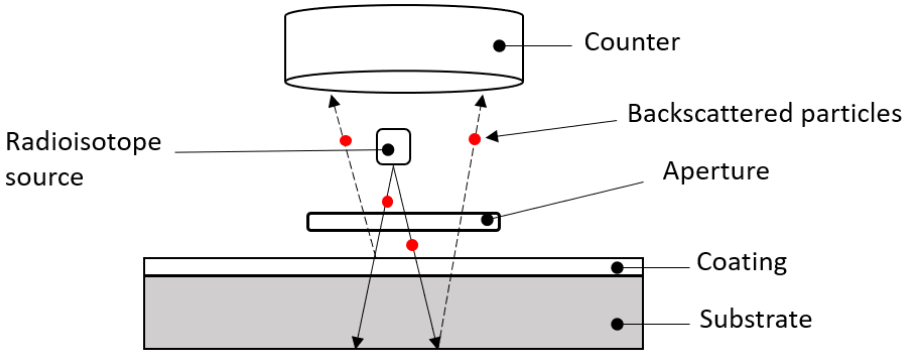

Figure 2-19. A schematic of a Beta Backscatter method.

Where a coating measurement is performed for a known mass-per-unit area, the backscatter intensity is directly proportional to the mean coating thickness of the measurement area [31]. The accuracy of the measurement depends on a variety of factors: the difference between the atomic numbers of the substrate and the coating, the source position in relation to the specimen under test, the substrate thickness, and the surface roughness, however, the latter has a negligible effect where the coating atomic number is low, and the beta particle energy is high. Due to the complex technology involved, beta backscatter equipment is expensive and requires trained personnel.

2.11 X-ray Fluorescence

An X-ray source is used to produce excitation radiation which passes through a collimator and on to the coating material as illustrated in Figure 2-20.

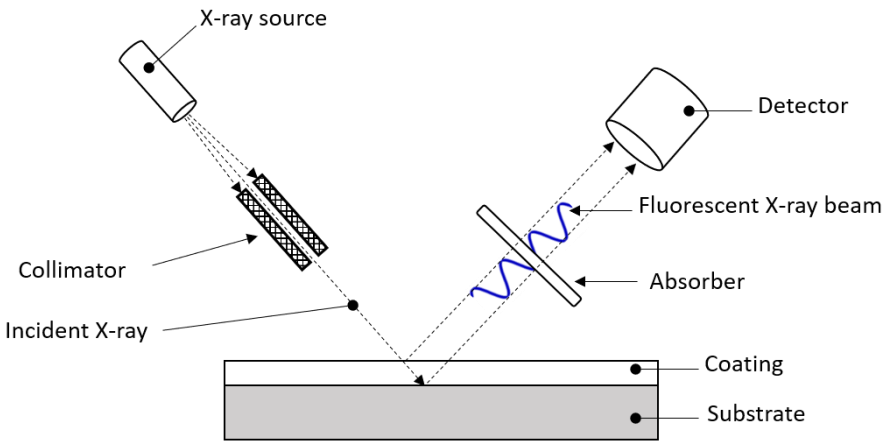

Figure 2-20. A schematic of the X-ray fluorescence coating thickness measurement method.

The X-rays are scattered by the coating and the substrate materials depending on the atomic numbers of the respective materials. The fluorescent X-ray radiation is detected and where a measurement is done for a specified area of known mass and density, the coating thickness is directly related to the radiation intensity. These values are compared to calibration standards [32].

Because of X-ray technology involved, these equipment are very costly and require trained personnel due to the hazards involved.

2.12 Electromagnetic

Terahertz radiation is a type of electromagnetic wave that lies in the frequency range of 0.3 THz to 30 THz. When terahertz radiation is incident upon an interface between two materials that have different refractive indices, some radiation will be reflected, and the rest will be transmitted through the material as a result of the discontinuity of the refractive index (Figure 2-21a).

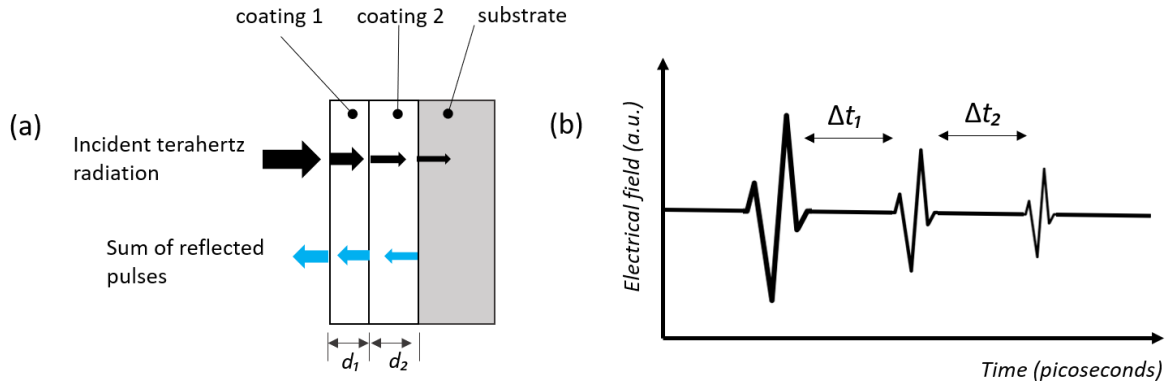

Figure 2-21. A schematic of the Terahertz principle of measuring coating thickness. (a) A two-layer coating system and (b) the time domain waveform of the echoes.

The first reflection is due to the air-coating interface. This discontinuity produces successive echoes with a time delay between (Δt) two echoes as illustrated in Figure 2-21b. For optically thick samples, the coating thickness is then calculated directly from the time delay between adjacent echoes (Equation 2-4):

$$d = \frac{\Delta t}{2\eta} \qquad \text{Equation 2-4}$$

where d is the coating thickness, Δt is the time separation in terms of picoseconds, and η is the coating refractive index. For optically thin samples where the echoes overlap in the time domain, the coating thickness can be extracted from a signal processing algorithm of a one-dimensional electromagnetic model as shown in Figure 2-22.

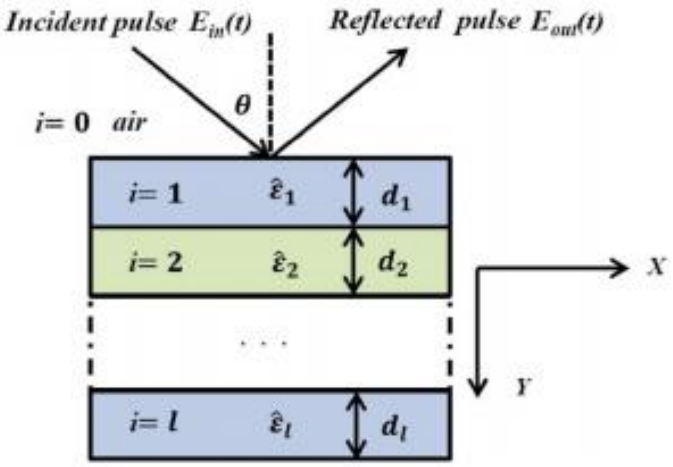

Figure 2-22. A one-dimensional Terahertz propagation model for optically thin coatings in a multi-layered medium (extracted from [33]).

Su et al., [33] report on the use of terahertz pulsed imaging to measure up to four paint coatings on metallic and non-metallic substrates. The complex dielectric functions $\hat{\varepsilon}$ of the layers were used to calculate the reflection coefficients at the measurement frequencies and an inverse Fourier transform was applied to convert the reflection coefficients back into the time-domain. The refractive indices and the thickness of the layers were then calculated from a data fitting algorithm. This technique was capable of resolving paint thickness down to 18μm and measurements showed a good correlation with eddy-current, X-ray, surface profilometry and ultrasound techniques. Commercial terahertz pulse imaging equipment nowadays is quite sophisticated and relatively expensive.

2.13 Capacitance

Traditionally, the metal substrate and usually a flat plate probe which is placed on top of the coating act as electrodes of a capacitor and the coating acts as the dielectric (Figure 2-23).

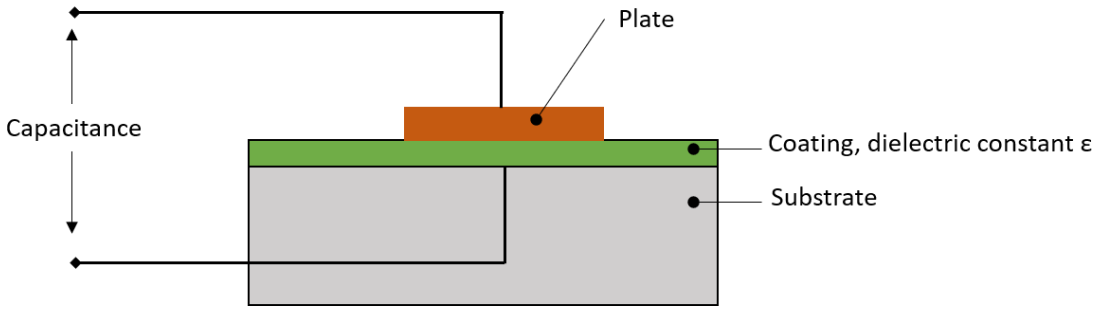

Figure 2-23. A schematic showing the principle of capacitance method for measuring coating thickness.

Provided the coating dielectric constant is known, the coating thickness d is calculated using Equation 2-5:

$$d = \frac{\varepsilon A}{C} \qquad \text{Equation 2-5}$$

where ϵ is the coating dielectric constant, A is the measurement area and C is the capacitance. For liquid films, especially those that are non-conductive, the conventional capacitance methods no longer apply. For liquid films such as oils inside pipes of vessels, where liquid film thickness distribution is required for flow control, electrical capacitance tomography (ECT) is normally applied on the perimeter to map the permittivity distribution profile and this has been used in oil and chemical plants [34]–[36]. The ECT images are then reconstructed to extract the liquid film thickness. The degree of accuracy is dictated by the complexity of the algorithm used and the iteration process is very time consuming due to the involvement of finite element analysis to estimate capacitance from an image.

2.14 Ultrasonic (Acoustic)

For this technique, a longitudinal ultrasound wave of sufficiently high frequency, generated in an ultrasound probe that acts as a transmitter and a receiver, is normally incident on a coating system (Figure 2-24).

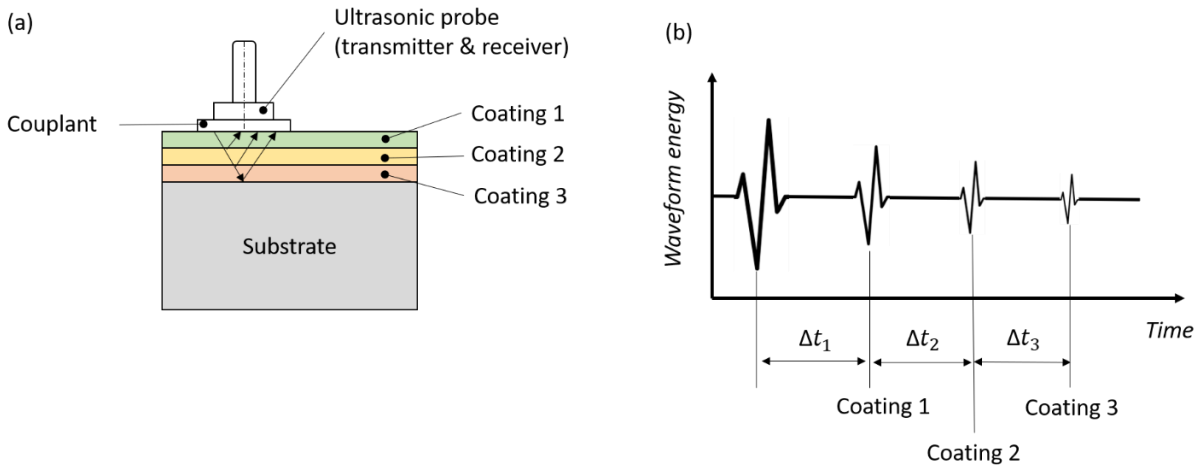

Figure 2-24. A schematic showing the ultrasound principle to measure coating thickness (a) a three-layer coating system and (b) the recorded time domain of the reflected echoes.

These ultrasound probes have varying frequency and come in various shapes and sizes as shown in Figure 2-25.

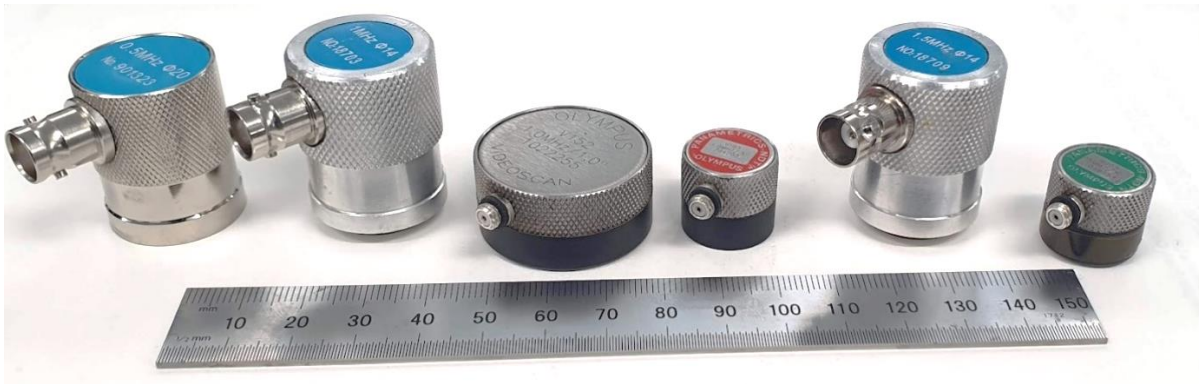

Figure 2-25. Single element longitudinal and shear wave contact transducers (Photograph taken by author).

Upon reaching the first coating, the wave is reflected, and the rest is transmitted. The transmitted wave then travels and is subsequently split up at the rest of the boundary interfaces into reflected and transmitted components. The received ultrasonic echoes are recorded and the time interval between successive echoes corresponds to ultrasound wave travel times between the coating layers. The first reflection is from the ultrasound wave impinging on the first coating. The magnitude of the successive echoes is dependent on the coating material reflection factors. Provided the ultrasound wave velocity is known in the coating materials, the coating thickness can then be calculated from Equation 2-6:

$$c = \frac{d}{\Delta t} \qquad \text{Equation 2-6}$$

where *c* is the sound wave, *d* is twice the coating material thickness because the wave has to travel there and back, and Δt is the time interval between the echoes. ISO 19397 provides a detailed guideline on the determination of coating thickness using ultrasound probes as used in industry [37].

The ultrasound waves can also be sent from a position on the back face of the substrate. Upon reaching the boundary between the substrate and the coating, some waves will be reflected, and some will be transmitted into the coating upon where they reach the upper coating boundary and are reflected towards the substrate and consequently detected by the transducer. The acquired ultrasound signals when analysed in the time domain show the reflections from the two interfaces as discrete echoes. This is illustrated in Figure 2-26 where echoes 1 and 3 are from the boundary between the substrate and the coating and echoes 2 and 4 arise due to the upper coating-air boundary.

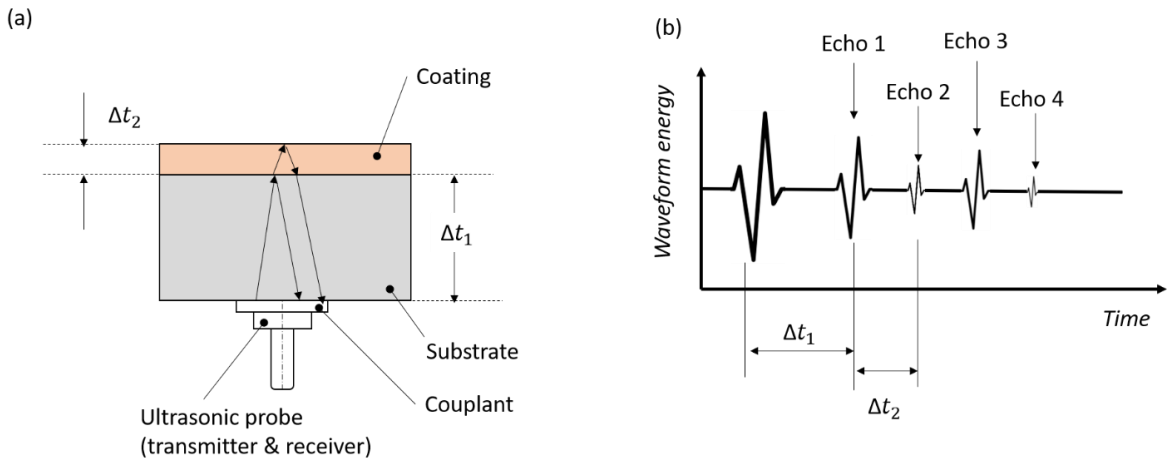

Figure 2-26. (a) A schematic to show the ultrasonic measurement of a surface coating from a substrate back face. (b) The recorded time domain of the reflected echoes.

The coating thickness is calculated using Equation 2-6. In this case, the time interval of interest is Δt_2 which is the time the echo has propagated through the coating material. When the thickness reduces to around 100μm these echoes overlap when using high frequency ultrasound waves, and it becomes increasingly difficult to resolve the round-trip time temporally. A resonance method can be used to resolve this and is capable of measuring thicknesses up to a minimum of around 10μm depending on the frequency bandwidth and the speed of sound in the coating material [8].

Bare piezoelectric elements can also be used to generate ultrasound waves, and these can be tailored to retrofitted onto most engineering components. They are manufactured in a variety of shapes and sizes depending on the frequencies to be excited as shown in Figure 2-27.

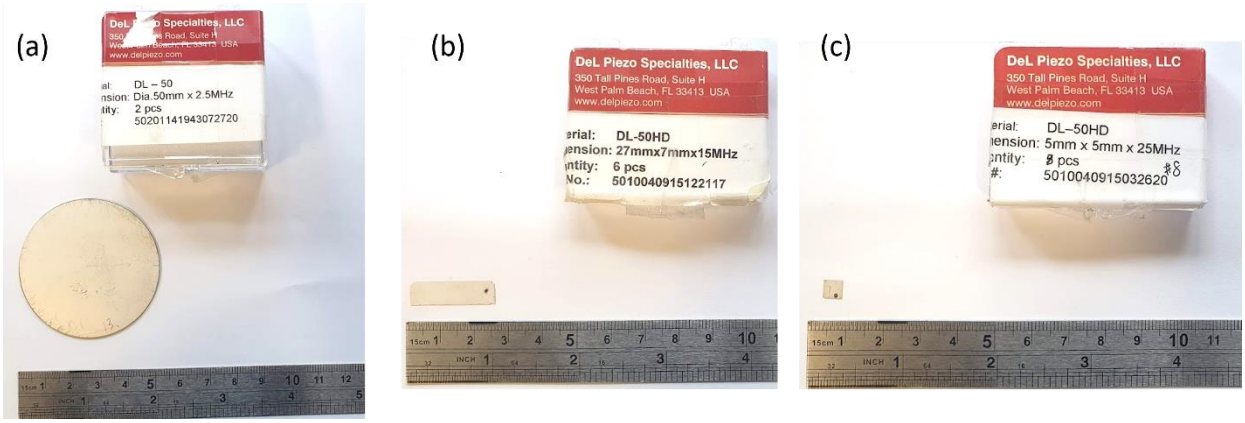

Figure 2-27. Photographs showing examples of (a) 2.5MHz (b) 15MHz and (c) 25MHz bare piezoelectric elements obtained from *Del Piezo Specialties LLC.* (Photograph taken by author).

They can be cut to an appropriate size and permanently bonded on to obscure surfaces where the commercial transducers would otherwise not be applicable.

2.15 Summary

A surface coating and thin film thickness can be measured directly or indirectly using a variety of techniques depending on whether the material is dry or wet. Both dry and wet films can be measured destructively and non-destructively. A specification of current surface coating and film thickness measurement techniques that have been discussed in the previous sections is shown in Table 2-1.

Table 2-1. A specification of current surface coating and film thickness measurement techniques.

Technique	Method of access to coating/film	Characterisation	Material
Inspection gauge	Direct	Destructive and non-destructive	Solid coating
Profile scanning	Direct	Destructive and non-destructive	Solid coating
Optical	Direct	Destructive	Solid coating
Comb gauge	Direct	Destructive	Wet film
Wheel gauge	Direct	Destructive	Wet film
Dial gauge	Direct	Destructive	Wet film
Gravimetric	Direct	Non-destructive	Solid coating and Wet film
Photothermal	Direct	Non-destructive	Solid coating and wet film
Magnetic	Direct	Non-destructive	Solid coating
Beta backscatter	Direct	Non-destructive	Solid coating
X-ray fluorescence	Direct	Non-destructive	Solid coating
Electromagnetic	Direct	Non-destructive	Solid coating
Capacitance	Direct and indirect	Non-destructive	Solid coating and wet film
Ultrasonic	Direct and indirect	Non-destructive	Solid coating and wet film

The work involved in this research is concerned with thin surface coatings and films that would normally be located on surfaces that have no direct access and so the need for indirect measurement takes precedence. The techniques that offer the greatest accuracy, such as X-Ray and optical technologies, are quite expensive and thickness measurements can only be performed directly in a laboratory setting. These are used in otherwise high-tech applications where it is considered cost-effective. Capacitance methods also have great potential for indirect thickness measurement but the image reconstruction process for ECT is time-consuming and quite complex. Therefore, there is a need for an inexpensive, reliable, and simple indirect in-situ technique to measure surface coating and film thickness.

Ultrasound has the capability of measuring surface coatings and films indirectly and in-situ. The ultrasound waves are sent from a component back face, reflect from the component-coating boundary and the upper coating boundary, and the reflected waves carry information that can be used to quantify the surface coating thickness. By doing so, ultrasound waves can be used to ‘see’ inaccessible surfaces. Ultrasound technique is relatively inexpensive when compared with the more sophisticated measurement techniques such as X-Ray. This technique of reflecting an ultrasound wave from an interface of interest and analysing the embedded information from the ultrasonic reflections has been useful in performing measurements on surfaces in difficult locations [9], [38]–[42]. When a normal incident wave strikes a surface, some of the energy will

be transmitted into the neighbouring component while the remaining energy will be reflected towards the wave source. Conventional ultrasound spectroscopy tools operate on this principle whereby a single burst of energy is sent to an interface of interest. The proportion of energy reflected is used in suitable mathematical models to characterise the conditions at the surface layer [43].

Therefore, the most practical technique for measuring surface coatings and thin films located in difficult-to-reach surfaces is ultrasound. A round-trip time is usually used to calculate the layer thickness, provided the speed of sound in the material is known. As the layer thickness reduces, the reflected pulses overlap temporally, and deconvolution and resonance methods are normally employed to overcome this limitation. It is hypothesised that a new ultrasonic approach that increases sensitivity for measurement of surface coating and thin film thickness can be used to overcome the limitations associated with conventional pulse-echo resonance techniques.

3 Background on Ultrasound

Chapter 2 concluded by suggesting ultrasound method as a convenient method to measure surface coating and film thicknesses that would otherwise occur on inaccessible surfaces. Therefore, in this chapter, only the background on key aspects of ultrasound will be discussed and these are the fundamentals that are applied in this research work.

3.1 Ultrasound in The Acoustic Spectrum

Sound refers to the mechanical vibrations of particles in an elastic medium that give a hearing sensation. Any disturbances that lie out of the normal human hearing range (20Hz to 20kHz) are classed as infrasound (<20Hz) or ultrasound (>20kHz). An illustration of the acoustic spectrum is shown in Figure 3-1.

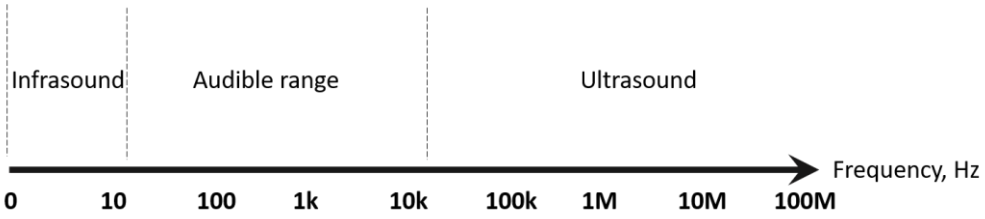

Figure 3-1. A simplified illustration of the acoustic spectrum.

Sound also applies to whatever else that is governed by the fundamental physical acoustic principles. Acoustics is defined as the science of sound production, propagation, and its effects. It is a multidisciplinary area of study that encompasses a broad range of disciplines as shown in Figure 3-2.

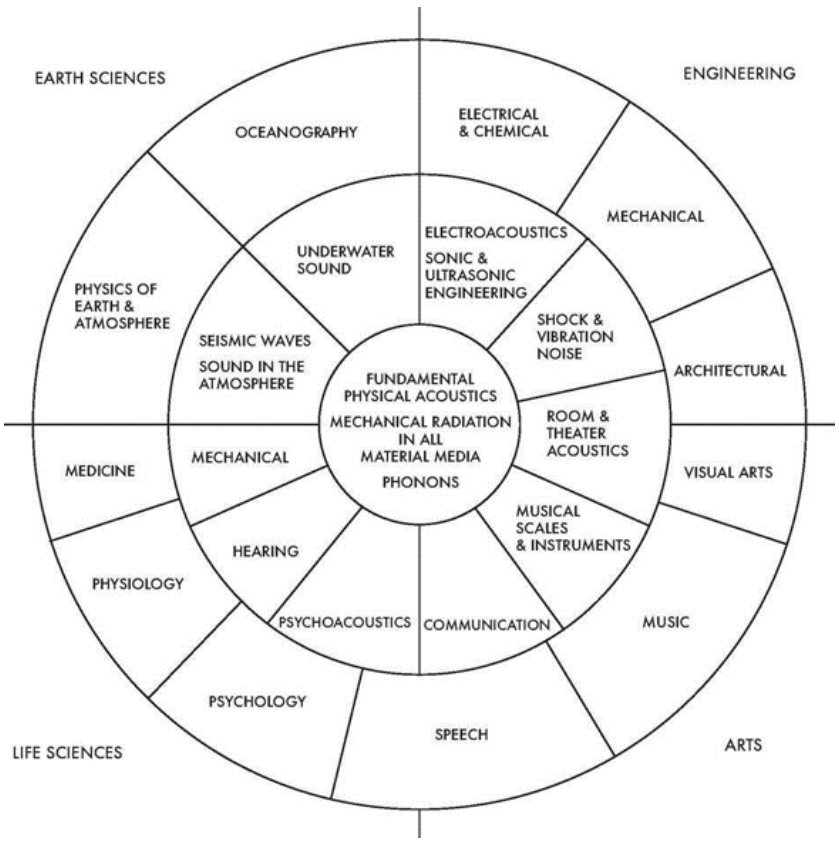

Figure 3-2. A chart of acoustics illustrating the broad scope of acoustics (adapted from [44]).

The branch of acoustics that proceeds for the rest of this research is concerned with ultrasound physics and how it is applied to measure and quantify surface coatings and films. This will involve discussing how ultrasound is generated, properties of an ultrasonic wave pulse, factors affecting ultrasound wave propagation and ultrasound wave interaction at an interface.

3.2 Ultrasound Generation

Generating an ultrasound pulse requires the displacement of particles in a manner that produces the wanted frequency. The particles can be displaced by a sudden expansion (usually caused by rapid heating), stress relief or even high-speed collisions. A more preferable and controlled method of generating ultrasound signals is to utilise piezoelectric materials.

3.2.1 The Piezoelectric Effect

The term 'Piezoelectric' is derived from the Greek words '*piezo*' which comes from the root '*piezin*' which translates to '*to press, squeeze*' and '*elektron*' for amber, which was an ancient source of electric charge. In 1880, Pierre and Jacques Curie discovered that if a material is deformed by external mechanical pressure, electric charges are produced on its surface. This is known as direct piezoelectric effect. In 1881, Lippman discovered the converse that when a material with piezoelectric properties is placed between two electrodes, it changes its form on the application of an electric potential. This is known as indirect piezoelectric effect. The former is used in signal capturing and the latter is used for signal generation. This material property allows for the generation and acquisition of ultrasonic waves using piezoelectric ceramics such as lead zirconate titanate (PZT), lead nitrate, lead metaniobate and barium sodium niobate [45]. The most commonly used ceramic is PZT and when it is sandwiched between two electrically conductive plates it forms a piezoelectric transducer. An arbitrary function generator (AFG) is used to control the expansion or contraction of PZT by regulating the electrical field applied to the transducer. The voltage produced by a transducer in response to a mechanical pressure is digitised using an oscilloscope.

3.2.2 Piezoelectric Transducers

Piezoelectric transducers have now been commercially optimised for various applications such as acoustic emission and crack detection. These commercial transducers have an enclosure that houses piezoelectric materials that are acoustically damped using backing material to minimise the natural resonant oscillation which would continue to vibrate after applying a voltage. This backing material also secures the electrical connection between the wires and the piezoelectric material. There are many variations of commercial transducers that are readily available off-the-shelf and are capable of producing various wave modes. Figure 2-25 from the previous chapter shows some examples of commercial longitudinal transducers.

Bare piezoelectric elements (some are shown in Figure 2-27) can act as ultrasonic transducers where they are directly bonded on to the back face of a substrate. They are made up of piezoelectric crystals often with a conductive coating and the curie temperature affects their operational limits. Signal generation becomes difficult at the curie temperature because of the electrical polling instability. However, some ceramic-based piezo elements can go up to a few hundred degrees Celsius. They are generally categorized into 'hard' and 'soft' materials, come in various polarities and dimensions, where some can be as small as $1mm^2$ in surface area and can be used in otherwise complex geometries where commercial transducers cannot be used. Therefore, bare ceramic-based

piezoelectric transducers have used throughout this work. Figure 3-3a shows a 10MHz wrap-around longitudinal transducer to emphasize its small size. Figure 3-3b shows a cabled longitudinal sensor pair to demonstrate simplicity.

(a)  (b) 

Figure 3-3. Photographs of bare piezoelectric materials showing (a) a 10MHz longitudinal transducer (b) a pair of longitudinal transducers bonded and cabled on to an aluminium substrate where one is used to send ultrasound waves and the other to receive (Photographs taken by author).

The wave mode and the frequency are determined by the size of the element and the direction of polarization. An example of longitudinal and shear polarised elements is shown in Figure 3-4.

	Longitudinal polarisation	**Shear polarisation**
Element shape dimensions	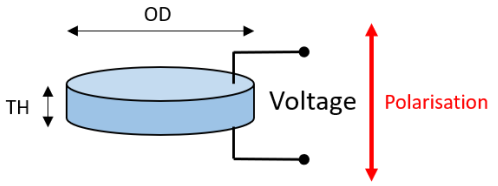	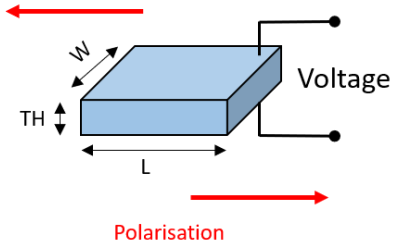
	OD >> TH	***L≈W >> TH***

Figure 3-4. Example of longitudinal and shear polarised elements.

The piezoelectric fundamental frequency, f is taken as the ratio of the frequency constant, N_f and the effective dimension of the piezo element, D (Equation 3-1).

$$f = \frac{N_f}{D} \qquad \text{Equation 3-1}$$

3.3 Ultrasound Wave Propagation

Ultrasound waves, or acoustic waves in general, are only able to propagate in elastic media. An elastic media can be visualised as a simple lattice-type structure where the particles are separated by elastic forces or bonds. An illustration of this is shown in Figure 3-5 [45].

Propagation of an ultrasound wave occurs in the form of kinetic energy transfer from one particle to the adjacent as a result of the interaction of the elastic forces which act as springs. When a particle is subjected to a disturbance, this results in energy to be transmitted to the adjacent particle in accordance with the *stiffness* of the elastic bond. This will then cause the next adjacent particles to move eventually causing a chain reaction further along the structure and a wave deformation will be set up.

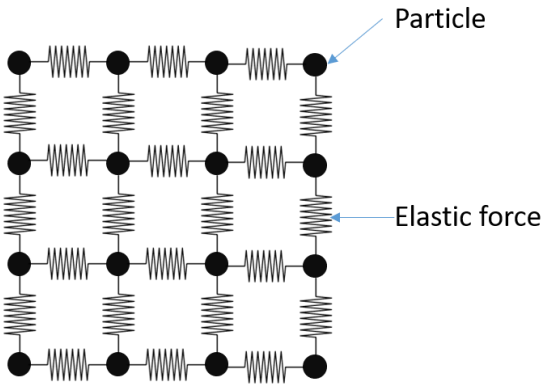

Figure 3-5. Schematic showing a material lattice structure, in one-dimension, at rest.

If all the particles in the first plane oscillate with the same amplitude and frequency (number of oscillations), the elastic forces transmit these oscillations to the second plane and the oscillatory movement is then passed on to the third plane and further along the lattice structure. Due to the interconnection of the planes, they would remain in a constant state of motion (phase). The stiffness of the elastic bond is finite and therefore the rate at which the wave propagates is dependent on the material properties and the phase. The elastic nature of the wave allows the final and initial positions of the particles after the wave deformation has taken place to be identical. Because no permanent material damage takes place, this makes ultrasound waves favourable for non-destructive testing.

The mode of ultrasound wave propagation is dictated by the source and the type of wave. For bulk waves, it is the longitudinal and shear waves that are predominant. Longitudinal waves have the particle motion in the same direction as the wave propagation (Figure 3-6) whereas shear waves have the direction of particle motion perpendicular to the wave motion (Figure 3-7).

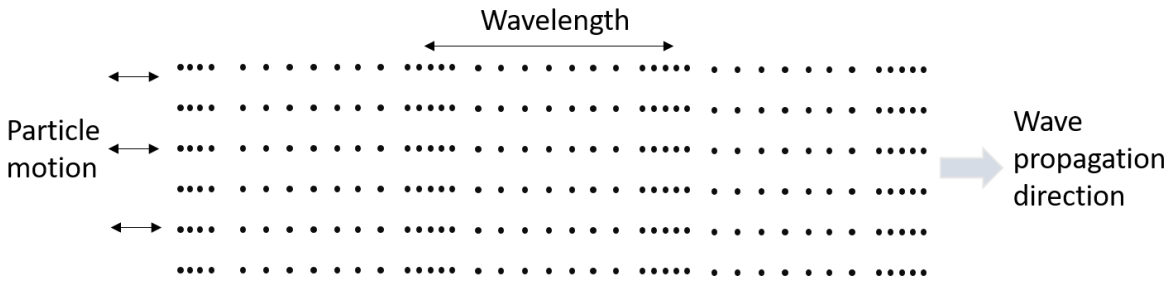

Figure 3-6. Propagation of a longitudinal bulk wave.

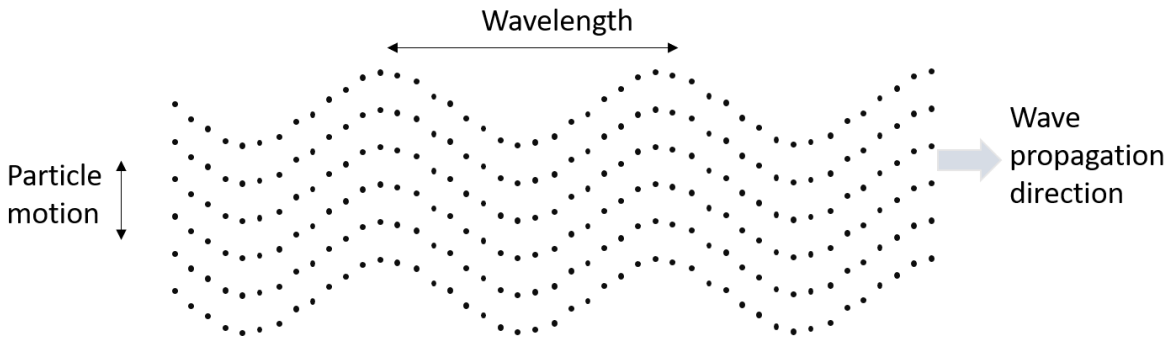

Figure 3-7. Propagation of a shear bulk wave.

The wavelength is defined as the distance between any two planes that have the particles in the same phase. For longitudinal waves, it is the distance between two regions of compression and for shear waves, it is the distance between two peaks or troughs. The wavelength, λ is inversely proportional to frequency, *f* therefore short wavelengths translate to a high frequency and vice versa (Equation 3-2):

$$\lambda = \frac{c}{f} \qquad \text{Equation 3-2}$$

where *c* represents the speed of sound. Shear waves can only propagate in solids whereas longitudinal waves are able to propagate through solids, liquids, and gas. This fact has seen longitudinal bulk waves used for crack detection and thickness and wear measurements. The work contained in this research primarily involves longitudinal wave propagation because the physical parameter measured is the surface coating and film thickness. There are however other types of wave propagation methods namely, Rayleigh waves, Lamb waves, and Love waves. These are examples of surface or guided acoustic waves [45].

3.4 Speed of Sound

The speed at which sound propagates through various media is governed by the wave mode, material properties and frequency. Material elasticity or compressibility is a property that describes how a material changes in volume when it is subjected to an external pressure force. It is defined by the bulk modulus of elasticity, the inverse of compressibility. The elastic forces between particles in a rigid structure determine how quickly they return to their original position and materials where the particles are able to return to their original position faster can vibrate at higher speeds. This explains why sound is able to travel faster through mediums like steel that have higher stiffness as compared to rubber which has lower stiffness.

The density of a material, ρ is the mass per unit volume. Materials with higher density in most cases have larger molecules. Because of their larger mass, they have more inertia and have a slower response to the effects of adjacent particles. This makes materials with larger molecules transmit sound slower. It is worth pointing out that although it widely stated that sound travels faster in solids than gases, it is the dominance of low elasticity over higher density that causes the difference. Elasticity and density depend on temperature and this effect is often observed in fluids than solids.

3.4.1 Plane Waves

For plane waves in solid media, the mode of propagation is assumed to be one dimensional and therefore the Poisson's ratio is not considered. The longitudinal and shear wave speeds are then calculated using Equation 3-3 and Equation 3-4, respectively.

$$c_{longitudinal} = \sqrt{\frac{E}{\rho}} \qquad \text{Equation 3-3}$$

$$c_{shear} = \sqrt{\frac{G}{\rho}} \qquad \text{Equation 3-4}$$

where *c* is the speed of sound, *E* is the Young's modulus of elasticity, ρ is the material density and *G* is the shear modulus. Only longitudinal waves are able to propagate in liquid media because shear waves are not supported in liquids. The longitudinal speed of sound in a liquid is calculated using Equation 3-5:

$$c_{longitudinal} = \sqrt{\frac{B}{\rho}} \qquad \text{Equation 3-5}$$

where *B* is the liquid bulk modulus.

3.4.2 Bulk Waves

Because this research is concerned with bulk material, it is more appropriate to define the bulk wave speed of sound equations because the one-dimensional plane wave speed equations do not hold.

Poisson's ratio does not affect shear bulk waves because there is no change in volume. The bulk shear wave speed is therefore the same as in Equation 3-4 [45]. However, Poisson's ratio affects longitudinal bulk waves that produce some shear deformations in the process. The speed of sound for a longitudinal bulk wave is written as:

$$c_{longitudinal} = \sqrt{\frac{E(1-\upsilon)}{\rho(1+\upsilon)(1-2\upsilon)}} \qquad \text{Equation 3-6}$$

where υ is the Poisson's ratio.

3.5 Acoustic Impedance

The acoustic impedance, *z* is an intrinsic material property that is the product of the material density and the acoustic velocity of an ultrasonic wave in the material property (Equation 3-7).

$$z = \rho c \qquad \text{Equation 3-7}$$

It is used to quantify the ease with which a sound wave is able to travel into a material and is expressed in *Rayl* (*Pa.s/m*). Acoustic impedance determines how an ultrasound wave interacts at a boundary between two different materials. Where two materials have similar acoustic impedances, there will be less of a 'resistance' to the smooth passage of ultrasound wave and so most wave energy will be transmitted through the boundary. However, when the acoustic impedances are dissimilar, most of the ultrasound wave tends to be reflected.

3.6 Attenuation

When an ultrasonic wave is propagating through a material, its amplitude will be reduced as a function of the distance travelled and the attenuation coefficient, α describes the rate at which this reduction in amplitude occurs in a given material.

Attenuation is caused by scattering and absorption. Scattering arises from the fact that a material is not entirely homogenous and can contain some inhomogeneities such as foreign material and pores. There may also be internal flaws within the material. In most common metals, the grains are randomly oriented, and the crystals have different elastic properties that have different sound velocities in various directions. This is known as anisotropy. Absorption occurs when the acoustic

energy is converted to some other form of energy, in most cases it is converted to thermal energy [45].

The attenuation rate depends on frequency, with higher frequencies being attenuated more when compared to lower frequencies over a given distance. When a wave passes through a material structure, a low frequency wave makes the local particles vibrate slower and vice versa. Because of the damping effect of absorption, more energy will be converted from higher velocity particle vibrations. This explains why higher frequency wave fronts are attenuated faster than lower frequency. The attenuation coefficient, α determines how much the amplitude of an initial wave will be reduced and it is expressed in Nepers per metre (Equation 3-8):

$$\alpha = \frac{1}{L} ln \frac{A_0}{A} \qquad \text{Equation 3-8}$$

where L is the material length, A_0 is the initial amplitude and A is the amplitude after the wave has undergone attenuation. This equation can also be rearranged to give:

$$A = A_0 e^{-\alpha L} \qquad \text{Equation 3-9}$$

3.7 Properties of An Ultrasound Signal

An ultrasound wave generated by an ultrasound transducer is characterised by amplitude, centre frequency, and bandwidth in the frequency domain. According to ISO 5577, the bandwidth is defined as the width between the frequency limits at which the pulse amplitude is greater than half the maximum amplitude (or -6dB amplitude reduction) [46]. This is illustrated in Figure 3-8b.

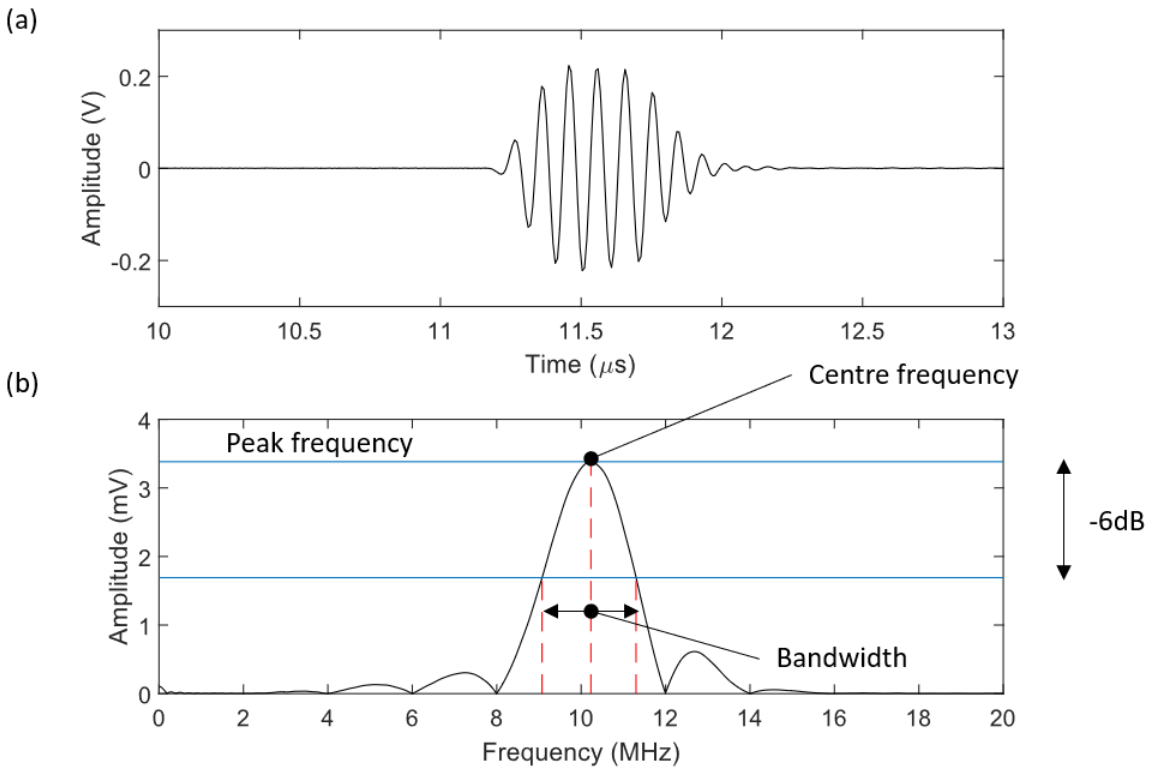

Figure 3-8. (a) A time domain signal of a 10MHz longitudinal pulse and (b) the frequency domain of the pulse signal.

The centre frequency is defined as the mean of the frequency limits of the bandwidth. The relative bandwidth is the ratio of the bandwidth to centre frequency and is usually expressed as a percentage (Equation 3-10).

$$relative\ bandwidth, \% = \frac{bandwidth}{centre\ frequency} \times 100 \qquad \text{Equation 3-10}$$

3.8 Ultrasonic Wave Equations

The wave equation that describes sound behaviour in matter is given in Equation 3-11 [47]. Considering a longitudinal wave propagating along the *x*-axis, the wave equation can be written as:

$$\frac{\partial^2 u}{\partial x^2} = \frac{1}{c^2}\frac{\partial^2 u}{\partial t^2} \qquad \text{Equation 3-11}$$

where *u* is the displacement, *x* is the direction, *t* is the time, and *c* is the wave speed of sound. A generalised solution of the wave equation was demonstrated by d'Alembert in 1747 [48] and is given by:

$$u(x,t) = A(x - ct) + B(x + ct) \qquad \text{Equation 3-12}$$

where *A* and *B* are functions, and the equation now represents two waves travelling in opposite directions (*A* in the positive *x*-direction and *B* in the negative *x*-direction). The wave equation expressed in terms of a simple harmonic motion is given as:

$$u(x,t) = A\ sin\big(k(x - ct)\big) \qquad \text{Equation 3-13}$$

where $k=2\pi/\lambda$ is the wave number. If angular frequency ω is defined as $\omega=kc$, then Equation 3-13 can then be expressed as:

$$u(x,t) = A\ sin(kx - \omega t) \qquad \text{Equation 3-14}$$

where the value $(kx - \omega t)$ represents the phase of the wave. For any integral value *n*, crests occur when $(kx - \omega t) = n\pi + \frac{\pi}{2}$. As time increases, *x* must also increase to maintain the phase $\frac{\pi}{2}$. A complex form of the wave equation is now:

$$u(x,t) = Ae^{i(\omega t - kx)} \qquad \text{Equation 3-15}$$

Considering continuity of wave pressure *P*, the wave equation can be expressed as [47]:

$$P(x,t) = P_x e^{i(\omega t - kx)} \qquad \text{Equation 3-16}$$

where P_x is the amplitude of the pressure wave.

3.8.1 Ultrasound Wave Interaction at A Boundary

When an ultrasonic wave reaches a boundary between two materials with dissimilar acoustic properties, some portion of the wave will be reflected, and some will be transmitted. A schematic of this is illustrated in Figure 3-9, where *P* stands for wave pressure. The subscripts *i*, *r*, and *t* stand for incident, reflected, and transmitted waves, respectively.

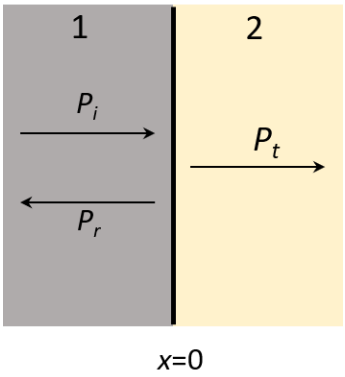

Figure 3-9. Reflection and transmission of an ultrasound wave at a boundary.

The proportion of reflected and transmitted waves in terms of reflection and transmission coefficients, *R* and *T*, respectively gives:

$$P_r = RP_i \qquad \text{Equation 3-17}$$

$$P_t = TP_i \qquad \text{Equation 3-18}$$

In terms of Equation 3-16 the waves on either side of the boundary *x=0* can be represented as:

$$P_i = P_0 e^{i(\omega t - kx)} \qquad \text{Equation 3-19}$$

$$P_r = RP_0 e^{i(\omega t + kx)} \qquad \text{Equation 3-20}$$

$$P_t = TP_0 e^{i(\omega t - kx)} \qquad \text{Equation 3-21}$$

Continuity of wave pressure at the boundary *x*=0 gives:

$$P_i + P_r = P_t \qquad \text{Equation 3-22}$$

Substituting Equation 3-19, Equation 3-20, and Equation 3-21 into Equation 3-22 gives:

$$P_0 e^{i(\omega t - kx)} + RP_0 e^{i(\omega t + kx)} = TP_0 e^{i(\omega t - kx)} \qquad \text{Equation 3-23}$$

Because at the boundary *x=0*, Equation 3-23 reduces to:

$$P_0 e^{i(\omega t)} + RP_0 e^{i(\omega t)} = TP_0 e^{i(\omega t)} \qquad \text{Equation 3-24}$$

Dividing by $P_0 e^{i(\omega t)}$ gives:

$$1 + R = T \qquad \text{Equation 3-25}$$

This is the assumption for a one-dimensional plane wave, and it neglects other waves that may be generated such as surface waves.

Continuity of normal component velocity at *x*=0 gives:

$$u_i - u_r = u_t \qquad \text{Equation 3-26}$$

where u_i, u_r and u_t represent the normal component velocity for the incident, reflected and transmitted waves. The negative sign indicates a reversal in direction of the wave. Where the acoustic impedance is expressed as $z = \frac{P}{u}$, Equation 3-26 can be expressed as:

$$\frac{P_i}{z_1} - \frac{P_r}{z_1} = \frac{P_t}{z_2} \qquad \text{Equation 3-27}$$

where the subscripts *1* and *2* represent the sides of the boundary. This can be simplified to give:

$$\frac{P_i - P_r}{z_1} = \frac{P_t}{z_2} \qquad \text{Equation 3-28}$$

Substituting Equation 3-19, Equation 3-20 and Equation 3-21 into Equation 3-28 gives:

$$\frac{P_0 e^{i(\omega t - kx)} - R P_0 e^{i(\omega t + kx)}}{z_1} = \frac{T P_0 e^{i(\omega t - kx)}}{z_2} \qquad \text{Equation 3-29}$$

At the boundary *x=0*, this reduces to:

$$\frac{P_0 e^{i(\omega t)} - R P_0 e^{i(\omega t)}}{z_1} = \frac{T P_0 e^{i(\omega t)}}{z_2} \qquad \text{Equation 3-30}$$

Equation 3-30 can now be simplified and in terms of *R*:

$$\frac{1 - R}{z_1} = \frac{1 + R}{z_2} \qquad \text{Equation 3-31}$$

This can further be rearranged to give *R* in terms of acoustic impedances of the materials on either side of the boundary:

$$R = \frac{z_2 - z_1}{z_2 + z_1} \qquad \text{Equation 3-32}$$

The transmission coefficient in terms of acoustic impedances is given as:

$$T = \frac{2 z_2}{z_2 + z_1} \qquad \text{Equation 3-33}$$

3.8.2 Ultrasound Wave Reflection for A Three-Layer System

Figure 3-10 shows ultrasound reflection at normal incidence in a three-layered system where medium 2 has a thickness *h* and is sandwiched between semi-infinite mediums 1 and 3. The continuity of displacement and pressure field is given in Equation 3-16 where P_x is a constant.

The wave normally incident in medium 1 arrives at the boundary *x=0* and a proportion is transmitted into medium 2 while the rest is reflected back. The transmitted wave then propagates through medium 2 until it reaches the boundary *x=h* upon which some proportion will be transmitted into medium 3 and the rest is reflected. This reflected wave then reaches boundary x=0 and the process repeats.

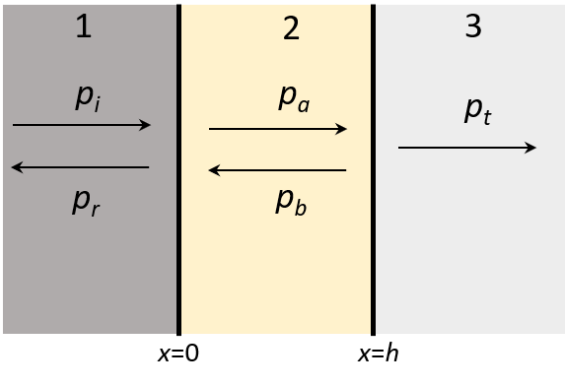

Figure 3-10. Reflection and transmission of an ultrasound wave in a three-layered system.

If the wavelength of the incident wave is smaller than the thickness *h*, the echoes in medium 2 will be discrete and will be separated in the time domain by $\frac{2h}{c_2}$. The thickness *h* can then be calculated as:

$$h = \frac{c_2 \times t}{2} \qquad \text{Equation 3-34}$$

where c_2 is the speed of sound in medium 2. This is otherwise known as the time-of-flight method. When the wavelength is much larger than the thickness *h*, the reflection of the wave is dependent on the embedded layer properties and the bounding materials. The complex wave pressures in Figure 3-10 are as follows:

$$p_i = P_i e^{i(\omega t - k_1 x)} \qquad \text{Equation 3-35}$$

$$p_r = P_r e^{i(\omega t + k_1 x)} \qquad \text{Equation 3-36}$$

$$p_a = A e^{i(\omega t - k_2 x)} \qquad \text{Equation 3-37}$$

$$p_b = B e^{i(\omega t + k_2 x)} \qquad \text{Equation 3-38}$$

$$p_t = P_t e^{i(\omega t - k_3 x)} \qquad \text{Equation 3-39}$$

At the boundary *x=0*, the continuity of wave pressure gives:

$$P_i + P_r = A + B \qquad \text{Equation 3-40}$$

Continuity of normal component velocity gives:

$$u_i - u_r = u_a - u_b \qquad \text{Equation 3-41}$$

Continuity of acoustic impedance gives:

$$\frac{P_i + P_r}{u_i - u_r} = \frac{A + B}{u_a - u_b} \qquad \text{Equation 3-42}$$

where $u = \frac{P}{z}$, this can then be expressed as:

$$z_1 \frac{P_i + P_r}{P_i - P_r} = z_2 \frac{A + B}{A - B} \quad \text{Equation 3-43}$$

At the boundary *x=h*:

$$Ae^{i(\omega t - k_2 h)} + Be^{i(\omega t + k_2 h)} = P_t e^{i(\omega t - k_3 x)} \quad \text{Equation 3-44}$$

And in terms of acoustic impedance:

$$z_2 \frac{Ae^{i(\omega t - k_2 h)} + Be^{i(\omega t + k_2 h)}}{Ae^{i(\omega t - k_2 h)} - Be^{i(\omega t + k_2 h)}} = z_3 \quad \text{Equation 3-45}$$

Algebraic manipulation of the boundary conditions *x=0* and *x=h* gives the reflection coefficient for a three-layered model with respect to continuity of acoustic impedance as [47];

$$R = \frac{\left(1 - \frac{z_1}{z_3}\right)\cos(k_2 h) + i\left(\frac{z_2}{z_3} - \frac{z_1}{z_2}\right)\sin(k_2 h)}{\left(1 + \frac{z_1}{z_3}\right)\cos(k_2 h) + i\left(\frac{z_2}{z_3} + \frac{z_1}{z_2}\right)\sin(k_2 h)} \quad \text{Equation 3-46}$$

Where medium 2 is trapped between solid half spaces, medium 2 is normally treated as a series of springs and the reflection coefficient *R* now becomes a function of medium 2 stiffness [49];

$$R = \frac{z_1 - z_3 + i\omega(z_1 z_3 / K)}{z_1 + z_3 + i\omega(z_1 z_3 / K)} \quad \text{Equation 3-47}$$

where *K* is medium 2 stiffness in terms of acoustic properties and thickness *h*.

$$K = \frac{\rho {c_2}^2}{h} \quad \text{Equation 3-48}$$

If the materials on either side are identical, for example the case of a constrained lubricant film, such that $z_1 = z_3 = z'$, Equation 3-47 reduces to:

$$R = \frac{1}{\sqrt{1 + \left(\frac{2K}{\omega z'}\right)}} \quad \text{Equation 3-49}$$

This is applicable to very thin films (~50nm to 10μm) that are assumed to be quasi-static [9]. Measurement of very thin films smaller than 50nm is often affected by inaccuracies due to noise and anything above 10μm is impractical because *R tends* to unity. Ideally *R* values in the range 0.1 to 0.9 are considered reasonable when using the spring model.

Above 10μm film thickness a resonance method is usually applied. The reflection coefficient spectra will show minima at a definite number of half wavelengths that are related to the layer thickness. The relationship between the resonant frequency f_m and the thickness *h* has been proven numerically by Pialucha and is given as [8];

$$f_m = \frac{mc_2}{2h}$$ Equation 3-50

where f_m is the resonant frequency and m is the mode number of the resonant frequency. This formula has received much attention and has been reported in literature in measuring embedded lubricant film thickness [9], [40], [41], [50].

3.9 Quarter Wavelength Theory

When there is a great acoustic mismatch between mediums 1 and 3 as seen in the scenario of a steel-coating-air, the reflection coefficient in Equation 3-47 tends towards 1 and calculating the stiffness K becomes difficult. In this instance, a special case arises when the thickness of the intermediate layer in Figure 3-10 is some multiple of the driving frequency wavelength. From Equation 3-46, when $k_2 h = (n - 1/2)\pi$ where n is any integer, then $k_2 h = \pi/2$ for fundamental frequency i.e. $(f = f_0)$ [47] :

$$\frac{\pi}{2} = \frac{2\pi f_0 h}{c_2}$$ Equation 3-51

and

$$h = \frac{c_2}{4f_0}$$ Equation 3-52

Equation 3-52 shows the relationship between the driving frequency f_0 and the thickness h of the intermediate layer such that ultrasound is transmitted when the thickness of the layer is a quarter of the driving frequency wavelength. This frequency is identified in the frequency domain signal. The sound will also be transmitted at other resonant modes and the equation can now be written as:

$$h = \frac{c_2(2n - 1)}{4f_n}$$ Equation 3-53

where n represents the mode. Chen et al. [7] also report on this relationship between f_0 and the layer thickness, h.

A schematic to show quarter wavelength destructive interference is shown in Figure 3-11. When the thickness of the layer is a quarter of the wavelength of the driving frequency, the incident wave will be *'neatly'* transmitted into the layer and will be reflected at two interfaces as shown in Figure 3-11. The reflected waves are 180° out of phase and therefore cancel out with each other.

This phenomenon has been widely used especially in clinical ultrasound applications to provide an acoustic bridge dubbed 'matching layer' between the piezoelectric elements and the human body to allow for the smooth transmission and receiving of ultrasound waves. There is normally an acoustic gradient between the piezoelectric transducers (high acoustic impedance) and the human skin (low acoustic impedance) such that most useful ultrasound wave is reflected back. However, a matching layer is chosen that has its acoustic impedance in between the transducer and the human skin and a thickness that is a quarter of the driving frequency wavelength. A liquid-based coupling is also used to allow transmission to the human skin.

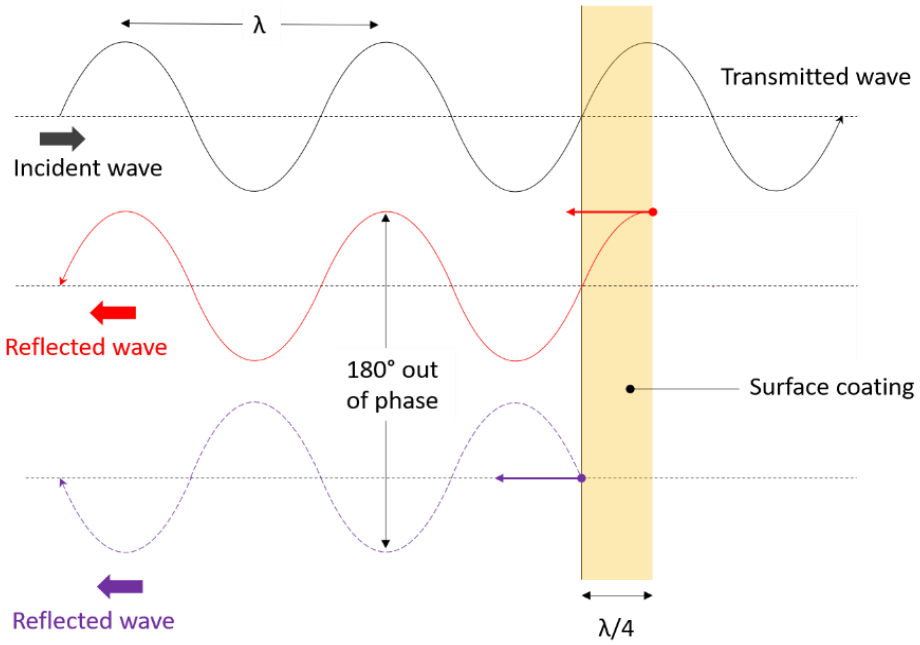

Figure 3-11. Schematic to show quarter wavelength destructive interference.

3.10 Standing Wave

When two waves are travelling in opposite directions, they will interfere, and a resultant standing wave will be set up which is dictated by the sum of the wave pressure amplitudes [45]. For simplicity sinusoidal waves can be considered in an incident and reflected manner. An example of a standing wave that is formed from an incident and reflected wave travelling in opposite directions is shown in Figure 3-12.

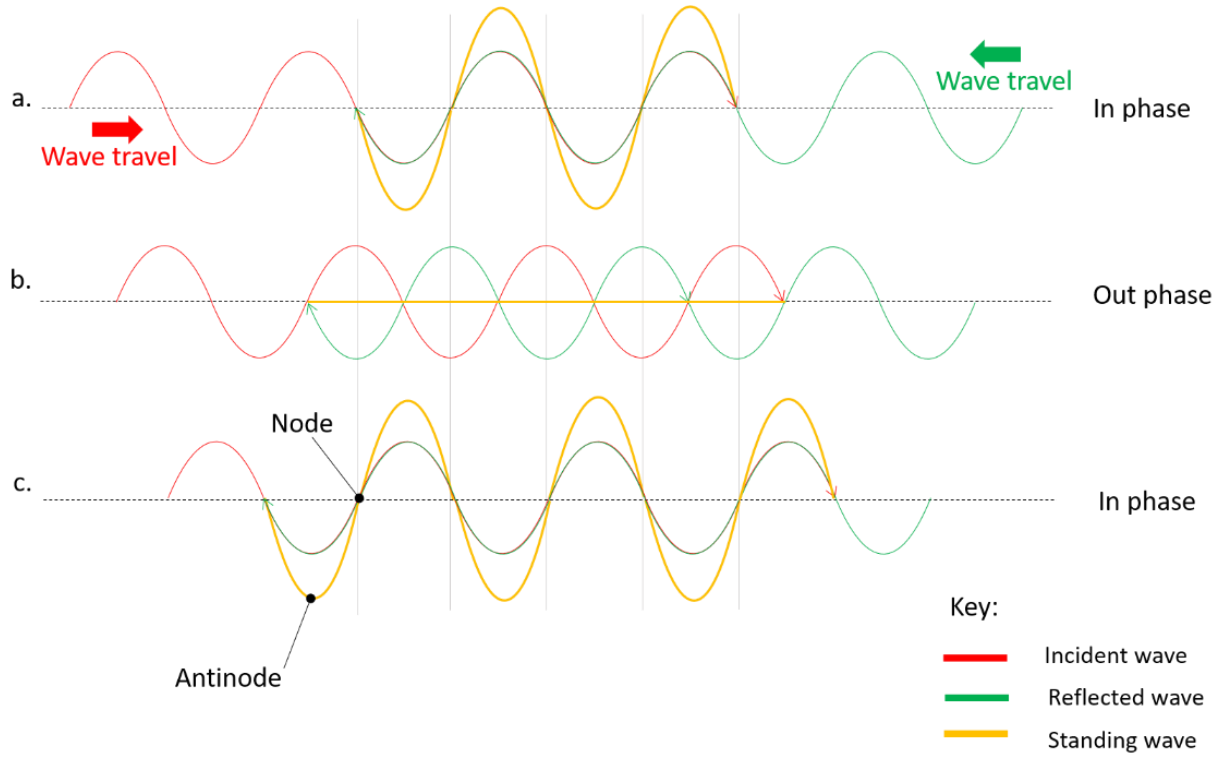

Figure 3-12. Constructive and destructive interference of two waves travelling in opposite directions to set up a standing wave (interference in time).

When travelling waves of identical frequency and amplitude cross at the same phase, the waves will constructively interfere to form a superimposed standing wave that is a sum of the wave amplitudes. When the waves cross at 180° out of phase, destructive interference occurs, and the resultant wave has zero amplitude. This interference is illustrated in Figure 3-13.

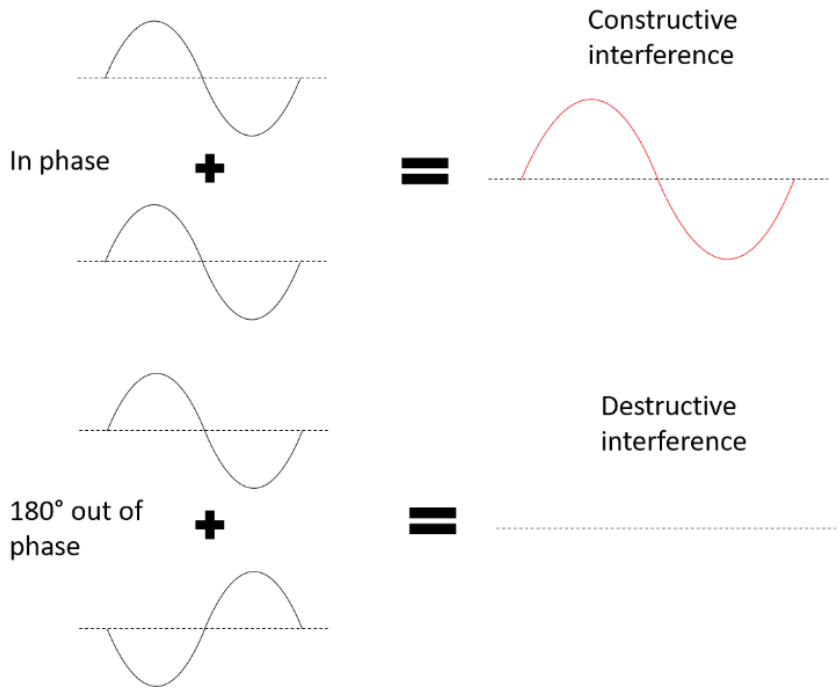

Figure 3-13. Constructive and destructive wave interference.

Going back to Figure 3-12, nodes are points with zero amplitude and antinodes are points with maximum amplitudes. Nodes appear to remain at rest whereas antinodes fluctuate at the extremities provided the incident wave is continuous. The standing wave is therefore a stationary wave even though it is a result of travelling waves. At a particular driving frequency, the standing wave amplitude will be at a maximum. This is a function of the component material properties. If the driving frequency, f_d matches the natural or resonant frequency of the component, f_s then this maximum amplitude occurs. Therefore:

$$f_d = f_s \qquad \text{Equation 3-54}$$

The resonant frequencies are otherwise known as harmonics and the lowest harmonic (fundamental frequency) occurs when the wavelength, λ is equal to twice the component length, L i.e.

$$\lambda = 2L \qquad \text{Equation 3-55}$$

The equation for resonant frequency is therefore written as:

$$f_s = \frac{nc}{2L} \qquad \text{Equation 3-56}$$

where n represents the integer mode ($n=1$ for fundamental frequency). The higher the harmonic the more the maximum peak amplitudes. This is demonstrated in Figure 3-14. These peak amplitudes are separated by the fundamental frequency in the frequency domain.

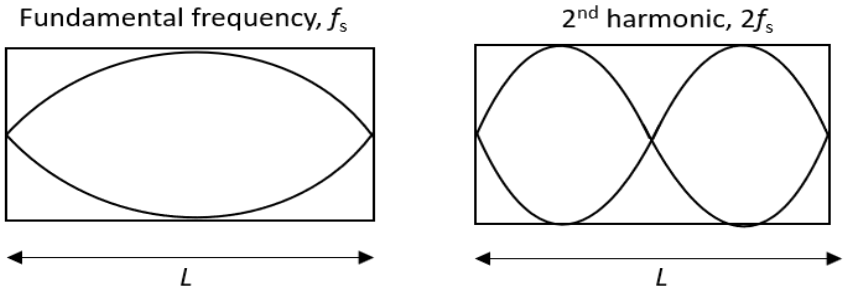

Figure 3-14. Schematic showing the fundamental frequency and second harmonic of a solid component.

Material resonant modes have been used to measure plate and pipe thickness in the past. Nowadays it is being used to determine the material elastic properties and for inspection of small part defects [51].

3.11 Multiple Reflections

The use of multiple reflections to increase the accuracy of resonant frequency identification from a reflection coefficient spectrum has recently been reported by Dou et al. [52]. The results showed that the reflection coefficient for a steel-oil-steel approaches zero when the number of reflections *n* is 50. A plot showing the influence of number of echoes on the reflection coefficient spectrum is shown in Figure 3-15.

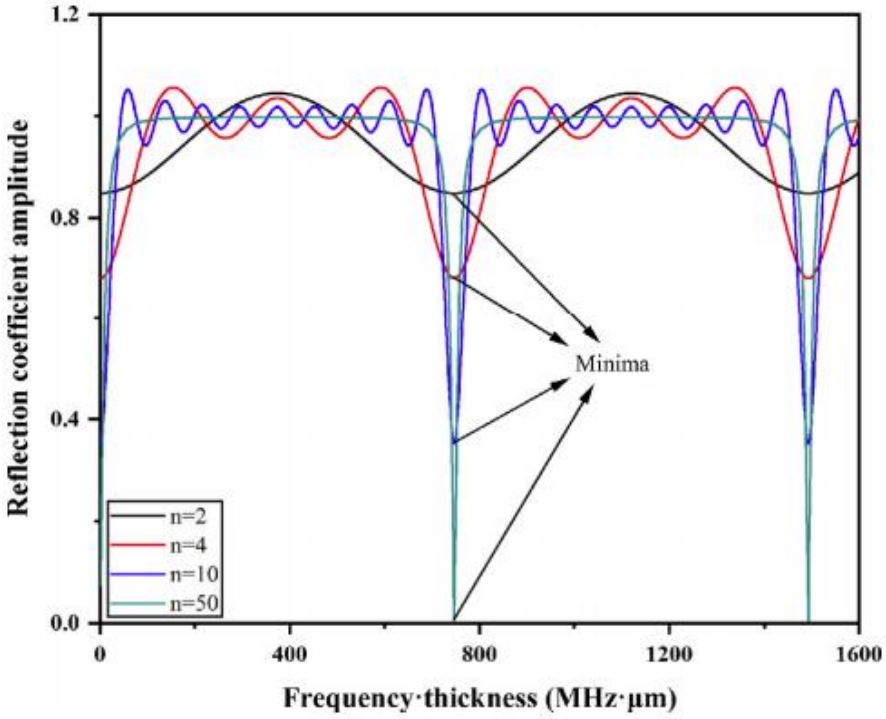

Figure 3-15. Change in reflection coefficient spectrum with increasing number of echoes (image taken from [52]).

It should be noted that the number of reflections does not affect the frequency position but rather improves on the accuracy of identification of the resonant frequency ergo the measurement

sensitivity. Therefore, the more the number of reflections the sharper the appearance of the resonant frequency.

Elsewhere, the use of multiple reflections has been used to increase the ultrasonic viscosity measurement sensitivity of a liquid at a solid-liquid interface [53]. The measured reflection coefficients difference between two liquids increased from 0.5% to 3% when six echoes were considered.

3.12 Summary

The ultrasound method is ideal for the thickness measurement of thin surface coatings and films non-invasively and in-situ. There are a number of commercial transducers available for this purpose, but bare piezoelectric materials are more convenient due to their ability to be miniaturised in order to fit most engineering components that have complex geometries.

The reflection of an ultrasonic wave from an interface of interest and the embedded information obtained from the ultrasound waves can be used in suitable mathematical equations to quantify the thickness of surface coatings and films. Of particular interest in this research is the ultrasonic thickness measurement of unbound thin surface coatings and films. Where the surface coating is sufficiently thick, the thickness of the coating is calculated from the time difference between the discrete echoes, otherwise known as the time-of-flight technique. However, a limitation encountered when using this technique is when the coating thickness becomes too thin, the reflected echoes overlap temporally, and it becomes difficult to extract the travel time in the time domain. A resonance method is one way to overcome this limitation, where the layer thickness is related to the resonant frequency by the quarter wavelength theory. These principles will be used to understand the thickness measurement of thin surface coatings and film using ultrasonic methods in the next chapter.

4 Literature Review

This chapter aims to build on the ultrasound principles that were discussed in chapter 3 by presenting a literature review of some key ultrasonic methods that are used for surface coating and film thickness measurement. These methods will be categorised into themes, and each will be discussed by highlighting a select few relevant works. Their limitations are then used to identify a potential research gap that is the foundation for the rest of this research work.

4.1 Time-of-Flight Method

For thick films where the thickness of a surface coating/film is significantly greater than the ultrasonic wavelength, a time-of-flight approach is applied where the time it takes for a pulsed wave to propagate the coating length is converted to a distance, provided the speed of sound in the coating is known and there is negligible effect on the dependence of the propagation velocity on temperature. A usual problem with this technique is the accurate identification of the start of the echo in the time domain. Noise within the system and shape distortion affect the signal that is transmitted, and this makes it difficult to identify the exact start of the echo. There are four main methods for the accurate determination of the start of the echo [54]. These are outlined in the following sub-sections.

4.1.1 Maximum Peak Detection

A common detection method that requires little processing time is to take the maximum peak position difference of the echoes temporally. This is illustrated in Figure 4-1.

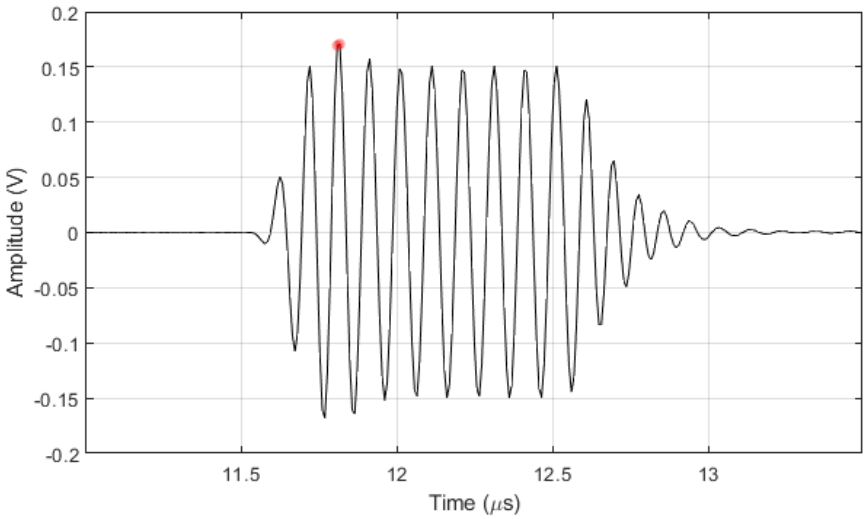

Figure 4-1. Maximum peak detection analysis.

This method is most convenient when the successive echoes have the same shape and the time difference between the maximum peaks will provide the time-of-flight measurement. However, in some instances, the echo may be inverted, and the maximum peak method becomes impractical. The maximum peak may also be located close to another peak with a slightly lesser amplitude such that noise interference may cause these peaks to change in amplitude. Phase change also affects this measurement technique. The sampling rate also affects the maximum peak position and interpolation is usually applied to increase the resolution by using a fitting algorithm. This added step of using an algorithm increases the complexity of the data analysis process and the signal is still affected by noise.

4.1.2 Zero Crossing

The zero-crossing technique is applied to detect the point along the wave form that crosses the horizontal axis. To do this, a half-cycle is normally selected and points on either side of the zero-cross point are fitted using a linear fit function. The point of intersection of the linear function with the horizontal axis is calculated as the zero-cross point. This is illustrated in Figure 4-2.

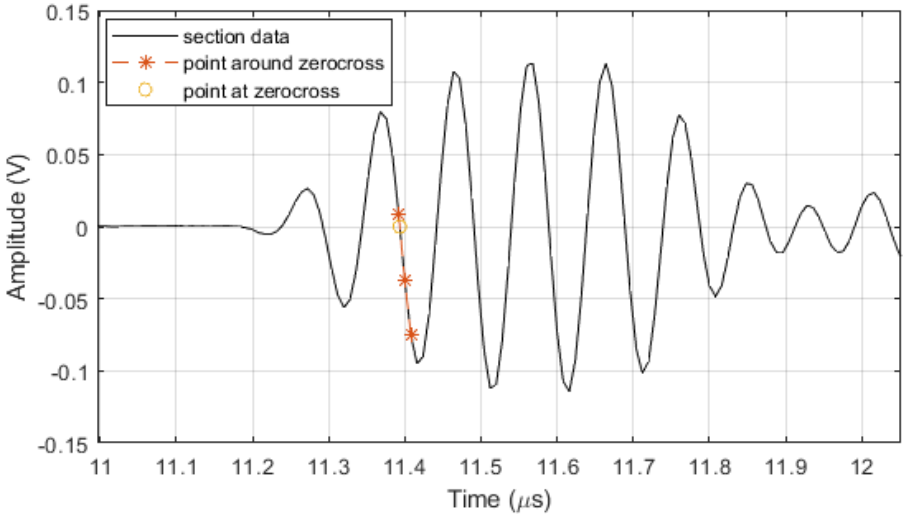

Figure 4-2. Zero-cross detection analysis.

4.1.3 Threshold

This technique takes the time at a particular amplitude threshold crossing. To do this, usually the maximum peak is selected, and the waveform is normalised using this. Then at a certain amplitude threshold, for example, at the first 40% amplitude point of the normalised waveform, points are fitted on either side and a linear fitting function is used to fit the points. Interpolation is used to calculate the time stamp. An example of this is shown in Figure 4-3.

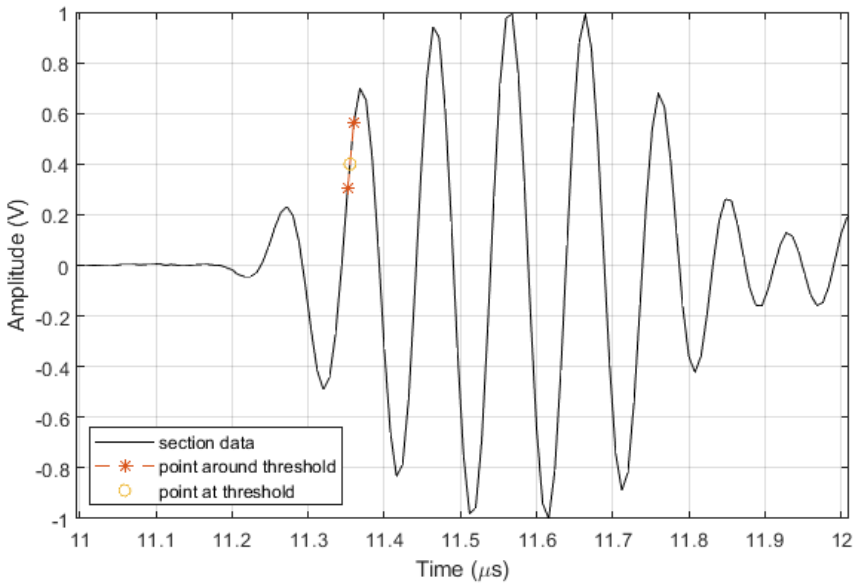

Figure 4-3. Threshold analysis.

4.1.4 Analytical

The aforementioned techniques are affected by the phase change and also rely on the shape of the pulse signal. In order to remove the phase change effect, an analytical signal is normally used. To do this, a Hilbert transform signal processing function is used to recreate the imaginary part from the recorded signal. Next, an envelope is applied that covers both the real and imaginary parts. A maximum peak detection analysis or even the threshold technique can then be applied to extract the time. An example of a peak detection technique on an analytical signal is shown in Figure 4-4.

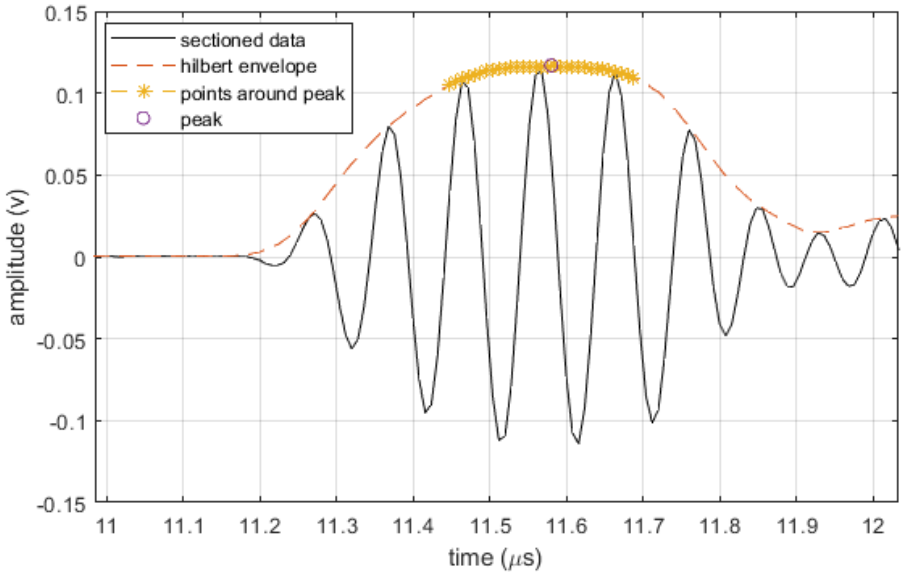

Figure 4-4. Analytical analysis.

This technique is complex as it requires multiple signal processing steps, although it provides the added advantage of not being susceptible to changes in phase in comparison to the rest. There are also cross-correlation algorithms and filtering techniques that can be used [55]–[57]. For thin films where the wavelength is greater than the surface coating/film thickness, the reflected echoes overlap in the time domain, and it becomes difficult to apply the time-of-flight analyses. Alternative signal processing techniques are necessary to resolve this. Examples include, but are not limited to, deconvolution techniques, resonance methods, and spring models. These will be discussed in the following sections.

4.2 Deconvolution

Deconvolution methods to improve the time resolution of overlapped echoes have been used that span the time, frequency and wavelet domains and a significant body of work has been reported on this. For example, a method to extract the time difference from the overlapped echoes in an embedded layer is to reconstruct the signal in the time domain using reflections from the solid-liquid boundary [5]. The signal from the layer, S_{layer}, is calculated by subtracting the reference signal, $S_{m,ref}$ (where the echoes do not overlap) from the measurement signal S_{ref} for discrete data. This is given by:

$$S_{layer}[k] = S_{ref}[k] - S_{m,ref}[k] \qquad \text{Equation 4-1}$$

These signals are a summation of the reflections *S* from an upper steel medium illustrated in Figure 4-5.

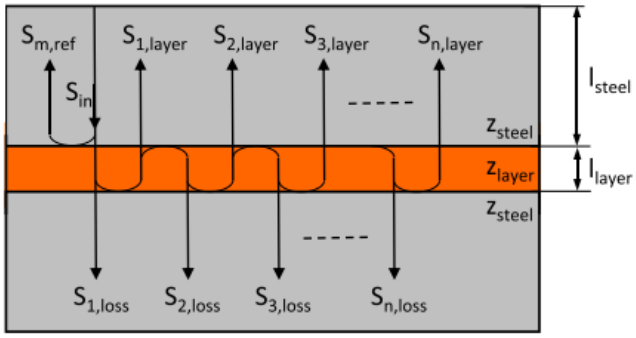

Figure 4-5. A schematic of the multiple reflections from within a layer (extracted from [5]).

The simulated signals $S_m[k-i]$ are reconstructed from amplitude weighting factors that are based on the reflection coefficient *R* (Equation 3-32) at the steel-layer and layer-steel boundaries. A linear correlation coefficient of the measured and simulated signals is calculated and stored in a vector *C(i)* until $i=i_{max}$. The vector has a maximum peak at $C(i_{peak})$ that corresponds to $ToF = i_{peak}\frac{1}{f_s}$. The layer thickness is then calculated by:

$$s = \frac{c_l ToF}{2} \qquad \text{Equation 4-2}$$

where c_l represents the speed of sound in the layer. The reference signal must not overlap with the solid-liquid signal for this method to work. The simulated and measured signals are compared and the TOF can be calculated. The authors reported a measured minimum thickness of 30μm with a relative error of 4.9%.

Elsewhere, Kimball et al. [6] reported on the ultrasonic measurement of n-pentane film on a copper plate from as low as 8μm to a few millimetres using a modified ToF signal processing technique with an accuracy of ±10% from experimental results. The modified technique involved simulating the echoes and then summing them up to recreate the signal response. The modelled signal was then compared to experimentally acquired signals for films of different thicknesses. The copper-pentane echo was removed from the total echo response by subtracting out a reference copper-air response. The resultant simulated and measured responses were compared by a least square fit. The predicted condensation rate and the measured n-pentane film thicknesses showed excellent agreement. The pentane film thickness was also predicted analytically using heat flux equations.

In another study, Mor et al. [58] reconstructed the overlapped echoes using an approximation method that was based on the representation of ultrasonic echoes by single prototype atoms that possess physical interpretation and this was used to measure the thickness of thin adhesive layers ranging from 0.1mm to 0.5mm. The authors reported on the accurate approximations of the simulated results to the measured results, although this technique is very complex and time consuming.

A wavelet transform method has been used to calculate the lubricant film thickness from reflected ultrasonic signals [59]. The transient characteristics in the ultrasonic signals were picked by a

modulus maximum method and the time difference between these points was used to estimate the time-of-flight. A flowchart representing this algorithm is shown in Figure 4-6.

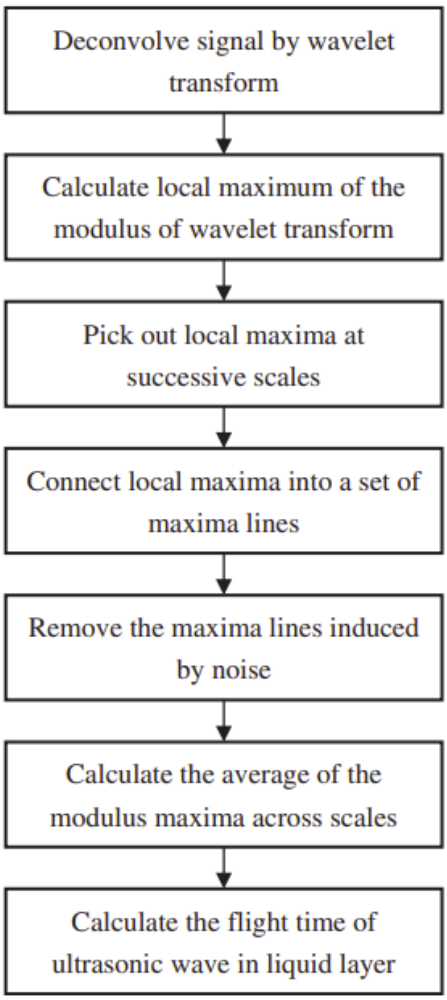

Figure 4-6. A flowchart of a wavelet transform as reported by Jiao et al. [59].

Honarvar et al. [60] have reported on the use of a Wiener filter to deconvolve the signals. The autoregressive coefficients from various frequency windows in a 3-10dB drop as a recommendation were calculated via a Burg method and the coefficients were extrapolated to the frequency windows. The coefficients were combined then averaged and an inverse Fourier transform was applied to acquire the extrapolated time signal. The authors report on an improved signal-to-noise ratio and time resolution.

4.3 Resonance Method

Resonance methods have been used that rely on the frequency dependence of wave interference in a thin film that causes the layer to act as a special reflector producing a periodic function in frequency [8]. The resonant frequency can be extracted by getting the frequency minimum in the reflection coefficient amplitude spectrum. The inverse for the transmission coefficient also holds.

There has been considerable work for measuring embedded fluid film thicknesses using the resonance method where the time-of-flight cannot be applied due to superimposition of echoes. However, because the work involved in this research is focused on unconstrained layers, the resonance method reviewed will be centred on such.

Pedersen et al. [61] have reported on the use of standing waves to measure the thickness of unconstrained fluid layers as low as 50μm on a copper block by sending broadband ultrasound pulses from the back face using a 10MHz contact transducer in a pulse-echo set-up. The layer reflectivity $R_{layer}(t)$ was calculated using:

$$R_{layer}(t) = R(t) - R_0(t) \qquad \text{Equation 4-3}$$

where $R(t)$ was the overall reflectivity and $R_0(t)$ reference reflectivity for a copper-air interface. The layer reflectivity was modelled, and the fluid resonances occurred in odd number harmonics. These harmonics were related to the fluid thickness using Equation 3-53. The authors also reported ultrasonically measured condensation rate of 1.77μm/s which had a good correlation with condensation rate of 1.55μm/s measured from heat transfer equations. The lowest thickness measured was limited by the bandwidth of the 10MHz transducer.

The thickness of condensing and non-condensing fluid layers on a copper block were measured using an array of eight 5MHz contact transducers operated in a pulse-echo mode [7]. A photograph of the set-up is shown in Figure 4-7 and a schematic is shown in Figure 4-8.

Figure 4-7. A photograph showing eight 5MHz planar piston contact transducers closely spaced that were coupled on to a copper block with coupling gel (extracted from [7]). Each contact transducer is 12.7mm in diameter.

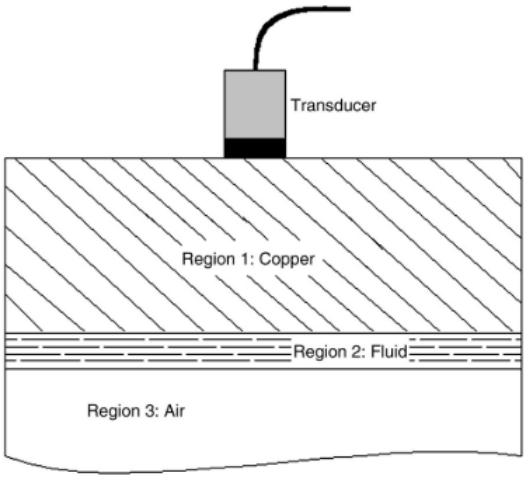

Figure 4-8. The schematic of a contact transducer in contact with the copper block (extracted from [7]).

Where the surface films were greater than 1000μm the time-of-flight technique was applied while for thin films, a resonance method was applied. Optical methods were used to validate the wavelengths and experimental results showed a good correlation with numerical modelling for stagnant film thickness measurements. The condensing and non-condensing thickness measurements applied the impulse-induced resonance method that has been reported by Lynnworth and Papadakis [62], [63]. The reflectivity of the layer is a periodic function in the frequency domain. Because the echoes from the copper-fluid interface were much larger in the time domain than the echoes from the fluid-vapor interface, the authors extracted the latter echoes from the total echo by subtracting the copper-air interface from the real part of the total echo signal. The result when modelled in the frequency domain showed oddly spaced spectral peaks that corresponded to the odd number harmonic response of the fluid layer. The fluid thickness was then calculated using:

$$h = \frac{nc_f}{4f_n} \qquad \text{Equation 4-4}$$

where *n* represents the mode number, c_f represents the speed of sound in the fluid and f_n represents the harmonic frequency. The film thicknesses measured ranged from 50μm to 500μm with an error of 11μm for thin films and 6% for thicker films. The lowest measurable film thickness was limited by the bandwidth of the transducer.

Haines et al. [64] have reported on the potential use of ultrasonic spectroscopy to measure the thickness of corrosion layers inside a nuclear reactor. The work described used broadband ultrasonic pulses in the range 1-30MHz to measure a 185μm epoxy layer on an aluminium substrate. They have also reported on the ultrasonic measurement of magnetite coatings ranging from 140μm to 650μm on mild steel substrates. The quarter wavelength theory was used in calculating the coating thicknesses. The authors reported that where the resonant frequencies for a thin magnetite coating could not be directly identified from the amplitude spectrum, the phase spectrum would still reveal these resonant frequencies as evidenced in the phase angle change. Deconvolution of ultrasound pulses was also noted as a promising avenue although it was limited by an increase in the computing time. The phase change measurement as a function of frequency was used in determining the acoustic properties of a layered medium such as the acoustic velocity, attenuation, and impedance.

Li et al. [65] have measured epoxy coating thicknesses ranging from 53μm to 510μm on an aluminium plate by analysing the frequency-shifts of the substrate resonances in the low frequency regime using 1MHz and 2MHz transducers in a pulse-echo set-up. Newton iterative and Taylor expansion methods were applied to solve for the frequency-shifts using the derived equations. Experimental results agreed with numerical modelling. The reflection coefficient due to the layer, calculated using a continuum model, showed minima at odd harmonics and the phase variation crossed the horizontal axis at these frequencies. The quarter wavelength theory was then used to calculate the epoxy coating thicknesses.

The thickness of plexiglass coatings (50μm-100μm) on aluminium substrate have been measured ultrasonically using 10MHz and 20MHz contact transducers with relative error of ±2μm [66]. Transfer functions were derived and an inverse algorithm that applied the Newton-Raphson

method was used to reconstruct the phase velocity and thickness by comparing experimental and theoretical transfer functions. The technique was capable of measuring both the coating thickness and phase velocity from the same measurement without knowing either one. Although the reported errors were low, the signal processing in itself was complex.

The thickness, density, longitudinal and shear elastic moduli and attenuation of polystyrene film embedded between aluminium plates have been measured using normal and oblique incidence ultrasound waves [67]. The ultrasonic response was described using six nondimensional parameters and an inverse algorithm was applied to determine the layer properties using simple analytical expressions. Where none of the nondimensional parameters were not known beforehand, the normal incidence measurement could not be applied, and this is the reason for applying oblique incidence measurement. Normal incidence measurement can however still be applied if one of the non-dimensional parameters is known. A polystyrene film thickness of 141μm was measured with a relative error of 2.3%. The ultrasonic technique of using normal and oblique incidence measurement was then extended to measure coating properties on a thin plate [68]. A 51μm thick polypropylene coating on a 203μm steel foil was measured ultrasonically, the same type of coating normally used in food cans.

A main disadvantage with the resonance model when using conventional pulsed wave methods is the selection of the correct mode number for resonance dips that lie within the transducer bandwidth. For multiple dips, the mode number can be estimated, but difficulty arises for a single dip where the mode number is in most cases assumed, and this introduces significant measurement errors [69].

4.4 Spring Model

The reflected echoes at the substrate and lubricant boundaries can become overlapped severely such that the frequency that causes resonance falls outside of the measurable range. When this happens, for a substrate-lubricant-substrate scenario, a spring model approach is used, based on the amplitude of the wave pulses. The spring model has been used in measuring constrained lubricant film thicknesses and a large body of research has reported on this [9], [40], [41], [50]. Although the focus of this research work is centred on the measurement of unconstrained film thickness measurement, it is still worthwhile to understand how the spring model method works.

When the wavelength of an ultrasound pulse is greater than the embedded film layer thickness, the layer acts as a special reflector and the reflection coefficient is given using Equation 3-47. The magnitude of the reflection coefficient vector can be written as:

$$|R| = \frac{1}{\sqrt{1 + (2K/\omega z)^2}} \qquad \text{Equation 4-5}$$

provided that the materials on either side of the embedded layer have identical acoustic impedance. The measured reflection coefficient can then be used to calculate the layer stiffness K with the prerequisite that the impedance of the surrounding material is known. The stiffness is related to the layer thickness using [9];

$$K = \frac{\rho {c_2}^2}{h} \qquad \text{Equation 4-6}$$

The film thickness is then calculated by combining Equation 4-5 and Equation 4-6. This is only applicable to quasi-static thin layers [69]. Dwyer-Joyce et al. [9] have reported that practical measurements when using the spring model are possible when *R* is less than 0.9 and greater than 0.1.

4.5 Surface Guided Waves

The use of surface guided waves in measuring the thickness of surface coatings has also received considerable attention over the past years due to their high sensitivities. The guided wave velocities are dependent on the frequency and the thickness of the coating. A large body of research exists that is beyond the scope of this research and therefore only the working principles for using surface guided waves will be discussed.

The thickness of vacuum plasma sprayed NiCoCrAlY coatings of varying thicknesses (190-330μm) have been estimated by measuring the Rayleigh wave velocities as a function of frequency [70]. The velocities were then compared to the theoretical dispersion curve to estimate the coating thicknesses. There was a good agreement between ultrasonically and optically measured coating thicknesses. Figure 4-9 shows a schematic of Rayleigh wave velocity measurement.

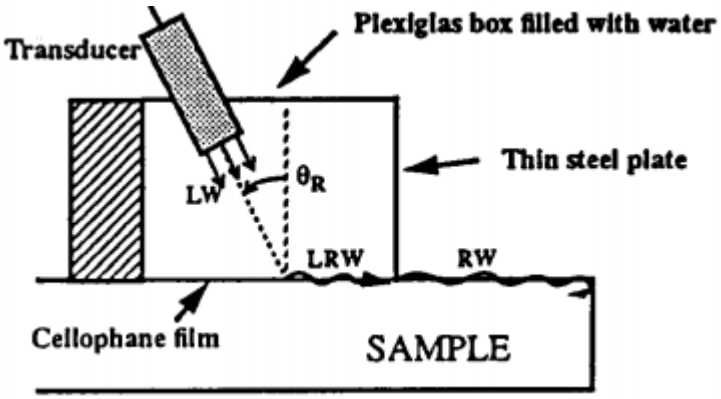

Figure 4-9. A schematic showing Rayleigh wave velocity measurements (extracted from [70]).

For this method, a special transducer is operated in a pulse-echo setting and is inclined to the surface of the sample. The transducer is contained in a water filled box such that the longitudinal waves (LW) from the transducer are converted to leaky Rayleigh waves (LRW) upon reaching the water-sample surface. Then the LRW are then converted to pure Rayleigh waves (RW) at the edge of the transducer and propagate to the corner edge of the sample and are reflected back to the same transducer. The RW of any velocity can be sent and received.

The transmission time of Lamb waves on a glass plate was measured for gelatine, acrylic lacquer and correction fluid of different thicknesses (20-120μm) and a direct correlation was found between the transit time and the layer thickness [71].

The propagation of surface guided waves for measurement of coating thickness has also been reported by various researchers [72]–[74]. Elsewhere, the thickness of very thin Langmuir-Blodgett films, as low as 3nm (one monolayer), have been detected and the monolayers can be distinguished by using piezoelectric surface guided wave devices [75]–[77].

4.6 Swept Frequency

The use of acoustic resonance spectroscopy (ARS) for non-destructive evaluation was first reported by Dipen Sinha in 1992 where an object's resonances are excited by slowly sweeping through frequencies, provided that there are no internal vibrations [78]. A linear frequency sweep, also known as a chirp, is a signal that is modulated in frequency, meaning that it is possible to excite a range of frequencies with a single chirp. An example of a chirp is illustrated in Figure 4-10.

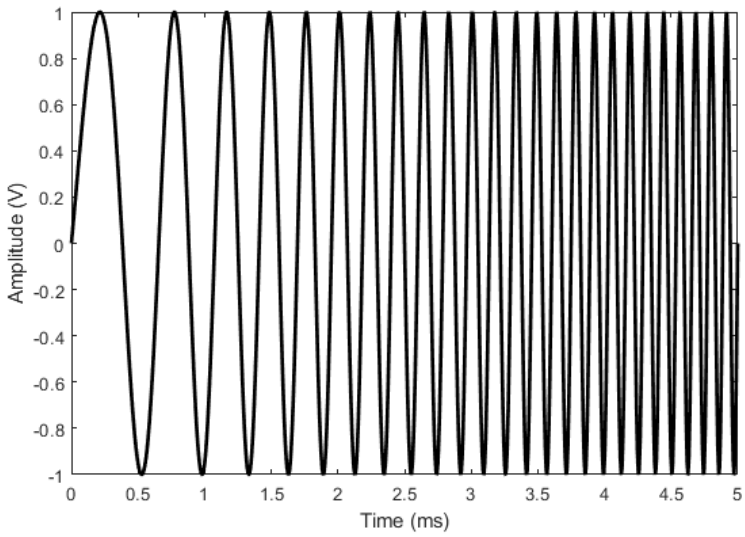

Figure 4-10. A representation of a 1kHz-9kHz chirp in the time domain.

ARS was later published in 1997 as a nonintrusive technique for detecting and characterising chemical warfare compounds inside closed ammunitions by determining the frequency-dependent sound attenuation and sound speed that was used to determine the liquid density [79]. ARS was reported to be highly sensitive for the detection of contamination (<0.01%). This technique has also been reported to utilise the acoustic signature of the closed vessel to extract the liquid density and viscosity data [80].

Three primary uses of ARS were identified namely:

I. Comparison of material acoustic signatures to reference materials to detect flaws and physical changes in the object.
II. Monitoring the acoustic signature to detect wear.
III. To identify objects within closed chambers using their acoustic signatures.

Two acoustic transducers are normally used in a pitch-catch setting so that one is used to excite the natural frequencies within the object and the receiver to detect and monitor the resultant vibrations (Figure 4-11a). The excitation frequency is uniformly swept having typical sweep times between 5-30 seconds depending on the application. Slower sweeping times are reported to be used for high-resolution data. A resultant acoustic spectrum shows the normal modes of the object and the size of the object determines the number of normal modes that are to be excited (Equation 3-56). An example of a swept frequency transmission spectrum for a transducer-wall-fluid-filled cavity is shown in Figure 4-11b [81]. Resonant peaks are formed where the incident and reflected waves constructively interfere resulting in a standing wave.

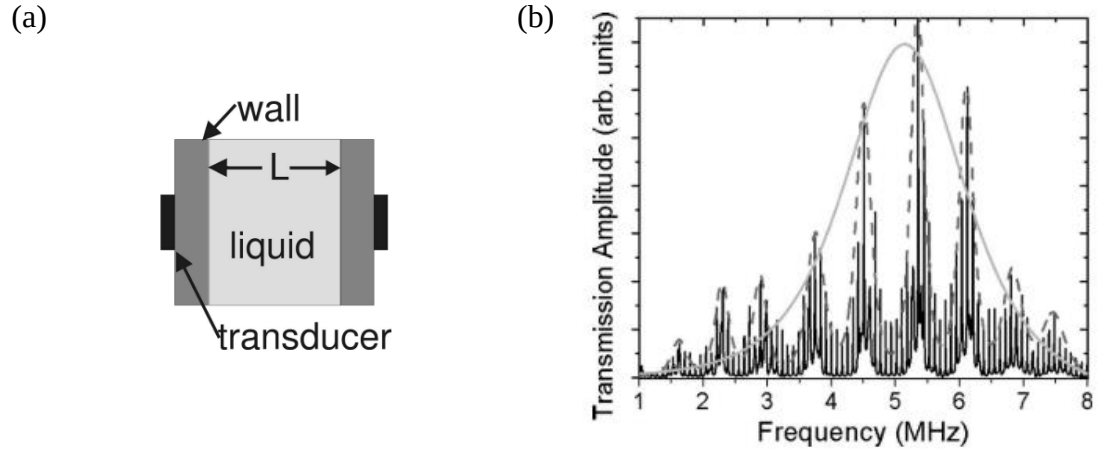

Figure 4-11. (a) A schematic of a swept frequency interferometry cell (b) A typical frequency response from a swept frequency interferometry cell (extracted from [81]).

From Figure 4-11b, three resonance patterns are superimposed on the overall spectrum. The solid grey profile represents the overriding 5MHz transducers frequency response. The dashed line profile represents the wall resonance that has a fundamental frequency of ~800kHz, evidenced by the spacing between the resonances. Lastly, the fluid resonances are observed spaced at ~80kHz. These resonances are caused by the incident and reflected travelling waves that interfere to create a standing wave. Provided the liquid length, *L* is known, the liquid speed of sound can be accurately determined by measuring the spacing between the liquid resonant peaks. Figure 4-12 shows the resonant peaks of degassed, distilled water in the fluid cavity *L* of 8.848mm at ambient pressure and temperature.

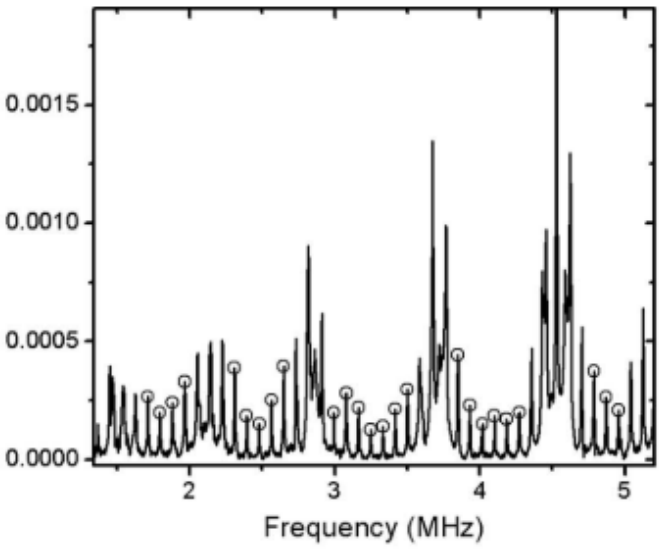

Figure 4-12. Liquid resonant peaks identified by open circles.

The spacings between the open circles were plotted against the mode number and a least-squares fit was used to estimate the liquid fundamental resonance. The speed of sound was then calculated as 1511.4 ± 0.6 m/s with the overriding uncertainty reported as the fundamental frequency deviation of 33 Hz. The speed of sound was later expressed as a function of pressure at 31°C and the experimental results showed excellent correlation with those predicted using values from literature [82].

4.7 Summary

Key ultrasonic techniques for surface coating and film thickness measurement have been discussed. For relatively thick coatings and films, the thickness measurement is usually inferred from the travel time of the ultrasound pulse in the time domain, provided the speed of sound in the layer is provided. As the thickness reduces, the echoes overlap, and deconvolution methods are usually used in the first instance to extract the time-of-flight. The deconvolution methods are, however, quite complex and involve numerous steps.

Resonance methods are applied where the wavelength is greater than the film thickness causing the layer to act as a special reflector producing oddly spaced spectral peaks in the frequency domain. The layer resonant frequency is related to the layer thickness using the quarter wavelength theory. The measurability of the layer thickness using the resonance method for the lower limit is limited by the bandwidth of the transducer. There is, however, no upper limit in using this method. The detectability of the layer resonant harmonics becomes difficult in the case where multiple resonances occur, but only one is detectable within the usable bandwidth.

Therefore, there is a clear need for investigating a pulsing technique that aims to expand the usable bandwidth to allow for detection of coating/thin layer resonances that would otherwise lie outside the narrow bandwidth encountered when using conventional methods. The use of a sweeping frequency technique can be used to increase the usable bandwidth where the component resonant frequencies can be used as measurement points. There is also a necessity for increased sensitivity in the identification of resonant frequency modes from a reflection coefficient spectrum. It has been proved numerically that the use of multiple reflections is able to resolve this by decreasing the resonant mode magnitude with increasing number of reflections [52]. A combination of these two vital factors indicate a potential research gap that requires investigation. The work that follows in this research aims to address this.

The body of this work is centred on the use of a continuously repeating chirp wave (swept frequency approach). The multiple reflections superimpose to form a standing wave within a substrate. The standing wave is highly sensitive to presence of a surface coating/film due to the multiple reflections and is furthermore able to detect coating/ thin layer resonances that would otherwise be undetectable using conventional pulse-echo methods.

It is hypothesised that this novel ultrasonic approach can be used to overcome the limitations that are normally associated with conventional pulse-echo resonance methods.

5 Standing Wave Experimental Approach

This chapter aims to discuss a novel experimental approach for measuring a surface coating and film thickness by using a continuously pulsed superimposed standing wave. The generation and structure of a standing wave that is formed by continuously sending a repeating chirp wave will first be discussed followed by a simple benchtop instrumentation and signal processing to determine an epoxy coating thickness. The coating thickness measured by a standing wave method was then compared with independent surface profilometry measurements for validation.

5.1 The Standing Wave Methodology

A standing wave method for the measurement of surface coating and film thickness has been proposed by Mills et al. [83] that relies on the underlying principles of ultrasound standing waves and resonances. A frequency sweep that is centred around the transducer nominal frequency is continuously repeated to set up a standing wave within a component as a result of constructive and destructive interferences between incident and reflected waves. The standing wave can be used to measure the various conditions at the boundary interface. However, of interest in this research work is the surface coating and film thickness parameter. This is done by analysing the standing wave responses for solid-air and solid-coating/film boundary conditions. An example of a standing wave signal is shown in Figure 5-1.

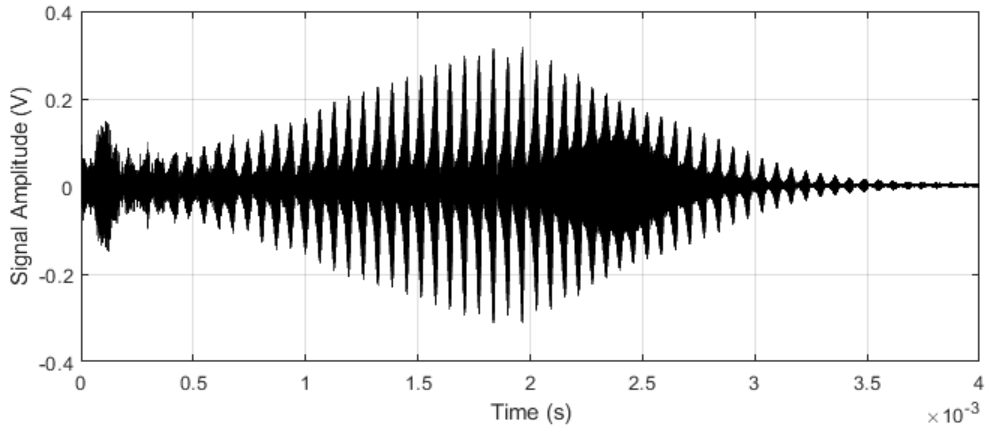

Figure 5-1. A standing wave time domain signal.

The generation of a standing wave will be discussed in the following section.

5.2 Standing Wave Generation

A standing wave with multiple frequencies is created by continuously sending a repeating chirp wave. A chirp is a linear frequency sweep meaning multiple frequencies are able to be excited using just a single chirp. An illustration of a chirp is shown in Figure 4-10 in the chapter 4. A pitch-catch arrangement is a necessity due to the continuous nature of the pulsing, such that one sensor is continuously sending ultrasound waves and the other sensor is capable of acquiring the reflected signals.

In order to understand the mechanisms that are responsible for establishment of a standing wave that has multiple frequencies, it is important to first consider the multiple reflections of a single frequency within a component.

When an ultrasound wave is incident upon a component, it will propagate and undergo attenuation depending on the material properties, and upon reaching the boundary interface, it will be reflected and returned towards the source and further attenuation will occur. This process then repeats itself until the wave decays to zero. The interference of the reflected waves with the incident waves, with the condition that the incident wave is continuous, creates a standing wave within the component (as discussed in section 3.10), with regions of maximum pressure (antinodes) and zero pressure (nodes). An illustration of this is shown in Figure 5-2.

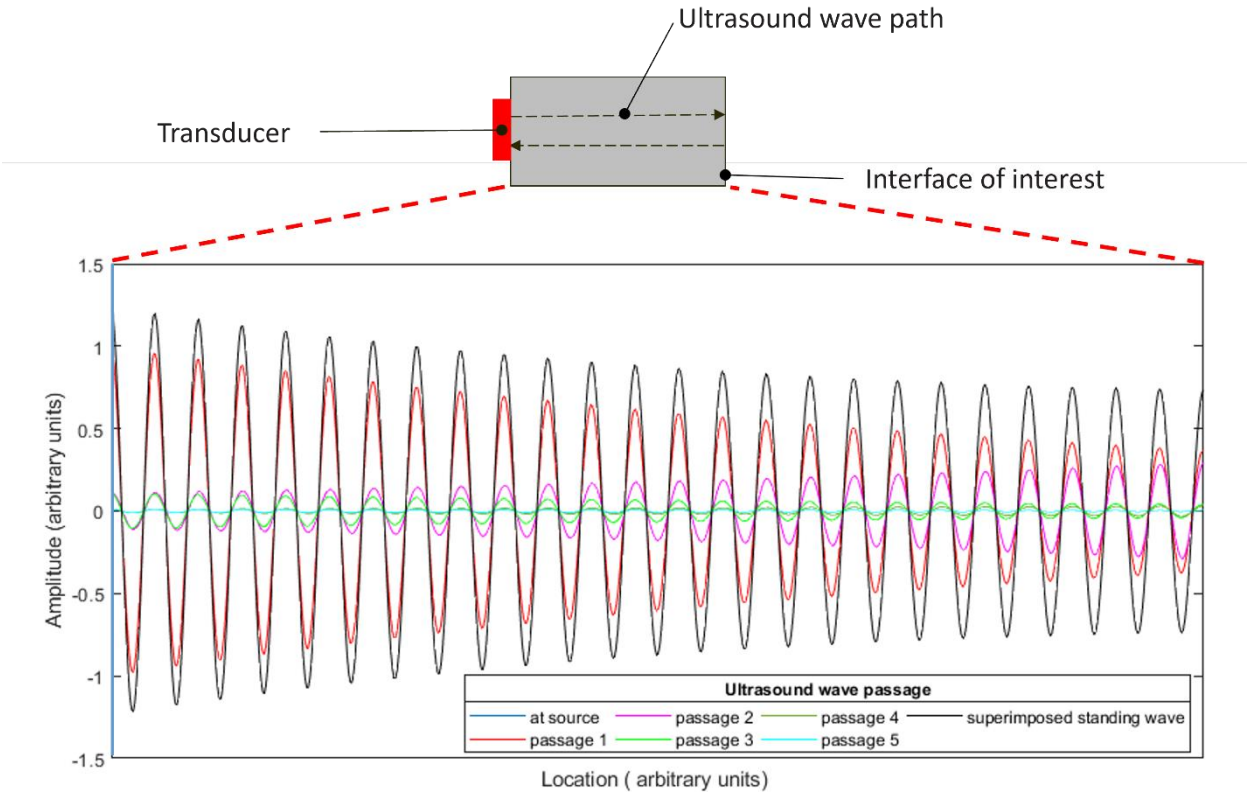

Figure 5-2. Schematic diagram showing the formation of a standing wave from a single frequency.

In this demonstration, the ultrasound wave amplitude decays to almost zero after five passages (a passage to mean travel from the source to the interface of interest or vice versa).

In order to experimentally generate a standing wave with multiple frequencies within a component, the frequency sweep, sweep time, centre frequency and input voltage parameters have to be taken into consideration. In this study, these parameters will be considered for a 10MHz transducer on a 10mm thick aluminium plate. A 4V peak-to-peak 19MHz frequency chirp was continuously repeated every 4ms, having a 10MHz centre frequency. These parameters settings are illustrated in Figure 5-3.

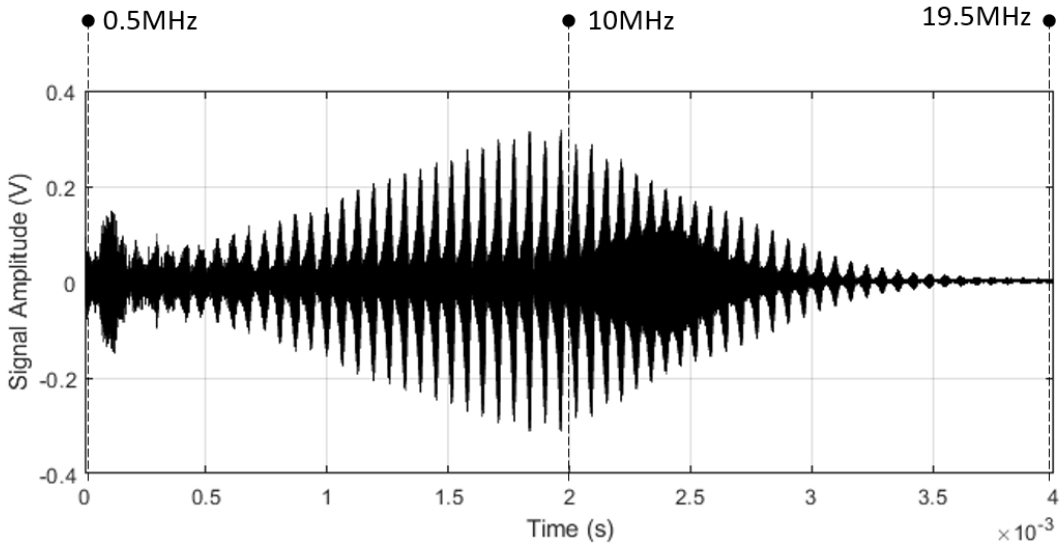

Figure 5-3. Parameters for the standing wave.

The frequency range was chosen to maximise on the usable bandwidth. Figure 5-4 shows a schematic illustration of the 4ms frequency sweep (Figure 5-3) for a duration of 12ms.

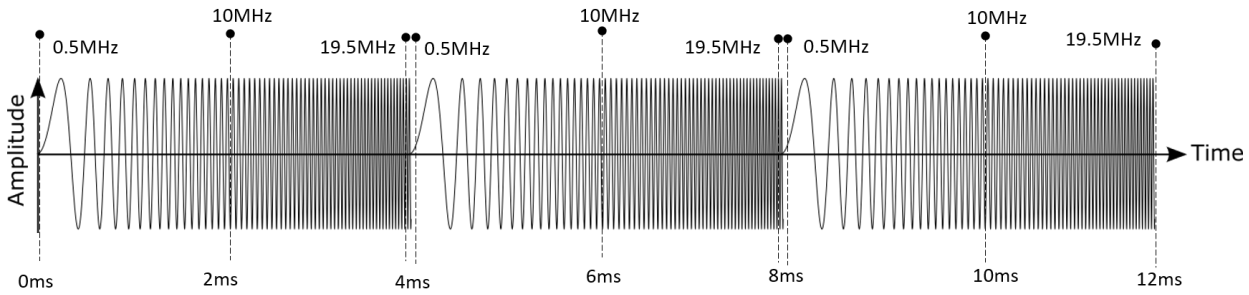

Figure 5-4. Illustration of the repeating nature of the frequency sweep.

This illustration is an oversimplification of the actual mechanisms, nonetheless it serves to demonstrate the repetitive nature of the pulsing technique.

In this study, the time it takes for an ultrasound wave to propagate through the aluminium component (10mm thick) for one reflection is 3.22μs (provided the speed of sound in the aluminium is known). This was calculated using Equation 5-1.

$$t(s) = \frac{2 \times L}{c} = \frac{2 \times 0.01m}{6211\ m/s} = 3.22\mu s \qquad \text{Equation 5-1}$$

For a linear frequency sweep of 19MHz over a 1ms sweep time duration, it was calculated that the output frequency would change by 61.18kHz for the duration of one reflection. The longer the sweep time the less the change in frequency as illustrated in Figure 5-5.

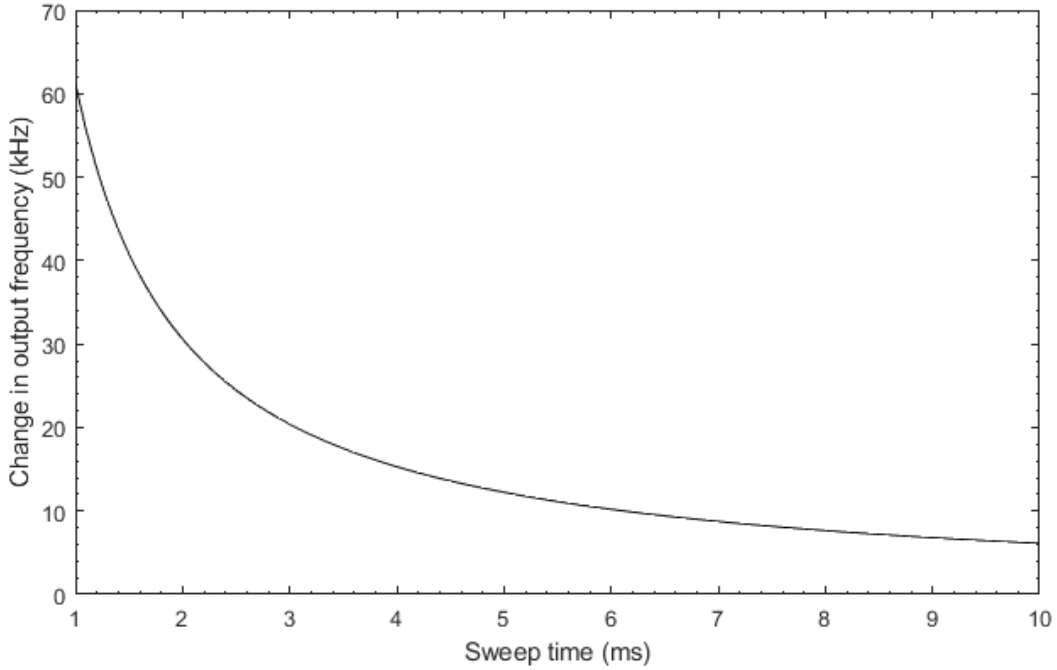

Figure 5-5. Change in output frequency for one reflection for various sweep times.

For frequencies in the MHz range this would correspond to a frequency change of 6.12% for a frequency of 1MHz, and 0.61% at 10MHz. Longer frequency sweep durations have a reduced frequency change as a percentage of the consecutive frequency in the frequency sweep and this percentage reduces with increasing MHz frequencies. This is shown in Figure 5-6.

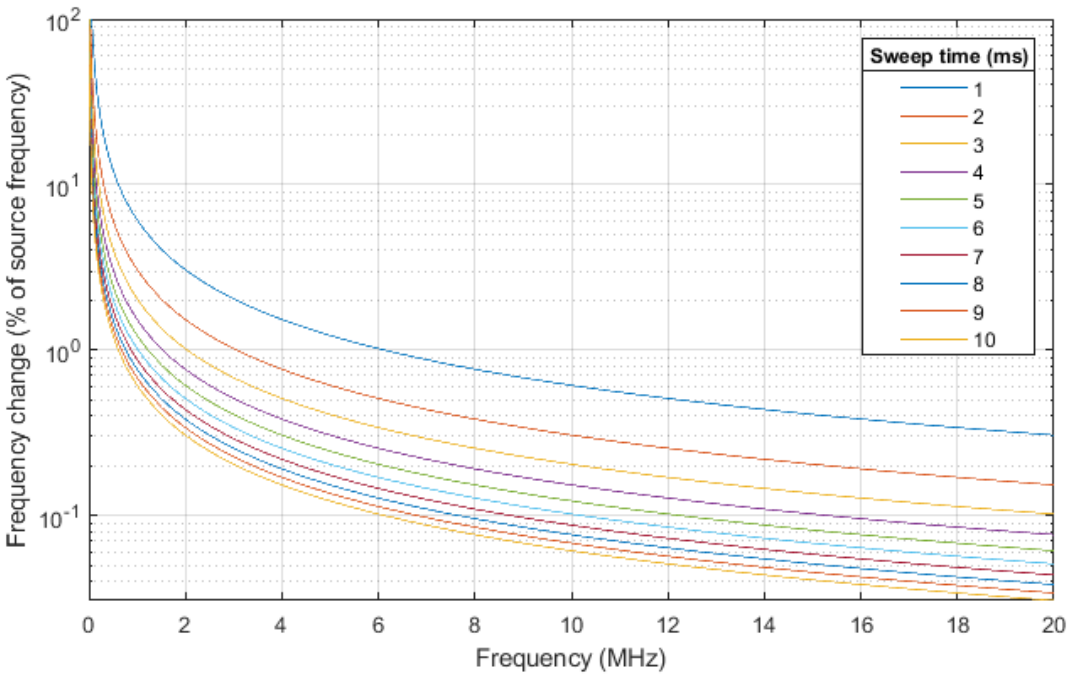

Figure 5-6. Frequency change as a percentage of frequency in a frequency sweep for various sweep times.

Therefore, the frequency sweep needs to be sufficiently long to allow for the full formation of the standing wave, but not too long such that it is formed inefficiently.

5.3 Structure of A Standing Wave

A standing wave that is formed as a result of the input parameters in Table 5-1 is shown in Figure 5-7.

Table 5-1. Standing wave input parameters for 10MHz transducer.

Input	Setting
Centre frequency, (MHz)	10
Frequency sweep (span), MHz	19
Sweep time, (ms)	4
Peak to peak voltage, (Volts)	4

The magnified profiles show that the standing wave is made up of discrete points that are a result of the multiple waves that interfere within the component. The multiple reflections within the component also contribute to the amplitude of the standing wave.

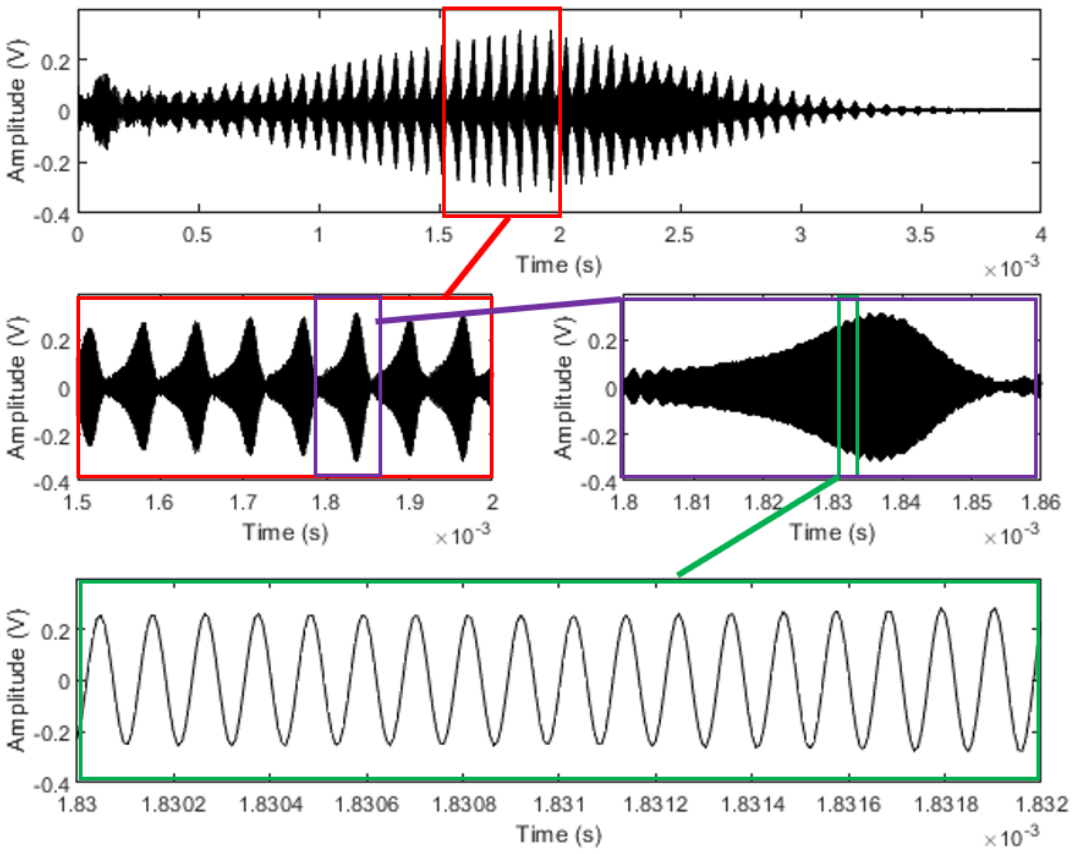

Figure 5-7. (Top) A standing wave profile shown in the time domain. (Middle and bottom) The magnified profiles of the standing wave.

Sweeping through multiple frequencies in a linear chirp allows for the identification of composite resonant frequencies of the component and the transducer in form of peaks (antinodes). The

transducer and component material properties therefore have a significant effect on the standing wave amplitude.

An illustration of a typical linear frequency sweep (chirp) is illustrated in Figure 5-8a.

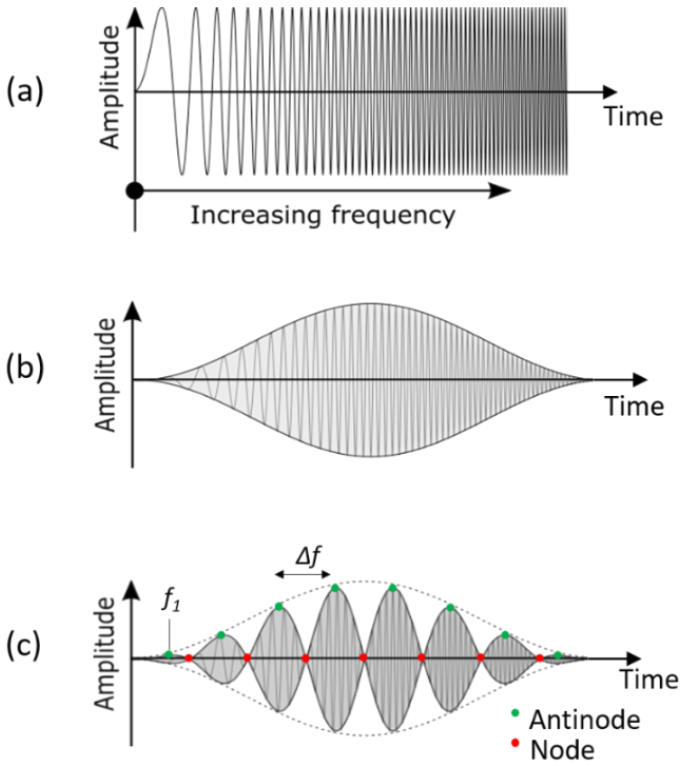

Figure 5-8. (a) A linear chirp (b) modulating effect of the transducer (c) modulating effect of the transducer and the component (f_1 is the first harmonic and Δf is the resonant frequency).

However, transducers normally have a finite bandwidth and are not able to generate all the frequencies in the linear chirp to have the same amplitude. A normal frequency sweep from a transducer therefore has the profile of an envelope as illustrated in Figure 5-8b such that the lower and higher frequencies are produced at generally lower amplitudes. When sweeping through frequencies, the driving frequency constructively interferes with its reflections to set up a standing wave and at certain points in time that are related to the driving frequency, a maximum amplitude (antinode) is generated. Zero amplitudes (nodes) are generated where destructive interference occurs. This is illustrated in Figure 5-8c and is dependent on the component length. If the acquisition window matches the sweep time of the standing wave, the nodes and antinodes appear to be stationary. In practise however, the nodes are never fully achieved, and the antinode profiles are rarely as smooth as illustrated in Figure 5-8. Performing a Fast Fourier Transform (FFT) of the time domain reveals the frequency components of the standing wave. A FFT of the standing wave in Figure 5-7a is shown in Figure 5-9.

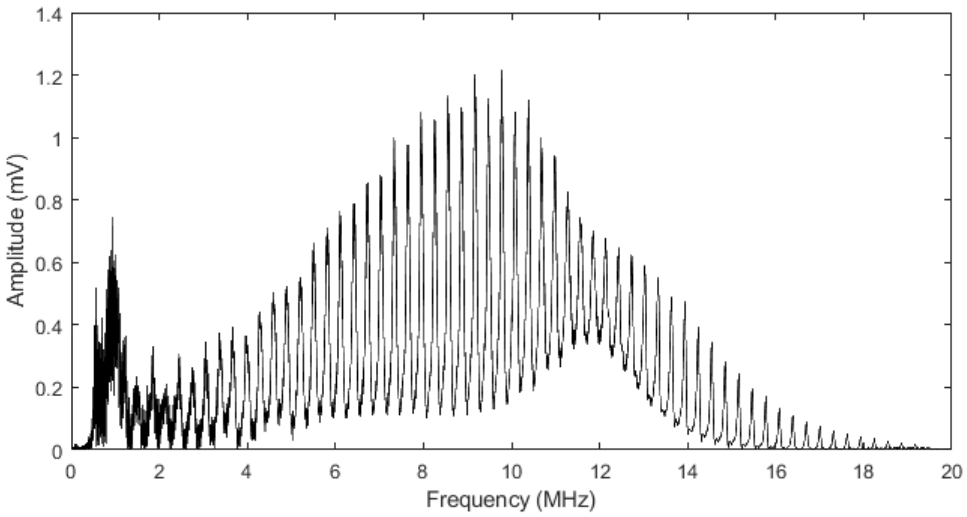

Figure 5-9. FFT of the standing wave response in Figure 5-7a.

The peaks correspond to the substrate harmonic frequencies. Using Equation 3-56, the resonant frequency for a 10mm aluminium plate was calculated as 311kHz. The first harmonic lies outside the frequency sweep, however, the separation between successive peaks of the standing wave frequency response corresponds to the component resonant frequency. Using Equation 3-50, the resonant peak at 9.17MHz was estimated as the 29th component resonant mode. Figure 5-10 shows a zoomed-in profile of the frequency response to illustrate the peak separations.

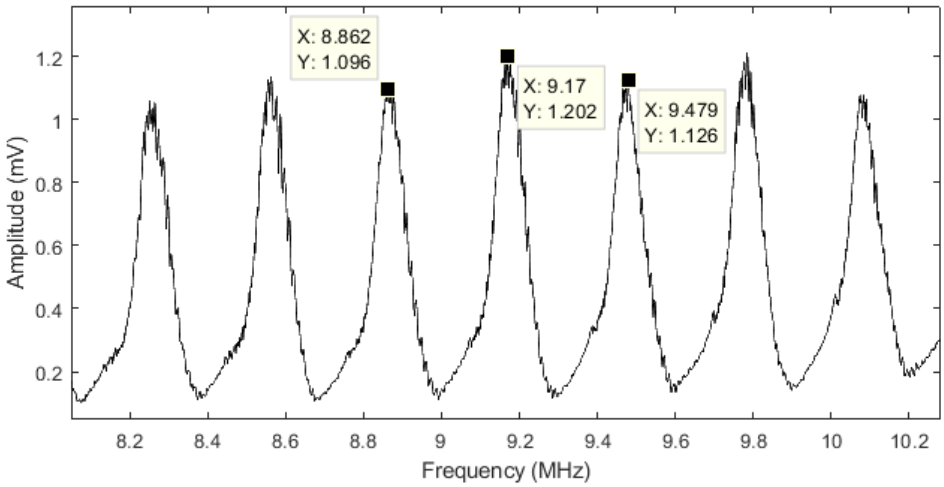

Figure 5-10. Magnified standing wave frequency signal to show separation between successive peaks. 26th to 31st resonant modes

The average peak separation was calculated as 305kHz with a standard deviation of 11.7kHz. Energy coupling at the aluminium and transducer interface was observed in the range 11-13MHz [80]. This range corresponded to the transducer resonance. This is illustrated in Figure 5-11. The fundamental frequency of a 10MHz longitudinal transducer with a 0.2mm thickness and an acoustic velocity of 4350 ms^{-1} was calculated as 10.9MHz. This showed a good correlation with the results.

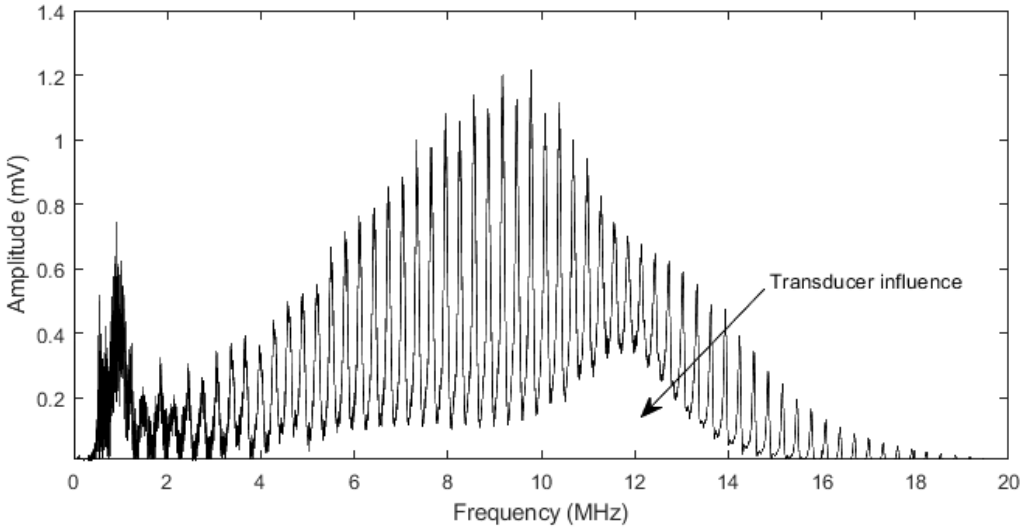

Figure 5-11. Frequency domain showing the transducer-solid coupling.

5.4 Ultrasonic Apparatus

A 10cm×10cm×10mm aluminium plate was instrumented with a pair of 10MHz longitudinal transducers in a pitch-catch arrangement. The pitch-catch arrangement allowed for one transducer to continuously send a repeating frequency sweep and the other transducer to act as the receiver. The transducers were connected to a Picoscope oscilloscope which is both an arbitrary waveform generator and signal digitiser. The Picoscope was connected to a laptop PC via a Universal Serial Bus (USB) where a dedicated LabVIEW software was used to control the pulsing and data acquisition. This set-up is illustrated in Figure 5-12 and it demonstrates the simplistic nature of the measurement approach and the highly portable and compact hardware involved.

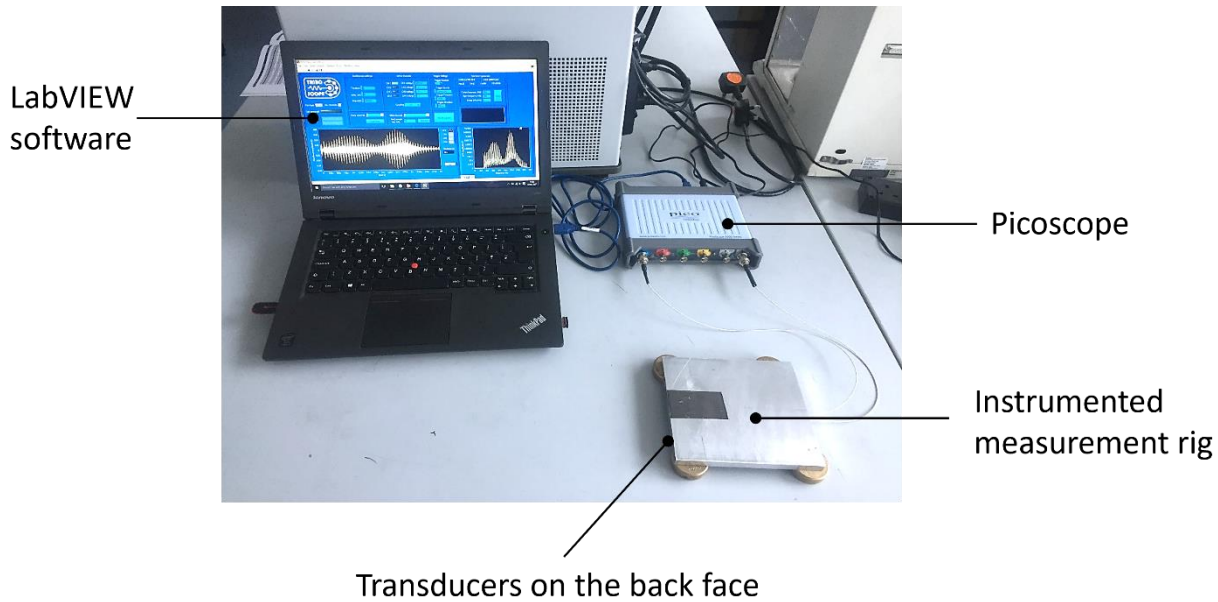

Figure 5-12. Photograph showing the measurement set-up (Photograph taken by author).

5.4.1 The Transducers

A 10MHz longitudinally polarised wrap-around lead-zirconate-titanate (PZT) piezoelectric transducer was used for this study. Wrap-around meant that the lower and the upper electrodes could both be connected to external wiring from the top surface as shown in Figure 5-13.

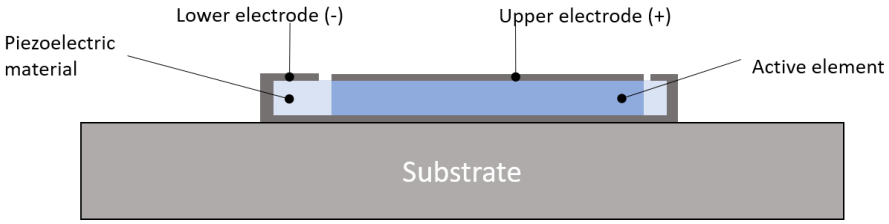

Figure 5-13. Schematic of a wrap-around transducer that is bonded on a metal substrate.

The bottom surface would then be in contact with the solid component. The active element only applies to the region where a voltage differential is applied.

The 10MHz transducer had a thickness of 0.2mm, 7.1mm in diameter (Figure 5-14a) and was chosen for its 'soft' properties and high sensitivity. The Curie temperature for the transducer was around 370℃ which meant that it could be used for laboratory applications. The transducer was cut into equal halves such that one was used to generate continuous waves whereas the other acted as a receiver (Figure 5-14b). These were placed in close proximity in order to acquire the strongest possible signal.

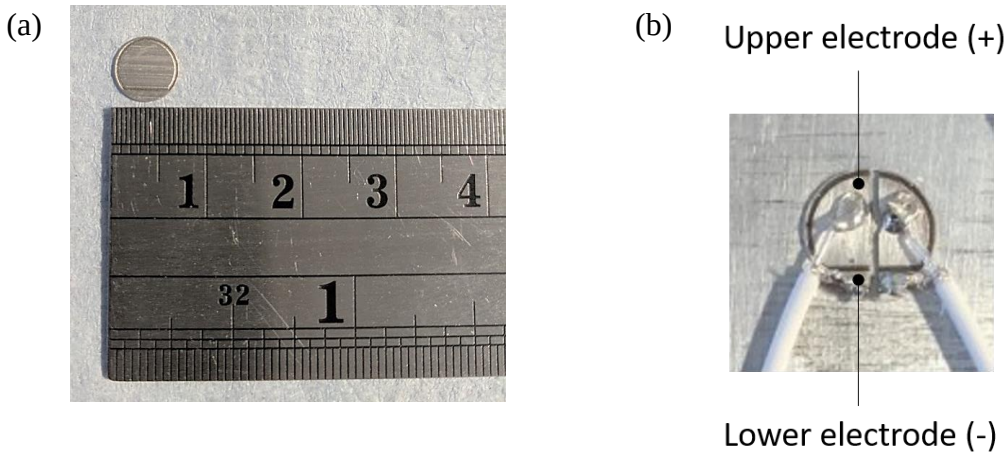

Figure 5-14. Photograph of (a) a 10MHz piezoelectric transducer and (b) the 10MHz cut in half and bonded to an aluminium plate (Photographs taken by author).

The transducers were bonded on to the aluminium component using M-bond 610 strain gauge adhesive, which is an epoxy-phenolic adhesive that is capable of creating a void-free, very thin layer (around 5μm). This helps to reduce damping in this layer. The adhesive was cured at 167.5°C for two hours, during which pressure was applied on the transducers by using clamps with silicone rubber between the clamps and the transducers that distributed the load evenly and prevented cracking of the transducers. This resulted in asperity contact between the electrode of the

transducer and the aluminium plate. Post curing was performed at 200°C (30°C above cure temperature).

5.4.2 The Cables

A 1.2mm external diameter coaxial cable (Figure 5-15) with a signal attenuation of 2.3 dB/m at 1GHz was soldered on to the transducers (Figure 5-14b). The conductor of the cable was soldered on to the upper electrode and the shield was used to connect the ground via the lower electrode. This cable was chosen due to its low signal attenuation and flexibility.

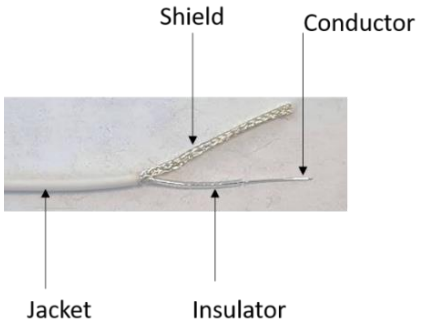

Figure 5-15. Photograph of coaxial cable showing the structure (Photograph taken by author).

The other end of the coaxial cable was attached to a Sub-Miniature version-B (SMB) connector which would allow connection to an oscilloscope via a Bayonet Neill–Concelman (BNC) connector. This is illustrated in Figure 5-16

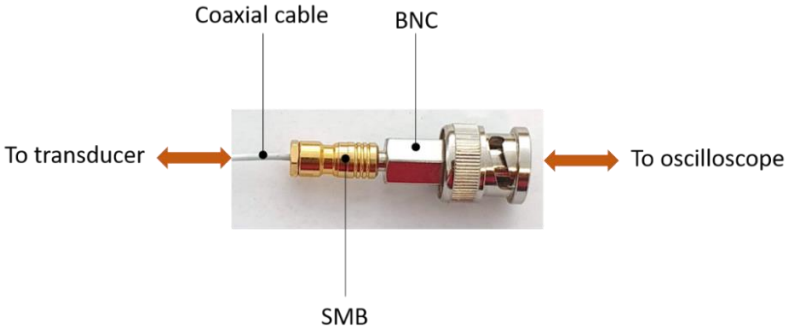

Figure 5-16. Photograph showing SMB and BNC connectors (Photograph taken by author).

5.4.3 Thermocouples

The temperature of the aluminium component was monitored using a RTD thermocouple that was bonded next to the transducers using a strain gauge adhesive. The RTD thermocouples are capable of an accuracy of ±0.2°C. However, because the measurements are carried out at room temperature, the temperature measurements were not expected to change significantly.

5.4.4 Ultrasonic Hardware and Software

A Picoscope 5442b USB type oscilloscope was used as an arbitrary function generator and signal digitiser. It is small, light, portable, and capable of being powered via a Universal Serial Bus (USB) where two channels are used or an AC adaptor in the case of four channels. It has a sampling rate of 1 GS/s and a maximum bandwidth of 200MHz. A high sampling rate reduces aliasing (where signal is lost due to insufficient sample points). Usually, the sampling rate of a waveform must be

at least twice the highest frequency in the signal. This applies to sinusoidal waveforms and is otherwise known as the Nyquist sampling theory. The sampling rate of the Picoscope is therefore sufficient for waveforms in the 1-30MHz range.

The sampling window for the standing wave method was the length of the frequency sweep. This was significantly larger than the sampling window usually used in conventional pulsed methods (in the tens of μs range). This allowed for the signal to be resolved even at lower sampling rates.

5.4.5 Surface Coating Manufacturing Procedure

The surface of the aluminium test component was first cleaned with isopropyl alcohol solution and then left to dry at room temperature. A solid-air signal was then recorded after which an epoxy mixture was applied on to the aluminium surface and a scraper (with an adjustable height controlled by a pair of micrometer screw gauges) was used to form a planar epoxy layer of known thickness that was then left to cure overnight (Figure 5-17).

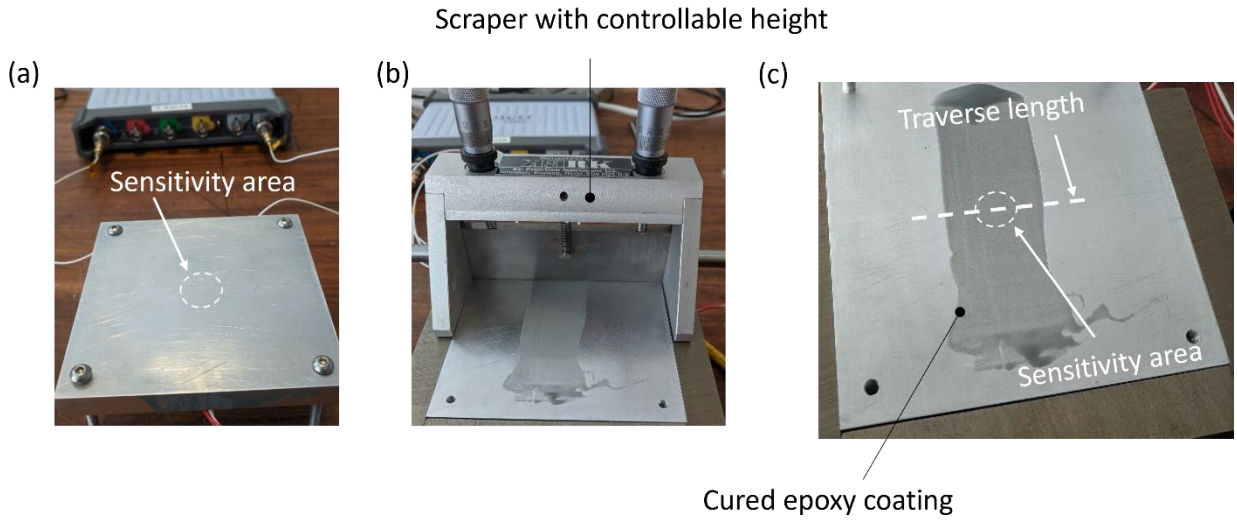

Figure 5-17. Photographs to show (a) a solid/air condition, (b) an epoxy mixture that was applied to the aluminium surface and (c) the cured epoxy coating (Photographs taken by author).

Once cured, a solid-epoxy signal was recorded. An independent contact profilometer was used to calculate the thickness of the cured epoxy by measuring the step change from the surface of the aluminium to the surface of the epoxy coating (Figure 5-18).

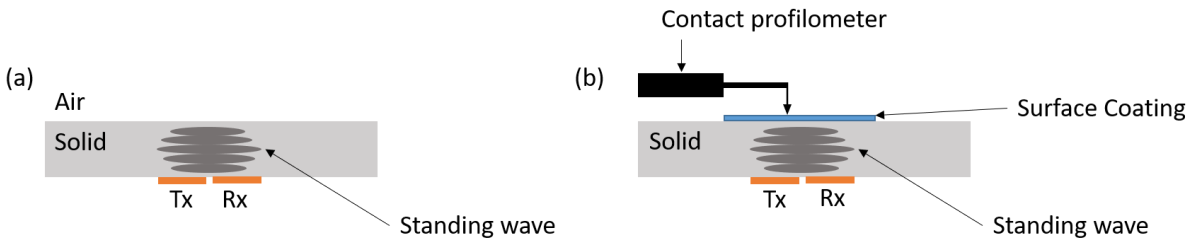

Figure 5-18. Schematic to show (a) a solid/air and (b) solid/surface coating boundary conditions.

The traverse length as shown in Figure 5-17c was chosen to pass through the sensitivity region. An example of a contact profilometer measurement of an epoxy coating on an aluminium substrate is shown in Figure 5-19.

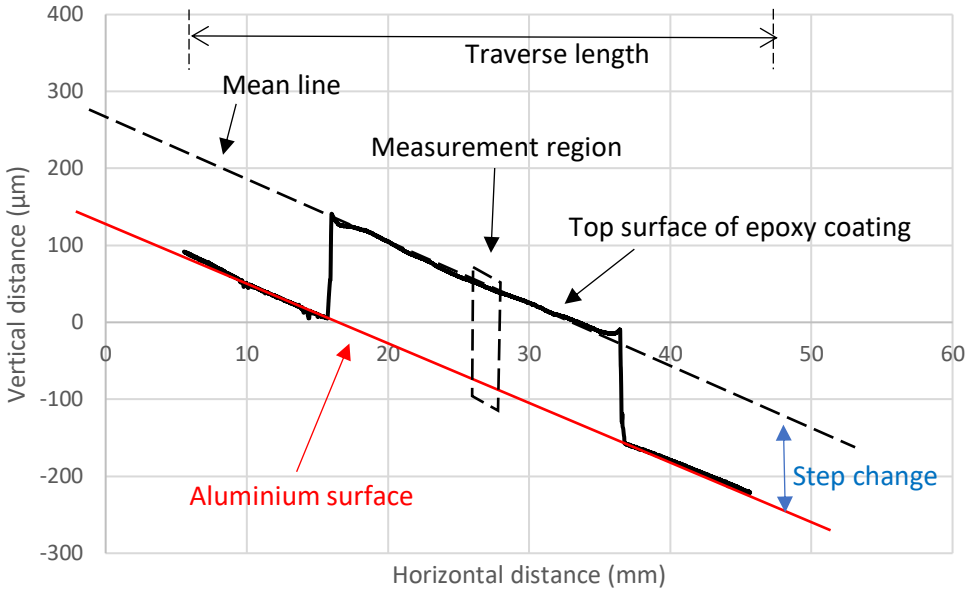

Figure 5-19. A contact profilometer raw data of an epoxy coating on an aluminium substrate showing the step change measurement.

The epoxy top surface was not entirely planar as shown in Figure 5-19. The measurement region was chosen to be the sensitivity area as illustrated in Figure 5-17c that was located at a region perpendicular to the transducers on the back face of the component. The thickness was calculated by taking a mean line at the measurement region and calculating the step change distance between the parallel aluminium surface line and the mean line. Three repeats were performed.

5.5 Pulsing and Data Acquisition

The Triboscope software program run on a laptop PC via LabVIEW software was used to control the parameters for the formation of a standing wave. The PC was used to store the digitised signals which were then processed and analysed using MATLAB2018 software. For this study, twenty waveform captures were stored for each boundary condition (Figure 5-18). The post processing steps are as illustrated in Figure 5-20. A contact profilometer was used to validate the epoxy thickness.

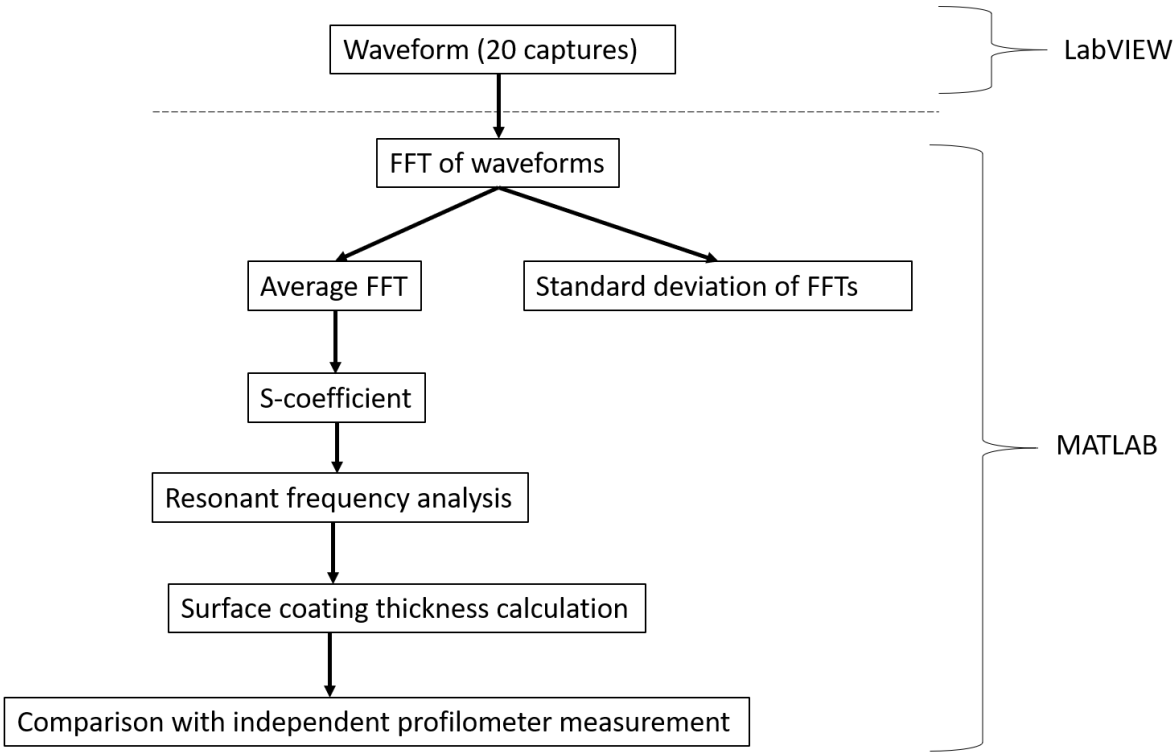

Figure 5-20. Standing wave signal analysis steps.

5.6 Effect of a Surface Coating on a Standing wave

The technique presented herein for the thickness measurement of a surface coating on a metal substrate uses the ratio, *S*, of a solid-coating to solid-air standing wave frequency response amplitudes to identify the surface coating resonant frequencies. This is expressed as:

$$S = \frac{A_{solid-coating}}{A_{solid-air}} \qquad \text{Equation 5-2}$$

where $A_{solid-air}$ is the signal amplitude of the solid-air measurement condition and $A_{solid-coating}$ for a solid-surface coating measurement condition. The coating resonant frequencies will be observed as minima when *S* is plotted against frequency. The mathematical description of *S* will be discussed in detail in Chapter 6.

The cured epoxy (Figure 5-17b) was measured by an independent optical 3D surface profilometer and the coating thickness was calculated as 138.20µm.

To do this, a scanning area was selected that covered the area of sensitivity as shown in Figure 5-21a. The area was scanned using an optical 3D measurement system and then analysed to produce a 3D map as shown in Figure 5-21b. Next, a step change profile measurement was carried out such that the traverse length passed through the sensitivity area.

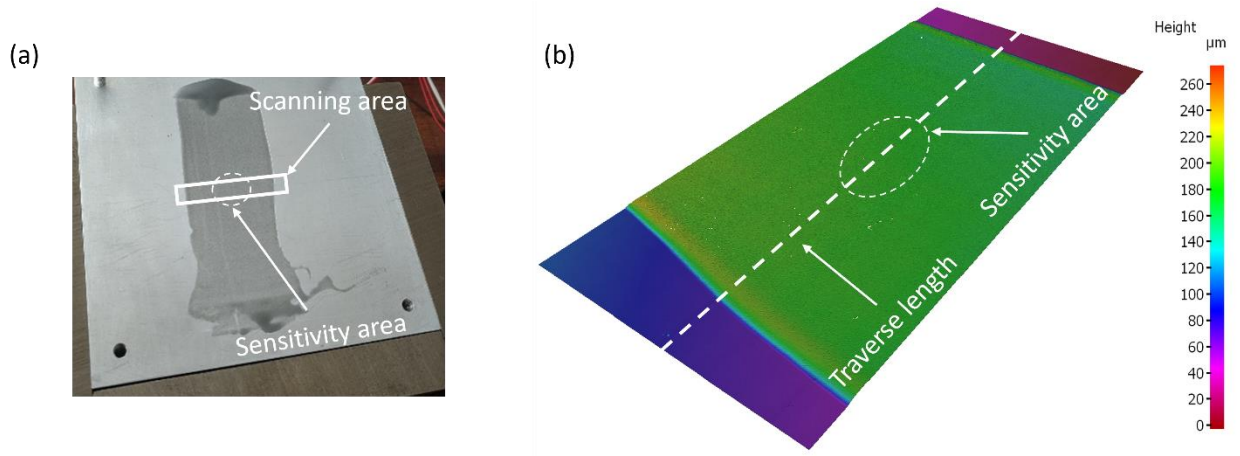

Figure 5-21. (a) A photograph to show the scanning area and (b) a 3D map of the scanned area.

The step change was then calculated as the distance between the parallel aluminium surface line and the mean line at the measurement region. This is shown in Figure 5-22.

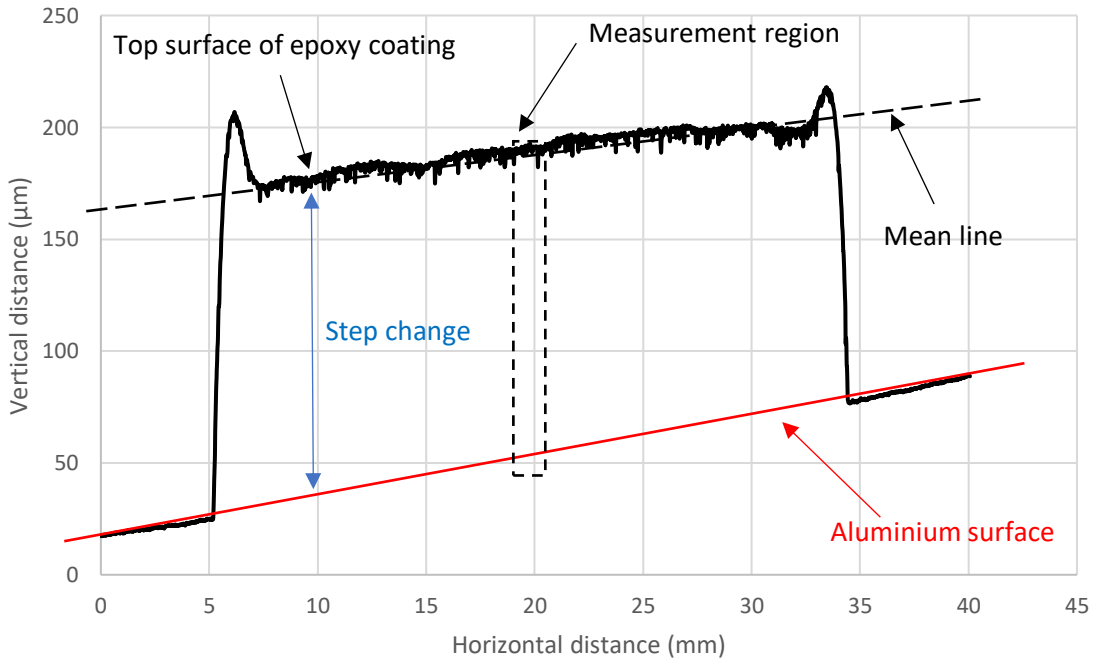

Figure 5-22. A 138µm step change measurement from the 3D surface profilometer.

The top surface of the epoxy coating was not entirely planar as shown in Figure 5-22. Three repeats were performed.

The influence of the cured epoxy on the standing wave frequency profile is shown in Figure 5-23a. At certain frequencies, the peak amplitudes reduced, and the *S* profile showed corresponding minimum locations at these frequencies. A magnified view of Figure 5-23a is shown in Figure 5-23b to show the drop in amplitude of the 13.93MHz frequency peak .

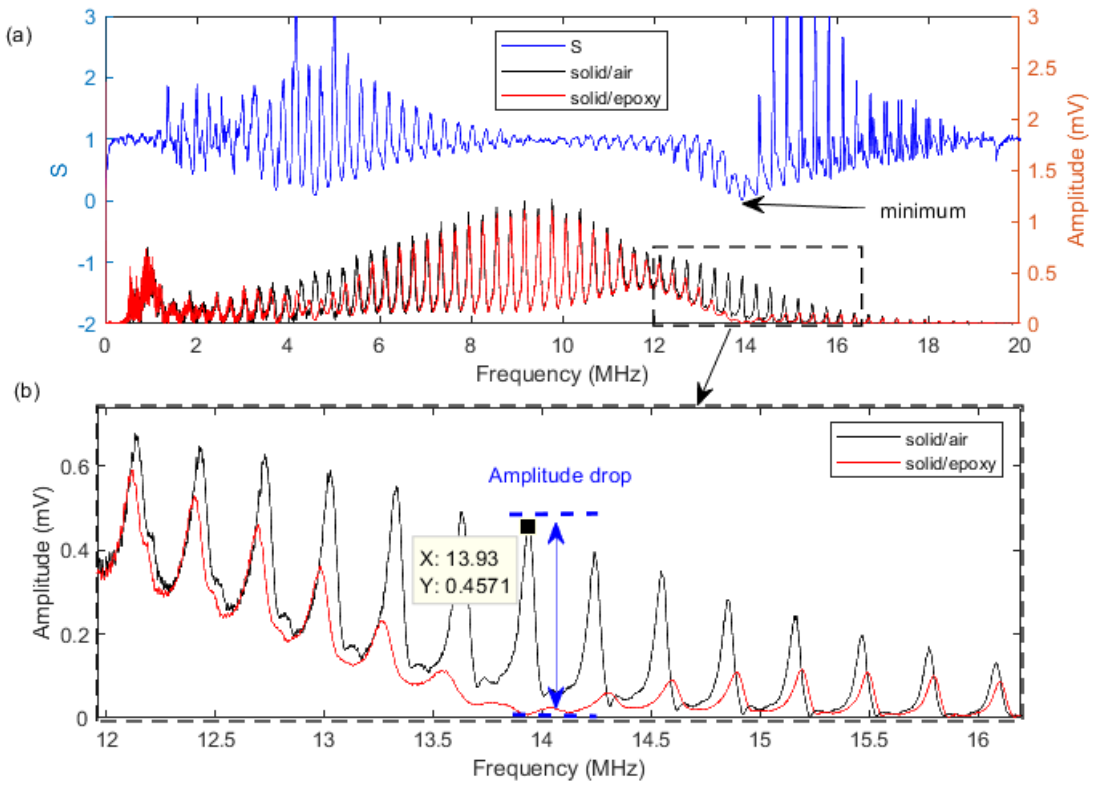

Figure 5-23. (a) The frequency spectra of the standing wave for solid-air and solid-epoxy responses and the associated *S* plot. (b) A magnification of the frequency responses showing drop in amplitude and phase change of the peaks.

The amplitude reduction is caused by destructive interference of the incident and reflected waves within the substrate that occurs when the thickness of the coating matches a quarter wavelength of the driving frequency. A simple wave destruction illustration has been explained earlier using Figure 3-11 in section 3.9 in chapter 3. Destructive interference also occurs at higher frequencies that are odd multiples of the driving frequency, and these are otherwise known as harmonics.

The phase of the solid/epoxy resonant peaks also changed as observed in Figure 5-23b. The phase spectrum was obtained from the FFT of the time domain signals. This is shown in Figure 5-24. The saw-tooth pattern observed in the phase plot is because of the phase continuously changing with frequency. This has been reported in literature [64], [84].

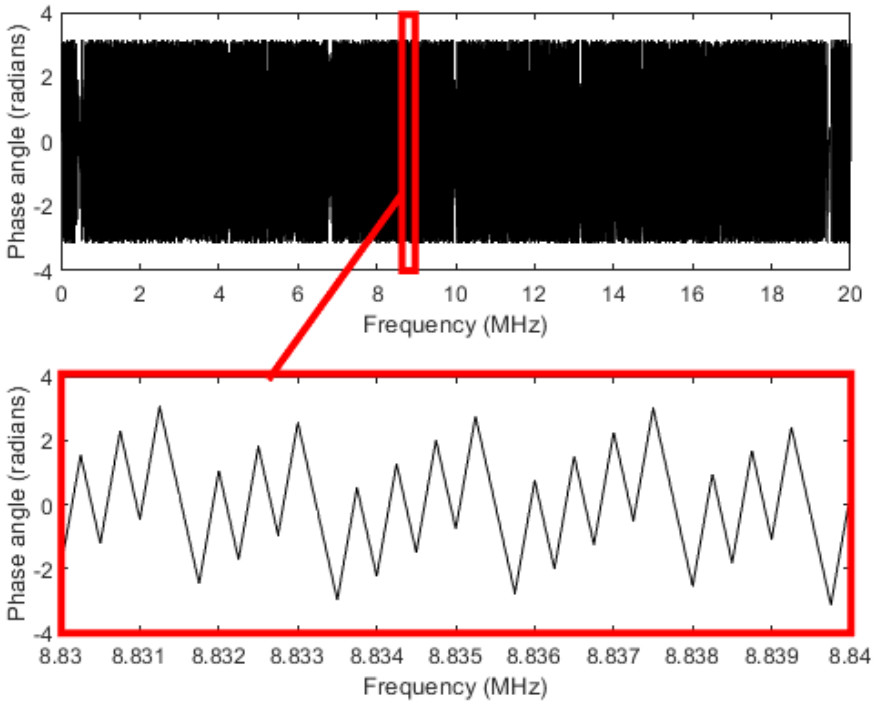

Figure 5-24. (Top) The phase profile of the standing wave for a solid-air measurement condition. (Bottom) A zoomed-in profile between 8.83MHz and 8.84MHz of the top phase profile.

The phase difference was calculated by subtracting the solid-epoxy phase angle profile from the solid-air phase angle profile. The resultant phase difference profile is shown in Figure 5-25.

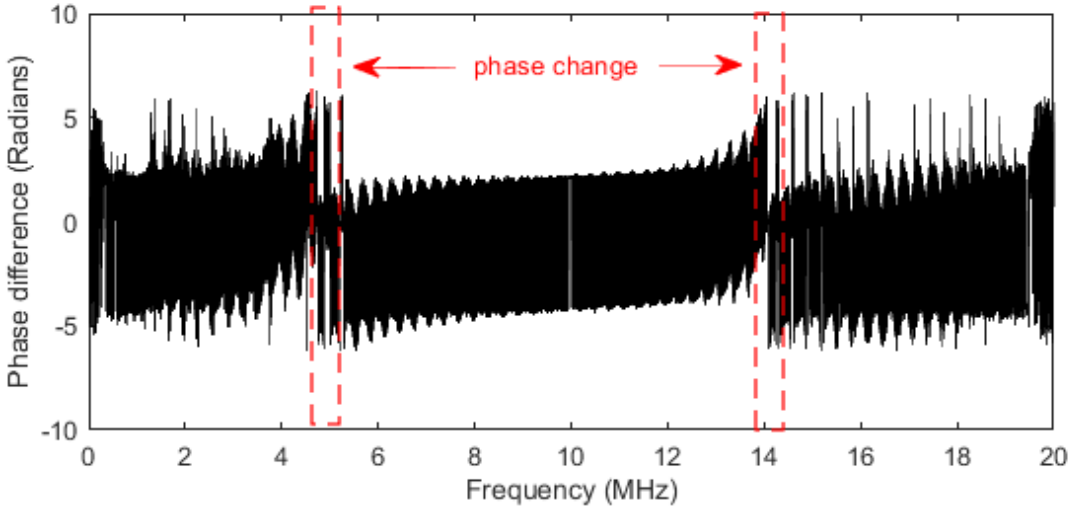

Figure 5-25. Phase difference spectrum showing phase change at 4.58MHz and 13.93MHz

The phase difference spectrum showed a phase change at 4.58MHz and 13.93MHz, respectively. These frequencies corresponded to the frequencies that had a significant amplitude reduction, as identified from the *S* profile. From the *S* profile, the epoxy resonant frequencies were therefore identified as 4.58MHz and 13.93MHz, respectively.

The influence of the frequency sweep time on the peak position of the resonant modes from the FFTs and the magnitude of *S* was investigated experimentally. The peak amplitudes at 4.58MHz and 13.93MHz for solid-air (ref) and solid-epoxy (meas) boundary conditions were compared as shown in Figure 5-26.

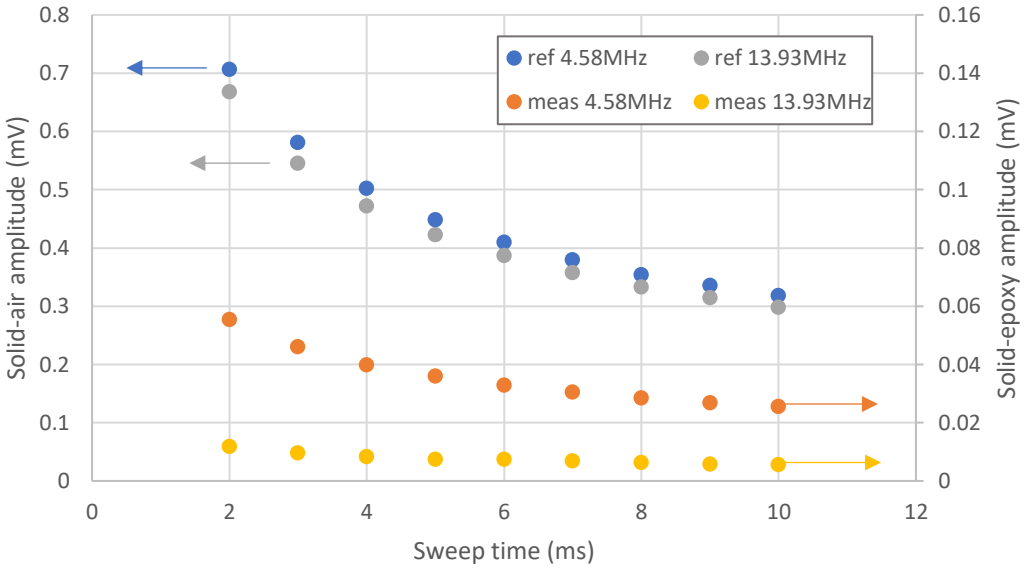

Figure 5-26. Resonant mode behaviour changes with increasing sweep times.

The peak amplitude decreased with increasing sweep time for both solid-air and solid-epoxy boundary conditions. It was observed, for example, that the peak for a solid-air boundary at 4.58MHz reduces from 0.71mV at 2ms to 0.32mV at 10ms. However, the *S* magnitude remained fairly constant as illustrated in Figure 5-27.

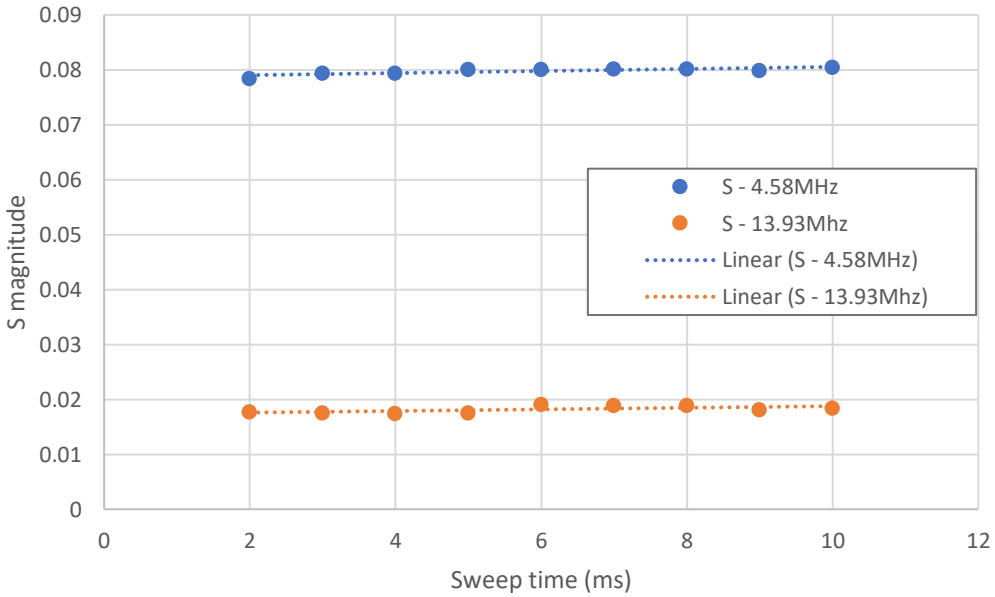

Figure 5-27. *S* magnitudes change with increasing sweep time.

The S magnitudes at 4.58MHz showed an average of 0.080 with a standard deviation of 0.0006, whereas the S magnitude at 13.93MHz showed an average of 0.018 with a standard deviation of

0.0006. Therefore, sweep times equal to or greater than 2ms practically have little to no effect on the magnitude of the coating resonant frequency identifiable in a *S* spectrum.

The frequency difference was halved to yield f_0, and the experimental thickness was calculated as 142.78µm using Equation 3-52, where the acoustic velocity in epoxy was 2670 m/s. This step of averaging the frequency interval between two adjacent resonances has been reported in literature [7], [85]. Experimental result showed a 3.3% increase from the profilometer measurement.

A further 4 epoxy layers of different thicknesses were cured, measured using the standing wave method and validated using standalone contact profilometer measurements. The frequency responses were analysed, and the epoxy resonant frequency was obtained from the respective *S* plots. Where a single minimum location (resonant dip) was identified within the operational bandwidth of the standing wave, the epoxy resonant frequency was taken at that location. For multiple dips, the frequency difference between adjacent dips was halved. A plot comparing the standing wave measurements and profilometer measurements is shown in Figure 5-28.

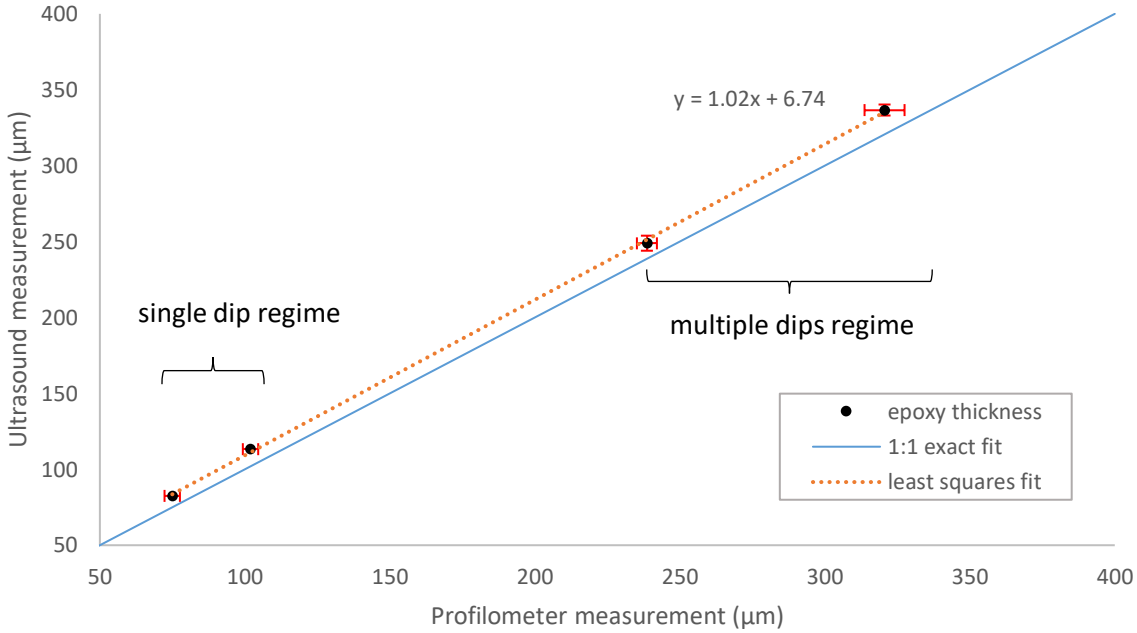

Figure 5-28. A plot to show comparison between ultrasound and profilometer measurements for four epoxy thicknesses.

The vertical error bars represent the standard deviation that arose when performing an average of the frequency difference between adjacent dips for the case where the multiple dips were greater than two. The horizontal error bars represent the boundary limits of the profilometer measurements. The profilometer measurement errors increased with increasing thickness with the lowest and highest errors being 2.65% and 6.90% respectively. A least squares regression line of best fit equation of the epoxy thickness data showed a system error of 6.74µm and a 2% error when compared to a 1:1 exact fit line.

Equation 3-53 was used to model the resonant modes of epoxy layers of different thickness as shown in Figure 5-29.

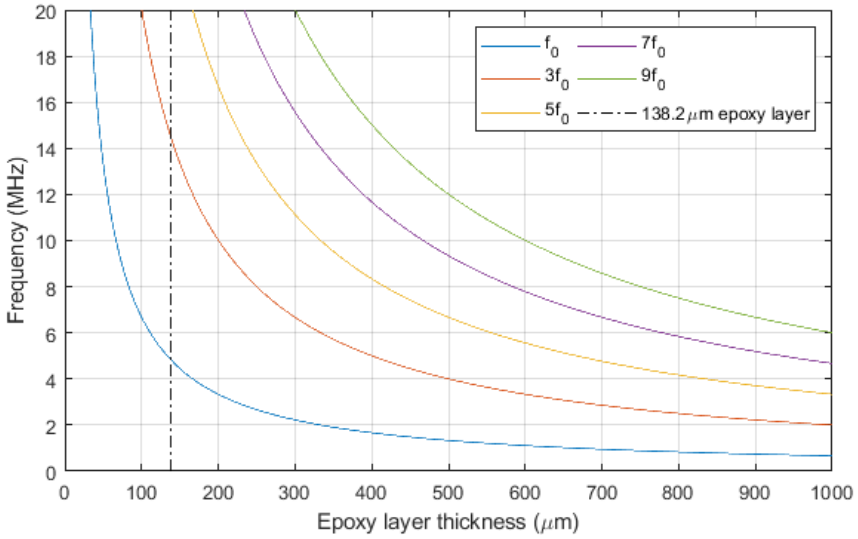

Figure 5-29. A chart to illustrate epoxy resonant mode distribution for 0µm to 1000µm thickness range.

From the figure, a 138.2µm epoxy layer thickness will have f_0 at 4.83MHz and $3f_0$ at 14.49MHz. Epoxy thicknesses below 100µm will show only one resonant dip in the S spectrum within a 0MHz to 20MHz bandwidth whereas thicknesses in the range 100µm to 168µm will show two resonant dips, or rather have f_0 and $3f_0$. The number of resonant modes that will be observed as dips in the reflection coefficient spectrum increases with increasing thickness and the frequency separation between the resonant dips decreases with increasing thickness. It was noted from Figure 5-29 that the lowest measurable thickness is dependent on the upper frequency limit. The lowest thickness is also dependent on the speed of sound in the coating material according to Equation 3-53. Therefore, for an epoxy material where the speed of sound is 2670 m/s at ambient pressure and temperature, the lowest epoxy coating that could be measured using the standing wave method in this study was 35.1µm, with the assumption of a centre frequency of 10MHz and span of 19MHz. This means that the lowest detectable epoxy resonance from the *S* spectrum is 19MHz provided there is a good signal-to-noise ratio. There is no upper limit to the maximum thickness that can be measured using this method.

An investigation was carried out to compare the resonant mode magnitude of *S* against those from a reflection coefficient *R* obtained from pulse-echo resonance method. To do this, a 10mm steel component was instrumented with two 10MHz longitudinally polarized piezoceramic elements in a pitch catch arrangement.

A standing wave was formed by sending a 19MHz frequency sweep centred around the transducer nominal frequency with a 4ms sweep time and then captured and stored. The ultrasound settings were then changed to pulse a 10MHz 1 cycle sinusoidal burst from one of the sensor pairs through the component in a pulse-echo set-up. The two pulsing set-ups were then compared to investigate the ultrasound interference at the solid-epoxy boundary.

A solid-air boundary condition was captured for both pulsed wave and standing wave settings. A planar epoxy layer was then applied at the interface of interest and cured overnight. A solid-epoxy boundary condition was captured. The epoxy thickness was validated by independent

measurement using a 3D optical surface profilometer and estimated to be 127µm. The optical 3D measurement procedure has been explained earlier in section 5.6. The raw data showing the step change profile measurement is shown in Figure 5-30.

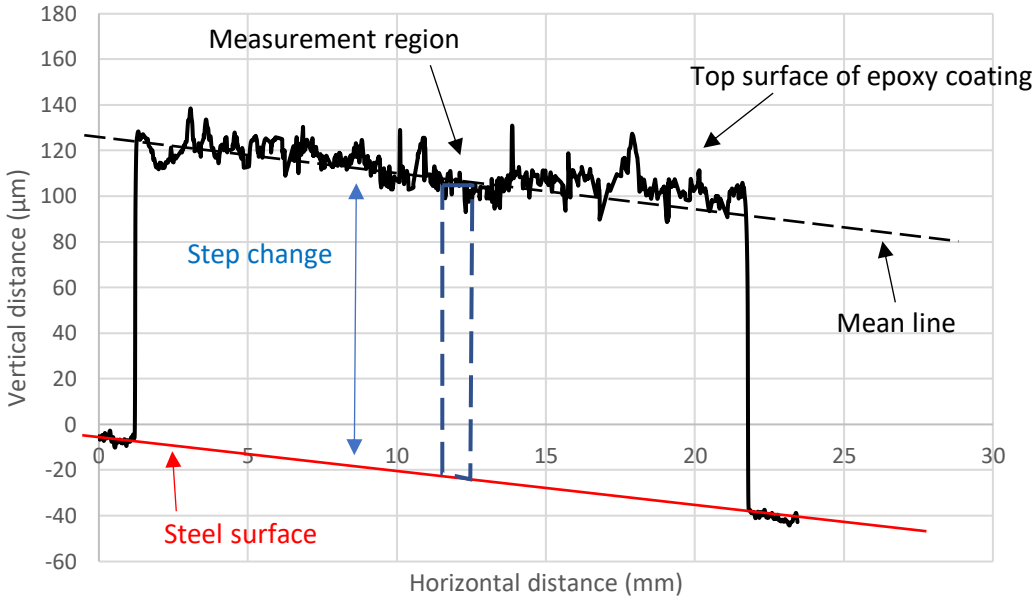

Figure 5-30. A 127µm step change measurement from the 3D surface profilometer.

The epoxy surface was not planar nor smooth as evidenced by the numerous asperity peaks and valleys. The thickness was calculated by taking the distance between the parallel steel surface line and the mean line at the measurement region.

For the pulsed wave data, the acquired time domain data was trimmed to isolate the first back wall reflection as shown in Figure 5-31.

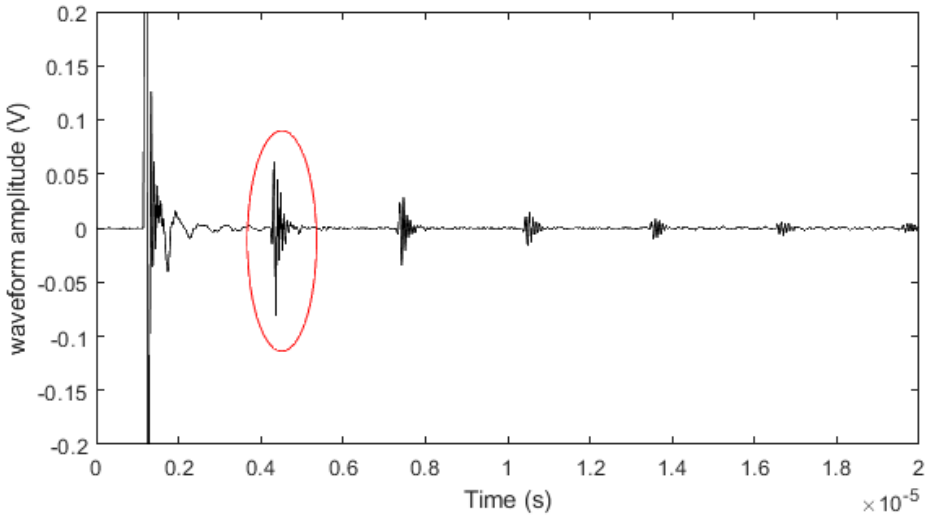

Figure 5-31. Time domain of a 10MHz 1 cycle sinusoidal wave for a solid-air boundary condition in a 10mm thick steel substrate (first backwall reflection is circled in red).

The trimmed data was then zero padded to increase the resolution and a Fast Fourier Transform (FFT) was applied to convert to the frequency domain. The reflection coefficient, *R* was then calculated by dividing the solid-epoxy frequency response with the solid-air response. These are plotted in Figure 5-32.

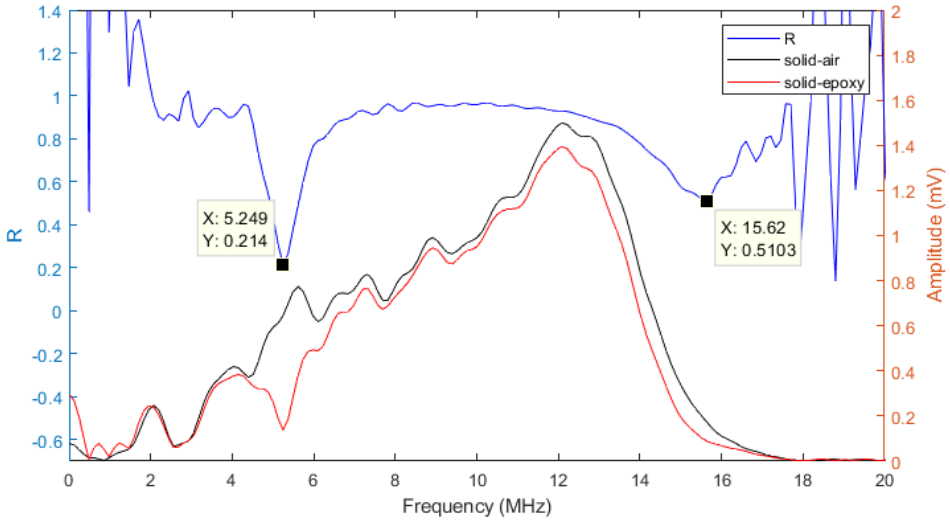

Figure 5-32. Frequency responses for solid-air and solid-epoxy boundary conditions and the associated reflection coefficient spectrum on a 10mm thick steel substrate.

The minimum points in the *R* spectra were observed at 5.249MHz and 15.62MHz. The f_0 was calculated as 5.1855MHz and subsequently the epoxy layer was calculated as 128.72µm where the speed of sound in the epoxy resin was 2670 m/s.

The minimum points in the *S* spectra from the standing wave measurements were observed at 5.347MHz and 15.75MHz as evidenced in Figure 5-33.

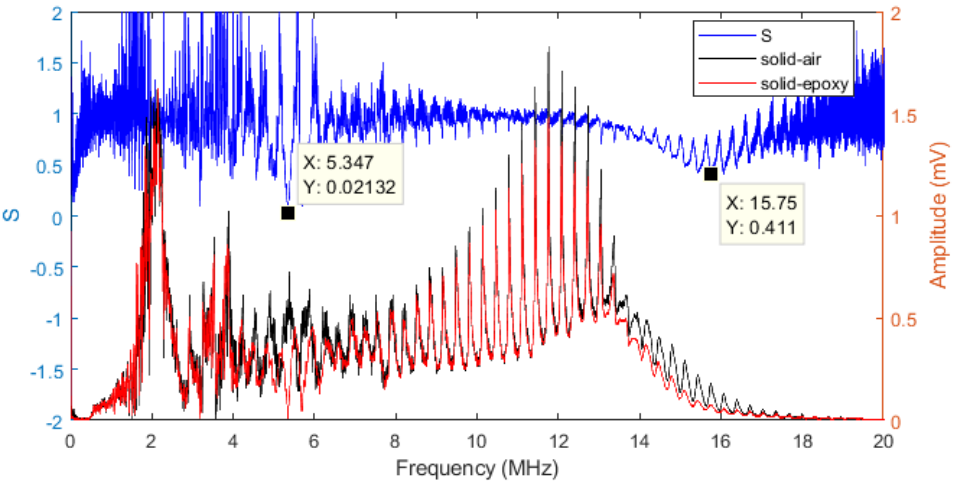

Figure 5-33. Standing wave frequency responses for solid-air and solid-epoxy boundary conditions and the associated reflection coefficient spectrum on a 10mm thick steel substrate.

The f_0 in this instance was calculated as 5.2015MHz and the epoxy thickness was calculated as 128.33µm. The thickness calculated using a standing wave showed a better agreement to

profilometer measurements. Of interest to note is that the resonant dip magnitudes from the *S* spectrum were more sensitive than those from *R* spectrum. This difference is clearly seen in Figure 5-32 and Figure 5-33 evidenced by the reduction in the resonant mode magnitudes.

A similar behaviour was observed when a 135µm epoxy layer was cured on the instrumented aluminium block explained previously. The epoxy resonances from the *R* spectrum were observed at 5.615MHz and 15.75MHz as shown in Figure 5-34.

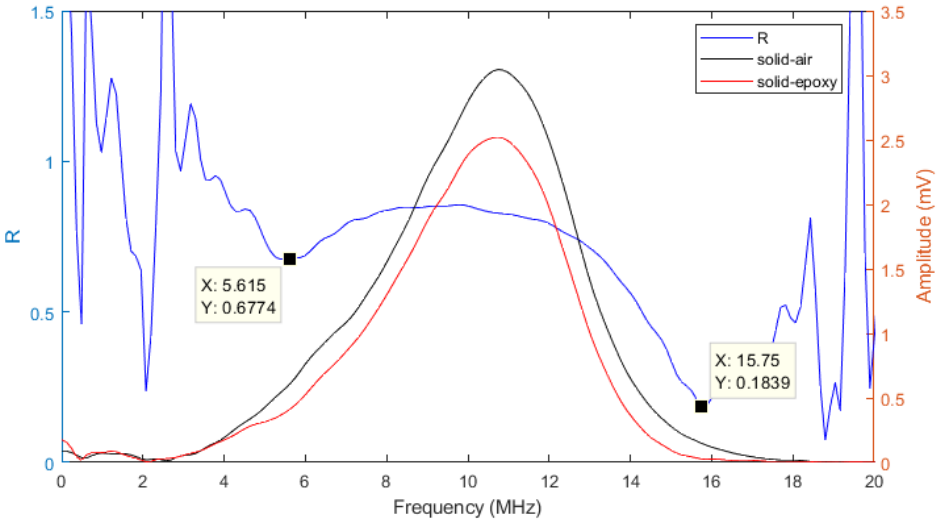

Figure 5-34. Frequency responses for solid-air and solid-epoxy boundary conditions and the associated reflection coefficient spectrum on an aluminium substrate.

The f_0 and the epoxy thickness were calculated as 5.07MHz and 131.72µm, respectively. On the other hand, the epoxy resonances from a *S* spectrum were 6.093MHz and 15.79MHz as shown in Figure 5-35.

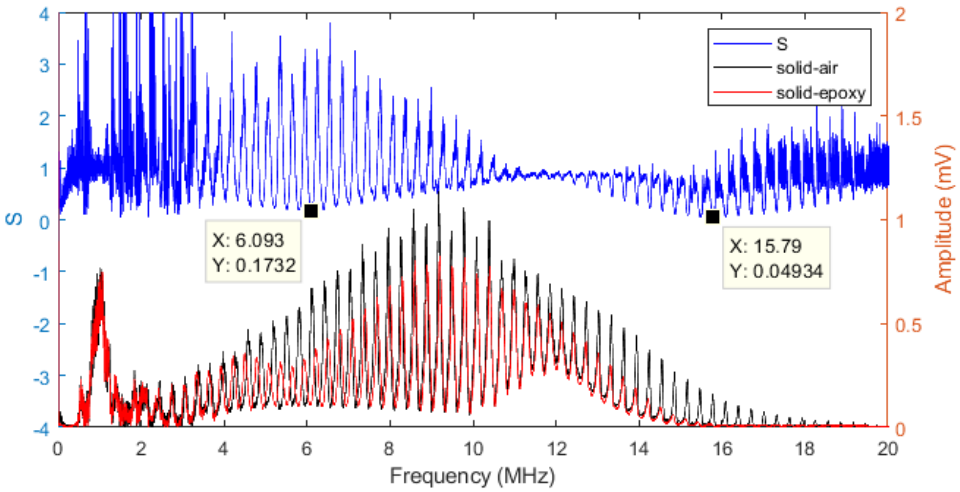

Figure 5-35. Standing wave frequency responses for solid-air and solid-epoxy boundary conditions and the associated reflection coefficient spectrum on an aluminium substrate.

The f_0 and the epoxy thickness were calculated as 4.85MHz and 137.67µm, respectively. The thickness calculated using a standing wave method showed a better agreement to standalone

profilometer measurements. The standing wave was much more sensitive to the epoxy layer when compared with the conventional pulse-echo technique as observed in the differences between the magnitudes of the epoxy resonances.

5.7 Effect of Transducer Backing on A Standing Wave

The effect of backing the transducers on the magnitude of the standing wave generated was experimentally investigated by analysing the FFTs of the frequency responses from unbacked and backed transducers. A 10mm thick steel specimen was bonded with two pairs of 10MHz bare piezoelectric elements. Each element measured 2mm×7mm×0.2mm. Coaxial cables were then bonded on to the sensor pairs using a conductive silver epoxy and one sensor pair was backed with a Robnor epoxy mixture that was left to cure overnight. This is shown in Figure 5-36.

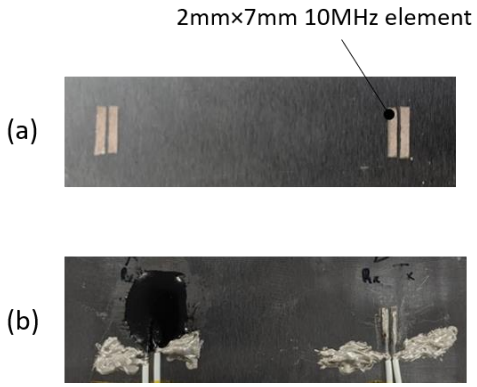

Figure 5-36. Photographs showing (a) 10MHz bare piezoelectric element pairs bonded onto a steel component (b) sensor pairs cabled using silver epoxy with one pair backed using Robnor epoxy.

A standing wave was generated by sending a 19MHz linear sweep with a centre frequency of 10MHz and a 4ms sweep time. The standing wave frequency responses are shown in Figure 5-37.

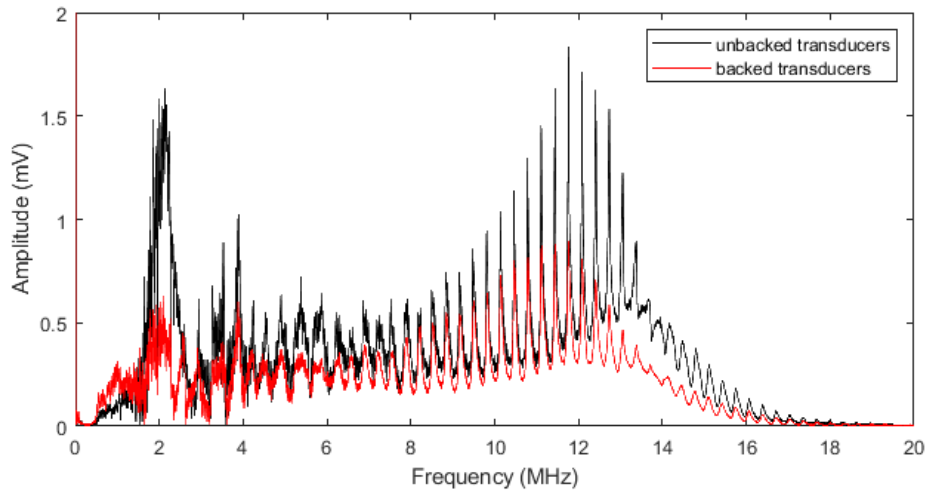

Figure 5-37. FFT spectra showing the standing wave response for unpotted and potted transducers for a 10mm steel component.

The maximum peak observed at 11.76MHz saw a 51% reduction from 1.83mV to 0.8913mV. There was also a significant reduction in the noise observed in the lower frequency range which

is evidenced by the smoothing of the spectrum. For conventional pulse-echo techniques, backing the sensor is thought to reduce the unwanted effects of surface waves which would increase the noise levels.

A study on the influence of the reflection coefficient *R'* at the transducer interface has previously been investigated by Manfredi [86] whereby the waveform amplitudes and phases between unbacked and backed 10MHz longitudinal transducers on an aluminium substrate were compared. The backing was a tungsten loaded epoxy. The aluminium plate was attached to an open water container such that the plate formed the bottom of the container. The container was filled with water and a 10MHz immersion probe was used to scan the aluminium plate as illustrated in Figure 5-38.

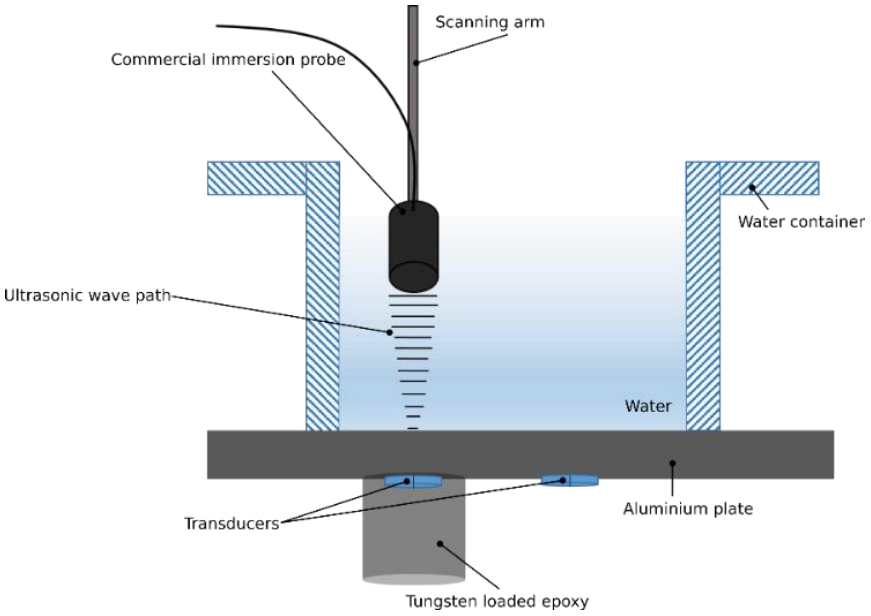

Figure 5-38. A schematic of the scanning of the aluminium plate using an immersion probe (picture extracted from [86]).

The probe was used to scan an area 29×15mm that spanned over the transducers with a resolution of 0.5mm. At every point in the scan, the amplitude of the FFT of a single echo was converted to a *R'* value using the maximum FFT measured for a reference value (air-backed). A colour plot showing the variance in the measured *R'* values for the transducers is shown in Figure 5-39.

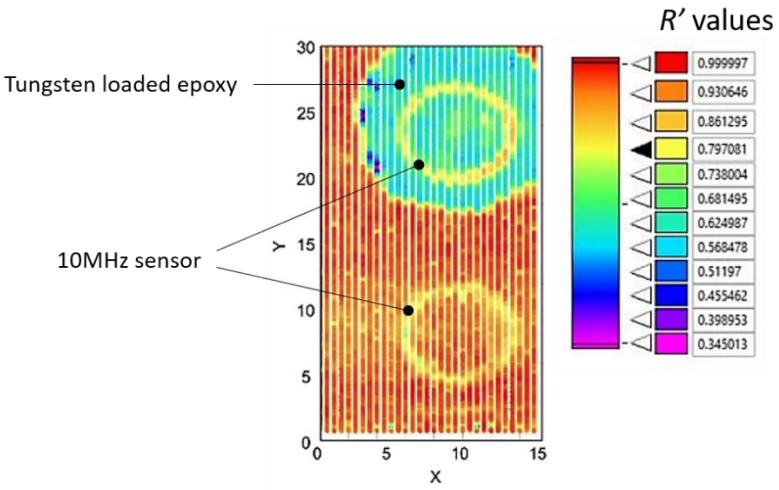

Figure 5-39. Measured *R*' values colour plot (picture extracted from [86]).

The effect of the tungsten loaded epoxy in reduction of the ultrasound energy was evidenced by the reduced *R'* values at the centre of the transducer. High *R'* values that averaged to 1, represented as red or dark orange in colour, indicated a transducer-air interface. The edges of the transducers reported *R'* values around 0.79 which indicated that ultrasound waves were scattered at the transducer edges. The area inside the perimeter of the epoxy-backed transducer had *R'* values in the range 0.5 to 0.7 whereas the area inside the perimeter of the air-backed transducer had *R'* values averaging 1. The low *R'* values indicated that some useful ultrasound energy was transmitted to the epoxy, effectively reducing the useful energy within the system. This reduction in the FFT amplitude was also reported for a standing wave method as shown in Figure 5-37. The maximum FFT peaks reported a reduction of 51%. It is therefore more preferable to not back the transducers in order to have higher energy content within the system by having maximum FFT amplitudes. The influence of *R'* is of great significance when considering a standing wave and will be explored further in the next chapter. Nonetheless, in most practical applications, a backing is necessary in order to protect the transducers and the cables from the elements. The reduced standing wave amplitude, however, does not greatly affect the thickness measurement of the surface layer.

5.8 Discussion

Epoxy coatings in the range 70μm to 350μm have been successfully measured using a standing wave method and a comparison between standalone profilometer measurements showed a good agreement. The results showed minimum and maximum percentage change accuracies of 1.04% and 10%, respectively with increasing coating thickness.

The experiments in this study were performed at room temperature and therefore the thermal effects were considered to be negligible. The thickness of the adhesive couplant between the transducer and aluminium component was assumed to be thin enough not to cause acoustic damping.

The epoxy layers applied were not entirely planar and the profilometer readings were taken at a position perpendicular to the sensors. It was also assumed that there were no air gaps in the epoxy after curing and that the contact between the aluminium and the epoxy material was smooth

enough to allow a clean transmission of ultrasound energy. Discrepancies arose due to the epoxy acoustic velocity being slightly different for each epoxy thickness.

The lowest measurable coating thickness in this study, 35.1μm, was limited by the upper frequency limit and the speed of sound in the coating material. There was no upper limit to the maximum thickness that can be measured using this method.

Higher frequency sensors can be used to extend the lowest measurable coating thickness. For instance, a 20MHz nominal frequency sensor can be used to set-up a standing wave with a centre frequency of 20MHz and a frequency span of 19MHz. In doing so, the upper frequency limit in this case is effectively extended to 29MHz, with the assumption of good signal-to-noise ratio and that the standing wave was set-up in a less attenuative solid material. The lowest measurable epoxy thickness would then be reduced by 12.1μm to 23μm, assuming the speed of sound in the epoxy remains constant. Therefore, the lowest measurable coating thickness is indirectly proportional to the upper frequency limit. However, the use of higher frequency sensors is limited by high ultrasound attenuation in the materials. Higher frequency sensors also have a thinner thickness, and this makes them very fragile. Contemporary technologies such as sputtering have been applied to manufacture thin film elements that have good signal strength and show increased measurement resolutions and it is suggested that these could be used in future work to overcome the limitations encountered when using bare piezoelectric transducers.

5.9 Conclusions

The ultrasonic hardware necessary to generate a standing wave within a component are readily available and are highly portable (laptop PC and Picoscope). The cost of instrumentation of the piezoelectric transducers is relatively cheap and they can easily be retrofitted on to existing real-life engineering component to detect and measure surface coatings and thin films noninvasively.

The standing wave generation parameters are determined by the component geometric and material properties and the coating thickness to be measured. An initial evaluation is necessary in order to optimise a standing wave signal of sufficient resolution. It has also been shown experimentally that backing the transducers reduces the useful energy within the system as evidenced in the reduced FFT amplitudes. However, it is common practice to back the transducers to protect them from damage.

The epoxy resonance dips obtained from a standing wave method showed a lesser magnitude than the epoxy resonances obtained from a pulse-echo method, signifying increased sensitivity due to the multiple reflections within the substrate.

The standing wave method has an added advantage of reduced processing time as compared to the conventional pulse-echo method. Usually, the first reflected echo from a pulse-echo method has to be isolated in the time domain and appropriately zero-padded then a FFT is performed to obtain the frequency response. This is not the case with the standing wave method because the frequency response is obtained directly by performing a FFT to get the frequency response, effectively bypassing the echo isolation and zero-padding steps entirely.

The results obtained from a standing wave method showed a better agreement with standalone measurements of an epoxy thickness as compared to a pulse-echo method.

6 Mathematical Modelling of A Standing Wave

The previous chapter demonstrated the capability of a standing wave method to experimentally measure the thickness of epoxy coatings on metal substrates. This chapter will now describe the development of a mathematical model that simulates a standing wave through a consideration of mathematical principles and parameters that are known to influence ultrasonic standing waves. The mathematical model aimed to predict the thickness of a surface coating through the identification of coating resonant frequencies from a *S* spectrum, which were acquired from an understanding of wave interference within a coated substrate.

6.1 Mathematical Description

In this work, the laws of reflection were applied for a continuous single frequency wave as discrete entities to the multiple waves responsible for the creation of a standing wave. When propagating through a material, an ultrasonic wave of a known frequency will be attenuated as a function of material attenuation coefficient, α, and length L. The exponential form of the waveform is described in Equation 6-1.

$$A = A_0 e^{-L\propto} \qquad \text{Equation 6-1}$$

When the ultrasonic wave reaches a boundary, it will be reflected along the incident wave path returning it to the source of the original wave upon which it will further be reflected. Figure 6-1 shows a schematic of an ultrasound wave path as it is reflected within a solid material multiple times.

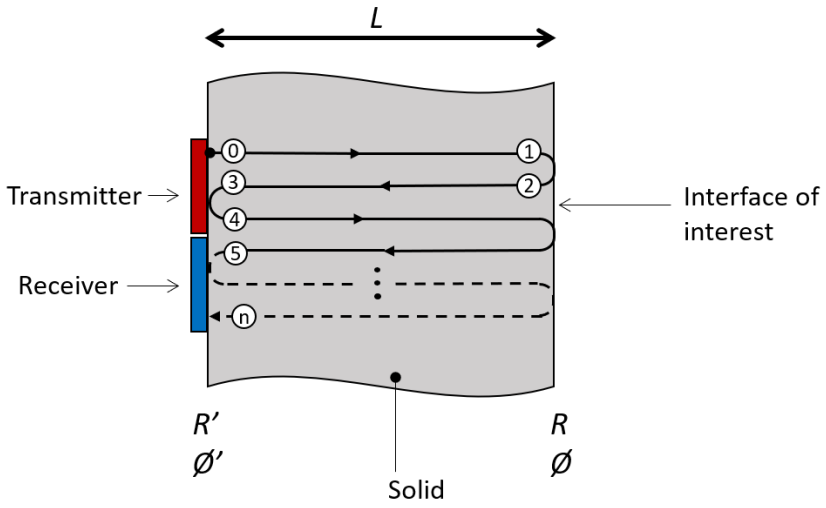

Figure 6-1. Schematic showing incident wave and subsequent reflection paths.

At position 0, the wave amplitude is given by:

$$A_0 e^{i\omega t} \qquad \text{Equation 6-2}$$

At position 1 immediately before the first reflection occurs, the wave amplitude has been attenuated (Equation 6-1) where *L* and *c* are the distance travelled and speed of sound in the solid, respectively and the amplitude is given by:

$$A_0 e^{i\omega(\frac{L}{c}-t)} e^{-L\alpha} \qquad \text{Equation 6-3}$$

At position 2 immediately after the first reflection the amplitude is given by:

$$A_0 e^{i\omega(\frac{L}{c}-t)} e^{-L\alpha} R e^{-i\emptyset} \quad \text{Equation 6-4}$$

where R and Ø are the reflection coefficient and phase change respectively at the interface of interest. $Re^{-i\emptyset}$ is the complex form of the reflection coefficient. The wave then passes back through the solid towards the source and immediately before the reflection at the transducer at location 3, the amplitude is given as:

$$A_0 e^{i\omega(\frac{2L}{c}-t)} e^{-2L\alpha} R e^{-i\emptyset} \quad \text{Equation 6-5}$$

The amplitude at location 4 immediately after the reflection at the solid-transducer interface is given by:

$$A_0 e^{i\omega(\frac{2L}{c}-t)} e^{-2L\alpha} R e^{-i\emptyset} R' e^{-i\emptyset'} \quad \text{Equation 6-6}$$

where *R'* and Ø' are the reflection coefficient and phase change respectively at the transducer boundary. $R'e^{-i\emptyset'}$ is the complex form of the reflection coefficient. After another passage of the wave through the solid, inclusive of reflection and attenuation, the amplitude at location 5 is:

$$A_0 e^{i(\omega(\frac{4L}{c}-t)-2\emptyset-\emptyset')} e^{-4L\alpha} R^2 R' \quad \text{Equation 6-7}$$

If we describe a passage as consisting of travel from the transducer to the interface and back again, we can represent the amplitude of the wave after *n* passages as:

$$A_0 e^{i[\omega(\frac{2nL}{c}-t)-n\emptyset-(n-1)\emptyset']} e^{-2nL\alpha} R^n R'^{(n-1)} \quad \text{Equation 6-8}$$

The significance of *R'* has been experimentally investigated and discussed in the previous chapter in section 5.7. An experiment was set up to demonstrate the effect of backing the transducers on the waveform amplitude. It was observed that when a transducer was backed with an epoxy, the FFT of the waveform experienced a reduction in the maximum amplitude. This was because some sound energy was transmitted into the epoxy at the transducer-epoxy boundary thereby reducing the useful wave energy within the transducer-solid system. Less energy is reflected back into the system meaning that the waveform with a reduced amplitude will undergo a lowered number of reflections before it is completely attenuated.

For a solid-air boundary condition where $R = 1$ the waveform amplitude is now a function of *R'*. Figure 6-2 shows the calculated waveform amplitude after each reflection for various *R'* values.

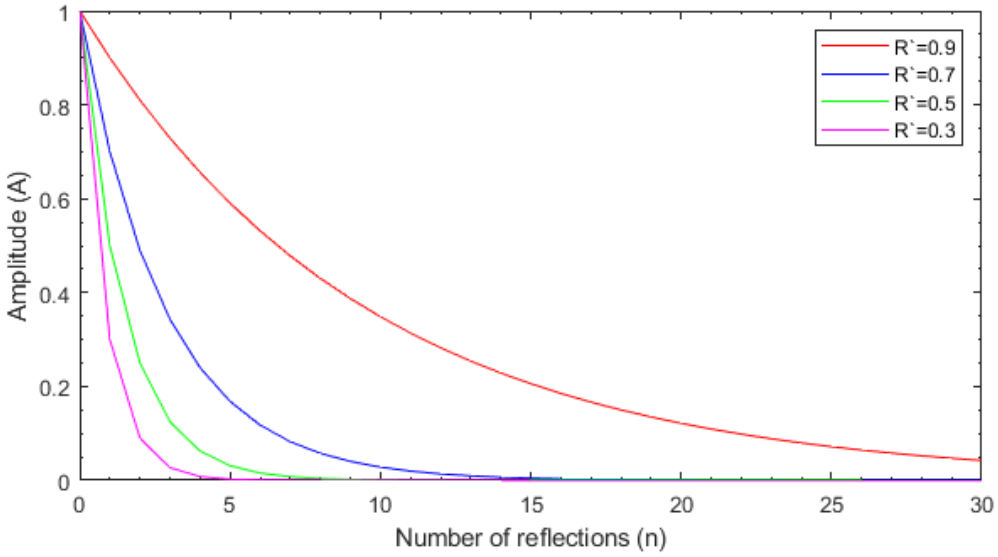

Figure 6-2. A graph to show the effect of various *R'* magnitudes on the wave amplitude with an increasing number of reflections *n*.

It was observed that when *R'* = 0.3, the waveform decays more rapidly than when *R'* = 0.9, the latter which requires 11 reflections to reduce to an amplitude of 0.3 as compared to *R'* = 0.3 which requires just one reflection. Ideally, the reflection coefficient at the transducer *R'* should be as close to unity as possible for the wave incident at the interface of interest to have maximum wave energy. This in turn increases the signal-to-noise ratio.

For any measurement condition, and for a single frequency, all the reflected waves will superimpose, and the standing wave amplitude at the receiving transducer is given as:

$$A = A_0 \sum_{n=1}^{\infty} e^{i[\omega(\frac{2nL}{c}-t)-n\emptyset-(n-1)\emptyset']} R^n R'^{(n-1)} e^{-2nL\alpha} \qquad \text{Equation 6-9}$$

Provided the conditions *n*, *R*, *R'* and material properties *L* and α are given, the maximum amplitude of the standing wave can be found for a given frequency input.

For a solid-air boundary condition, *R*=1 and *Ø*=0, therefore the amplitude is given by:

$$A_{solid-air} = A_0 \sum_{n=1}^{\infty} e^{i[\omega(\frac{2nL}{c}-t)-(n-1)\emptyset']} R'^{(n-1)} e^{-2nL\alpha} \qquad \text{Equation 6-10}$$

When there is a layer present at the boundary, *R* is obtained from Equation 3-46 and *Ø*=π therefore:

$$A_{solid-surface\ layer} = A_0 \sum_{n=1}^{\infty} e^{i[\omega\left(\frac{2nL}{c}-t\right)-n\pi-(n-1)\emptyset']} R^n R'^{(n-1)} e^{-2nL\alpha} \qquad \text{Equation 6-11}$$

Equation 6-10 and Equation 6-11 when plotted will show resonant modes (harmonics) separated at regular intervals as peaks for frequencies that are contained in ω. The ratio of the standing wave amplitudes, *S* can be defined as:

$$S = \frac{A_{solid-surface\,layer}}{A_{solid-air}} = \frac{\sum_{n=1}^{\infty} e^{i[\omega\left(\frac{2nL}{c}-t\right)-n\pi-(n-1)\emptyset']} R^n R'^{(n-1)} e^{-2nL\alpha}}{\sum_{n=1}^{\infty} e^{i[\omega(\frac{2nL}{c}-t)-(n-1)\emptyset']} R'^{(n-1)} e^{-2nL\alpha}} \quad \text{Equation 6-12}$$

The mathematical expression *S* is periodic with time. A root mean square (RMS) of the amplitude provides a frequency response. The solid-air and solid-surface layer frequency responses can then be simulated and used to obtain a *S* spectrum that can be used to identify a surface layer resonant frequencies.

6.2 Components of A Standing Wave

The standing wave equation, *S* described is influenced by collective parameters that affect the phase and amplitude separately as shown in Figure 6-3.

Phase Amplitude

$$A = A_0 \sum_{n=1}^{\infty} e^{i[\omega(\frac{2nL}{c}-t)-n\emptyset-(n-1)\emptyset']} R^n R'^{(n-1)} e^{-2nL\alpha}$$

Figure 6-3. A breakdown of the standing wave equation to show contributing parameters that influence the phase and amplitude.

The position of the standing wave is influenced by the phases at the interfaces, *Ø* and *Ø'* respectively. It is also affected by the phase of the wave as it propagates through the material and this is seen as the influence of the angular frequency function, *ω* at a given time *t*.

The reflection at the transducer *R'* and the interface of interest *R* contribute to the magnitude of the waveform amplitude. The length of the component along with the attenuation coefficient affects the amplitude as the wave propagates through the component.

6.3 Modelling A Standing Wave

A mathematical model was implemented in MATLAB2018 software to simulate the standing wave frequency response within an aluminium substrate used in the previous chapter. The model had three functions: the first to calculate the reflection coefficient functions (Equation 3-46), and the second to sum the number of reflections (Equation 6-10 and Equation 6-11). The waveform amplitudes A_r and A_s were then used to find the standing wave ratio *S*, where A_r represents the solid-air boundary condition and A_s represents the solid- coating boundary condition. A flowchart of the mathematical model script is shown in Figure 6-4. A MATLAB script that modelled a standing wave frequency response is provided in Appendix A.

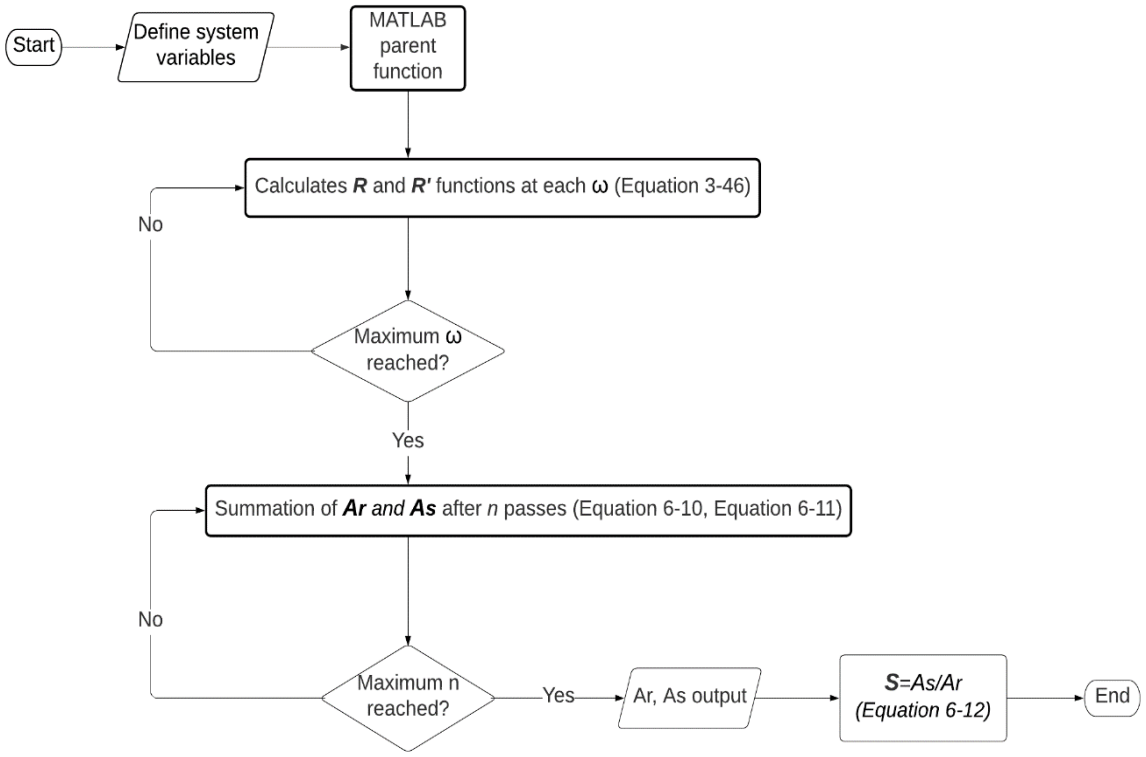

Figure 6-4. A mathematical model flowchart for the generation of a standing wave.

6.3.1 Model Input

The experimental parameters used in the previous chapters were used here to simulate a standing wave within an aluminium component. These variables are listed in Table 6-1.

Table 6-1. System variables.

Material properties				**Units**
z_1	Aluminium acoustic impedance		16.8×10^{6}	Rayl
z_2	Acoustic impedance	Epoxy for *R* condition	3.15×10^{6}	Rayl
		Transducer for *R'* condition	33.7×10^{6}	Rayl
z_3	Air acoustic impedance		384	Rayl
c_2	Surface film longitudinal acoustic velocity	Epoxy for *R* condition	2670	m/s
		Transducer for *R'* condition	4350	m/s
h	Surface film thickness	Epoxy for *R* condition	138×10^{-6}	m
		Transducer for *R'* condition	2×10^{-4}	m
L	Aluminium thickness		0.01	m
c	Aluminium longitudinal acoustic velocity		6211	m/s
Ultrasound chirp wave input				
f	Frequency		0: 1MHz: 20MHz	
n	Number of reflections		1:60	

Once the system variables were defined, the reflection coefficients at the transducer and the epoxy interfaces were calculated at each angular frequency. Once this was complete, the waveforms were summed after the number of reflections, *n*. The standing wave ratio *S* was calculated by taking the ratio of the solid-epoxy to solid-air waveform amplitudes.

6.3.2 Model Output

A standing wave frequency response for a solid-air boundary condition shown in Figure 6-5 was modelled using the variables listed in Table 6-1. The standing wave frequency response for a solid-epoxy boundary condition will be discussed later on in section 6.5.

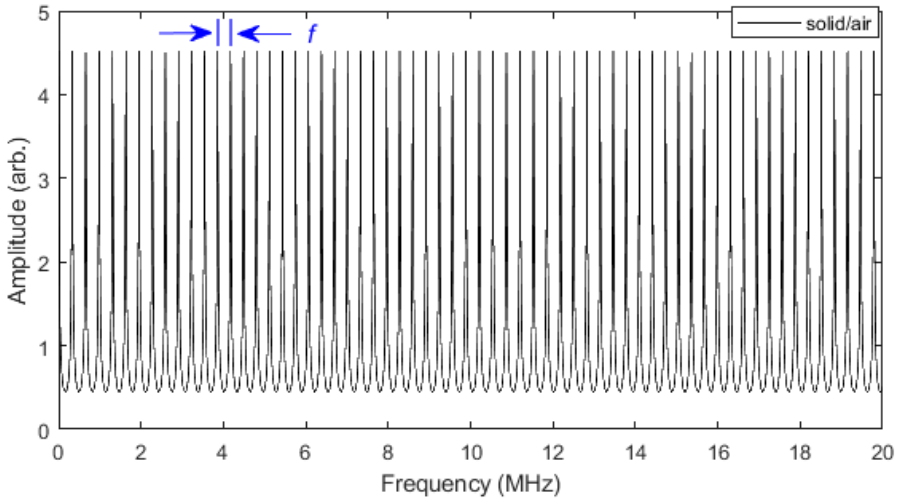

Figure 6-5. Standing wave frequency response for a 10mm thick aluminium component. The peak spacing identified as *f* represent the component resonant frequency.

A component resonant frequency *f* of 320kHz was calculated as the average of the difference between any two successive peaks in the frequency range 0-20MHz. The calculated *f* showed a standard deviation of 4.72kHz. An experimental *f* was calculated in the previous chapter in section 5.3 as 305kHz with a standard deviation of 11.7kHz. These results showed a good correlation.

The factors that influence the mathematical model will be discussed in the section that follows.

6.4 Factors That Influence the Mathematical Model

In order to simulate a standing wave that best describes the experimental results we need to consider a number of factors that affect the formation of the standing wave when using the mathematical model. The component length, the number of wave reflections within the aluminium component and the attenuation coefficient affect the model output.

6.4.1 Component Length

A normal solid-air waveform profile for a 10mm aluminium component after a sufficient number of reflections for a 0-20MHz frequency span is shown in Figure 6-5. The frequency response showed peaks and troughs with a uniform pattern. This was expected because not all frequencies constructively interfered to have maximum amplitudes. At certain frequencies that are a multiple of the component resonant frequency the waveform was at its maximum. Reiterating Equation 3-56:

$$f_n = \frac{nc}{2L}$$ Equation 6-13

where f_n represents the resonant frequency, and n represents the mode number. This equation calculates that for a 10mm aluminium substrate, approximately 62 resonant peaks are formed from a 0-20MHz frequency chirp. A 5mm aluminium component showed 30 resonant peaks for the same frequency chirp and the spacing between adjacent peaks will be greater as illustrated in Figure 6-6.

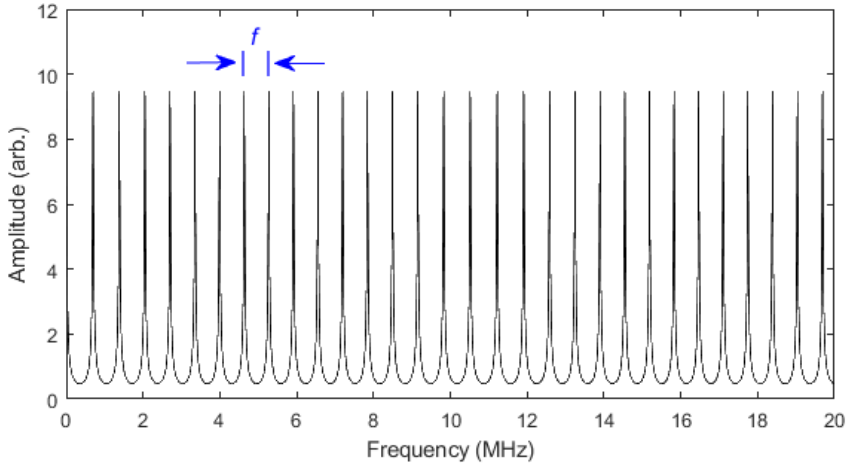

Figure 6-6. Mathematical modelling of a standing wave profile for solid-air boundary condition for a 5mm aluminium component.

The average spacing *f* for a 5mm was calculated as 660kHz with a standard deviation of 19.76kHz. It should be noted that the waveform for a 5mm component now has peak amplitudes greater than for a 10mm. This is because the waves undergo less attenuation due to the fact that attenuation is dependent on the length of the component (Equation 6-1).

6.4.2 Number of Reflections

The influence of the number of reflections, *n* was investigated by analysing a single resonance peak from the standing wave profile. This is because the model was only capable of producing the frequency response of the system at a steady state by first considering single wave frequencies individually and then summing them up to produce a standing wave frequency spectrum. The experimental method on the other hand considers the interferences of mixed frequencies. Therefore a single standing wave peak amplitude that was caused by a single frequency wave interference was investigated to determine the effect of the number of reflections on the amplitude of the standing wave.

In reality the number of reflections within the solid are many and especially when considering the boundaries of the material. In this study a single path was considered as originating from the transducer-solid boundary interface.

A resonant peak at 6.07MHz from a 10mm frequency response was considered for this investigation. The influence of the number of reflections on the amplitude of the resonant peak is shown in Figure 6-7.

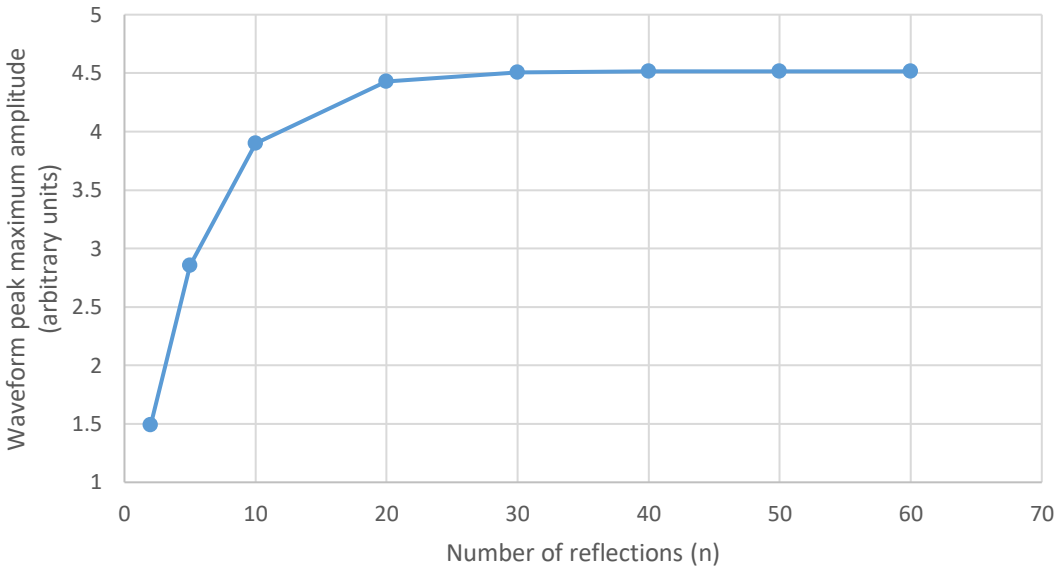

Figure 6-7. The effect of number of reflections, *n* on the peak amplitude.

The peak amplitude rises sharply for the first 20 reflections before reaching a maximum amplitude after 50 reflections after which it stabilises. Table 6-2 gives the values of the peak maximum amplitude for increasing values of *n*.

Table 6-2. The change in peak maximum amplitude as *n* increases.

Number of Reflections	Peak Maximum Amplitude (arb.)
2	1.489
5	2.855
10	3.9
20	4.43
30	4.504
40	4.514
50	4.515
60	4.515

It was noted that the peak value plateaus after 50 reflections with no significant change between 50 and 60 reflections. A change in amplitude of 0.01 might be difficult to differentiate from noise when analysing experimental results.

The time that it would take for a single frequency wave to complete 40 reflections in the solid can be calculated as:

$$\frac{2 \times 0.01m \times 40}{6211\ m/s} = 1.29 \times 10^{-4}s \qquad \text{Equation 6-14}$$

The value $\Delta f/s$ for a 19 MHz frequency sweep with a 4ms sweep time duration was calculated as:

$$\frac{19 \times 10^{6}Hz}{4 \times 10^{-3}} = 4.75 \times 10^{9}Hz/s \qquad \text{Equation 6-15}$$

Therefore, after 40 reflections, the experimental change in frequency was calculated as:

$$1.29 \times 10^{-5} s \times 4.75 \times \frac{10^9 Hz}{s} = 611.82\ kHz$$ Equation 6-16

If we consider a resonant frequency of 10 MHz, the frequency will change by 6.12% to the next frequency (<10% change). This change in frequency is relatively small when considering frequencies in the MHz range to allow the assumption of single wave interferences to form the standing wave. When sweeping through the frequencies, the individual frequency residence time was small enough to allow the standing wave resonances to be equally spaced.

6.4.3 Attenuation Coefficient

Attenuation is considered a function of frequency and the different frequencies in the chirp will be attenuated differently. Early experimental and theoretical work on aluminium by Merkulov in 1956 shows that attenuation increases with increasing frequency [87]. Figure 6-8 shows this frequency dependence of attenuation in aluminium from 100kHz to 1 GHz.

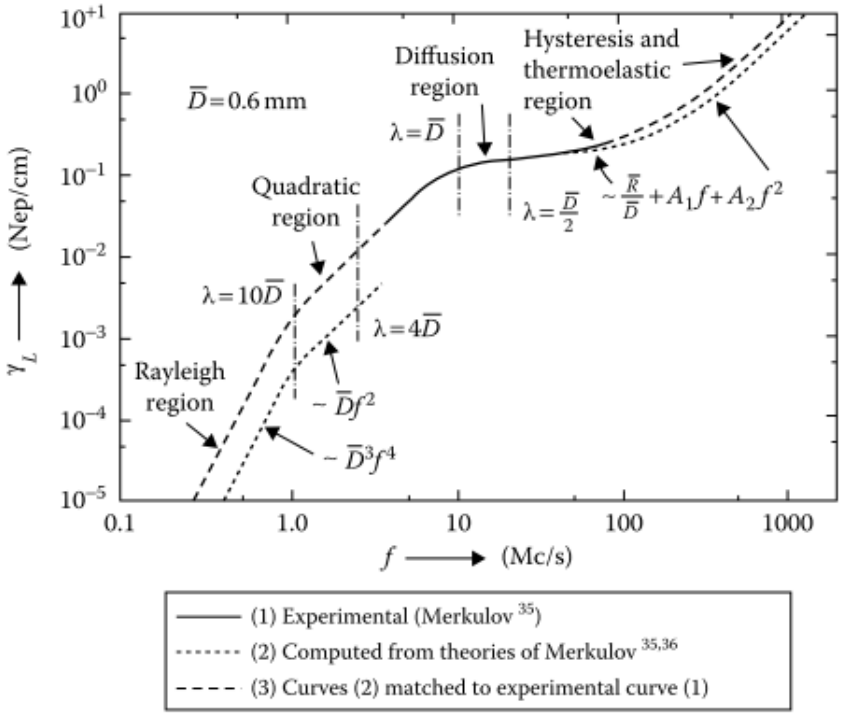

Figure 6-8. Attenuation of ultrasonic longitudinal waves in aluminium (image adapted from [87])

However, Equation 6-12 shows that the attenuation coefficient normalises out and the thickness measurement of surface coating remains unaffected by the dependence of attenuation coefficient on frequency. The magnitude of the frequency responses, however, is dependent on the material acoustic properties.

To illustrate the effect of attenuation between two different metal substrates, a 10mm thick steel component was instrumented with piezoelectric transducers in pitch catch arrangement. The ultrasound hardware was set to send a frequency sweep of 19MHz with a sweep duration of 4ms. The standing wave frequency response for the steel substrate was compared with that shown from Figure 5-9. The results were collated as shown in Figure 6-9.

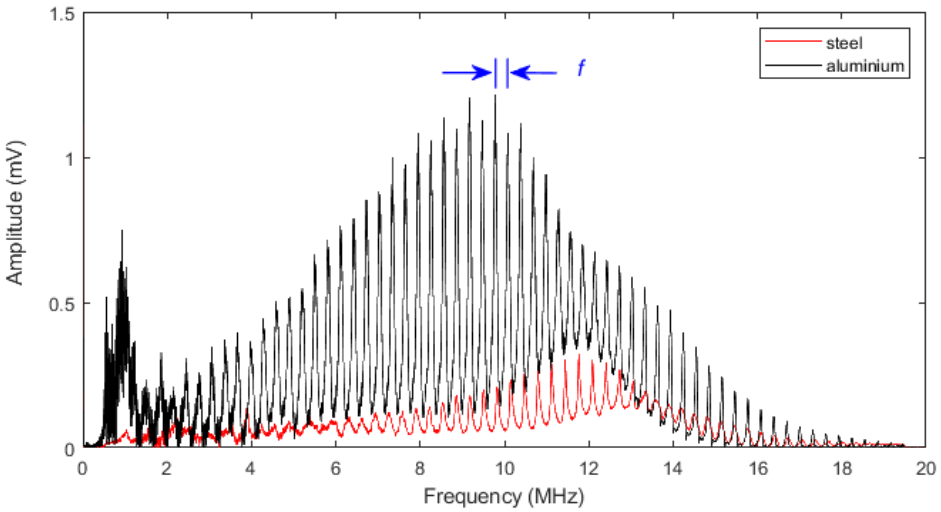

Figure 6-9. Experimental standing wave frequency responses for a 19MHz frequency sweep on 10 mm thick aluminium and steel components for solid-air boundary condition.

The steel resonant frequency was calculated by taking the average of the differences between adjacent peaks *f*. The results showed a steel resonant frequency of 316.44kHz with a standard deviation of 16.19kHz. The aluminium results on the other hand showed a resonant frequency of 305kHz with a standard deviation of 11.7kHz. These results showed a good correlation. It was observed that the aluminium response had a greater amplitude than the steel response. The 10.14MHz peak for the steel response had an amplitude of 0.23mV whereas the 10.08MHz peak observed for the aluminium response had an amplitude of 1.08MHz. This shows a nearly three times reduction in the amplitude. Aluminium has an acoustic impedance of 17MRayls whereas mild steel has an acoustic impedance of 45MRayls [45]. The results showed a good agreement. Therefore, experimentally speaking, the compound effect of attenuation coefficient is to affect the magnitude of the substrate resonant modes depending on the solid acoustic properties.

6.5 Calculating A Surface Coating Thickness Using A Mathematical Model

A surface coating causes the phase $\emptyset$ of the driving frequency to change by π radians when the thickness is a multiple of a quarter wavelength of the driving frequency. The reflected waves would therefore destructively interfere at these frequencies and this would change the coherent standing wave resonant frequencies.

The frequency responses for a solid-air and solid-epoxy from the model were plotted to show the distribution of the maximum peaks. The results are shown in Figure 6-10.

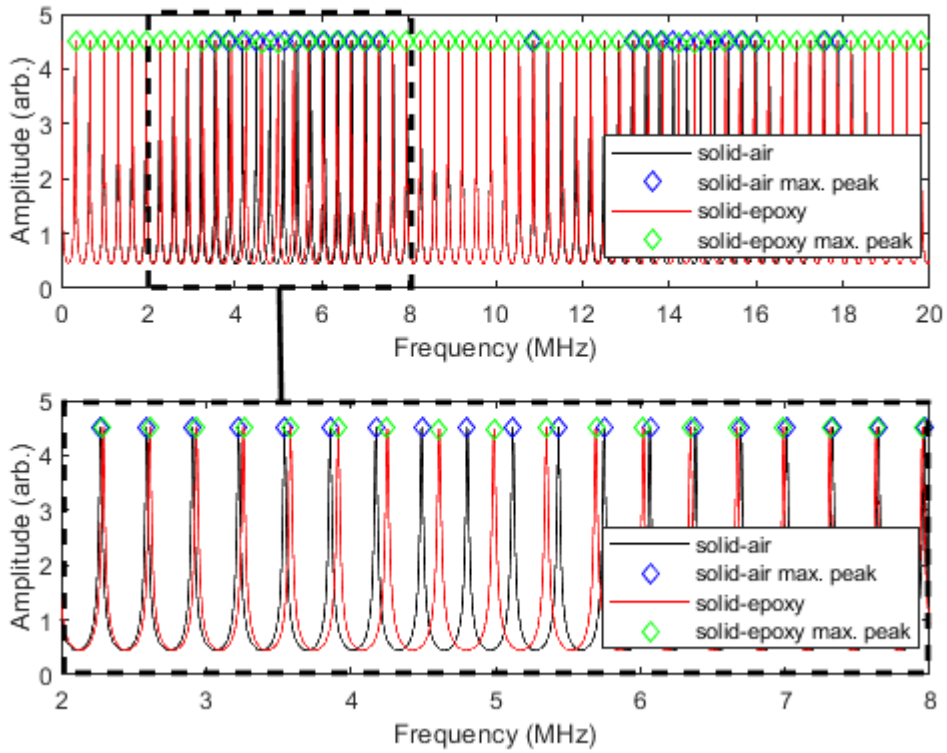

Figure 6-10. (Top) The frequency responses for solid-air and solid-epoxy boundaries with the peaks identified by coloured diamond shapes (bottom) a magnified view in the frequency range 2MHz-8MHz.

It was observed that the solid-air response had 62 peaks whereas the solid-epoxy response had 60 peaks. The difference between the solid-air and the solid-epoxy resonant peaks was observed to increase from 0 up to a point where the phase would be reversed. The difference, now negative, increased to 0 where the peaks had the same phase, and the process repeated itself at regular intervals. This pattern is illustrated in Figure 6-11.

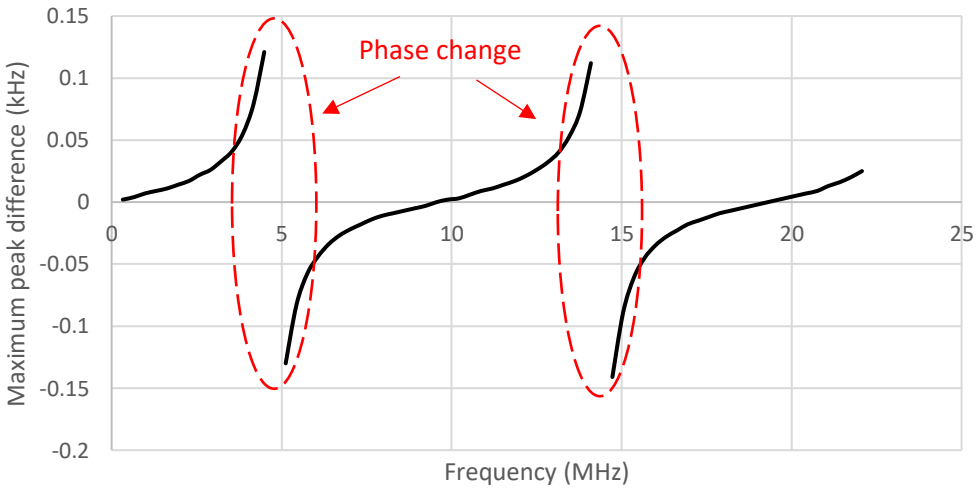

Figure 6-11. A plot to show the maximum peak amplitude differences between a solid-air FFT and solid-epoxy FFT for a 138.2µm epoxy layer.

At certain frequencies, the phase is changed as shown. It was also observed that the resonance peaks at these frequencies were missing. The peak difference pattern showed similarities with the phase change pattern that was observed in Figure 5-23. The exact frequencies where the phase change occurred were identified from a *S* plot. The *S* plots for both the experimental data and model are shown in Figure 6-12.

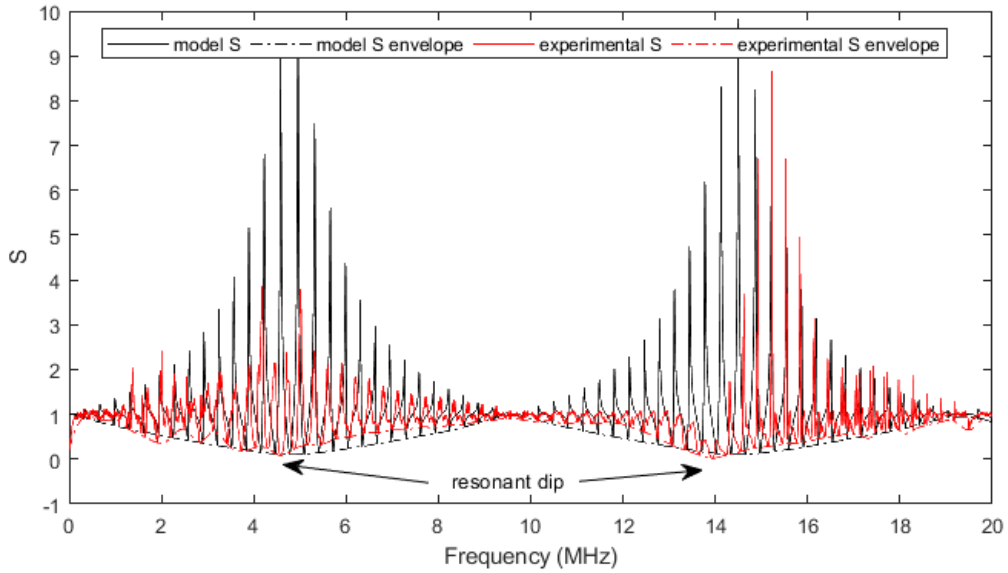

Figure 6-12. Comparison between experimental data and simulated *S* spectra for a 138.2μm epoxy layer.

A strong correlation was observed between the two spectra where they almost overlapped. The *S* peaks occurred where the magnitude of the solid-epoxy response was much greater than the solid-air response whereas the minimum points occurred vice versa. A lower envelope function was used to interpolate the *S* spectra to accurately identify the lowest points. The minimum points corresponded to the frequencies where a phase change occurred. The phase change occurred at f_0 = 4.82MHz and $3f_0$ = 14.49MHz, respectively from the model results. The experimental phase change frequencies were identified as f_0 = 4.58MHz and $3f_0$ = 13.93MHz, respectively. The results in Table 6-3 show the magnitudes of the epoxy resonances obtained from the *S* plots.

Table 6-3. Experimental and mathematical modelling difference between the epoxy resonant modes

	Experimental data	Simulation
f_0 frequency	4.58MHz	4.823MHz
f_0 *S* magnitude	0.08359 (dimensionless)	0.1014 (dimensionless)
$3f_0$ frequency	13.93MHz	14.49MHz
$3f_0$ *S* magnitude	0.0192 (dimensionless)	0.1038 (dimensionless)

The results showed a strong correlation. The epoxy fundamental frequency f_0 was calculated by halving the difference between the resonant dips. These were calculated as 4.675MHz and 4.834MHz for the experimental data and model, respectively. The epoxy thicknesses were then

calculated as 142.78μm and 138.08μm, respectively. The thickness calculated from the model was not exactly 138.2μm due to rounding off errors.

It is thought that the slightly higher thickness approximation from experimental data was due to the transducer bonding and also that the epoxy material may have contained some impurities that would have affected the speed of sound. The speed of sound could also have been affected by temperature effects although these were assumed negligible.

6.6 Conclusions

A mathematical model was used to simulate a standing wave formed at a steady state in the frequency domain. The standing wave was modelled from single frequency wave interference principles. The principle equations were derived from the work of Mills et al. [83] and consideration was given to a number of parameters that influence the formation of the standing wave.

The reflection coefficient at the transducer, *R'* was investigated and it was identified that *R'* should be as close to unity as possible in order to retain as much energy as possible within the system and to overcome the noise levels when analysing experimental signals. The effect of the component length, *L* was investigated, and it was demonstrated that the number of resonance peaks (harmonics) is dependent on the length of the component. The amplitude of the resonant peaks was also found to be affected by the component length due to dependence of attenuation on the material length. The number of reflections, *n* was also investigated, and it was identified that, for a 10mm thick aluminium component, the waveform amplitude reaches a maximum after 50 reflections. The change in frequency when sweeping through the multiple frequencies in a chirp wave was sufficiently small, when considering frequencies in the MHz range, to allow the assumption of single wave interferences to form the standing wave. The residence time was small enough to allow the standing wave resonances to be equally spaced.

The frequency spectra showed that the frequencies with a maximum reduction in amplitude showed a lowest point in the *S* plot. These corresponded to frequencies where a phase change occurred. The *S* spectra between the experimental and modelling results showed a strong correlation. A quarter wavelength theory was applied to calculate the coating thickness using these resonances and a comparison between epoxy thickness calculated from standing wave response and independent profilometer measurements showed a strong agreement.

A practical application of using the mathematical model would be in simulation scenarios to compare with real data from coatings inside closed vessels. The model could then be optimised to estimate a variety of coating physical parameters.

7 Thermal Effects on Standing Wave Measurement

The aim of this chapter was to assess the possibility of using a standing wave method to measure a surface coating thickness at different temperatures. To do this, a steel substrate was instrumented with longitudinal sensors and a temperature calibration was first carried out to provide a reference. Next, an epoxy layer was cured on the steel substrate and standing wave measurements were performed at various temperatures to calculate the coating thickness. The results and limitations of the method are then discussed.

7.1 Specimen Instrumentation

A 10mm thick steel component was instrumented with a pair of 10MHz wrap around piezoceramic elements (2mm×7mm dimensions) in a pitch-catch arrangement as shown in Figure 7-1a.

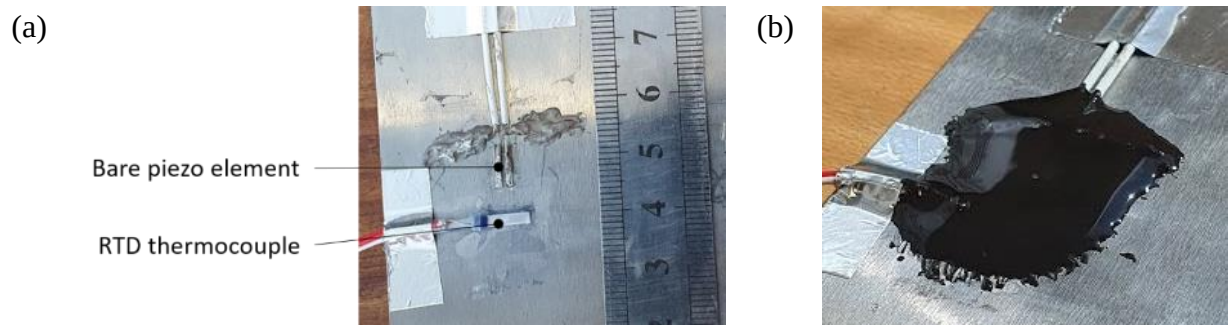

Figure 7-1. Photographs showing (a) the bonded sensor pair and the RTD thermocouple (b) the heat resistant epoxy cured over the sensors.

Steel was chosen over aluminium as the substrate of choice because of the lower thermal conductivity or heat transfer. Steel has a thermal conductivity of ~15W/m.k (Watts per metre per Kelvin) whereas aluminium has a thermal conductivity of 237W/m.k [88]. This meant that the steel substrate would retain heat better during data acquisition.

A RTD thermocouple was bonded next to the sensors to record the temperature of the component. A heat resistant epoxy was cured over the sensors and thermocouple layout (Figure 7-1b) for protection.

7.2 Temperature Calibration

The instrumented specimen was placed in a programmable oven and the temperature was ramped up from ambient temperature (24℃) to 30℃, then in increments of 10℃ to a maximum temperature of 120℃. The ultrasound measurements were controlled using a Triboscope software. The temperature at each step was left to stabilise for 5 minutes. The standing wave frequency response at ambient temperature for a 19MHz sweep having a 10MHz centre frequency is shown in Figure 7-2.

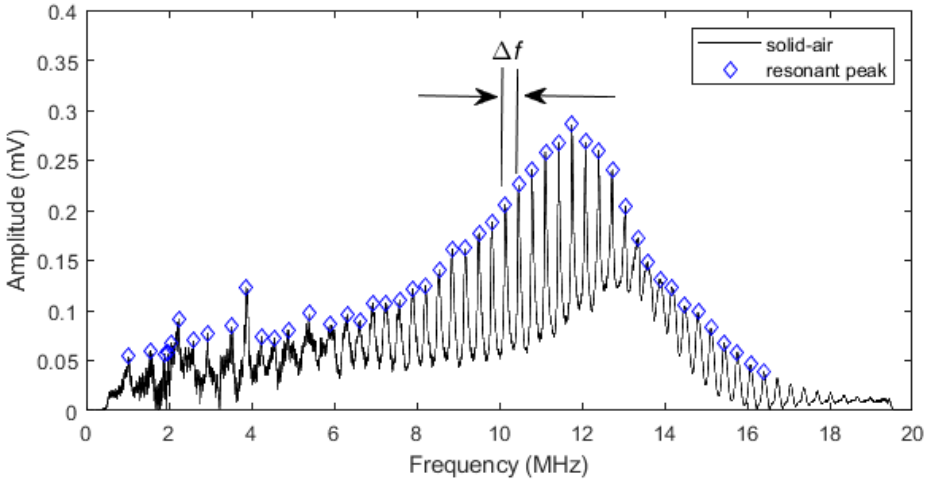

Figure 7-2. Standing wave frequency response for a solid-air boundary condition at ambient temperature.

The steel resonant mode frequencies (Equation 3-56) were observed as peaks. The differences between adjacent peaks Δf were calculated and plotted as shown in Figure 7-3.

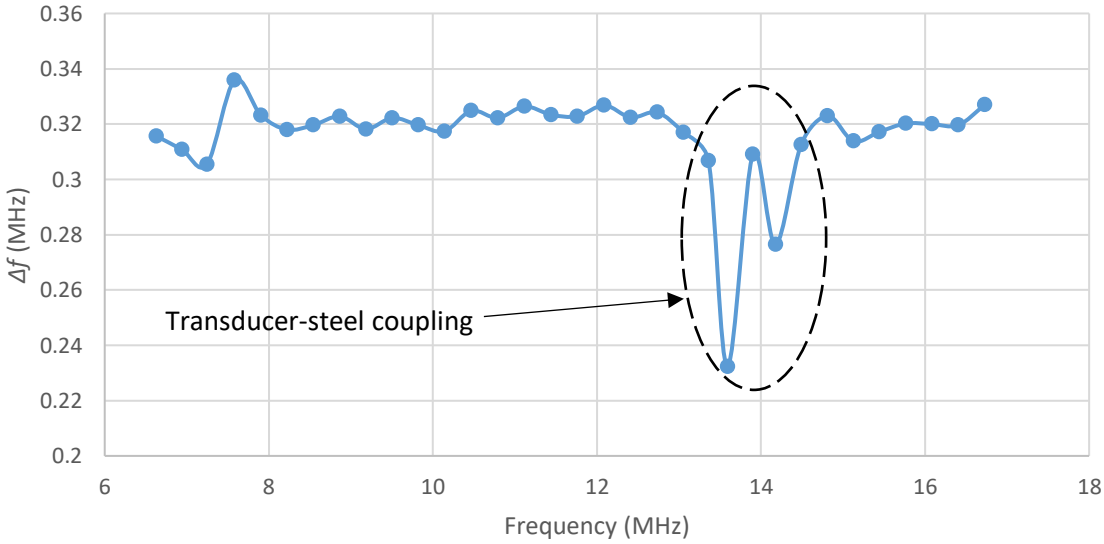

Figure 7-3. Adjacent peak separation showing the transducer-steel substrate coupling effect.

The peak separation around the transducer resonance (13.4MHz-14.4MHz) was noted to show a significant reduction due to energy coupling between the transducer and the steel component and these were omitted from calculations [80], [81]. The peaks in the frequency range 8MHz-13MHz were averaged to give a fundamental frequency, f_0 of 321.99kHz with a standard deviation of 0.00295kHz. Using Equation 3-56, the speed of sound in the steel, c was calculated as 6439.73 ± 59.03 m/s.

The standing wave frequency response behaviour for the 24°C to 120°C temperature range is shown in Figure 7-4.

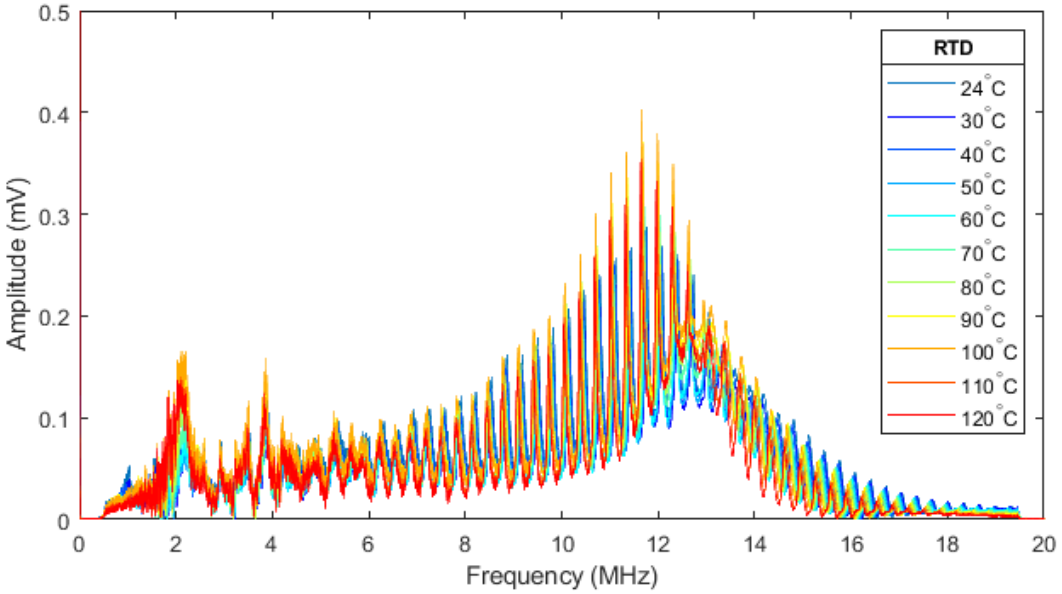

Figure 7-4. Standing wave frequency response behaviour at different temperatures.

The peaks were observed to have shifted to the left along the horizontal axis with increasing temperature. A magnified view of Figure 7-4 for the resonant peak in the frequency range 11.5MHz-11.8MHz is shown in Figure 7-5 to illustrate this shift behaviour.

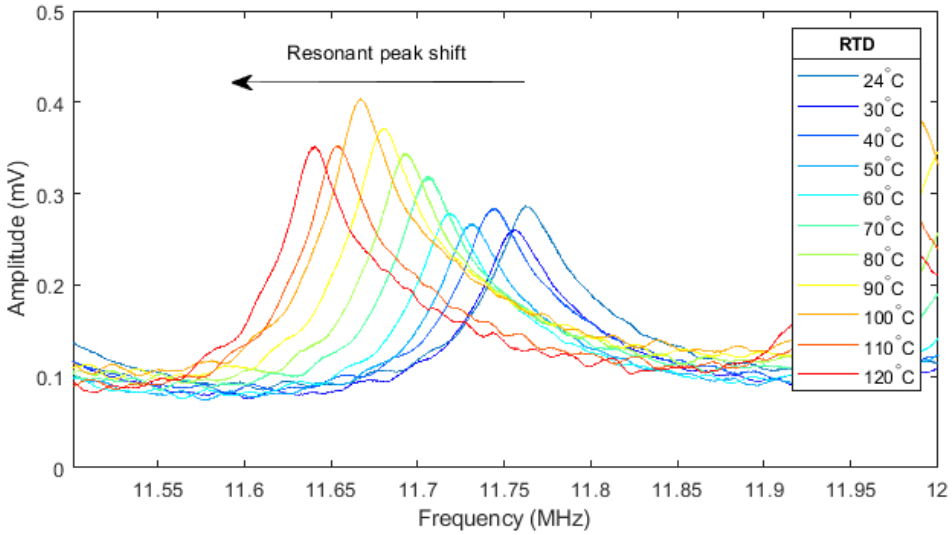

Figure 7-5. A magnified view of the standing wave frequency response behaviour at different temperatures.

The resonant peak at 24℃ was observed to have its peak at 11.76MHz whereas the maximum peak at 120℃ was at frequency 11.61MHz. This showed a change of 150kHz. The maximum peak amplitude also showed a general increase in amplitude with increase in temperature.

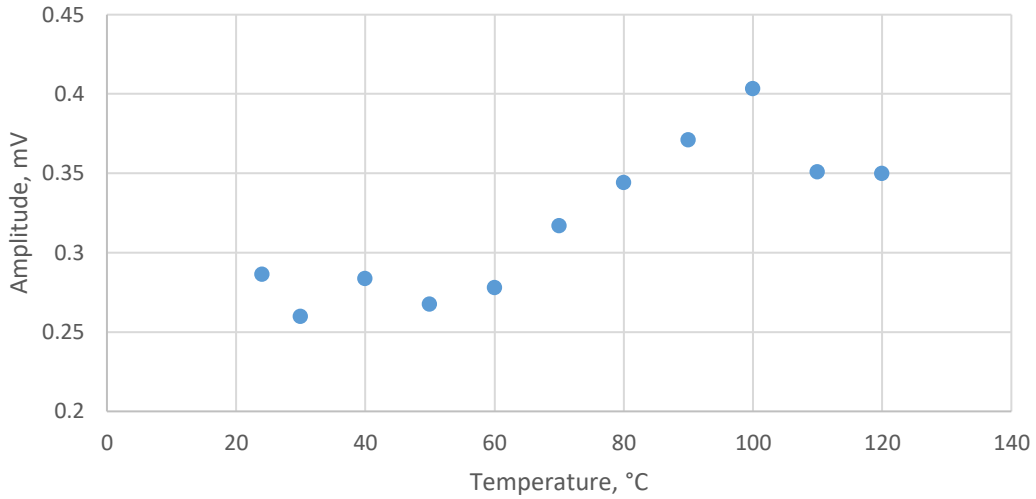

Figure 7-6. The maximum peak amplitude increase with increasing temperature.

The lowest amplitude was recorded as 0.26mV at 30°C and the highest as 0.4mV at 100°C. The increase in amplitude was thought to be a caused by the attenuation coefficient reduction with increasing temperature.

Van Thanh et al. [89] have shown that the attenuation coefficient of a 5MHz longitudinal pulsed ultrasound wave in a 99.8mm thick AISI 1018 steel substrate reduces with increasing temperature in the range 0-50°C. As a result more ultrasound energy is retained in the system producing higher amplitudes. However, the dependence of attenuation coefficient on temperature was not linear and was thought to be affected by grain size.

Wan et al. [90] showed that the attenuation coefficient of pulsed ultrasound waves in the frequency range 5-30MHz in a 2mm thick 316L steel substrate was affected by random grain size and fell in a stochastic scattering regime. The attenuation coefficient followed a power law relationship with frequency. Their model assumed that the grain size was cubic and that the alloy was pure. Their results showed that the grain size increased with temperature. However, there were some discrepancies with numerical simulation, and it was thought that inhomogeneity in the grain size distribution in the samples that resulted in larger scattering was a possible cause. Presence of impurities in the metal could also be a contributing factor. Nonetheless, their results showed a good agreement with numerical modelling of attenuation coefficient dependence on grain size.

The difference between adjacent peaks in the frequency range 8MHz-13MHz were calculated at the different temperatures and then averaged to give f_0. These results are shown in Figure 7-7.

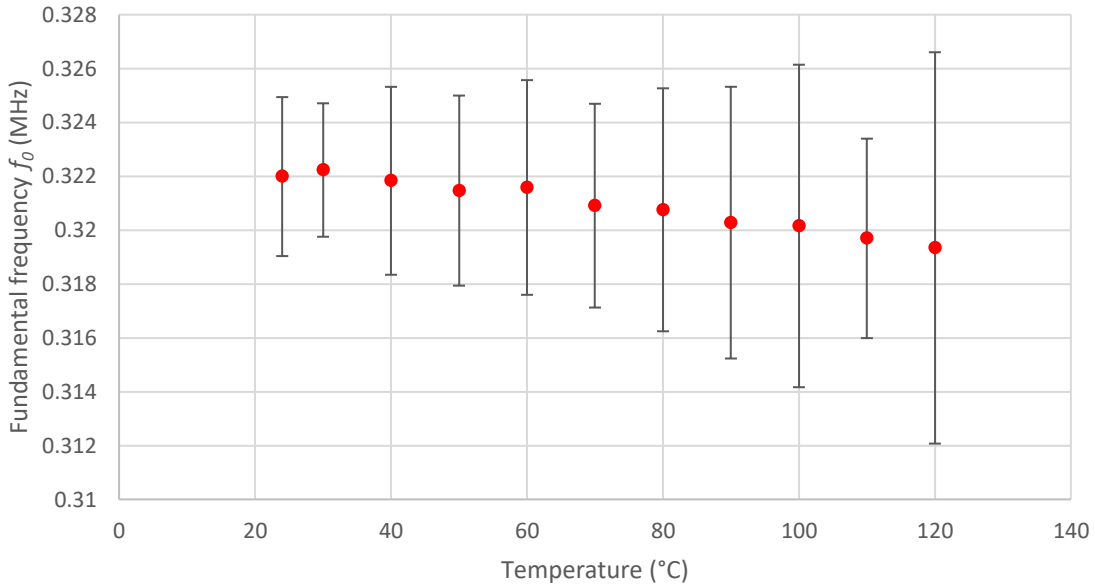

Figure 7-7. A graph of fundamental frequency at different temperatures for a solid-air boundary condition.

The vertical error bars represent the standard deviation. The errors were observed to increase with temperatures. The results showed that f_0 reduced with increasing temperature. The fundamental frequency reduced from 0.322MHz at 24℃ to 0.319MHz at 120℃.

When a solid object undergoes expansion due to a heating effect, the length changes from L_0 to L_1 and the new length L_1 can now be written in terms of linear thermal expansion as:

$$L_1 = L_0 + \Delta L = L_0 + L_0\alpha(T_1 - T_0) \qquad \text{Equation 7-1}$$

where L_1 and L_0 represent the final and initial lengths, ΔL represents the change in length, α represents the linear thermal expansion coefficient, T represents the temperature in degrees Celsius, and the subscripts 1 and 0 represent the final and initial temperatures, respectively. The linear thermal expansion of steel lies in the range 10- 17.3 µm/m˚C (12 for most common steels) [91]. The linear expansion of the steel substrate was calculated using Equation 7-1 for the temperature range 24℃ to 120℃. The steel substrate was calculated to increase by 11.52µm from 24℃ to 120℃.

The experimental speed of sound at the different temperatures was then calculated using Equation 3-56 where L was obtained from the linear thermal expansion of the steel substrate and f_0 was obtained from the results shown in Figure 7-7. The results are shown in Figure 7-8.

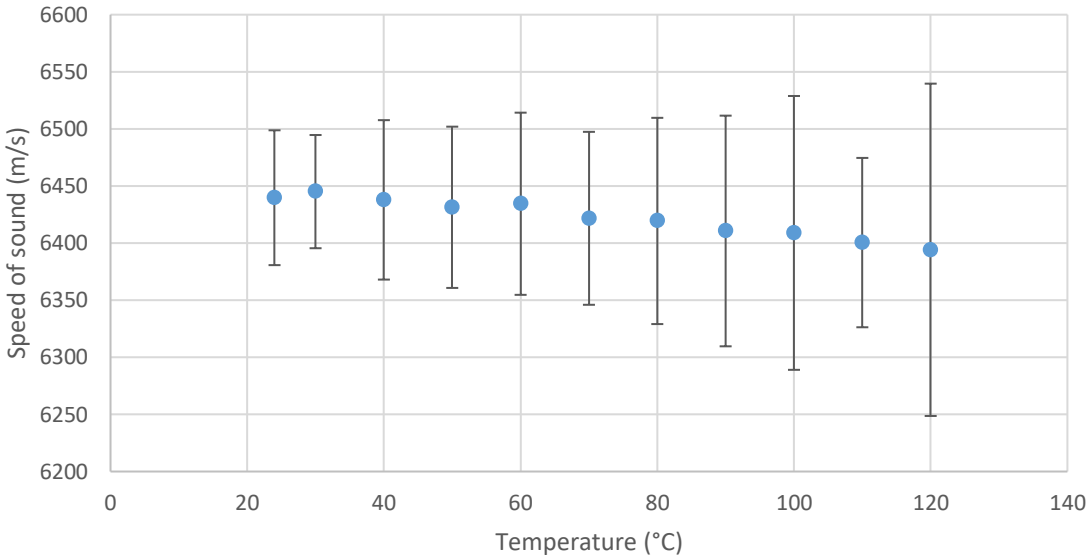

Figure 7-8. The speed of sound in a 10mm thick steel substrate at different temperatures.

The results showed a generally linear trend where the speed of sound was observed to reduce with increasing temperature, reducing from 6439.73 m/s at 24°C to 6394.13 m/s at 120°C. The vertical error bars represent the standard deviation that was obtained from the fundamental frequency calculations. The standard deviation was observed to increase with an increase in temperature.

When the temperature is increased, the density of a solid material slightly decreases, and the Poisson's ratio increases with increasing temperature [92]. The temperature dependence of the speed of sound in the steel can be written as [89], [93]:

$$c(T) = c(T_0) + \frac{dc}{dT}\Delta(T - T_0) \qquad \text{Equation 7-2}$$

where c is the speed of sound in the steel, T is the final temperature, T_0 is the reference temperature, and $\frac{dc}{dT}$ is the temperature dependence coefficient which lies mostly in the range -0.8 m/s°C and -0.9m/s°C for carbon steels. The speed of sound in the steel substrate at the different temperatures was calculated using Equation 7-2 where $\frac{dc}{dT}$ was taken as -0.8m/s°C. The speed of sound at 24°C had already been calculated previously and was used as a reference. The results are shown in Figure 7-9 together with those obtained earlier from Figure 7-8.

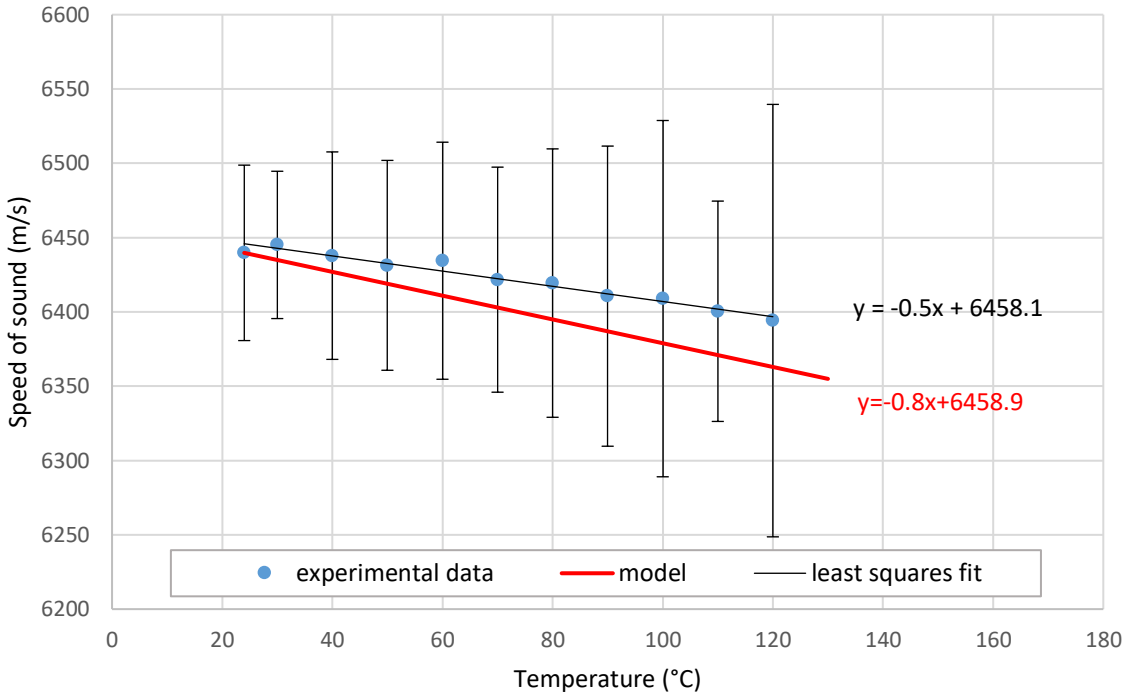

Figure 7-9. Speed of sound comparison between experimental data and temperature dependence speed of sound model.

The vertical error bars represent the standard deviation in the experimental data. A least squares regression line of best fit of the experimental data showed a $\frac{dc}{dT}$ value of -0.5 m/s°C and a speed of sound value 6458.1 m/s at 0°C, which was similar to the model prediction of 6458.9 m/s. The difference between the $\frac{dc}{dT}$ value of -0.5 m/s°C from the least squares fit and the standard carbon steel temperature dependence coefficient range of -0.8 m/s°C to -0.9 m/s°C suggested that the substrate could potentially be a type 304 stainless steel variant [94]. When a stainless steel thermal coefficient of 10.4 µm/m˚C [95] was used in the calculations, a least squares fit equation was given as *y=-0.5x+6458.4* therefore the difference was negligible.

7.3 Effect of Temperature on A Surface Layer Thickness Measurement

When a surface coating is at the interface of interest, the component standing wave amplitude reduces at specific frequencies, and the reflection coefficient *S* (Equation 5-2) will show coating resonances as dips. This has been discussed in the previous chapters. A Robnor epoxy layer was placed on the front surface of the instrumented steel substrate and left to cure overnight. The epoxy thickness was then measured independently using a surface profilometer at ambient temperature to give an estimate of 327.49µm.

The standing wave frequency responses for a solid-air and solid-epoxy boundary conditions at ambient temperature (24°C) along with the *S* plot are shown in Figure 7-10.

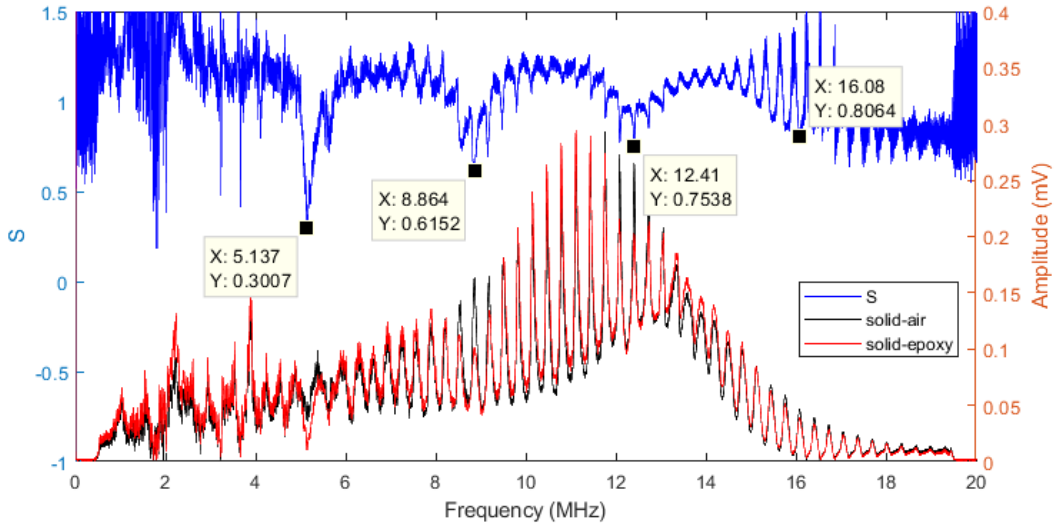

Figure 7-10. The frequency spectra of the standing wave for solid-air and solid-epoxy responses and the S plot.

The *S* plot showed four resonant dips at 5.137MHz, 8.864MHz, 12.41MHz, and 16.08MHz. The epoxy fundamental frequency was calculated as 1.824 ± 0.0372MHz. The Robnor material had similar physical properties when cured to polyimide material and the polyimide material has been shown to have a speed of sound roughly at 2386 m/s at ambient temperature [96].

Tezuka et al. [96] report on an equation for speed of sound in a polyimide material that is a function of temperature as shown in Equation 7-3:

$$c = 2410 - T \qquad \text{Equation 7-3}$$

where c is the speed of sound in the polyimide and T is the temperature in ℃. It can be seen that the speed of sound reduces with increasing temperature. Because the Robnor epoxy and polyimide material have similar properties it is assumed that Equation 7-3 could also be applied for Robnor. Although a more accurate method of establishing the temperature dependence of speed of sound in Robnor would be to perform measurements experimentally.

As a result, the epoxy thickness was estimated to be 327.19 ± 5.83μm using Equation 3-52. This showed a 0.1% decrease from the standalone profilometer measurements. The standard deviation 0.0372MHz is the uncertainty reported here. It contributed to a relative coating thickness uncertainty of 5.83μm. This showed excellent agreement with the independent profilometer epoxy thickness measurement.

The *S* plots for the rest of the temperature data were calculated by taking the ratio of the solid-epoxy and solid-air frequency responses at the respective temperatures. The measurable epoxy resonant dips for the different temperatures were extracted and compared as shown in Figure 7-11.

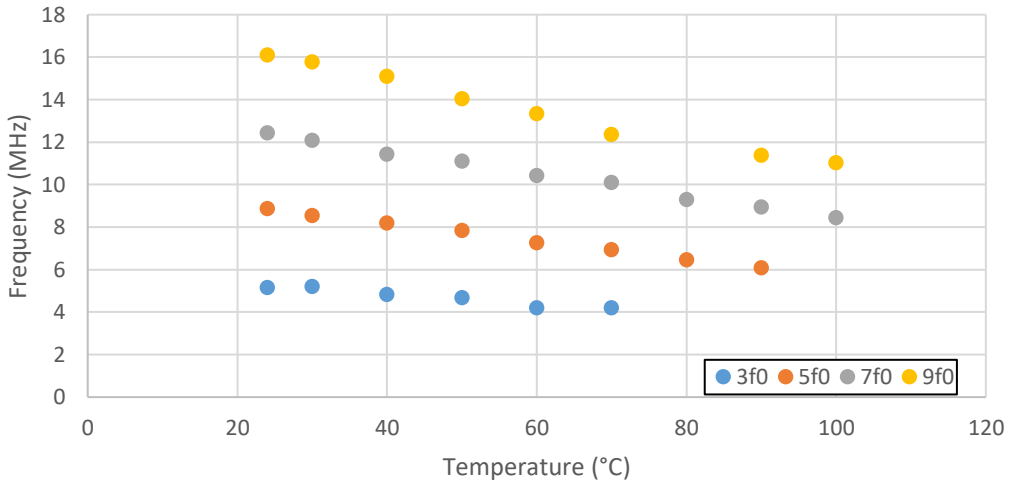

Figure 7-11. Epoxy resonant dip frequencies at different temperatures.

The respective epoxy resonance frequency locations were observed to reduce with an increase in temperature. $3f_0$ was observed to reduce from 5.14MHz to 4.19MHz. $9f_0$ was also observed to reduce from 16.08MHz to 11.02MHz. However, some resonant frequencies were difficult to identify at higher temperatures (80°C to 100°C). For example, the amplitude of the resonant frequency $3f_0$ increased from 0.28 to 0.64 from 24°C to 50°C. Difficulties were also experienced in identifying any resonant frequency beyond 100°C. The difficulties encountered arose due to the epoxy transitioning from a glassy state to a rubbery state. An illustration to demonstrate this is shown in Figure 7-12.

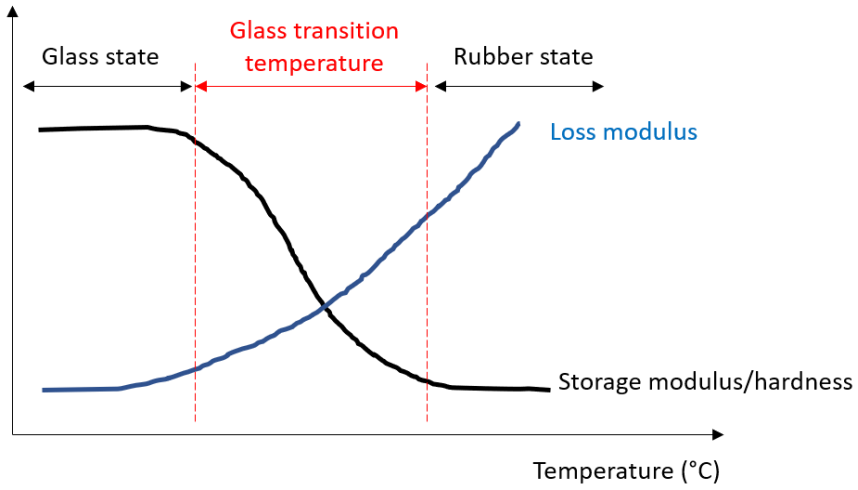

Figure 7-12. Illustration of a typical epoxy storage and loss modulus profiles at different temperatures.

At low temperatures, the epoxy is hard or glassy and has a high storage modulus. At a certain temperature range the epoxy changes to a rubbery or pliable state. At this temperature range the storage modulus rapidly reduces [97]. Beyond this temperature range the epoxy is now gel-like and more compliant. The rapid decrease in the storage modulus is followed by a rapid rise in the loss modulus which makes the epoxy become more viscous and highly attenuative. The large-scale motions of the polymer chains at this stage causes the epoxy volume to increase

exponentially. The glass transition temperature of Robnor epoxy is given as 120°C to 145°C [98] with some reported to be as low as 90°C [99].

McHugh et al. [100] have reported a decrease in the speed of sound of a 2MHz ultrasound pulsed wave propagating in a 6mm and 3mm thick L385:340 epoxy samples in the temperature range 20°C to 200°C. The temperature dependence of sound velocity showed a similar trend to the temperature dependence of storage modulus illustrated in Figure 7-12. The sound velocity in a 3mm epoxy sample reduced from 2650 m/s at 20°C to 1200 m/s at 200°C. Their results also showed an increase in attenuation. The sound attenuation showed an exponential increase from 0.9 dB/mm at 20°C up to maximum at 4 dB/mm 120°C.

Therefore, the difficulties that were experienced in the identification of epoxy resonances beyond 80°C could be attributed to increased ultrasound attenuation. Only the results in the temperature range between 24°C to 70°C will be considered. It was assumed that the epoxy coating at these temperatures was in a glassy state.

The separation between the resonant frequencies was noted to decrease with increasing temperature. The epoxy fundamental frequency, f_0 was calculated by taking half the difference between the adjacent resonant dips and then averaging. The results are shown in Figure 7-13.

Using Equation 3-52 where the speed of sound c at the different temperatures was calculated using Equation 7-3, the epoxy thickness was calculated and plotted in Figure 7-13.

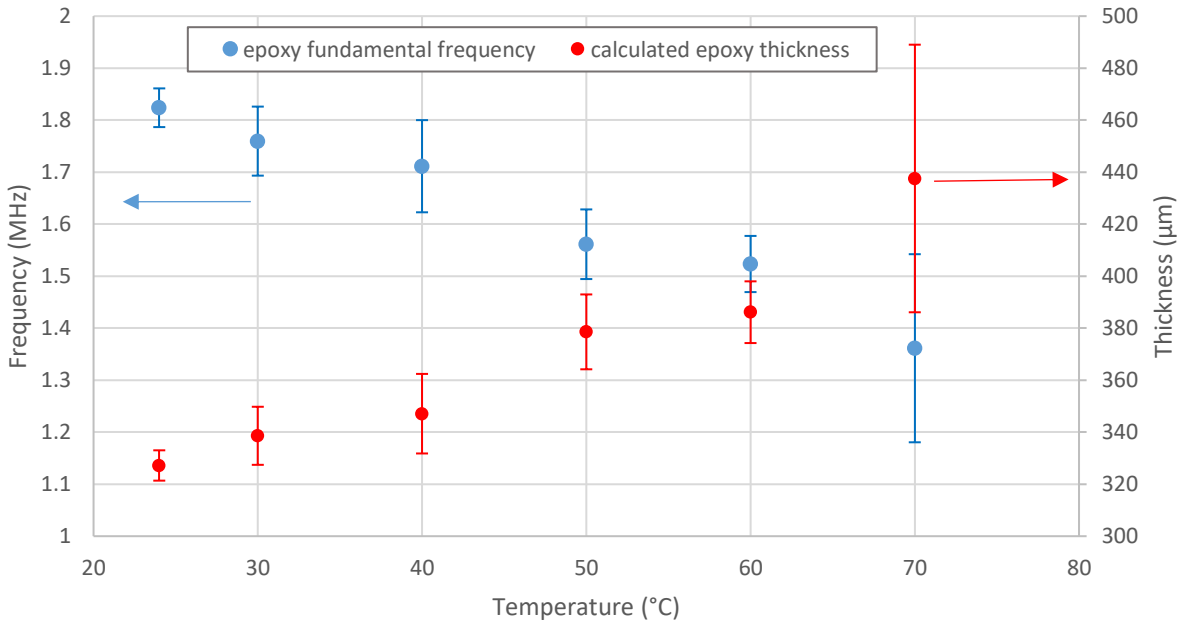

Figure 7-13. Epoxy fundamental frequency and calculated thickness at different temperatures.

The vertical error bars represent the standard deviation in the fundamental frequency and calculated epoxy thickness, respectively. It was observed that the fundamental frequency decreased from 1.82MHz at 24°C to 1.36MHz at 70°C. Consequently, the calculated epoxy thickness increased from 327.19 µm at 24°C to 437.56 µm at 70°C, a 33.7% increase.

An epoxy linear temperature expansion coefficient, α is provided as 30–40ppm/°C [98]. The linear thermal expansion of a 327.19µm epoxy layer for a 24-70°C temperature range was calculated using Equation 7-1 using an upper limit α=40ppm/°C and the results are shown in Figure 7-14.

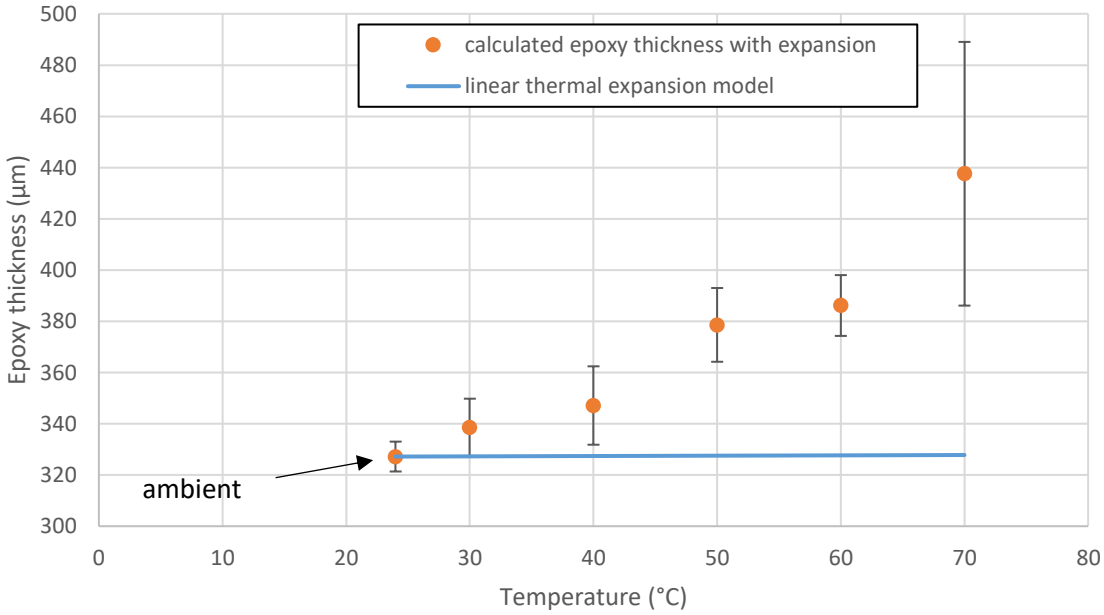

Figure 7-14. The epoxy thickness calculation from the experimental data and a linear thermal expansion model.

The model results showed an increase of 0.6µm from 327.19µm at 24°C to 327.79µm at 70°C. This increase was insignificant due to the small thickness of the epoxy coating. A good correlation was observed in the temperature range 24°C to 40°C. The difference between the averaged epoxy thickness from the experimental data and the model results increased with temperature. A comparison between the experimental data and the model did not show a good correlation above 40°C. The results at 50°C, 60°C, and 70°C showed a 15.59%, 17.85%, 33.49% increase respectively between the model and experimental data.

7.4 Discussion

A standing wave method been used to measure the expansion of a steel substrate in the temperature range 24°C to 120°C for a solid-air boundary. The maximum peaks from the frequency responses that corresponded to the component resonant frequencies were observed to have shifted to the left with increasing temperature. The magnitude of these peaks also showed a general increase in magnitude.

The steel fundamental resonant frequency was calculated by averaging the difference between adjacent maximum peaks from the frequency response and it was observed to have reduced from 0.322MHz at 24°C to 0.319MHz at 120°C. The increase in the resonant peaks with temperature was caused by reduction in attenuation at higher temperatures.

The experimental speed of sound in the steel component was calculated by considering a linear thermal expansion model and then comparing with a model that considered the temperature dependence of speed of sound in steel. The results from a linear least squares regression line of

best fit showed that the temperature dependence coefficient indicated that the substrate could potentially be stainless steel. The component thickness measured was in a direction perpendicular to the sensor location, but in reality, the steel component expands in all directions. This could also have been a cause for the differences that were observed.

The expansion of the piezoelectric sensors was assumed to be negligible and the bond between the piezoelectric material and the steel substrate was assumed to be perfect and constant at different temperatures.

An epoxy layer was cured on the steel substrate and measured as 327.49μm using standalone profilometer. The frequency responses for solid-epoxy boundaries were recorded and *S* plots showed the epoxy resonant frequencies. Difficulties arose in the identification of epoxy resonant frequencies with increasing temperature particularly beyond 80°C. These difficulties were caused by the epoxy transitioning from a glassy state to a rubbery state. Robnor epoxy has a glass transition temperature of as low as 90°C. The storage modulus at this temperature reduced rapidly whereas the loss modulus increase. The attenuation coefficient for epoxy also increases at this temperature. Therefore only the measurements in the temperature range 24°C to 70°C were considered in calculating the epoxy thickness using a standing wave method. It was observed that the epoxy fundamental frequency decreased from 1.82MHz at 24°C to 1.36MHz at 70°C. Consequently, the calculated epoxy thickness increased from 327.19 μm at 24°C to 437.56 μm at 70°C. The epoxy thickness measured at ambient temperature using a profilometer and standing wave method showed excellent agreement with only a 0.1% decrease change between them. The speed of sound in the epoxy was calculated from a polyimide temperature dependence model because the epoxy and polyimide materials had similar properties. Although a more accurate method of establishing the temperature dependence of speed of sound in Robnor would be to perform measurements experimentally.

A comparison between the epoxy experimental data and a linear thermal expansion model showed an increasing difference with temperature. The model showed an epoxy increase of 0.6μm from 24°C to 70°C. A good correlation was observed for temperatures below 40°C. However, beyond 40°C the difference between the results increased. It is thought that as the steel substrate expands, so does the epoxy coating. The bond between the substrate and the epoxy was assumed to be perfect and that epoxy expanded vertically. But in reality, this is not the case because epoxy expands in all directions, and this could have especially compromised the solid-epoxy contact.

It is suggested that a study into the acoustoelastic effect should be carried out in the future in order to better understand the thermal effects on the measurement of surface coatings that have different glass transition temperatures using a standing wave method.

The standing wave method could also be improved by reducing the temperature steps during a calibration process and increasing the wait times to ensure temperature stability. A calibration process could also be implemented where the substrate is heated first then measurements are recorded as the temperature is cooled. This could also be applied for the solid-epoxy boundary condition.

7.5 Conclusions

The thickness measurement of a solid coating on a metal substrate at different temperatures using a standing wave method has shown some promising results. The epoxy resonant frequencies identifiable from a reflection coefficient spectrum *S* have been shown to reduce with increasing temperature indicating an increase in the epoxy thickness. However, difficulties were encountered in identifying these resonant frequencies with increasing temperature and this was caused by the epoxy entering a glass transition temperature range. Therefore, a standing wave method can potentially be used to monitor the onset of a glass transition temperature regime on top of measuring the coating thickness. A calibration of the instrumented substrate needs to be performed first in order to have a reference point.

Although this study greatly simplified the thermal expansion of both the solid and the epoxy, the results however show that it is possible to measure a surface coating at temperatures above ambient, but up to a certain degree as dictated by the properties of the coating. It is suggested that future work could be carried out that optimises this method by incorporating a comprehensive expansion model and acoustoelastic effects. This endeavour could potentially benefit applications where thin coatings are subjected to varying temperatures such as the aviation industry.

8 Polyimide Thickness Measurement

The aim of this chapter was to investigate the lowest measurable polyimide thickness using a standing wave method. To do this, a 500μm thick polyimide layer on a steel substrate was ground off and a standing wave method was used to measure the polyimide thickness at different thicknesses. The results were compared with conventional pulsed ultrasound methods and the limitations of the standing wave method are discussed.

8.1 Coating Material Selection

Various research work has shown that organic coatings are capable of protecting reactive metals (aluminium and steel) from damage due to corrosion, wear and in some cases even noise reduction. Monitoring and quantifying these coatings is crucial in the evaluation of the risk of failure and maintenance to acceptable risk levels.

Polyimides are used in place of organic coatings in applications that require the surface coating to have good thermal, mechanical and electrical properties and are capable of withstanding chemical reactions to some extent [101], [102]. A classic example of a polyimide is Kapton, developed by DuPont in the 1960s, which is made from the condensation of pyromellitic dianhydride (PMDA) and 4,4'-oxydiphenylamine. It has excellent thermal stability and has operating temperatures as low as -269°C and as high as 400°C. It is flexible and comes in a variety of thin sheets, has low creep and high wear resistance. Thin Kapton films in the range 8μm to 125μm are amber in colour and transparent. Any thicker than this the films are black and opaque in appearance.

For this study, a 500μm thick Kapton sheet was bonded on a 30mm thick metal substrate, and it was ground off to a range of thicknesses. The grinding process used in this research work was an over-simplification of the mechanisms that lead to actual thickness reduction of a corrosion-protection layer on real metal substrates in industry, nevertheless it demonstrates the practicality in engineering applications where thickness measurement of a coating from a back face is preferable, an example being the thickness measurement of a protective coating inside pipelines.

The ability of a polyimide layer material to be ground off while bonded on a steel substrate to produce a planar layer was first investigated. Four test materials were bonded on to a 15cm×7cm×10mm steel substrate namely:

I. 500μm thick Polyimide Film (Kapton)
II. Robnor Epoxy Resin
III. 230μm thick Polyimide Film (Kapton)
IV. Aerospace-grade epoxy resin

The polyimide films were bonded on to the steel substrate using M-bond 610 strain gauge adhesive. Pressure was applied on the polyimide films using G-clamps to ensure a robust contact between the film and the steel substrate, and then cured in an oven at 167.5°C for two hours. The resins were applied and also cured in the oven.

The test block was mounted on a surface grinder and the material was taken off by means of a fine grinding wheel. This would represent the actual testing grinding conditions where the polyimide thickness would be reduced by grinding. A photograph of the testing materials after grinding process is shown in Figure 8-1.

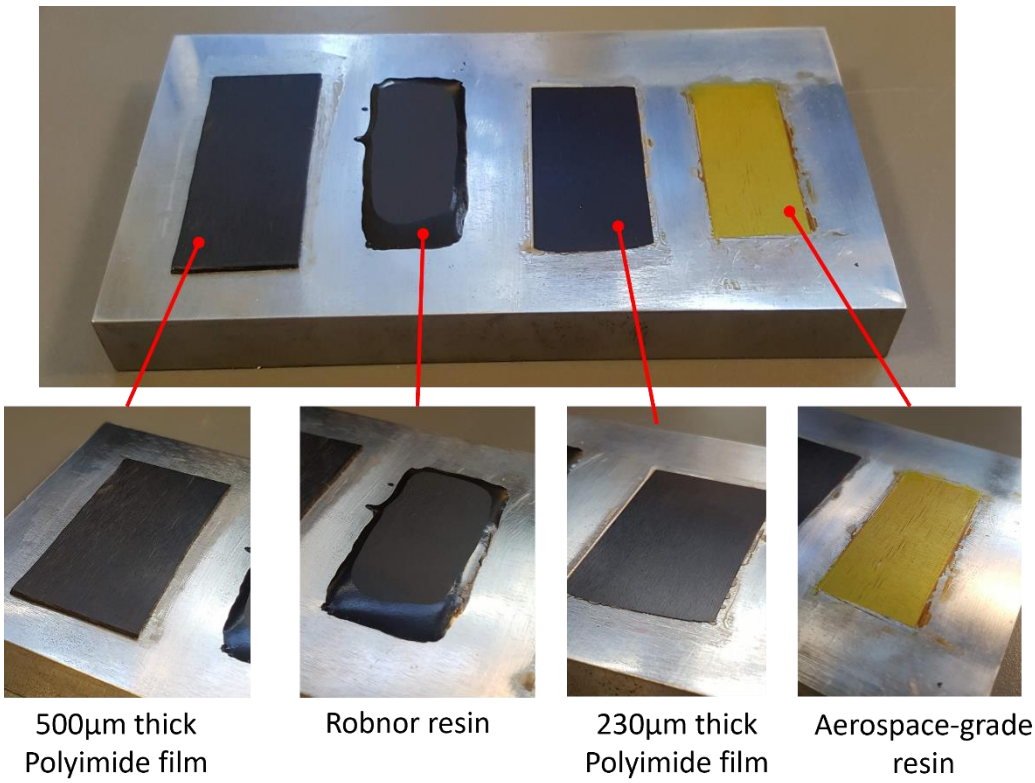

Figure 8-1. A photograph showing the different surface coating materials after grinding.

It was visually observed that the polyimide materials and the resins could be ground off while bonded on the steel substrate to produce visually smooth surfaces. This step was crucial for validation purposes. A 500µm polyimide sheet was chosen for the rest of this study over the resins in order to minimise the errors that would be associated with a resin such as air packets in the mixture occurring during curing and to ensure a strong bond between the steel substrate and the polyimide by means of clamping. The 500µm film was chosen over the 230µm film to cover a wider thickness range.

8.2 Metal Substrate

EN24 steel was chosen as the metal substrate for this study because of its wide use in the automotive, aircraft and general engineering fields. The testing substrate was machined to have the dimensions shown in Figure 8-2.

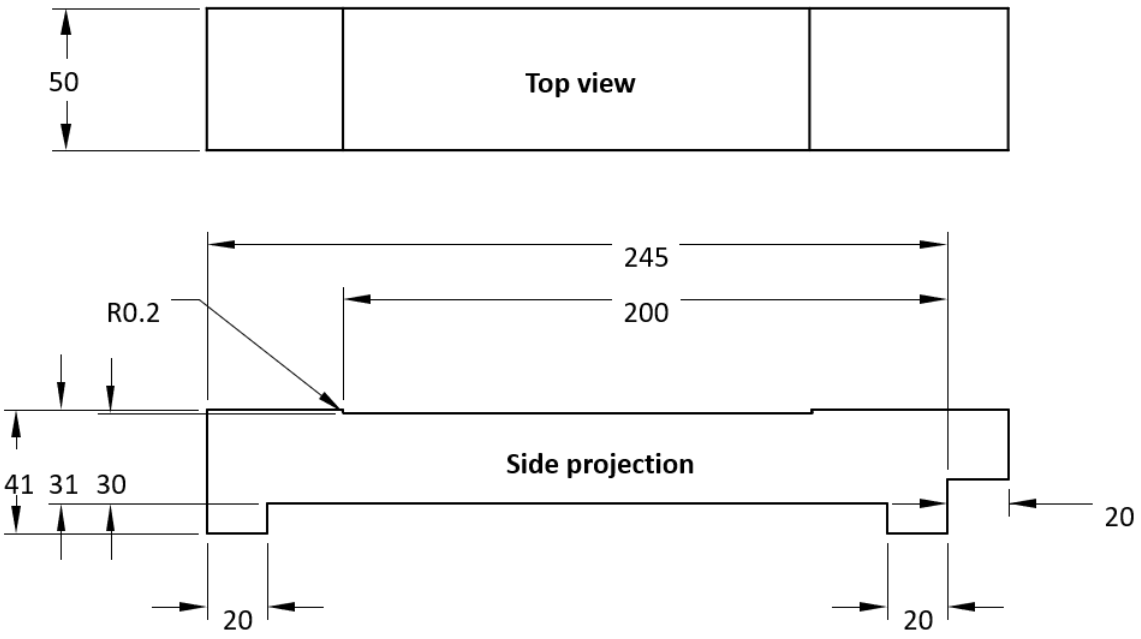

Figure 8-2. A schematic showing the dimensions of EN24 steel substrate (units shown in millimetres)

The machined specimen was elevated 10mm by leg supports. This facilitated the bonding of sensor arrays on the bottom surface. The specimen also had a 1mm deep trough on the top surface that would allow the bonding of a 500μm polyimide sheet. The top surfaces were machined flat such that during the grinding process, the polyimide would be removed evenly with the exposed steel substrate material. The specimen also had a shoulder on one end from where micrometer measurements could be taken to validate the thickness reduction.

8.3 Polyimide and Transducer Bonding

A 500μm thick polyimide sheet was bonded on the topside of the machined steel specimen using M-bond 610 strain gauge adhesive. 2MHz, 3.5MHz, 5MHz, 8MHz and 10MHz nominal frequency sensor pairs were bonded on the bottom side of the specimen perpendicular to the polyimide layer. Figure 8-3 shows photographs of the polyimide and sensor pairs on the machined specimen.

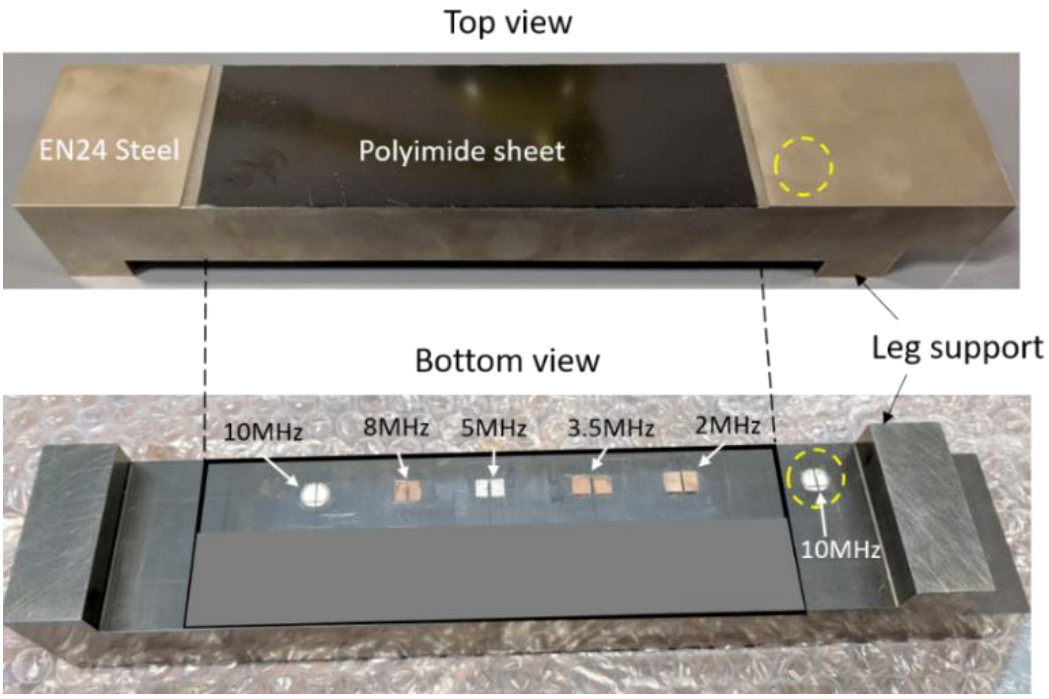

Figure 8-3. Photographs to show (Top) the polyimide layer on the topside of the machined specimen and (Bottom) the sensor pairs array on the bottom side. A pair of outlier sensors is circled in yellow.

The various sensor pairs were bonded to allow for multi-use of the specimen in measuring epoxy thickness resonances of different coating materials. The 30mm thickness also meant that the instrumented component could be used multiple times.

A pair of 10MHz transducers were also bonded as outlier sensors to measure the thickness of the mild steel block as it was taken off using a pulse-echo technique. This would serve as a validation of the polyimide layer thickness reduction.

Coaxial cables were wired to the sensor array using conductive silver epoxy and an epoxy compound was cured over the sensor array to protect the sensors and the wiring connections from damage from the immediate environment. The epoxy backing had good electrical insulating characteristics, excellent chemical and heat resistance, and low shrinkage. The other ends of the coaxial cables were soldered on to BNC connectors which were then connected to the ultrasonic apparatus.

RTD thermocouples were bonded on the outer sides of the specimen as shown in Figure 8-4 using M-bond 200 strain gauge adhesive. These were used to measure and monitor the steel temperature profile of the top surface.

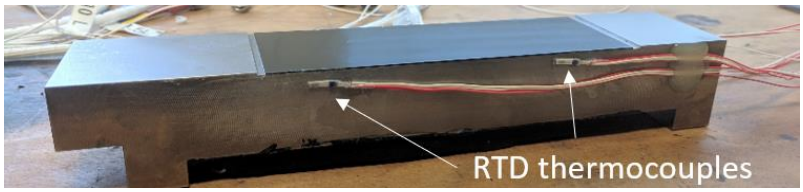

Figure 8-4. A photograph showing RTD thermocouples bonded on outer side of the steel specimen.

8.4 Ultrasonic Apparatus

Due to the number of sensors on the specimen (12 sensors in total) exceeding the capability of a normal 4-channel Picoscope 5442b USB oscilloscope, a 16-channel multiplexer (MUX) was used to allow all the sensors to be connected to the Picoscope without having to manually switch between data acquisition. The MUX would then allow automatic switching, programmable via a dedicated, bespoke LabVIEW software (Triboscope) between sensors so that the correct electrical signals were sent to the correct sensor and the response was received from the desired sensor and sent for digitisation. Figure 8-5 shows a photograph of a benchtop connection between the instrumented steel specimen, MUX, Picoscope and laptop PC.

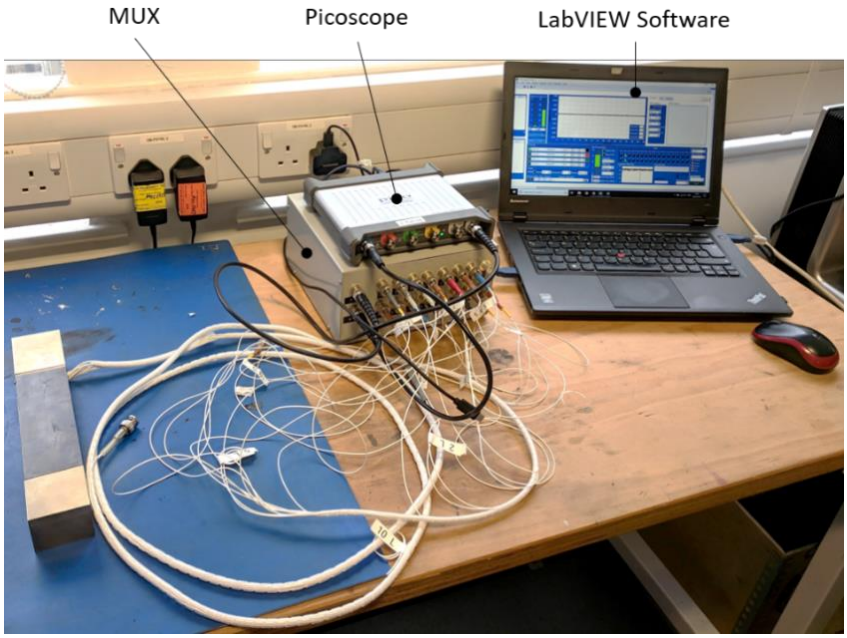

Figure 8-5. A photograph showing connection between the test specimen, MUX, Picoscope and PC.

The Picoscope signal generator output was connected to the MUX signal input via a BNC cable. The MUX signal output was connected to input channel A of the Picoscope. The MUX switchboard allowed for the multiple channels to be routed individually to the appropriate sensor input and output. A photograph of the MUX-Picoscope connection is as shown in Figure 8-6.

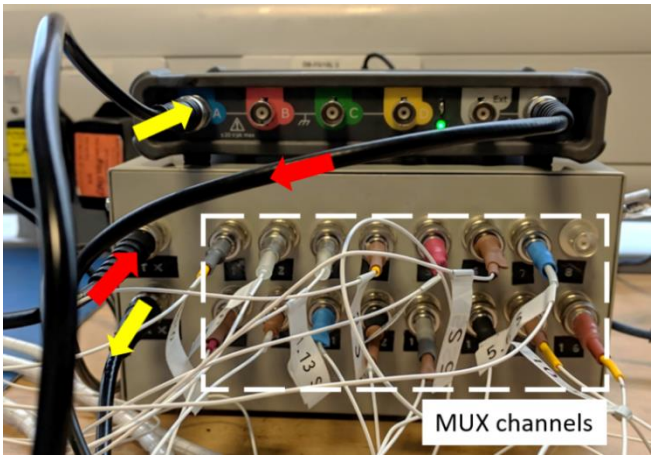

Figure 8-6. A photograph showing connection between MUX, Picoscope and testing specimen cables. [Red and yellow arrows indicate transmitter and receiver connections respectively]

The Triboscope software allowed the sensor pairs to be excited sequentially and for the digitised signal to be stored on the PC for post-processing. The sensor pairs were programmed to excite and capture ultrasound waveforms for sine wave, chirp wave and standing wave settings.

8.5 Experimental Procedure

The polyimide was ground off on an industrial surface grinding machine as shown in Figure 8-7.

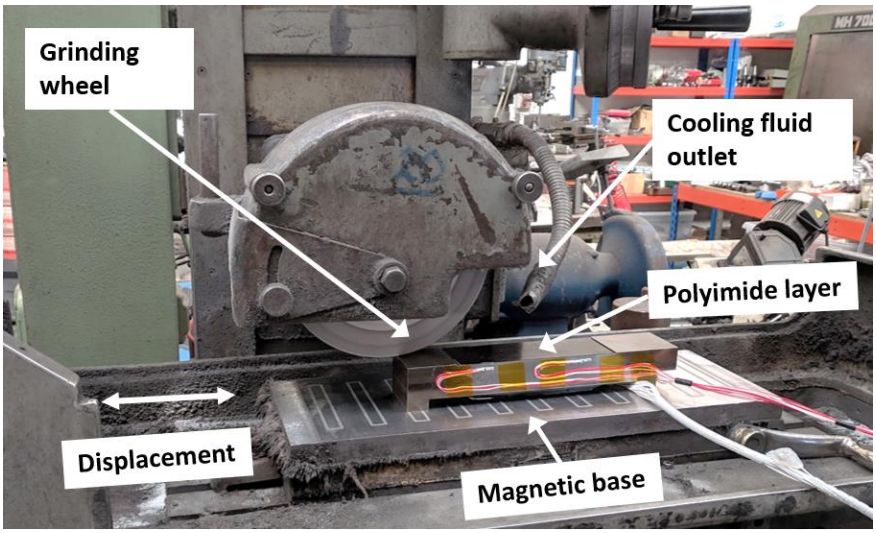

Figure 8-7. A photograph showing the steel specimen on the magnetic base with the grinding wheel in place.

The steel specimen was secured in place by a magnetic base which reciprocated backwards and forwards and a fine grinding wheel rotating at 2500 revolutions per minute (RPM) was used to grind the top surface to the desired level. A cooling fluid was used to reduce friction effects, provide cooling and to increase material removal rate. The experimental procedure was carried out as follows:

i. A reference ultrasound measurement for the sensor pairs was taken before the grinding commenced. This was also to ensure that the ultrasound apparatus and sensors were in working condition.

ii. A reference micrometer steel thickness measurement was taken on the shoulder profile of the specimen. This is illustrated in Figure 8-8.

Figure 8-8. A photograph to show micrometer measurement.

iii. Once the specimen was secured on the magnetic base, the grinding wheel was adjusted to the desired height and the grinding wheel was switched on as well as the cooling fluid.
iv. The grinding machine and cooling fluid were switched off after the grinding process had finished and the top surface of the specimen had been ground off to the desired level.
v. The cooling fluid and debris on the top surface were wiped off and the polyimide surface was cleaned using isopropanol and left to dry.
vi. The magnetic base was switched off and ultrasound measurements were taken.
vii. A micrometer reading was also recorded at this stage.
viii. Once the ultrasound and micrometer measurements were recorded, the magnetic base was switched on and the grinding wheel was adjusted for the next grinding step.
ix. This process was repeated until there was no polyimide left on the top surface and a visually smooth steel surface finish was produced.

8.6 Steel Thickness Measurement

One sensor out of the outlier sensor pair was used to send and receive ultrasound signals in a pulse-echo setting. The pulse settings used are listed in Table 8-1.

Table 8-1. Pulsed wave ultrasound settings

Signal	Ultrasound pulse setting
Sine wave	Frequency: 10MHz Cycles: 5 cycle single capture Voltage: 4V peak-to-peak

The longitudinal wave velocity in the steel specimen was determined by acquiring the difference in the maximum peak arrival times between the subsequent back-face reflections. To do this, 20 A-Scans were acquired before and after each grinding pass. The A-Scans were subtracted from the mean to remove any DC offset by using a MATLAB® detrend function. Next, a mean was applied to the detrended data to give a single A-Scan data. Figure 8-9 shows the detrended A-Scan

for a calibration measurement before any grinding process had taken place. The time difference is represented by *t*.

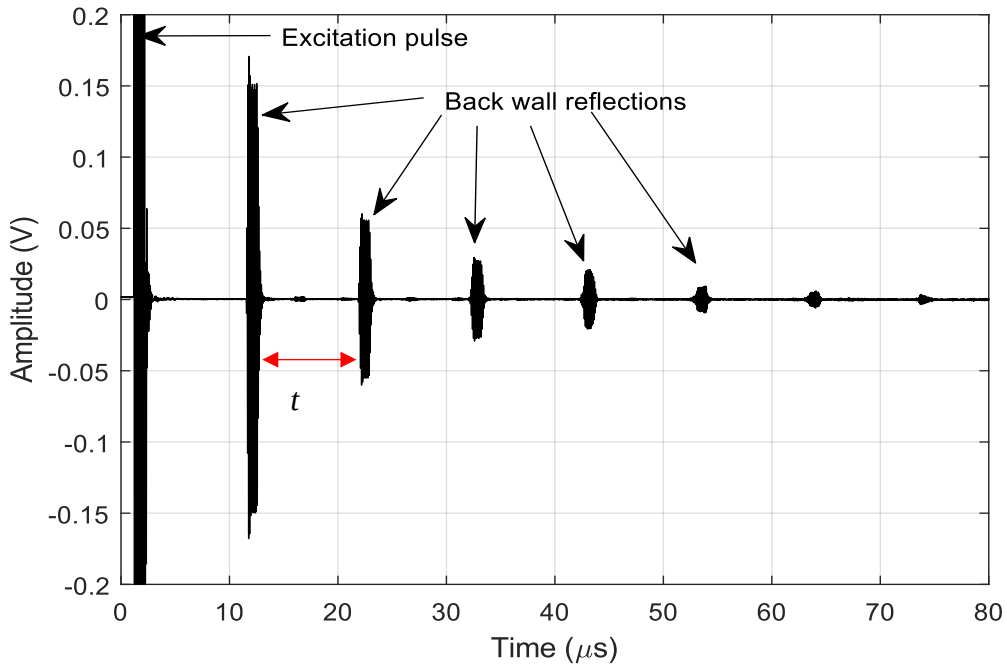

Figure 8-9. Time domain voltage signal for a calibration measurement showing excitation pulse and subsequent back wall reflections used for calculating longitudinal wave velocity in the mild steel block.

The features observed at approximately 1μs to 3μs corresponded to the excitation pulse and were therefore not usable. In order to determine the maximum peak for each back-wall reflection, each back-wall reflection was isolated and an analytical envelope using MATLAB® envelope function was applied to the isolated data to create an analytical signal profile. A MATLAB® find function was used to find the maximum peak and a second order polynomial fit was applied to 15 points on either side of the maximum peak point. This is illustrated in Figure 8-10.

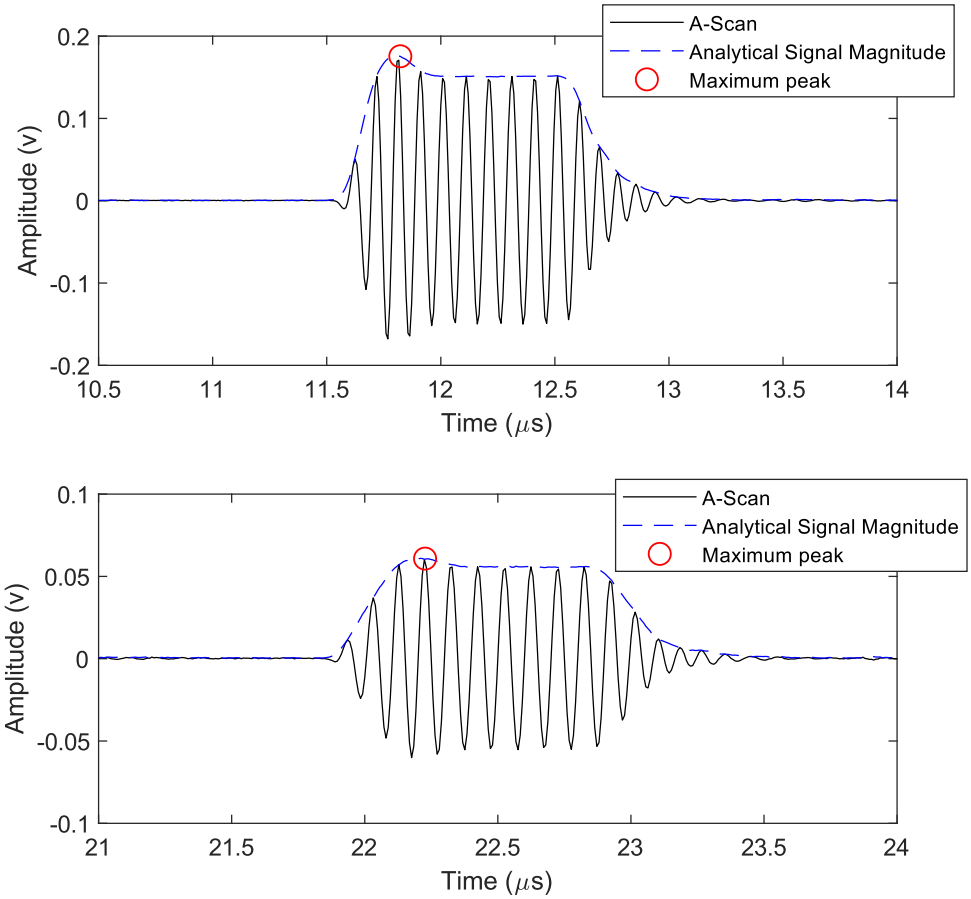

Figure 8-10. Maximum peak detection of the (top) first and (bottom) second back wall reflections.

The exact maximum peak point and corresponding time stamp were calculated by using the coefficients from the differential of the polynomial fit equation. The arrival time difference t was used in Equation 8-1 to calculate the longitudinal wave velocity with L = 31 mm being the calibration specimen thickness.

$$c_l = \frac{2L}{t} \qquad \text{Equation 8-1}$$

For the example shown in Figure 8-10, the maximum peaks were observed at 11.82MHz and 22.23MHz, respectively. This gave a time difference t calculation of 10.41µs. This was repeated for the rest of the back-wall features, with the seventh back-wall reflection being ignored as outlying. The time difference between the echoes was averaged as 10.44µs with a standard deviation of 0.16µs. As a result, a longitudinal wave velocity was calculated as 5939.13 m/s with a mean error of 41.80 m/s.

The maximum peak from the first backwall reflection was then plotted for the steps as shown in Figure 8-11.

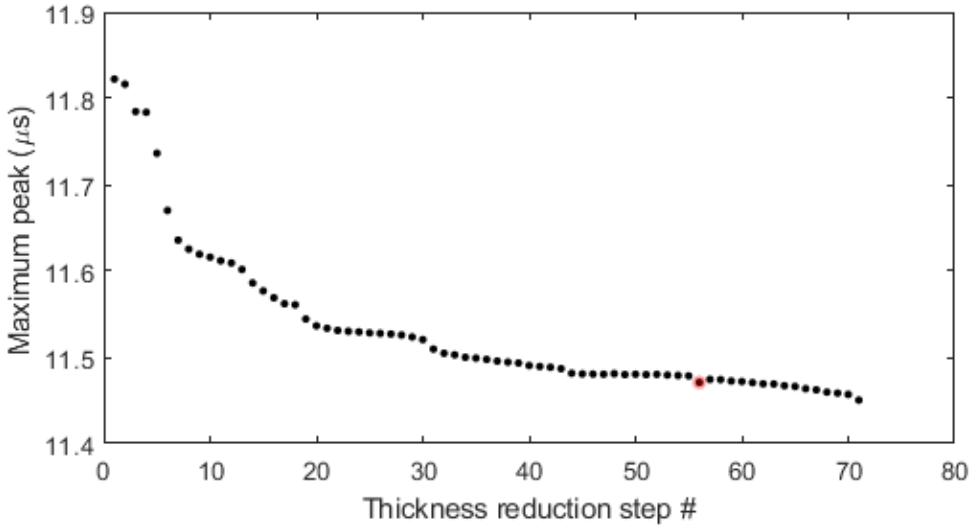

Figure 8-11. The change in the maximum peak of the first back wall reflection.

The anomalous data highlighted in red was caused by the analytical envelope identifying a maximum point that was lesser than expected. Nonetheless, this was omitted from further calculations moving forward. It was observed that the maximum peak reduced by 0.37μs from 11.82μs to 11.45μs after 71 steps.

The change in the maximum peak of the first backwall reflection Δt was calculated after every step. The steel thickness was then calculated using Equation 8-2:

$$L = 31 - \frac{\Delta t \times c_l}{2}\ (mm) \qquad \text{Equation 8-2}$$

where the subscript c_l represents the speed of sound in the steel substrate that was calculated previously. Figure 8-12 shows the thickness reduction step.

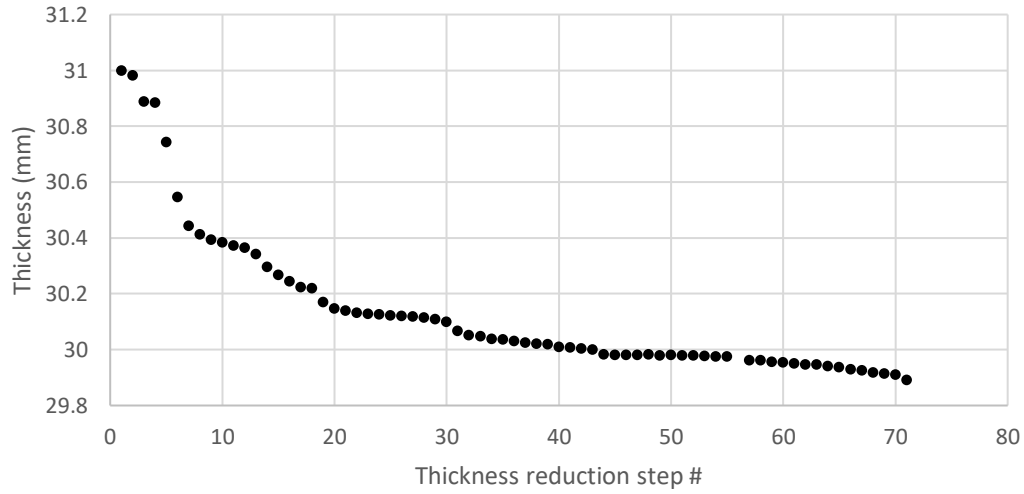

Figure 8-12. A plot to show the steel thickness reduction after every step.

The steel thickness showed a reduction of 1.11mm from 31mm to 29.89mm after 71 steps.

8.7 Micrometer and RTD Thermocouple Measurements

Independent micrometer readings, as demonstrated in Figure 8-8, were also recorded after every thickness reduction step. A 0-25mm external micrometer was used and the results recorded are shown in Figure 8-13.

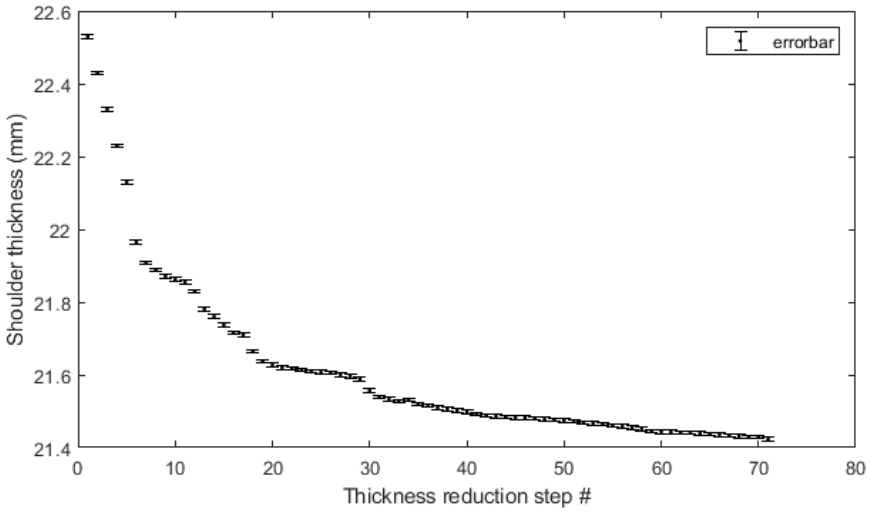

Figure 8-13. Micrometer measurement readings taken on the shoulder side of the specimen.

The vertical error bars represent the micrometer error. The results show a reduction of 1.11mm from 22.53mm to 21.42mm after 71 steps. This showed a strong agreement with the steel thickness calculations presented earlier in Figure 8-12.

Four RTD thermocouples were bonded on the sides of the steel specimen, with two on either side as shown in Figure 8-4. The temperature was recorded after every thickness reduction step and the temperature distribution on the top surface is plotted in Figure 8-14.

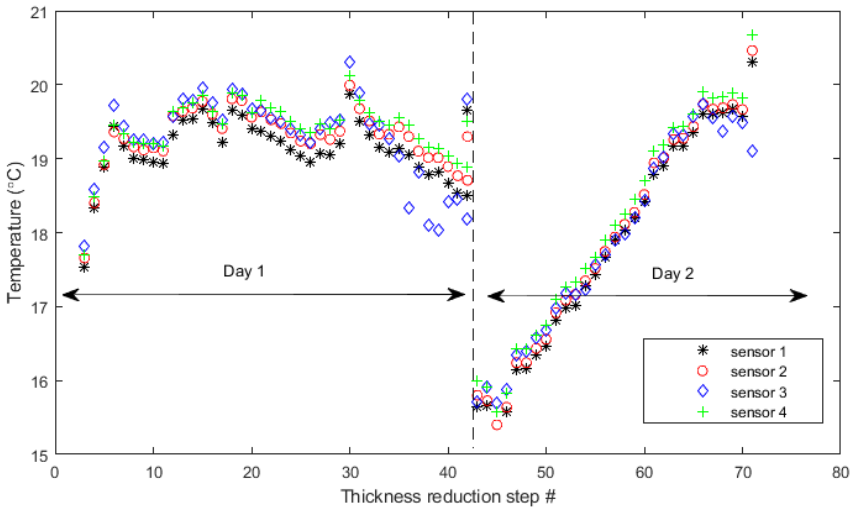

Figure 8-14. RTD temperature measurements.

The experiment was conducted over a period of two days and at different times of the day. On the first day, the experiment was done in the afternoon hours and on the second day the experiment was conducted in the morning hours. This is reflected in the temperature difference that was

observed in the measurements. The overall temperature distribution falls in the range 15.5℃ to 20.5℃.

8.8 Influence of Polyimide Layer on Standing Wave Measurements

For this study, only the results from the 10MHz sensor pair will be analysed and discussed. This is because these sensors could be pulsed over a wider bandwidth. In keeping with the aim of the project, the highest available transducer frequency would measure thinner coating thicknesses therefore the 10MHz sensors were chosen to investigate the lowest measurable coating thickness possible.

The parameters for the standing wave signal generation are outlined in Table 8-2.

Table 8-2. Standing Wave generation parameters.

Signal	Ultrasound pulse setting
Standing wave	Centre Frequency: 10MHz Frequency Span: 19.8MHz Sweep time: 5ms Voltage: 4V peak-to-peak

The standing wave frequency response for a solid-air boundary is as shown in Figure 8-15.

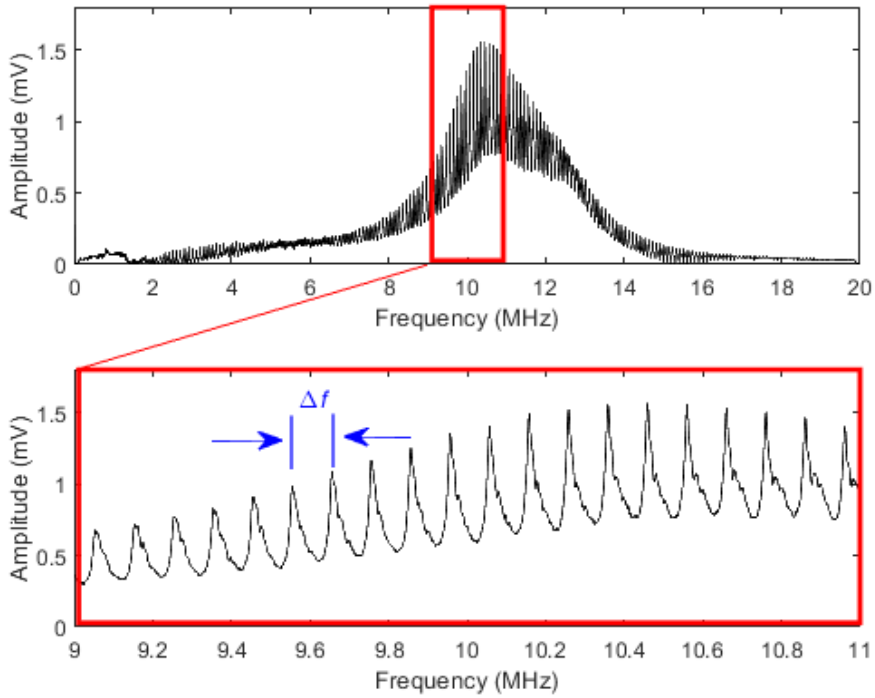

Figure 8-15. (Top) Standing wave frequency response for a solid-air boundary condition (bottom) A magnified profile of the frequency response showing the peak separation *Δf*.

The wave interference within the steel component produced maximum peak amplitudes that were separated by the component resonant frequency in the frequency domain.

In this study, the steel thickness was 30mm. The calculated steel acoustic velocity of 5939.13 m/s was used in Equation 3-56 to calculate the steel fundamental frequency to give 98.99 kHz, where n=1. The experimental steel fundamental frequency was calculated by averaging the difference Δf (illustrated in Figure 8-15) between adjacent peaks to give 100.33 kHz with a standard deviation of 1.62kHz. These results showed a strong correlation, to three significant figures.

The influence of the polyimide layer on the standing wave before grinding is shown in Figure 8-16.

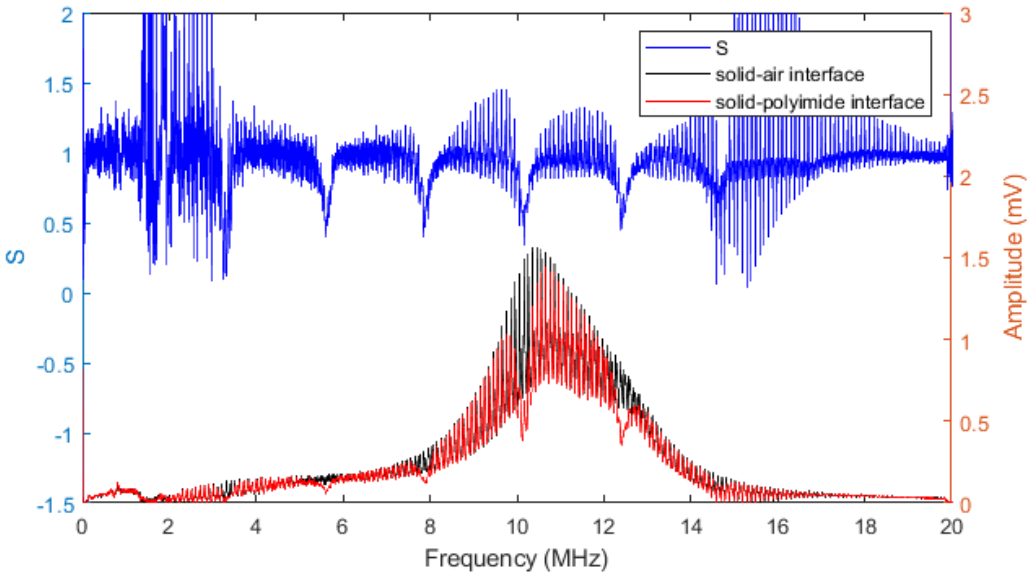

Figure 8-16. The FFTs of the solid-air and solid-polyimide responses and the associated S profile showing the resonant frequencies.

At certain frequencies, the standing wave amplitude reduced. The *S* plot identified these resonant frequencies as minimum points. These were observed at 3.25MHz, 5.59MHz, 7.86MHz, 10.16MHz, 12.40MHz, 14.67MHz and 16.83MHz. These frequencies corresponded to where there was a phase change when compared with a phase difference plot as shown in Figure 8-17.

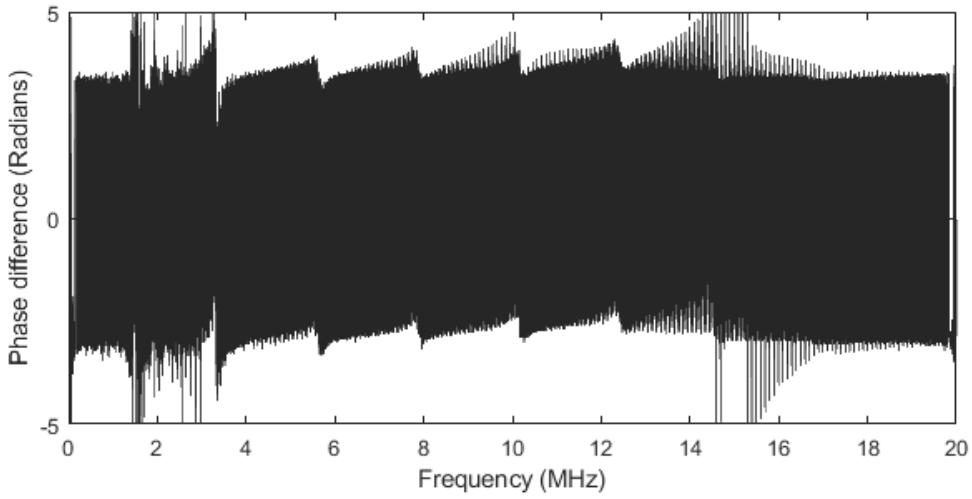

Figure 8-17. The phase difference of the frequency responses in Figure 8-16.

The resonant dips were observed to be oddly spaced. Figure 8-18 shows the resonant dip frequency evolution that was obtained from the experimental data.

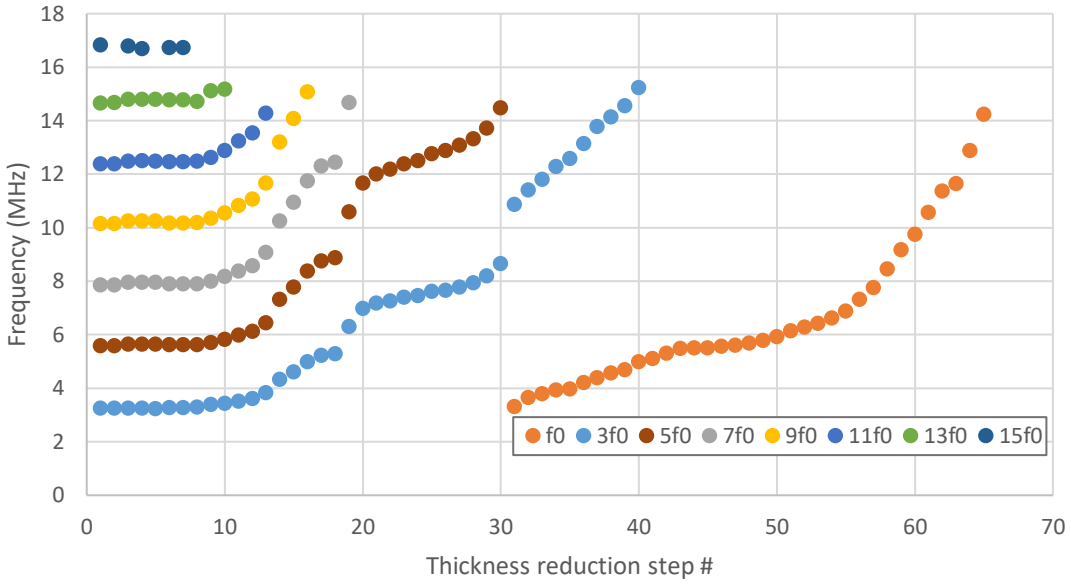

Figure 8-18. Polyimide resonant dip frequency modes evolution from experimental data.

The separation between the resonant frequencies increased as more polyimide was ground off indicating an increase in the polyimide resonant frequency. This meant a reduction in the polyimide layer thickness (Equation 3-52) with the assumption of constant speed of sound in the polyimide layer. The resonant modes distribution for a polyimide layer thickness reduction from 550µm to 0µm was modelled using Equation 3-53 where the polyimide layer acoustic velocity was assumed to be constant at 2420m/s [96]. A change in the speed of sound across a 5°C gradient was considered negligible in this study. The mode distribution from the model (Equation 3-53) is shown in Figure 8-19.

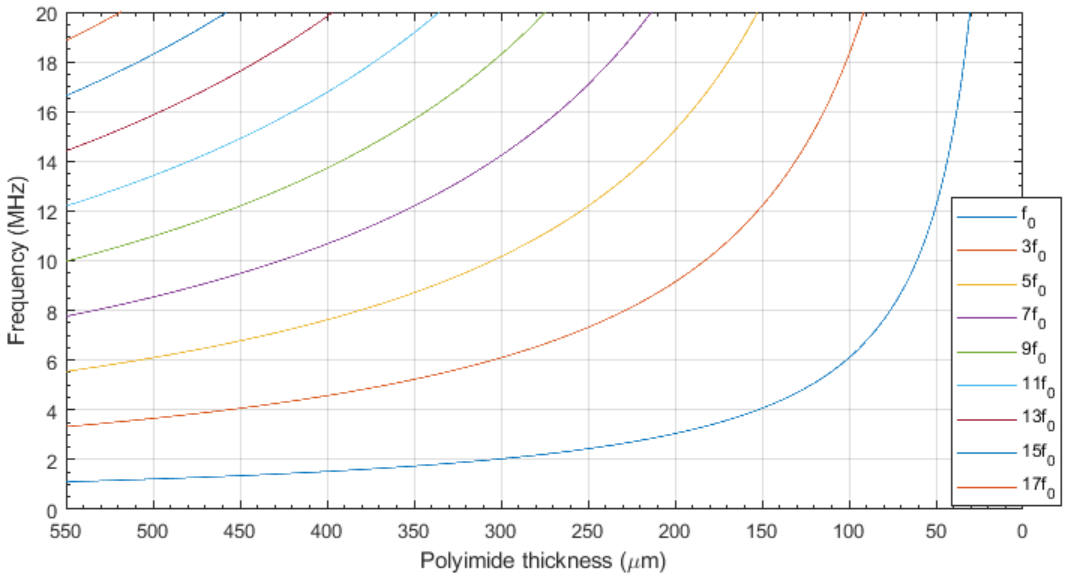

Figure 8-19. Modelled polyimide resonant mode distribution.

There was a good correlation between the modelled and experimental data polyimide resonant modes. Of interest to note is that the lowest possible polyimide thickness that could be measured was identified as 30.4µm at a resonant frequency of 19.9MHz from the model.

The resonant frequency f_0 beyond step 65 was difficult to identify. The frequency difference between adjacent dips from the experimental data was averaged then halved to yield f_0. For single resonant dips identified from steps 41 to 65, the f_0 was acquired at the minimum resonance frequency locations. Using Equation 3-52 the polyimide layer thickness was calculated, and the results are shown in Figure 8-20.

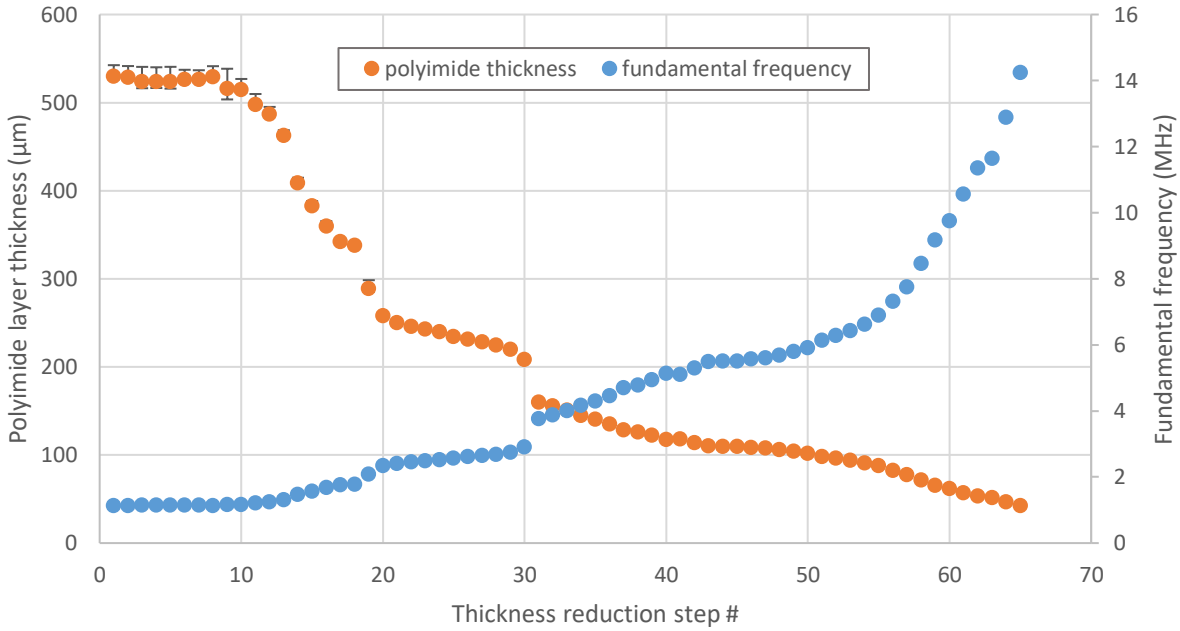

Figure 8-20. Plot showing polyimide layer thickness and fundamental frequency.

The vertical error bars from the fundamental frequency data represent the standard deviation. This was only applicable where the resonant modes identified within the bandwidth were more than two as was the case from the start of the experiment up to thickness reduction step 20. After this, only two resonant modes were observed until step 40 where only one resonant mode was observed after this as observed in Figure 8-18. The standard deviation from the resonant modes data was used to calculate the error bars plotted alongside the polyimide thickness data in Figure 8-20.

The thickness of the polyimide layer reduced from an averaged 529.94µm at the start of the experiment to the lowest measurable thickness of 42.49µm. The lowest measurable thickness was limited by the upper frequency limit of 14.24MHz.

The polyimide thickness measured using a standing wave method showed a strong correlation with the steel thickness measurements using the outlier sensor. The results are shown in Figure 8-21.

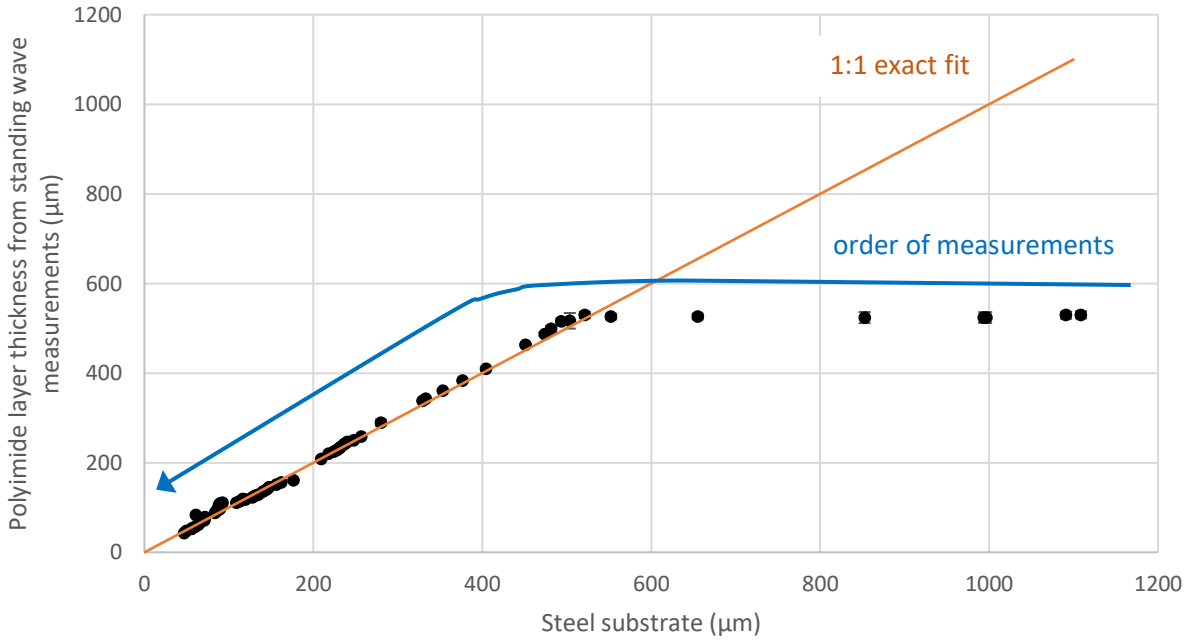

Figure 8-21. A comparison between polyimide layer and steel substrate thickness measurements.

The vertical error bars represent the standard deviation in the polyimide thickness measurements. This was discussed previously. The results showed a strong agreement with a 1:1 exact fit line for thicknesses below 550µm. The lowest thickness indicated the lowest measurable polyimide thickness using the standing wave method. Thickness measurement above 550µm indicated that the steel substrate step profile was greater than the polyimide layer thickness.

The polyimide layer started to be ground off after seven steps due to the step change difference between the shoulder of the trough and the polyimide as illustrated in Figure 8-22.

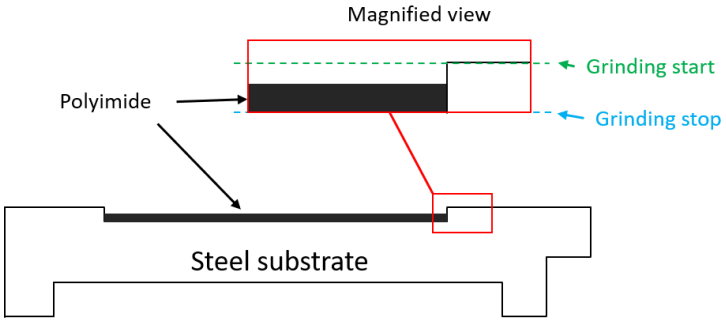

Figure 8-22. A magnified illustration of the step change between the polyimide layer and the shoulder of the trough.

At the start, the top surface of the step profile was higher than the top surface of the polyimide layer. After sufficient steel material had been taken off the top, the polyimide material was then taken off together with the steel material as the thickness was reduced.

The polyimide thickness measured using the standing wave was compared with steel thickness measurements performed using a micrometer screw gauge. The results are shown in Figure 8-23.

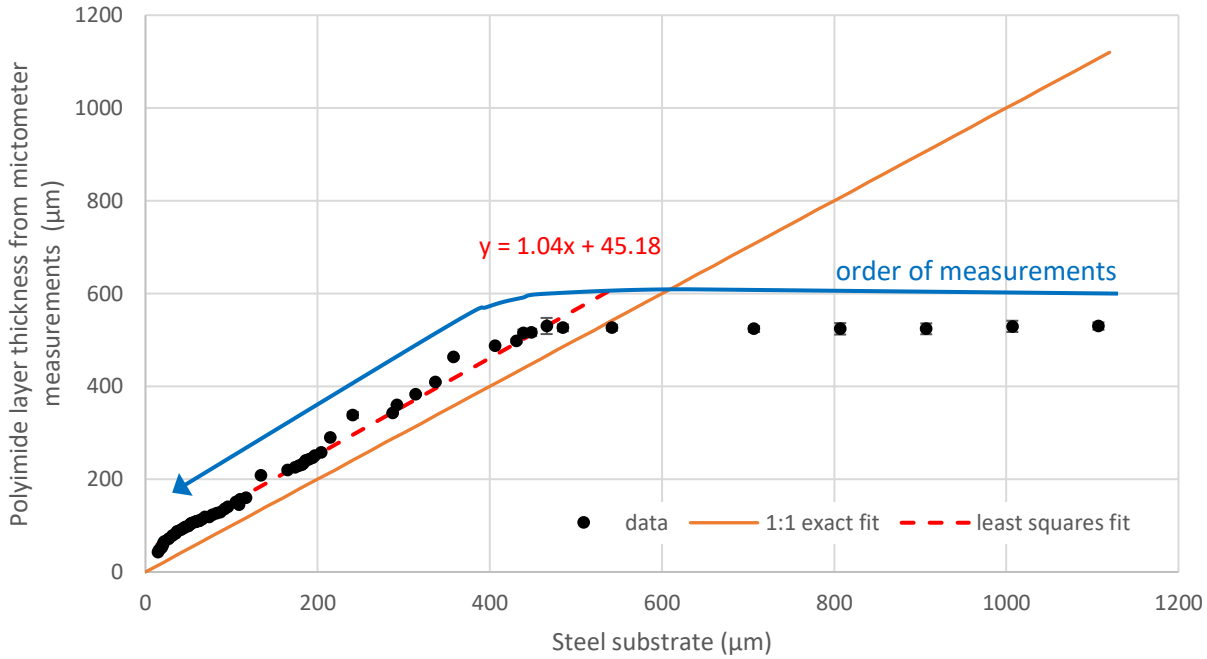

Figure 8-23. A comparison between polyimide layer and steel substrate thickness measurements by micrometer.

The vertical error bars represent the standard deviation in the polyimide thickness measurements. A linear least squares regression line of best fit equation for the data below 550µm showed an error of 45.18µm and a 4% error when compared to a 1:1 exact fit line. Micrometer measurements were prone to human error when reading from the instrument scale. It is possible the force that was applied on the ratchet was either too much or not sufficient such that false readings were recorded. Another cause of uncertainty occurred when removing the micrometer from where it was attached at the shoulder profile of the component in order to read from the measurement scale. The spindle and the anvil could have been compromised in the process resulting in some false readings. The micrometer could also have had zero error.

Possible errors from the steel thickness measurements from the outlier sensor were thought to have originated from the speed of sound in the steel substrate not being constant due to temperature fluctuations (15.5°C to 20.5°C as previously mentioned) and the accurate extraction of the maximum peak times from the reflected echoes. Because the speed of sound that was used in calculating the steel thickness reduction was acquired at the start of the experiment, the measurement errors that followed were reported to have a mean error in the speed of sound as of 41.80 m/s as previously identified. The temperature effects were neglected.

8.9 Influence of Polyimide Layer on Pulse-Echo Measurements

The parameters for generation of pulsed wave bursts for pulse-echo setting used are listed in Table 8-3.

Table 8-3. Pulse setting parameters for pulse-echo ultrasound technique.

Signal	Ultrasound pulse setting
Sine wave	10MHz, 5 cycles, 4V peak-to-peak
Chirp wave	7MHz - 13MHz, 5 cycles, 4V peak-to-peak

The signal processing for both sine wave and chirp followed the same algorithm. 20 A-Scans were acquired before and after each grinding pass. The A-Scans were subtracted from the mean to remove any DC offset and a mean was applied to the detrended data to give a single A-Scan for each grinding steps. For a sine wave setting, an excitation pulse was observed at approximately 1µs to 3µs (Figure 8-24).

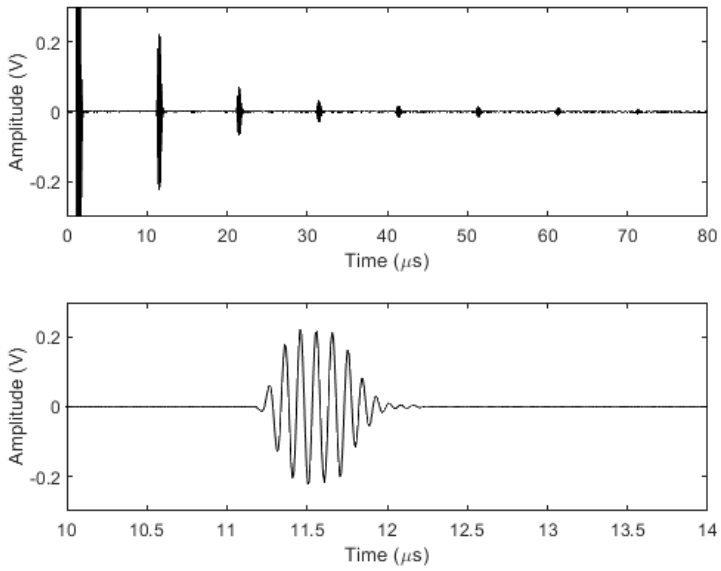

Figure 8-24. (Top) Averaged A-Scan data for a 10MHz 5-cycles sine wave for a solid-air boundary (bottom) the first echo of interest.

The first echo in the time interval 10-14µs was isolated as shown in Figure 8-24. The amplitude of the echo was normalized with the maximum peak. This was done for all the steps and the normalized data was stacked to produce a surface plot as shown in Figure 8-25 and Figure 8-26.

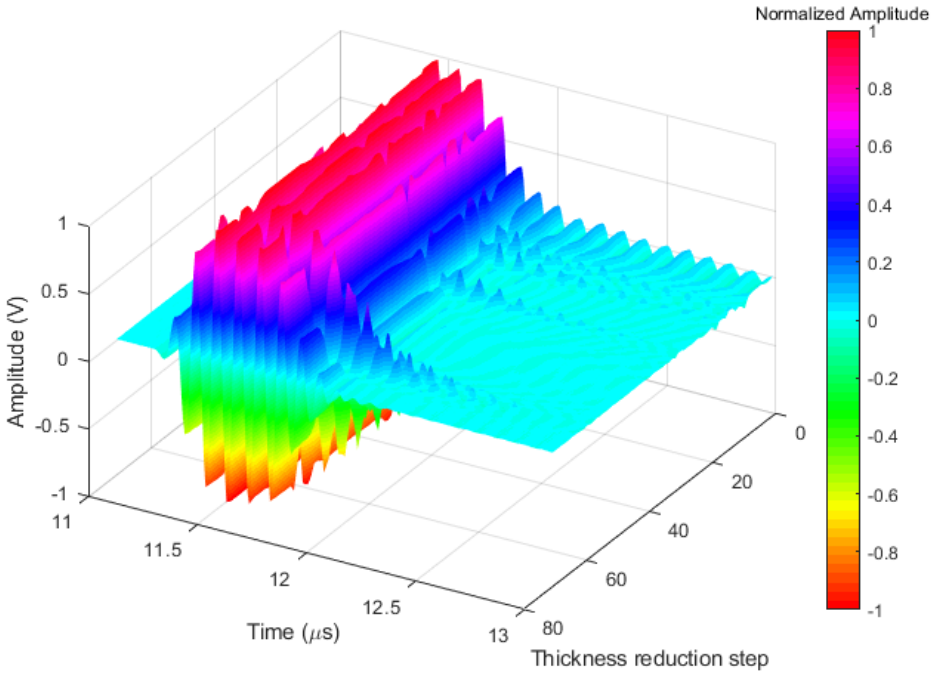

Figure 8-25. Surface plot of the normalized sine wave data.

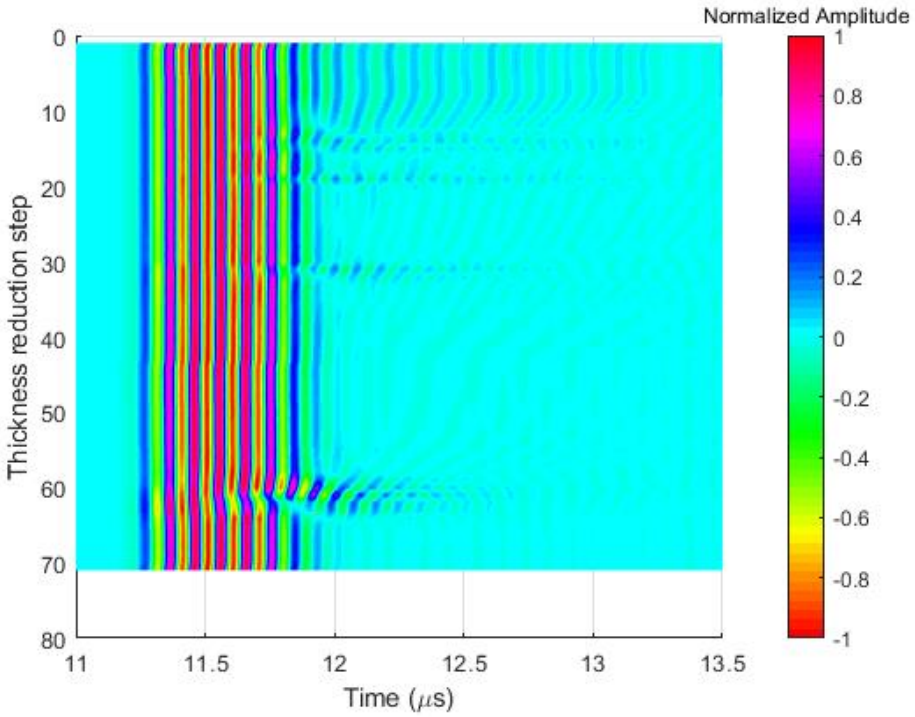

Figure 8-26. Top view of the surface plot in Figure 8-25

The wavelength of a 5 cycles 10MHz pulse in the polyimide was greater than the thickness of the polyimide layer therefore the echoes from the polyimide-air boundary overlapped with those from the steel-polyimide boundary. However, it was observed that at certain thickness steps, the wave was transmitted into the polyimide layer and this was evidenced by the long tail features observed at steps 1-20, ~30 and ~58-63.

The quarter wavelength theory suggests that sound will be transmitted into the polyimide layer and destructively interfere with the incident wave when the polyimide thickness is an odd multiple of a quarter wavelength of the ultrasound pulse. For a 10MHz ultrasound pulse incident on a polyimide layer, the thicknesses that would cause resonance are given by:

$$L = \frac{(2n-1) \times c}{4 \times 10MHz} \qquad \text{Equation 8-3}$$

where *n* is any integer, *c* is the speed of sound in the polyimide layer. When the steps where the tail features appeared were compared with the polyimide thickness calculated using the standing wave method, the resonant thicknesses for a 10MHz wavelength showed a strong correlation with these steps. This is illustrated in Figure 8-27.

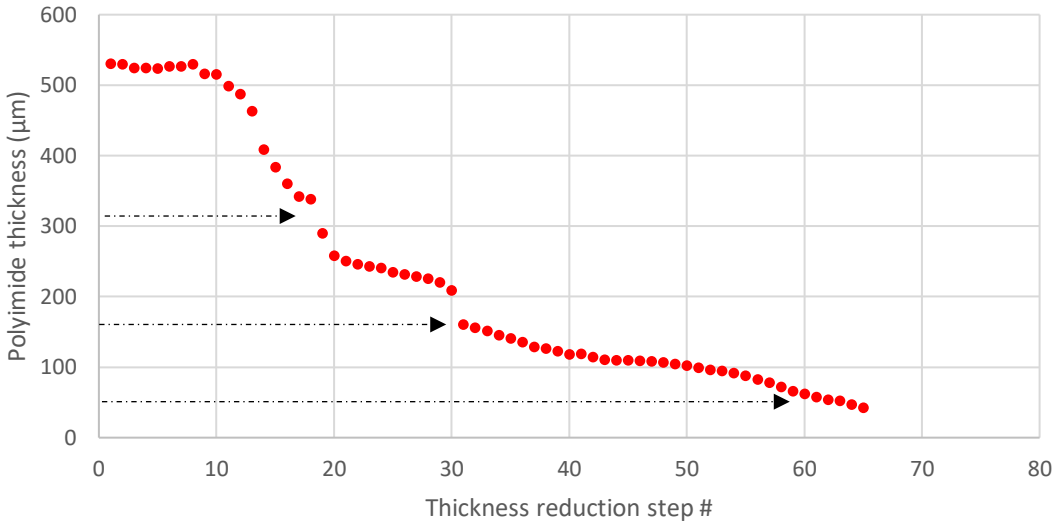

Figure 8-27. The polyimide layer thicknesses that correspond to a quarter wavelength of a 10MHz wave (shown by arrow).

The thicknesses at 60.5µm, 181.5µm and 302.5µm identified from Figure 8-27 correspond to the steps where the tail features were observed.

A resonance method is usually applied to extract the resonant frequency from a pulse-echo method. But because we know that sound has been transmitted at certain steps as evidenced by the long tail features, we expect that these would correspond to the thicknesses calculated earlier using Equation 8-3. A frequency domain analysis was necessary in order to extract the polyimide resonant frequencies.

The first echo was isolated, zero padded and windowed using a Hanning window function. A Fast Fourier transform (FFT) was then applied to give a frequency spectrum. A FFT of the isolated echo in Figure 8-24 is shown in Figure 8-28.

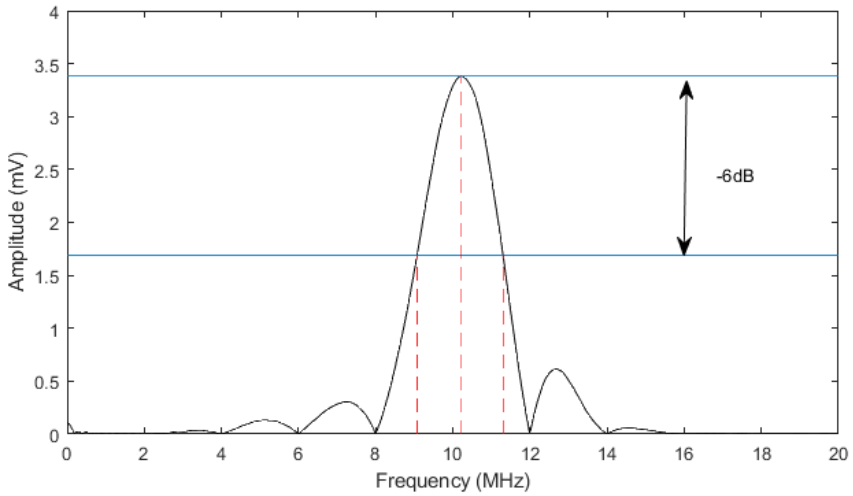

Figure 8-28. Frequency response of a 5-cycles 10MHz Sine pulsed wave.

Side lobes were observed as a result of spectral leakage. A maximum peak was observed at 10.23MHz and a narrow bandwidth of 9.073MHz-11.3MHz at -6dB.

The reflection coefficient, *R* was calculated as the ratio of the solid-polyimide FFT amplitude to the solid-air FFT amplitude (Equation 8-4).

$$R = \frac{A_{solid-polyimide}}{A_{solid-air}} \qquad \text{Equation 8-4}$$

Using the quarter wavelength theory, the polyimide resonant frequencies were identified as minimum points from *R* when plotted against frequency. Considering grinding steps 28 to 34, the *R* spectra plotted in Figure 8-29 showed that where the resonant dip occurred within the bandwidth at -6dB, the tail features would be observed in the time domain surface plots from earlier (Figure 8-26).

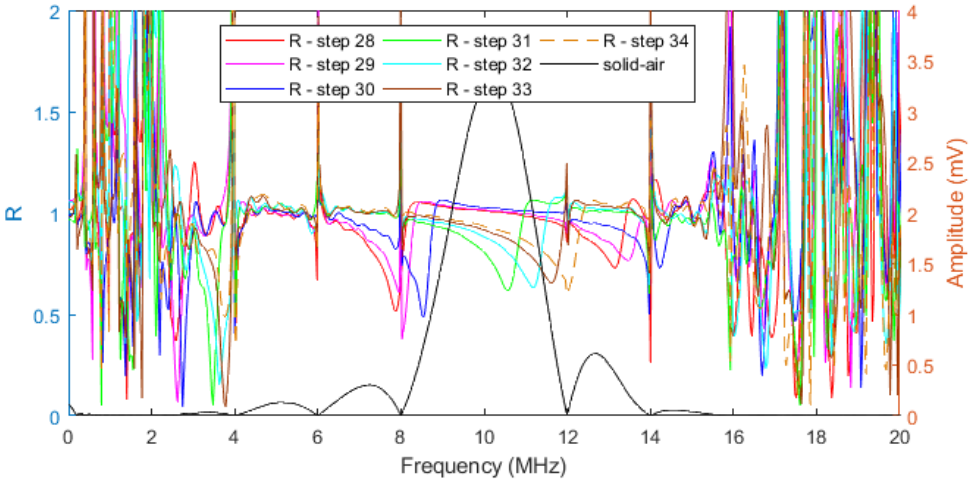

Figure 8-29. *R* spectra for steps 28-34 for sine wave.

In this case it was step 31 and step 32.

The *R* plot for a 500µm polyimide layer is shown in Figure 8-30.

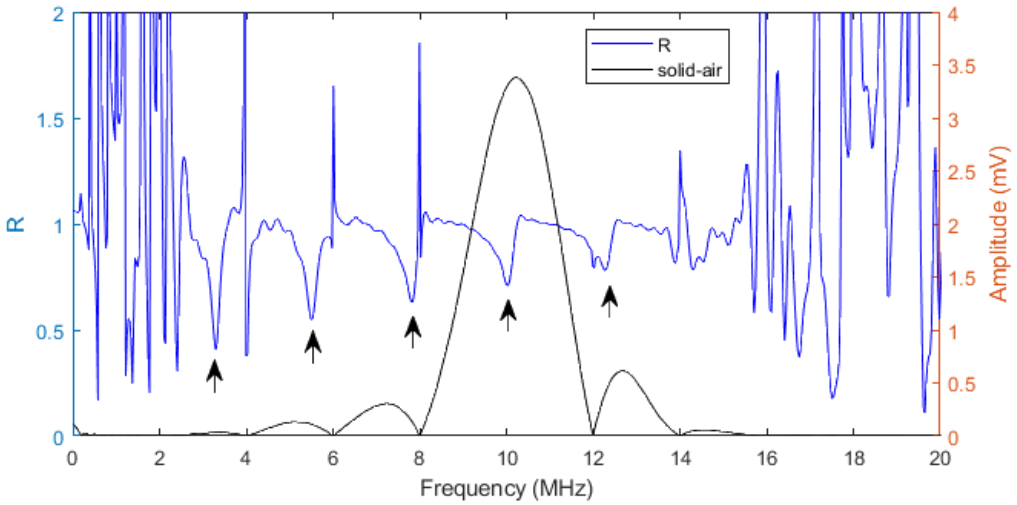

Figure 8-30. *R* plot for a 500µm polyimide layer showing resonant dips (identified by the arrows) for sine wave data.

The identified resonant dips shown by the arrows occurred at 3.296MHz, 5.523MHz, 7.811MHz, 10.04MHz, 12.27MHz and 14.31MHz. It was observed that the magnitude of the resonant dip decreased with increasing frequency. Because of multiple dips, the differences between adjacent resonant modes were averaged then halved to yield f_0. In this case f_0 = 1.10MHz with a standard deviation of 0.04MHz. Considering the narrow bandwidth, only the 10.04MHz resonant mode lay within the -6dB bandwidth. The bandwidth limits would therefore affect the thickness measurement capability by limiting the resonant frequency acquisition window.

A similar trend was observed in the chirp wave pulsed responses. A FFT of the first echo from the time domain is plotted in Figure 8-31.

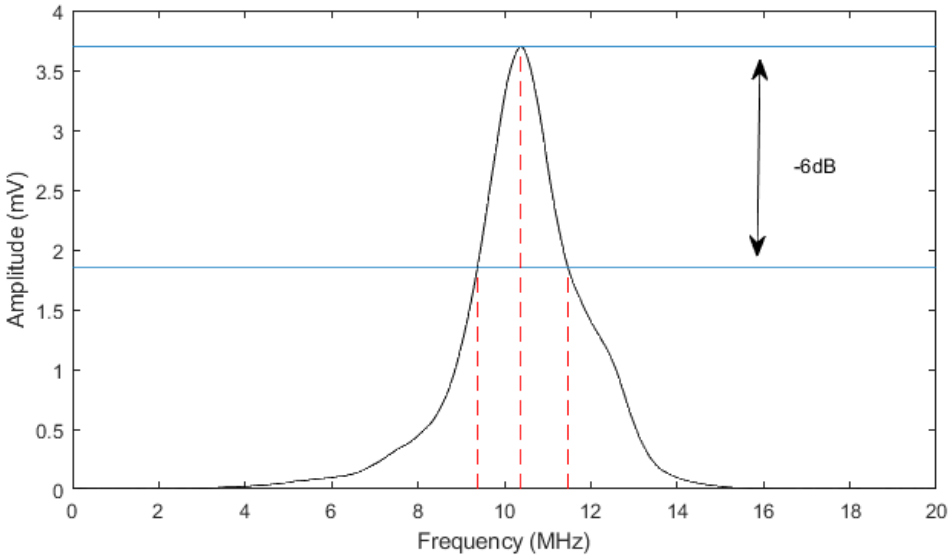

Figure 8-31. Frequency response of a 5-cycle 7MHz-13MHz linear Chirp pulsed wave.

It was observed that the frequency response for the linear chirp did not have spectral leakage and had a narrow bandwidth (9.374MHz-11.47MHz) at -6dB. The bandwidth was slightly wider than the sine wave counterpart.

The normalized chirp echoes were used to produce a surface plot as shown in Figure 8-32 and Figure 8-33.

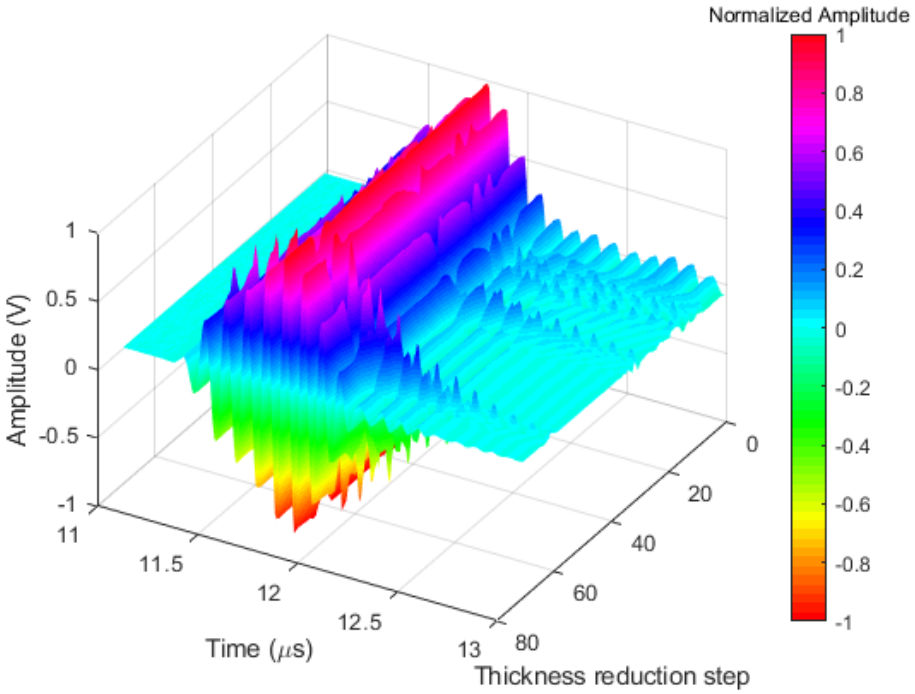

Figure 8-32. Surface plot of the normalized chirp wave data

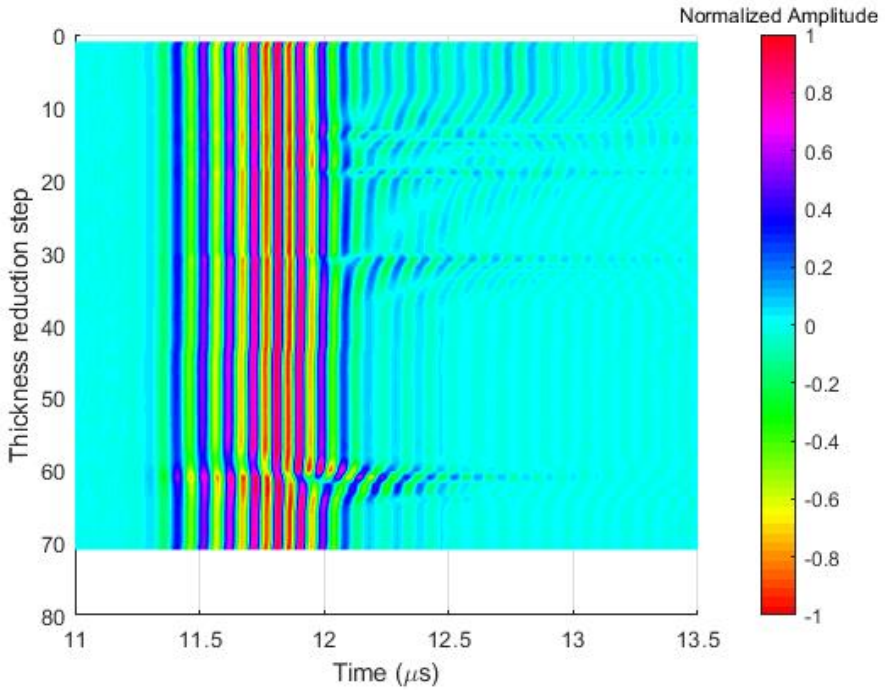

Figure 8-33. Top view of the surface plot in Figure 8-32.

There was a similar tail feature pattern as compared to the sine wave data (Figure 8-25).

Again, considering steps 28 to 34, the *R* spectra were plotted to identify the polyimide resonant frequencies as shown in Figure 8-34.

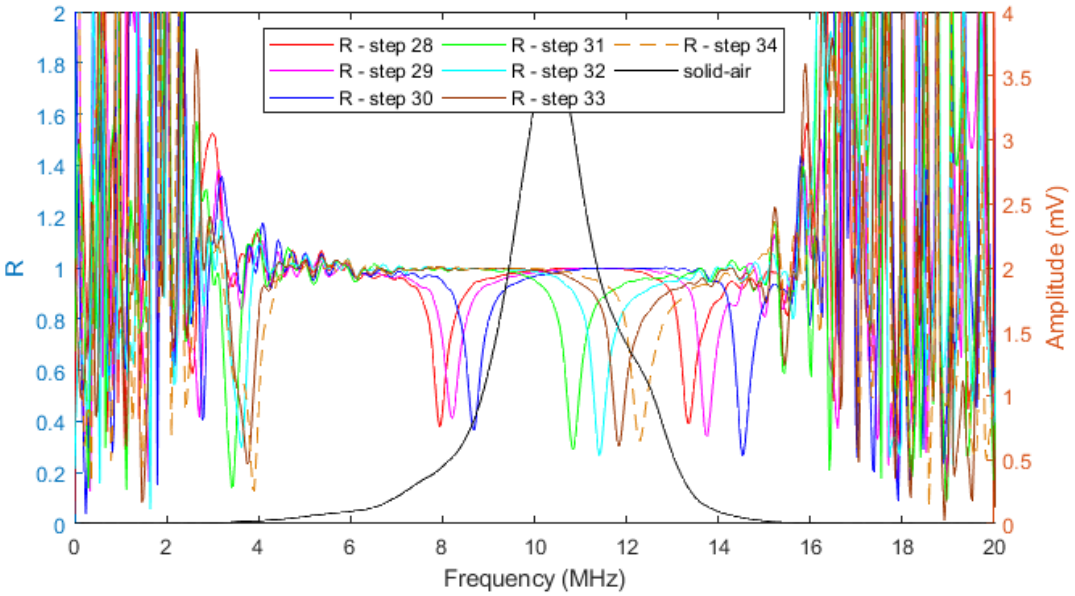

Figure 8-34. *R* spectra for steps 28-34 for chirp wave

Because of the wider bandwidth due to the chirp wave frequencies, the polyimide thicknesses that corresponded to quarter wavelength of the frequencies from the chirp allowed for sound transmission at a wider range as compared to the sine wave data. It was noted that a wider polyimide layer thickness range dictated by Equation 8-3 was able to show resonance when using a 7MHz-13MHz chirp wave as compared to a 10 MHz sine wave pulse.

The resonant dips were more defined and had a narrower shape as compared to the sine wave data. The *R* plot for a 500µm polyimide layer is shown in Figure 8-35.

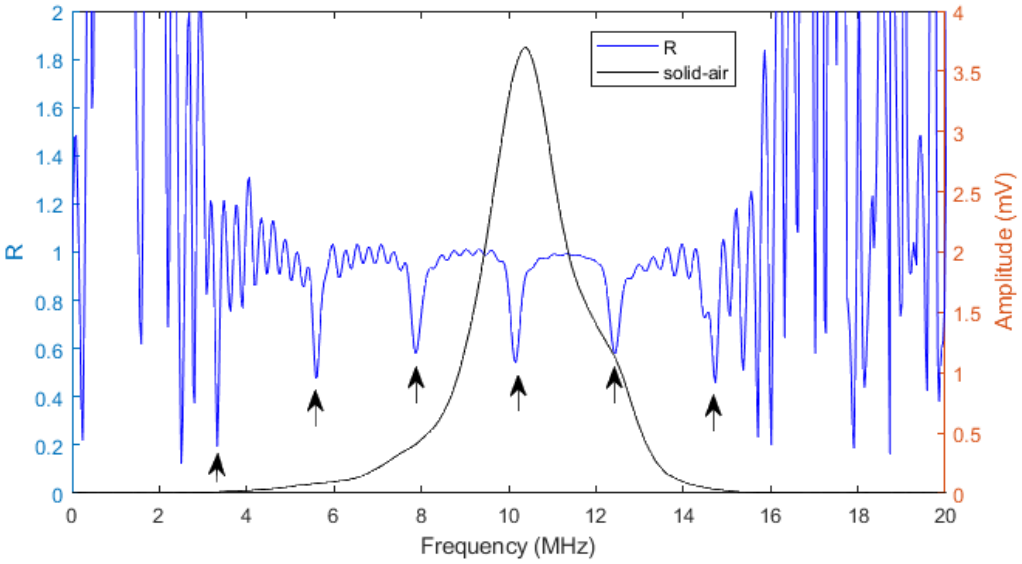

Figure 8-35. *R* plot for a 500µm polyimide layer on the steel substrate showing resonant dips (arrows) for chirp wave data.

The resonant dips were observed at 3.33MHz, 5.58MHz, 7.874MHz, 10.16MHz, 12.42MHz and 14.74MHz. The fundamental frequency f_0 was calculated as 1.14MHz with a standard deviation

of 0.01MHz. However, the narrow bandwidth also affected the resonant frequency modes acquisition window.

8.10 Polyimide Thickness Measurement Comparison

The fundamental frequencies were calculated by averaging the differences between adjacent resonant dips and the polyimide layer thickness was calculated using Equation 3-52 with the assumption that the speed of sound in the polyimide layer was 2420m/s. The results from the standing wave and the pulsed wave experimental data are shown in Figure 8-36.

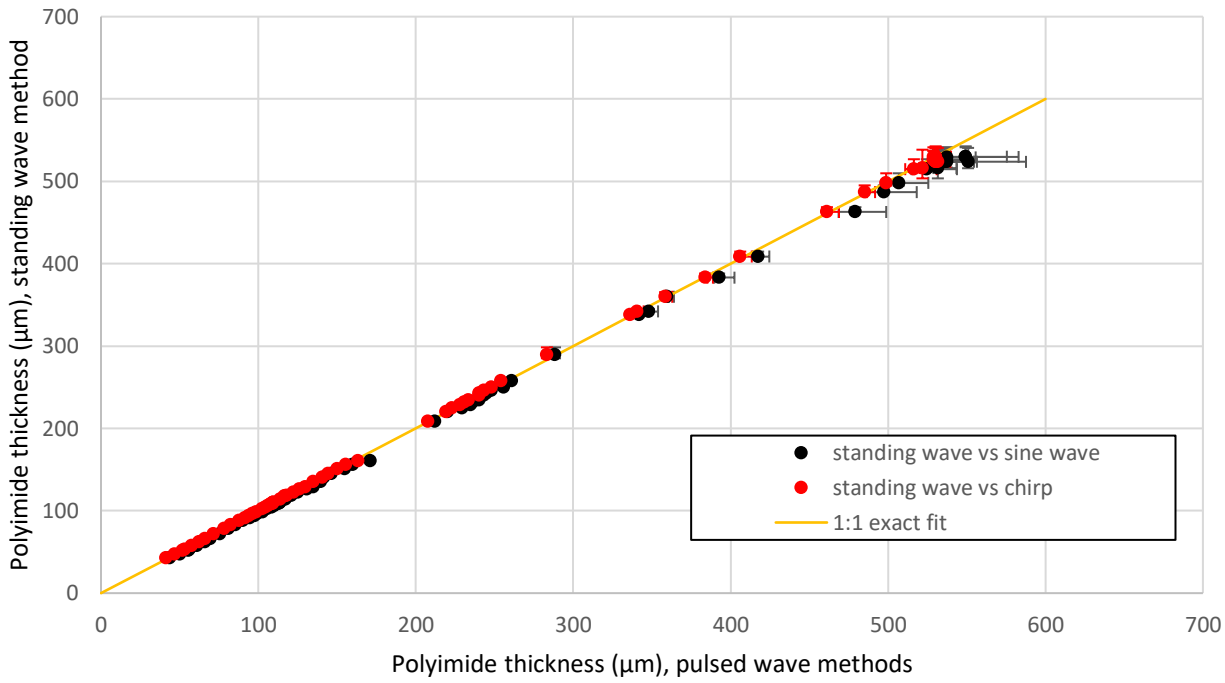

Figure 8-36. A comparison between polyimide layer thickness calculated using a standing wave method and pulsed wave methods.

The vertical error bars represent the standard deviation in the standing wave measurements whereas the horizontal error bars represent the standard deviation with the pulsed wave measurements. The origin of the errors has been discussed previously. There was a strong agreement in the standing wave and pulsed wave results when compared with a 1:1 exact fit line. The sine wave results showed the highest polyimide thickness measurement as 549.29µm whilst the chirp wave and standing wave methods showed 530.2µm and 529.94µm, respectively. The standing wave method showed the strongest agreement to a 500µm thick polyimide layer. The differences between the ultrasound results and a 1:1 exact fit line increased with thickness. The increasing difference was thought to be cause by a change in the speed of sound. The lowest measurable thickness using the sine wave method was calculated as 43.77µm whereas the chirp wave and standing wave methods showed results of 41.23µm and 42.49µm.

8.11 Resonant Dip Magnitude Comparison

A plot of the resonant mode magnitudes against frequency measured using a standing wave, sine, and chirp pulsed waves for a 500µm polyimide layer is shown in Figure 8-37.

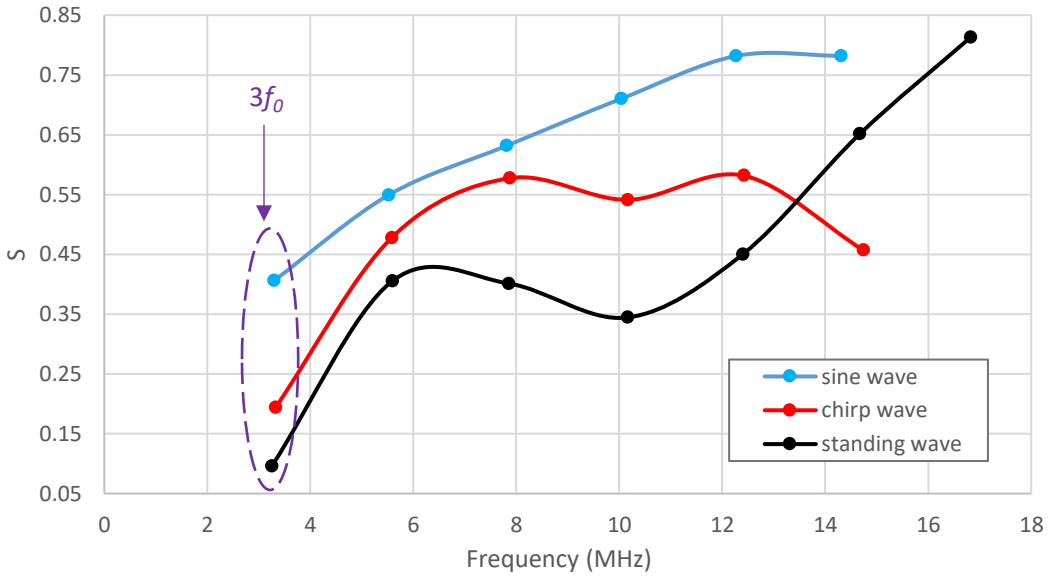

Figure 8-37. Polyimide resonant mode magnitudes for standing wave, sine, and chirp pulsed waves for a 500µm polyimide layer on a 30mm thick steel substrate.

The resonant dip magnitudes were obtained from the respective *S* and *R* spectra. The data circled in purple represents the $3f_0$ data. It was observed that the standing wave approach had the greatest sensitivity as evidenced by the lowest resonant modes magnitude when compared with the sine and chirp pulsed wave approaches. The use of a chirp wave showed greater resonant mode sensitivity as compared to a sine wave approach.

A plot of f_0 and $3f_0$ resonant modes magnitudes for the pulsed wave (sine and chirp) and standing wave data are shown in Figure 8-38 and Figure 8-39, respectively.

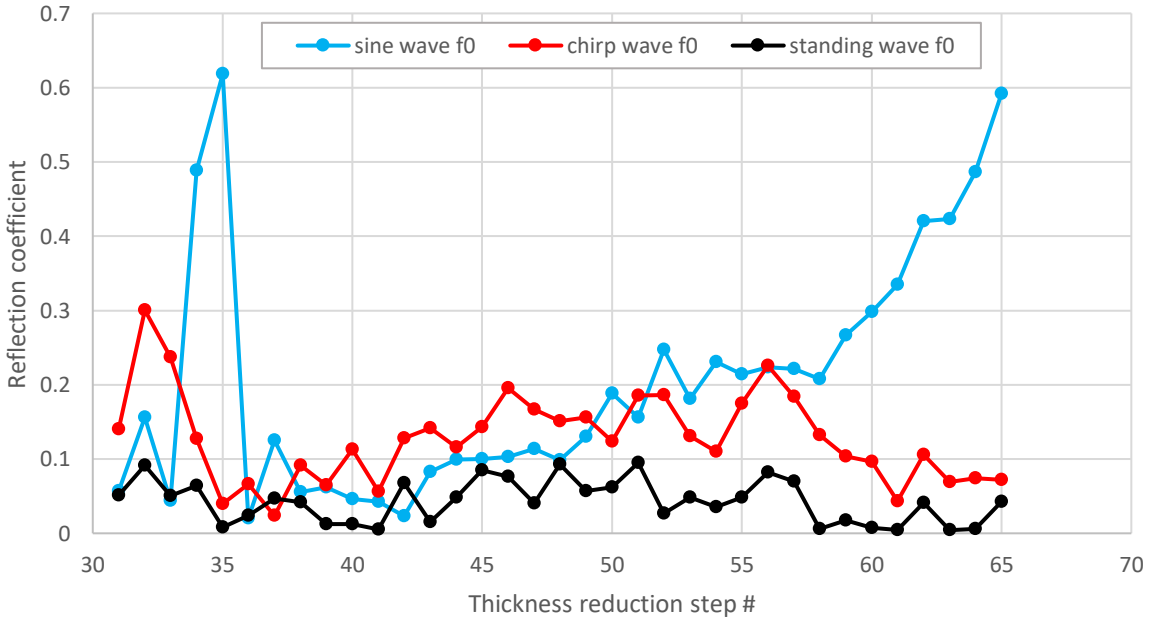

Figure 8-38. f_0 magnitude comparison between pulsed wave and standing wave approaches.

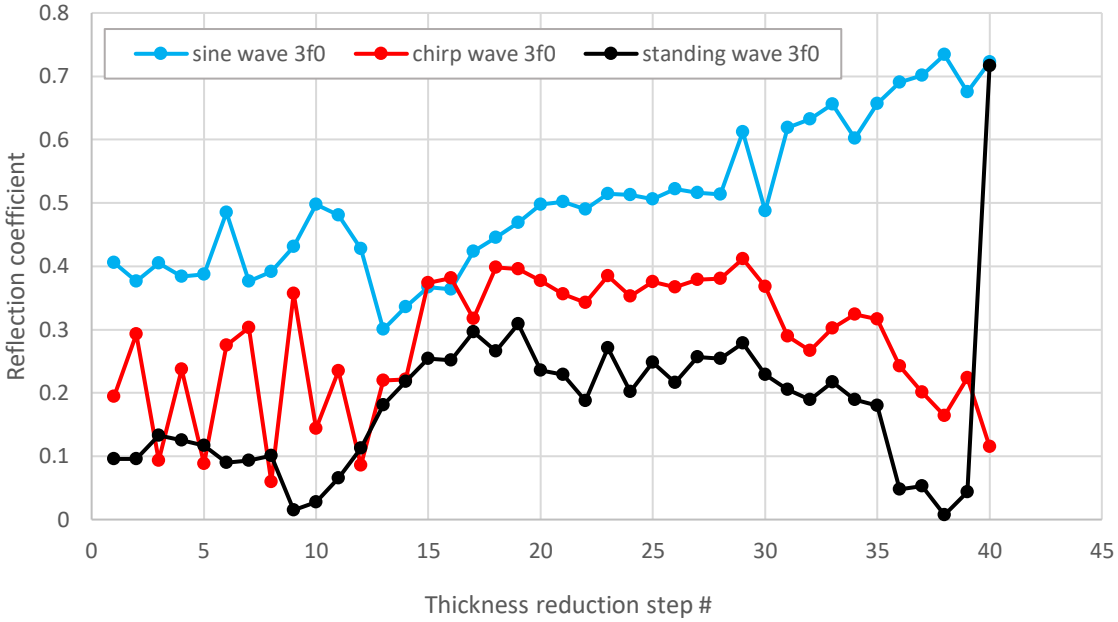

Figure 8-39. $3f_0$ magnitude comparison between pulsed wave and standing wave approaches.

The standing wave method showed the greatest sensitivity by having the least resonant mode magnitude with decreasing polyimide thickness. This trend was also reflected for $5f_0$, $7f_0$, $9f_0$, $11f_0$, and $13f_0$ comparisons shown in Figure 0-1, Figure 0-2, Figure 0-3, Figure 0-4, and Figure 0-5, respectively in Appendix B. The resonant mode magnitudes from the sine wave data showed a reduction in sensitivity with increasing mode number. Considering the decreasing polyimide thickness trend, the f_0 data showed magnitude increase from 0.05 to 0.6, $3f_0$ showed magnitudes increase from 0.4 to 0.7, $5f_0$ magnitudes increased from 0.5 to 0.7, and the $7f_0$ magnitude increased from 0.6 to 0.8. The $9f_0$ magnitudes did not increase significantly, showing an increase from 0.7 to 0.8 whereas $11f_0$ and $13f_0$ magnitudes remained fairly constant around 0.8. The chirp wave and standing wave data also reflected an increase in the resonant mode magnitudes, although not as significant as compared to the sine wave data. For the respective resonant modes, the chirp wave and standing wave magnitudes showed a reduction in the magnitudes with decreasing polyimide thickness, however, the standing wave data reported greater magnitude reduction. It was observed that the difference between the resonant mode magnitudes from the pulsed wave and standing wave data increased with increasing mode number and decreasing polyimide thickness.

8.12 Discussion

The thickness of a polyimide layer that was bonded on a steel substrate was measured using a standing wave method. A 500µm polyimide sheet on a mild steel substrate was ground off to different thicknesses by means of an industrial grinding machine to determine the lowest measurable thickness possible by using a standing wave method. A pulsed sine wave was used to measure the thickness of a shoulder step on the mild steel adjacent to the polyimide layer as a validation of the polyimide thickness measurement using a time-of-flight method . A comparison between the mild steel thickness validation measurements using a pulsed sine wave time-of-flight method and micrometer readings showed strong correlation to the standing wave thickness measurements. The lowest measurable polyimide thickness of 42.49µm was limited by the upper

frequency bandwidth. Mathematical modelling showed that the lowest possible polyimide thickness would be measured as 30.4μm with an upper frequency limit of 19.9MHz with the assumption of good signal-to-noise ratio. The steel thickness was also measured using a micrometer screw gauge and the results showed a good correlation although the errors associated in using the micrometer were many. It is suggested that repeat micrometer measurements at different points could have reduced some of these errors.

The pulsed sine wave and chirp wave measurements showed a narrow bandwidth in the frequency domain and therefore, where the polyimide resonant frequency lay outside this bandwidth, the polyimide layer did not resonate as evidenced by the absence of a tail pattern observed in the surface plot of the first echo. Although the resonant modes could be observed outside of the respective bandwidths, when considering the pulsed wave methods the narrow bandwidths would prove difficult in normal practice. The polyimide resonant modes from the chirp wave measurements were narrower and showed a fairly consistent magnitude with increasing resonant mode number whereas the resonant magnitudes from the sine wave measurements showed an increase with increasing resonant mode number. The standing wave method had a much wider bandwidth due to the multiple frequencies being used as measurement points and the polyimide resonant modes showed a fairly consistent magnitude with increasing resonant mode and decreasing polyimide thickness. The standing wave approach was also able to detect some of the polyimide resonant modes that occurred at 17MHz for thick polyimide layers whereas the pulsed wave approaches were unable.

A comparison between the standing wave and pulsed wave polyimide thickness measurements showed strong agreement when compared with 1:1 exact fit lines. However, when the magnitudes of the resonant modes were compared, the standing wave responses showed the greatest sensitivity as evidenced by the lowest resonant mode magnitudes obtained from the *S* plots.

The temperature effects were considered negligible because the temperature range remained largely at room temperature and also because a coolant was used during the experiment. The thickness of the steel substrate was sufficiently thick to dissipate any absorbed heat from the grinding process at the surface.

There were no external forces acting on the instrumented surface and the magnetic base was switched off when the ultrasound data was acquired to reduce anisotropy and hysteresis effects.

8.13 Conclusions

The lowest measurable polyimide thickness was limited by the upper usable bandwidth. There was no limit on the highest measurable polyimide thickness, although for much thicker layers it is more convenient to use a time-of-flight method. The polyimide thickness measurements using a standing wave measurements showed good correlation with micrometer and steel thickness measurements. The polyimide thickness measurements results between a standing wave and pulsed wave methods showed excellent agreement implying that the standing wave method can be used to measure coating thickness on metal substrates.

The frequency response of a standing wave showed a wider bandwidth because the multiple peaks that represented the substrate harmonics were used as measurement points. Therefore, with the standing wave method, it is possible to have a 0.5MHz to 19.5MHz bandwidth for good signal-to-

noise ratio, although lower frequencies (<2MHz) and higher frequencies (>15MHz) in practise have shown to be affected by noise. The sine wave and chirp wave pulsed data showed narrow bandwidths at -6dB as 9.073MHz-11.3MHz and 9.374MHz-11.47MHz, respectively. The chirp wave showed a slightly wider bandwidth because of the multiple frequencies within the chirp.

The pulsed wave methods that have narrow bandwidths in practice become inconvenient especially where a coating layer thickness is not known beforehand, and the layer resonant frequency lies outside the bandwidth. A standing wave method has shown capability in increasing this bandwidth allowing for a larger frequency range from which to extract the layer resonant frequencies.

The standing wave measurements showed greatest sensitivity in terms of the resonant mode magnitudes. The multiple reflections that interfered within the substrate increased the measurement sensitivity at the interface of interest. The signal-to-noise ratio was also increased. This is particularly useful in improving the identification of the coating/film resonant modes.

The use of a standing wave method was simpler because it had fewer processing steps involved when analysing the data as compared to the conventional pulsed wave techniques. The hardware to be used was also relatively cheap.

9 Case Study On Penetrant Spreading

The aim of this chapter was to measure a penetrant viscosity and film thickness simultaneously during spreading using ultrasonic approaches. To do this, a measurement concept was developed that involved a standing wave method to measure the film thickness using longitudinally polarised transducers and a pulsed wave method that utilised shear polarised transducers and an acoustic matching layer that increased the proportion of energy that gets transmitted into the liquid to measure the sample viscosity. The ultrasonic viscosity measurement method was developed by Schirru et al. [103]. The correlation between sample viscosity and film thickness measurements during spreading are discussed and the limitations of measurement concept are addressed.

9.1 Measurement Concept

The viscosity of a lubricating oil is arguably the most important property of an oil sample. This is because viscosity greatly affects the wettability and consequently the film thickness of any lubricating oil during spreading conditions on a free surface.

A study into the penetration of specialised lubricants into threaded contacts has previously been conducted where the difference between penetration times was thought to be caused by presence of bubbles and some loading variations [104]. Therefore, in this study, the viscosity and thickness of specialised lubricants will be investigated simultaneously using ultrasound techniques as they spread over a free surface. The main objective is to extend the previous penetration studies by eliminating the presence of air pockets, loading variations, and capillary effects that occur in threaded contacts and to solely look at the spreading evolution of lubricants and solvents on a free surface in order to understand the performance properties of the various WD40™ formulations and how the viscosity and thickness properties are related.

The standing wave method has already been shown in chapter 8 to have increased measurement sensitivity of surface coating thicknesses on metal substrates. It also has less signal processing steps involved as compared to conventional pulse-echo techniques, and the equipment required is relatively cheap and affordable. Various researchers have already reported on the use of ultrasound technique to measure lubricant film thicknesses non-invasively by utilising a pulse-echo approach [9], [38]–[42]. As a result, the work presented herein reports on the detection and measurement of lubricant film thickness evolution due to spreading and solvent evaporating conditions on a free surface using a standing wave approach. The standing wave generation principle and estimation of a surface film thickness from ultrasound frequency responses has already been discussed in chapters 5,6, and 8.

The ultrasonic viscometry approach used here borrows from the early works of Schirru et al. [103], [105]. Because there is usually a large acoustic mismatch between common metal substrates (steel and aluminium for instance) and lubricating oils, an acoustic bridge dubbed ‘matching layer’ has been used to increase the proportion of energy that propagates into the oil. The matching layer is carefully selected such that its acoustic impedance lies between that of the substrate and the oil, and its thickness is a quarter wavelength of the driving frequency. Results showed a strong correlation when compared with conventional viscosity measurements of Newtonian lubricating oils.

9.2 Specialised Lubricants Background

Dearomatized hydrocarbon fluids are nowadays used to replace traditional solvents such as mineral and white spirits. They have excellent solvency properties whilst maintaining environmental, health and safety standards. These hydrocarbon fluids are comprised of a mixture of carbon chains of different lengths that are a result of the hydrogenation of petroleum by-products. They have very low aromatic content (<1% weight), low toxicity, have a relatively broad evaporation range, and can be tailored with additives. Selected examples of dearomatized hydrocarbon fluids and their physical properties that were obtained from the WD-40™ Company are listed in Table 9-1.

Table 9-1. Dearomatized hydrocarbon fluid physical properties.

Sample	Relative density at 15.6°C/15.6°C	Kinematic viscosity at 25°C, mm^2/s (cSt)	Kinematic viscosity at 40°C, mm^2/s (cSt)	Flash point (°C)	Evaporation rate at 25°C [n-BuAc=100]
D40	0.779	1.29	1.06	44	17
D60	0.791	1.69	1.35	64	4.0
D80	0.796	2.21	1.66	83	1.2
D95	0.802	2.78	2.02	96	0.4
D110	0.809	3.59	2.57	115	<0.1

The respective carbon chain distribution is shown in Table 9-2.

Table 9-2. Dearomatized hydrocarbon fluid carbon chain distribution as a percentage.

	Percentage (%)								
Sample	C8	C9	C10	C11	C12	C13	C14	C15	C16
D40	1	13	36	37	12	1			
D60			2	45	45	8			
D80				9	29	40	20	2	
D95					9	36	33	19	3
D110						2	35	46	17

An increase in the carbon chain number content resulted in an increase in relative density, viscosity, flash point and a decrease in the evaporation rate. In the formulated WD-40™ products, these hydrocarbons are mixed with a base oil and additive packages to produce specialised lubricants that have low viscosity, low surface tension and high wettability properties [104]. These properties allow the lubricant to be dispersed as an aerosol in order to reach inaccessible contacting surfaces such as threaded contacts. The lubricants are then able to penetrate the threaded contacts and remove any residue allowing for loosening of the contact. The lubricants also provide lubrication between the contacts and prevent rusting. These formulations have better performance compared to more traditional lubricants. The specialised lubricants that were obtained from the WD-40™ Company are listed in Table 9-3.

Table 9-3. WD40™ samples composition.

Sample	Concentrate content %	VOC %
Base Oil 100	N/A	N/A
Concentrate	100	N/A
WD40 w. D40	33	67 (D40)
WD40 w. D60	33	67 (D60)
WD40 w. D80	33	67 (D80)
WD40 w. D95	33	67 (D95)
WD40 w. D110	33	67 (D110)
WD40 MUP 10% VOC	33	10 (D40), 57 (D95)
WD40 MUP 19% VOC	33	19 (D40), 48 (D95)
WD40 MUP 25% VOC	33	25 (D40), 42 (D95)
WD40 MUP 67% VOC	33	67 (D40)

Base oil 100 is a light hydrocarbon that is used as a base stock for several industrial lubricants. It is clear and bright in appearance and has a typical kinematic viscosity of 18.5 to 21 cSt at 40°C. It also has a relative density of 0.850 at 15.6°C. Concentrate is a mixture of a base oil and specialised performance additives. These two are mixed in different proportions to yield concentrates that are further mixed with different solvents (dearomatized hydrocarbons) and then used in different market products. Although during this study the exact constituents that make up the additives were unknown, it was known that they added to the lubricating properties of the WD40 products by reducing friction. The rest of the samples were composed of a mixture of the concentrate and solvents. The solvents were branded as volatile organic compounds (VOCs) due to their volatility.

9.3 Component Instrumentation

A 5mm thick aluminium component having 200mm×200mm lateral dimensions was instrumented with four 10MHz longitudinal sensor pairs on the back face that were separated 20mm apart with the first sensor pair located centrally. Four 5MHz shear sensor pairs were also bonded adjacent to the longitudinal sensors but at a position far apart to prevent crossover or interference of ultrasound signal reception between the two types of sensors. A schematic of this is shown in Figure 9-1.

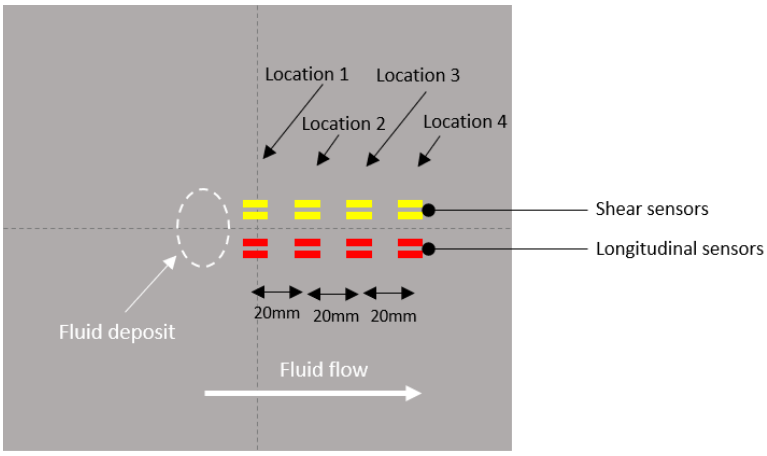

Figure 9-1. Schematic of the back face of the aluminium component showing sensor pair spacing.

The longitudinal sensors were operated in a pitch catch arrangement, a requirement for standing wave method. The shear sensors were also operated in a pitch-catch setting, although they could also be operated in a pulse-echo setting by using only one sensor. A 50μm thick polyimide matching layer was also bonded on the front face of the aluminium component using M-bond 610 strain gauge adhesive and cured in an oven. This method was similar to the transducer-bonding technique. A visual inspection was carried out to ensure there were no air bubbles nor solid particles underneath the matching layer both before curing and after the curing process.

The characteristic lateral dimensions of the matching layer were such that the layer spanned the region of shear and longitudinal ultrasonic sensitivity. A photograph to show the bonded matching layer with an oil spreading laterally on the front face is shown in Figure 9-2.

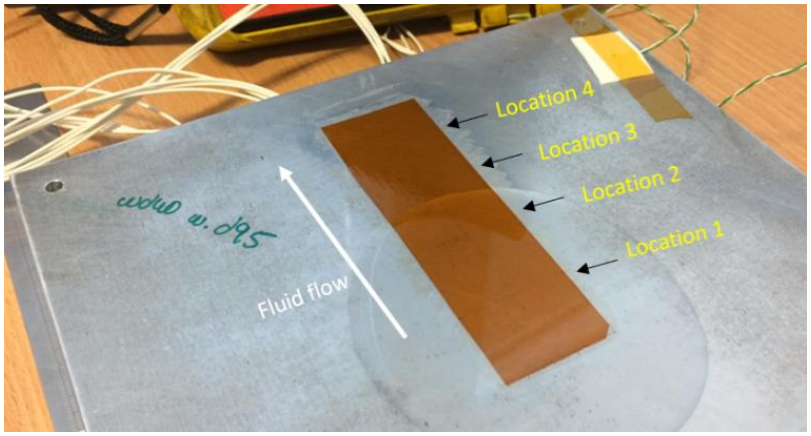

Figure 9-2. A photograph showing the bonded matching layer (orange layer) on the aluminium component with an oil sample spreading over the surface.

The data pulsing and acquisition was controlled via Triboscope software. A k-type thermocouple was used to monitor the temperature on the top surface of the aluminium.

9.4 Viscosity Background

Viscosity is defined as the measure of resistance of a fluid to flow. It is used to describe the internal friction within a fluid. When a liquid is constrained between two components that are separated by a gap, *h*, as illustrated in Figure 9-3, and with the assumption that one component is stationary, the shear force *F* that is applied to the other component is expressed as:

$$F = \eta A \frac{u}{h} \qquad \text{Equation 9-1}$$

where *A* is the wetted surface area, *u* is the velocity and η is the viscosity of the liquid.

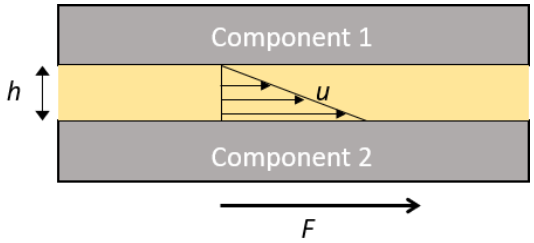

Figure 9-3. Schematic showing a constrained liquid layer of thickness *h* with two components on either side.

Shear viscosity describes the liquid resistance to shear stress and can be defined as dynamic viscosity, η:

$$\eta = \frac{F}{A}\Big/\frac{u}{h} = \frac{\tau}{\dot{\gamma}} \qquad \text{Equation 9-2}$$

where τ is the shear stress and $\dot{\gamma}$ is the shear rate. The dynamic viscosity is usually expressed in terms of *P* (Poiseuille) such that $1P=0.1Pas$ (Pascal second). Kinematic viscosity v, which is defined as the liquid's resistance to flow under gravity, is calculated by dividing the dynamic viscosity with the liquid density, ρ:

$$v = \eta/\rho \qquad \text{Equation 9-3}$$

The standard unit for kinematic viscosity is Stoke (*St*) but it is common practise to find it expressed as centi-Stoke (*cSt*) in literature.

The viscosity of liquids is normally measured using conventional viscometers. Some major examples include:

i. Capillary viscometers – the time it takes for a liquid sample to propagate through a capillary tube is correlated to its kinematic viscosity.
ii. Falling body viscometers – the time it takes for a spherical or cylindrical body to fall through a capillary tube is correlated to the liquid internal resistance.
iii. Rotational viscometers – the viscosity of the liquid is measured by the fluid resistance to applied shear stress (rotating motion) of a cylinder in a cylinder filled with the liquid.
iv. Vibrational viscometers – the liquid viscosity is determined by the power that is required to displace a known liquid amount.

However, the necessity for in-situ viscometry in real time led to the development of an ultrasound viscometry technique that uses shear waves to measure the viscosity of a liquid at the interface of interest [106]. There is usually a high acoustic mismatch between a metal substrate and a lubricating oil at the surface such that most useful ultrasound energy is reflected. However, the use of an acoustic matching layer to increase ultrasonic measurement sensitivity has been developed by Schirru et alc. A matching layer is selected to have an acoustic impedance that is the square root of the product of the metal substrate and the liquid impedances and to have a thickness that is a quarter wavelength of the excitation frequency. The shear waves are neatly transmitted from the metal substrate into the matching layer where destructive interference occurs. The frequencies where destructive interference occurs are highly sensitive to the matching layer-liquid interface. The proportion of energy that is transmitted into the liquid is increased and the signal-to-noise ratio is improved. The reader is directed to the relevant literature by Schirru et al. [103] that has already covered this in detail. As a result, the signal processing and data analysis method employed for ultrasonic viscometry of specialised lubricants and solvents in this research work has borrowed from the pioneering work of Schirru et al.[103]. Therefore only the pertinent aspects of ultrasonic viscometry will be discussed in the section that follows.

9.4.1 Ultrasonic Viscometry

The reflection coefficient, R^* for shear wave interaction at a boundary between a solid and a liquid (illustrated in Figure 9-4a) that have different acoustic impedances is expressed as:

$$R^* = \frac{z_l - z_s}{z_l + z_s} = |R|e^{-i\omega\theta} \quad \text{Equation 9-4}$$

where the subscripts *l* and *s* represent liquid and solid, respectively and *z* is the material acoustic impedance. $|R|$ is the magnitude of the reflection coefficient. The shear acoustic impedances for the solid and liquid are defined as:

$$z_s = \rho_s c \quad \text{Equation 9-5}$$

$$z_l = \sqrt{\rho_l G} \quad \text{Equation 9-6}$$

where G represents the complex shear modulus $(G = G' + iG")$. G' is the storage modulus whereas $G"$ is the loss modulus. For the case of a Newtonian liquid where the relaxation is negligible, $G' = 0$ and $G" = \omega\eta$. Equation 9-6 can then be written as [107]:

$$z_l = \sqrt{i\rho_l\omega\eta} \quad \text{Equation 9-7}$$

Substituting Equation 9-5 and Equation 9-7 into Equation 9-4 gives:

$$R^* = \frac{\sqrt{i\rho_l\omega\eta} - \rho_s c}{\sqrt{i\rho_l\omega\eta} + \rho_s c} \quad \text{Equation 9-8}$$

The shear acoustic impedance of a liquid is a function of frequency, and the impedance increases with increasing frequency. For the case of metal solids such as aluminium or steel, which are common in most industrial applications, a high z_s value in comparison to the liquid shear acoustic impedance z_l results in a high *R* magnitude value. This explains why it is impractical to perform ultrasonic viscometry on a common metal-oil interface due to sensitivity issues.

Schirru et al. [103], [105] developed a technique that increases the ultrasonic viscometry sensitivity by introducing a matching layer (ML) between the solid and the liquid. The matching layer increases the acoustic response of the system and is selected to have an acoustic impedance that is a square root of the solid and liquid acoustic impedances:

$$z_{ml} = \sqrt{z_s z_l} \quad \text{Equation 9-9}$$

where the subscript *ml* represents matching layer. This was derived from the assumption of a three-layered model (solid-ML-liquid). It is also selected to have a thickness that is a multiple of a quarter wavelength of the driving frequency:

$$t_{ml} = \frac{nc_{ml}}{4f} \quad \text{Equation 9-10}$$

where *n* represents a natural integer. At the driving frequency, *f* the waves are transmitted from the solid into the matching where superimposition occurs, and the reflected wave destructively interferes with the incident wave inside the solid. A schematic to show reflection at a solid-ML-oil boundary system is shown in Figure 9-4b.

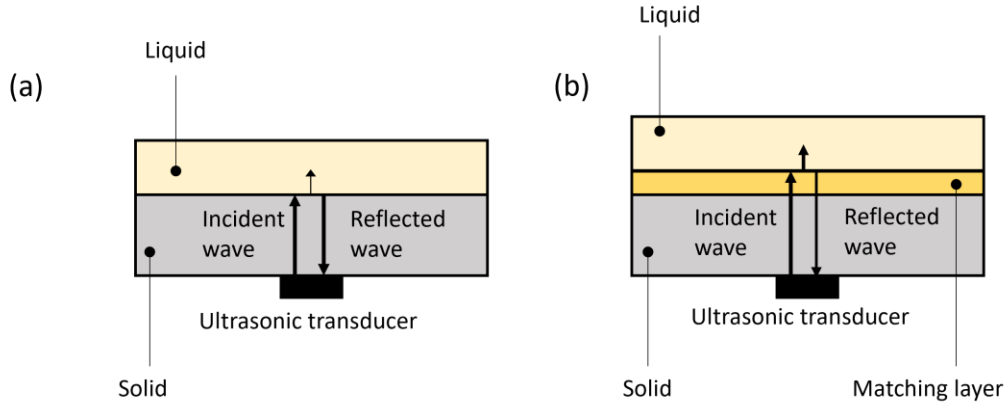

Figure 9-4. Schematic to show shear wave interaction at (a) a solid-liquid boundary and (b) a solid-ML-liquid boundary.

The measurement at the ML-liquid interface is highly sensitive due to acoustic matching. Usually, shear waves never fully propagate through a liquid and the penetration depth, δ is calculated as:

$$\delta = \sqrt{\frac{\eta}{\pi f \rho_l}} \qquad \text{Equation 9-11}$$

The penetration depth lies <1μm for light oils where a shear wave frequency of 5MHz is used. It has been shown from the previous chapter that the lowest possible oil film thickness measurable using a resonance method is dictated by the upper driving frequency output. The upper frequency limit when using a standing wave method (centre frequency of 10MHz and span of 19MHz) is ~19MHz (assuming good signal-to-noise ratio) thereby allowing a measurable oil film thickness of ~19μm, where the oil speed of sound at ambient pressure and temperature is 1450 m/s. Ultrasonic viscometry measurements to be carried out in this study to be compared with film thickness measurements therefore hold.

A study was carried out to investigate the influence of a matching layer on the reflection coefficient of two oils of different viscosities [105]. It was observed that a matching layer significantly reduced the reflection coefficient at 5MHz where a 45μm thick polyimide matching layer was used. This reduction is shown in shown in Figure 9-5.

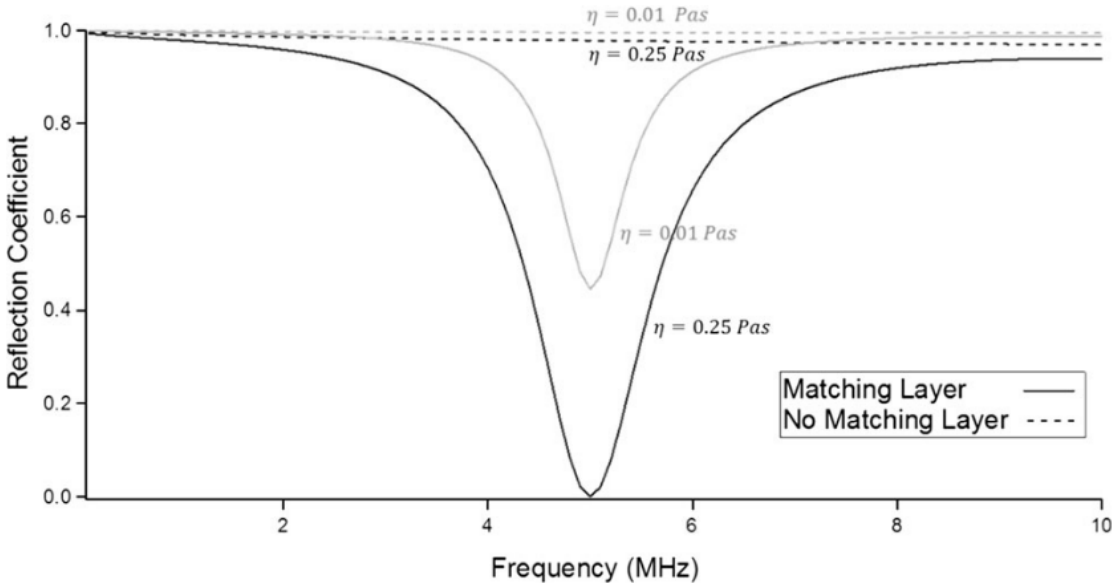

Figure 9-5. Reflection coefficient model spectra for two liquids with viscosities 0.01 Pas and 0.25 Pas showing increase in reflection coefficient sensitivity due to a matching layer (Image obtained from [105]).

This shows evidence that a matching layer increases viscosity measurement sensitivity. Schirru et al. [105] used a chirp wave input to excite multiple frequencies. In doing so, the exact matching layer resonant frequency will be observed as a dip in the reflection coefficient spectra, a result of destructive interference. It is at this resonant frequency that the reflection coefficient, *R* values are used in viscosity calculations. The reflection coefficient was practically obtained by dividing the amplitude of the frequency response of a solid-ML-oil boundary condition with the amplitude of the solid-ML-air boundary condition:

$$R = \frac{A_{solid-ML-oil}}{A_{solid-ML-air}} \qquad \text{Equation 9-12}$$

Furthermore, the experimental *R* values of standard mineral oils when plotted against viscosity values that were measured using conventional viscometers showed strong agreement with a Maxwell model results when a logarithmic fit for the experimental data was used as compared to Greenwood and Newtonian reflection models [103]. An empirical law method was therefore developed that first calibrated the measurement specimen with standard Newtonian mineral oils to obtain a *R* against η plot. The data was interpolated, and a curve fitting equation was used to estimate the viscosity of unknown oil samples. It is therefore possible to estimate oil viscosity by knowing the *R* value only with this method.

9.4.2 Viscosity Calibration

A 3MHz-7MHz 10 cycles chirp wave was pulsed through the instrumented component and the first reflected pulse was isolated. Data was collected for both solid-ML-air and solid-ML-oil boundary conditions. The isolated pulses were zero padded and a FFT was performed to give the frequency spectra of the reflected pulses. Figure 9-6 shows examples of reflected pulses and their associated frequency and *R* spectra. *R* was calculated using Equation 9-12.

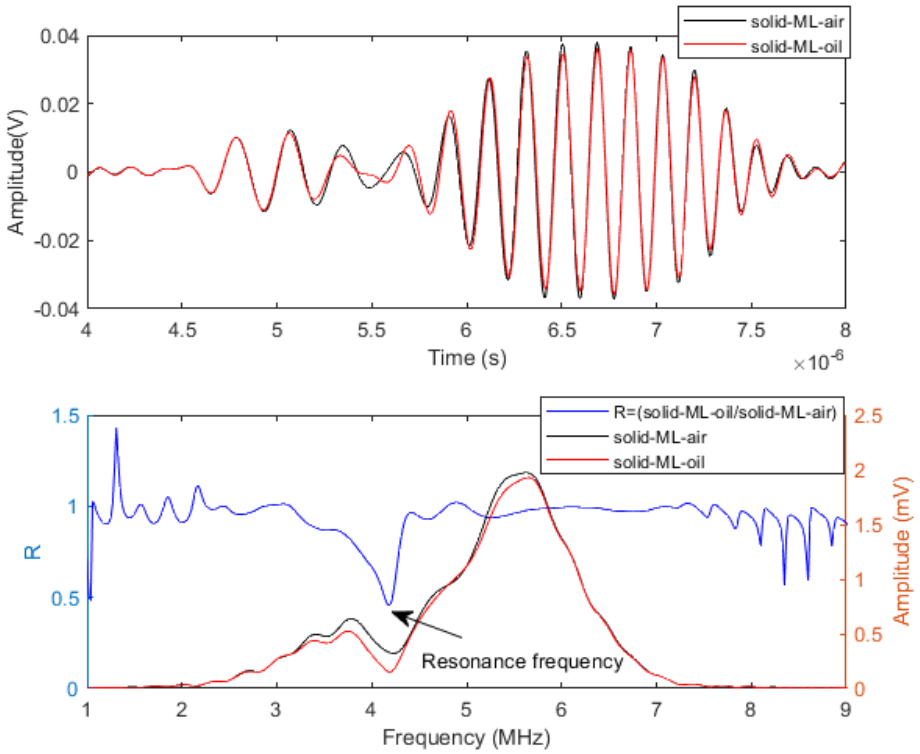

Figure 9-6. (Top) The reflected pulses for solid-ML-air and solid-ML-oil boundary conditions and (bottom) the respective frequency spectra. The reflection coefficient, *R* has been plotted to identify the resonance frequency location (shown as dip). The oil sample used in this case was S60 Cannon™ calibrated mineral oil.

The resonance frequency occurred at 4.17MHz with a *R* value of 0.46.

The samples used for viscosity calibration were Cannon™ calibrated viscosity standard mineral oils and these are listed in Table 9-4.

Table 9-4. Cannon™ viscosity standard mineral oils and their properties.

Cannon™ viscosity standard mineral oil	Dynamic Viscosity at 25°C, mPa.s (cP)	Density, g/mL
S3	3.3	0.864
N10	16	0.881
S20	29	0.86
S60	104	0.873
N100	202	0.879

The samples used were chosen to span a sufficient viscosity range. The calibration measurements were performed at three different room temperatures on three different days and each room temperature measurement was repeated three times. This gave a total of nine readings for each mineral oil. The room temperatures recorded were 21.7°C, 22.9°C and 22.2°C. It was therefore necessary to calculate the viscosity of the mineral oils at the different room temperatures.

The viscosity of mineral oils changes with temperature and the Vogel equation best describes this [108]:

$$\eta = ae^{\frac{b}{T-c}} \qquad \text{Equation 9-13}$$

where a, b, c are constants, η is the dynamic viscosity and T is the temperature measured that is used to calculate the viscosity. This is the most accurate as compared to other viscosity-temperature equations and is used in most engineering calculations. Three viscosity readings at different temperatures are required to obtain the constants and these are usually obtained from viscosity data tables from suppliers of mineral oils. In this study, the dynamic viscosity and temperature data was obtained from Cannon™. For example, the viscosity of S60 sample from the manufacturer viscosity standards at 20℃, 25℃, and 40℃ is 141mPa.s, 104 mPa.s, and 47 mPa.s, respectively. Therefore, at 21.7℃ using Vogel equation, the viscosity was calculated as 126.8mPa.s. The viscosity values were averaged for the three temperatures.

The R values were obtained for the mineral oil samples at the respective resonance frequency and then averaged. Figure 9-7 shows the relationship between reflection coefficient, R, and dynamic viscosity, η for the mineral oils at location 1.

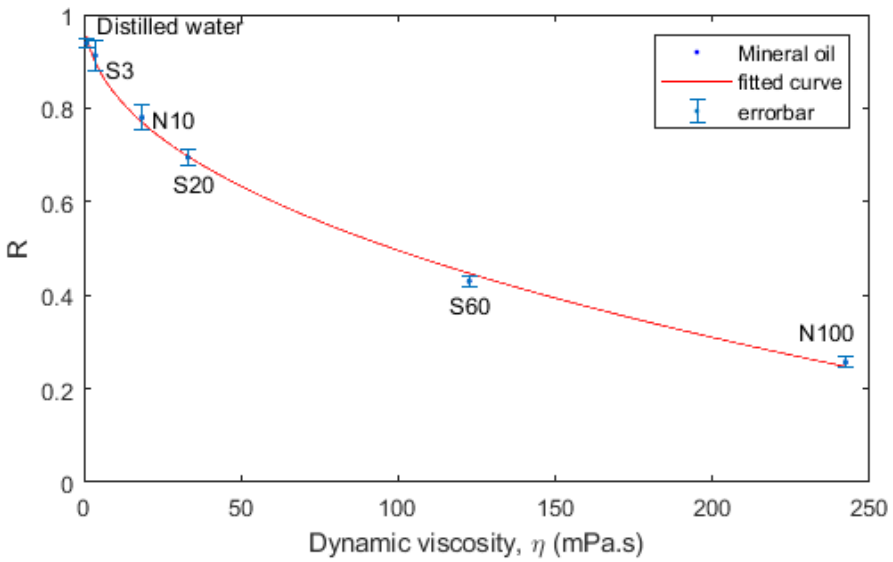

Figure 9-7. R-η relationship for Cannon™ standard mineral oils for shear sensors at location 1.

Error bars represent the standard deviation. The differences between the experimental viscosity values from Figure 9-7 and the manufacturer values listed in Table 9-4 were because the viscosity calibration was performed at a temperature lower than 25℃ (21.7°C, 22.9°C, and 22.2°C, respectively as mentioned earlier) therefore the sample viscosities at these temperatures were calculated to be higher using the Vogel equation.

A power fit model was used to plot the fitted curve such that:

$$R = a\eta^b + c \qquad \text{Equation 9-14}$$

where *a, b, c* are coefficients. The unknown viscosities could then be found by knowing only the *R* value. Distilled water viscosity measurements were also included to ensure completeness.

9.5 Oil Film Thickness Validation

The thickness of an oil film between two similar metal substrates that were separated by means of metal shim plates was measured using a standing wave method. This was performed to validate the lubricant film thickness measurements using the standing wave approach. A schematic to illustrate this set-up is shown in Figure 9-8.

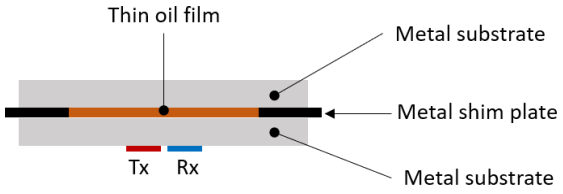

Figure 9-8. Schematic illustrating a cross-section of the experimental set-up.

G-clamps were used to provide an even load on the top metal substrate to ensure uniformity. Oil film standing wave measurements were performed and the superimposed oil film resonances were extracted from an *S* plot. Because the oil film was embedded between two similar substrates, Equation 3-50 was used to calculate the oil film thickness based on the embedded oil film resonant frequencies. Furthermore, because the testing was performed at ambient temperature and pressure, the speed of sound in oil was assumed to be 1450 m/s [9]. However, it is worth noting at this point that a significant increase in temperature and pressure would increase the speed of sound in oil.

A concentrate sample was embedded between two aluminium plates and metal shims were used to separate the plates to give a gap of known thickness. 50µm, 100µm, 150µm, 200µm and 300µm metal shims were used. The corresponding oil film thicknesses calculated using a standing wave method for the different sensor locations is shown in Figure 9-9.

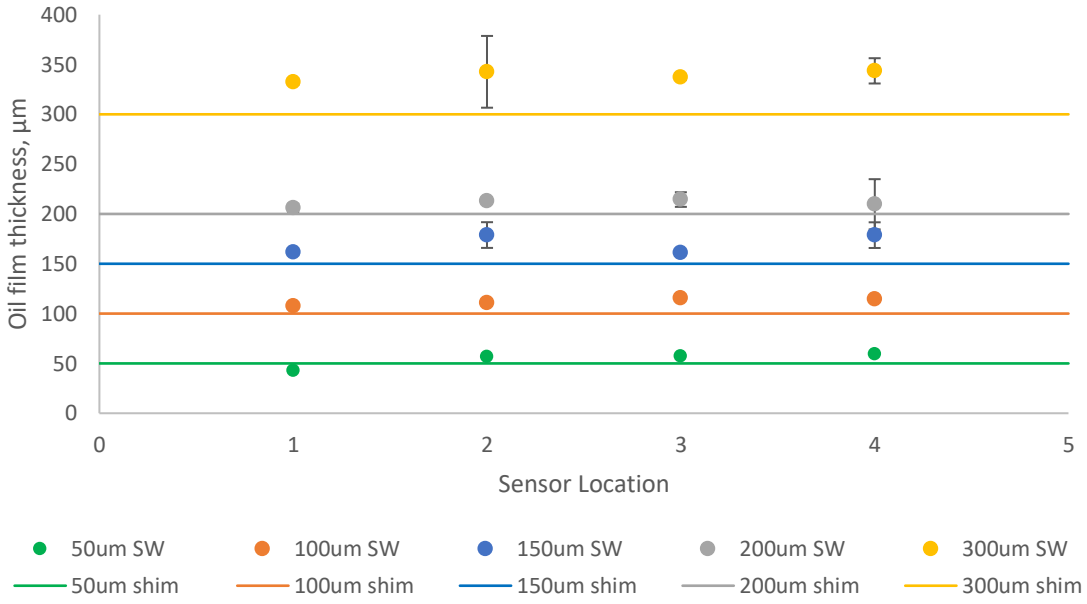

Figure 9-9. Oil film thickness for different shim thickness at the sensor locations calculated using a standing wave (SW) method.

The vertical error bars here represent the standard deviation obtained from the differences between adjacent peaks where more than two resonant dips occurred within the bandwidth. The results showed an increase in difference between the oil film thickness measured using a standing wave method and the shim thickness. The oil film thickness measured using a standing wave method across the four locations at each shim thickness was averaged and compared with the shim thickness as shown in Figure 9-10.

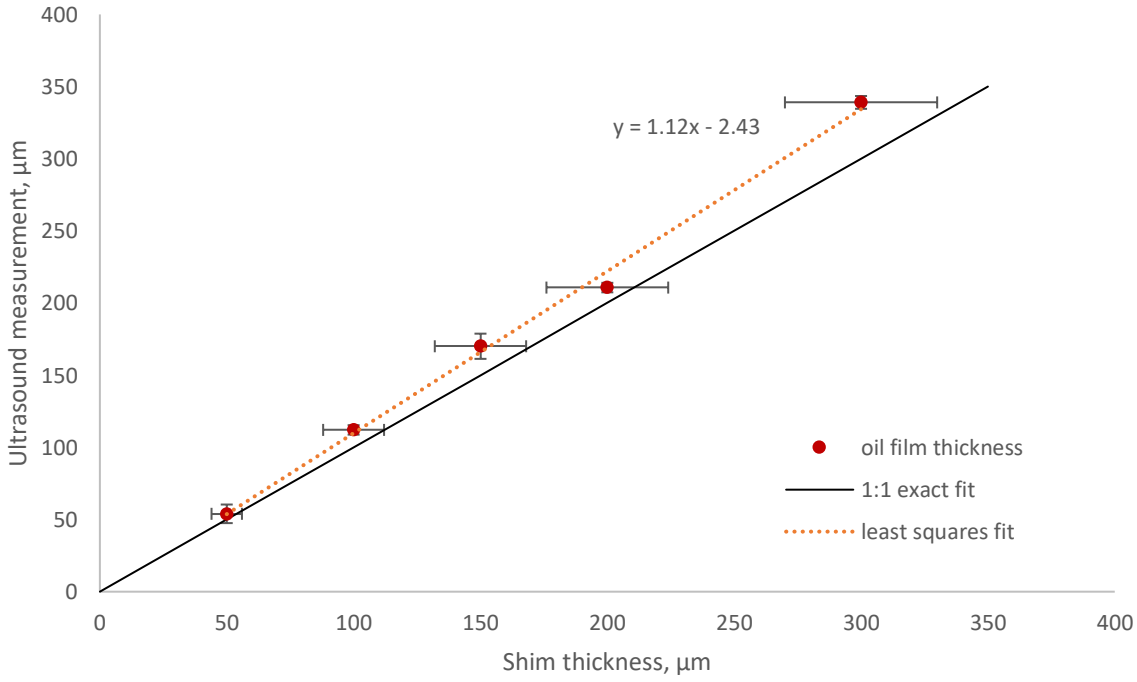

Figure 9-10. Comparison of oil film thickness measured using a standing wave method against metal shim thickness.

The vertical error bars shown here were calculated by taking the standard deviation of the thickness readings for the four sensor locations. The horizontal error bars represent the shim tolerances from the manufacturer. A linear least squares regression best line of fit of the oil film thickness measurements showed a system error of -2.43μm and a 12% error when compared to a 1:1 exact fit line.

9.6 Standard Mineral Oil Film Thickness Measurements

The oil film thickness of S3, N10, S20 and N35 Cannon™ oil samples on a free surface during spreading conditions were measured using a standing wave method. The properties of S3, N10 and S20 oil samples are listed in Table 9-4. N35 Cannon™ mineral oil has a dynamic viscosity of 56 mPa.s at 25°C with a density of 0.864 g/mL.

The measurements were carried out on a 10mm thick aluminium specimen that was instrumented with a pair of 10MHz longitudinal transducers. A schematic to show the oil film thickness spreading when deposited on a surface is shown in Figure 9-11a. The oil was deposited on the surface at the region of ultrasound sensitivity. This position was at a position perpendicular to the sensors as illustrated in Figure 9-11b.

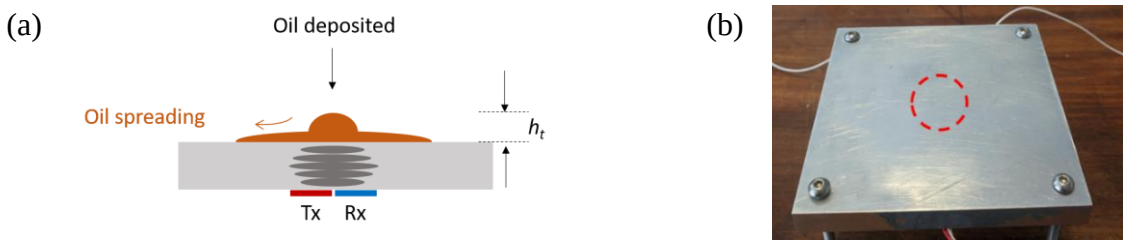

Figure 9-11. (a) A schematic to show oil spread when deposited on a surface. (b) Photograph to show region of ultrasound sensitivity (red dotted circle) on the surface of interest at a position perpendicular to ultrasonic sensors.

Over time, the localised film thickness reduced as the oil sample spread across the surface. The rate at which the localised film thickness reduced was dependent on the viscosity and wettability properties of the oil sample. The measurements were performed at ambient temperature and pressure.

A standing wave centred around 10MHz with 19MHz frequency span and 4ms sweep time was generated. Solid-air frequency responses were captured for 30 seconds at a capture rate of 1 Hz and averaged. The surface was cleaned with isopropyl alcohol solution and solid-oil frequency responses were obtained for 170 seconds also at a capture rate of 1 Hz. The oil was deposited after 15 seconds by means of a pipette from a constant height (<5cm) from the surface of the aluminium. The samples were measured to have a volume of 0.3mL. Figure 9-12 shows the frequency responses for solid-air and solid-oil boundary conditions and the associated *S* profile at 140 second time stamp for S3 sample.

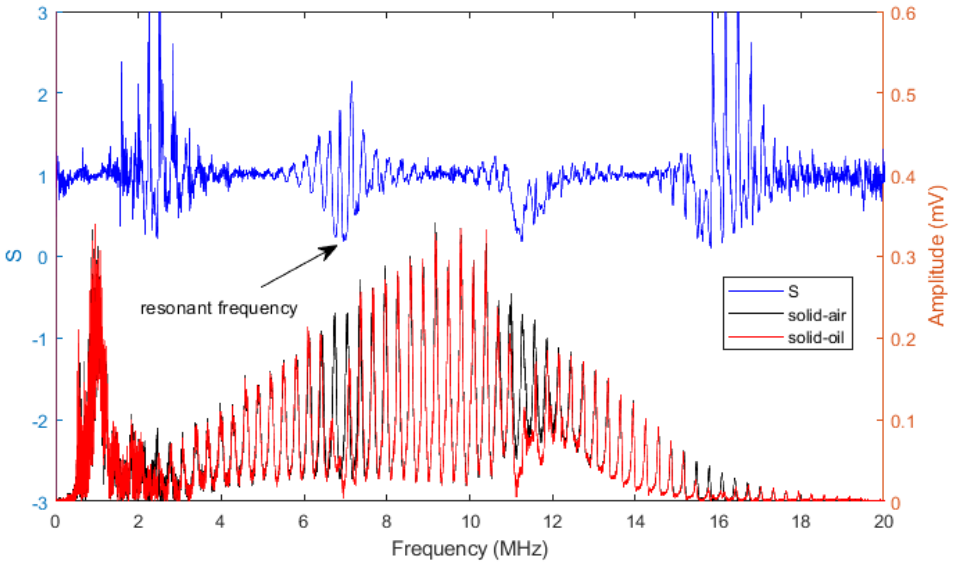

Figure 9-12. Solid-air and solid-oil frequency responses and the *S* plot for S3 oil sample at 140 second time stamp showing resonant dip frequency locations.

The superimposed oil resonant frequencies were observed as dips in the *S* spectrum. The *S* spectra were stacked to produce a colour plot shown in Figure 9-13. The colour map shows the intensity of the *S* values.

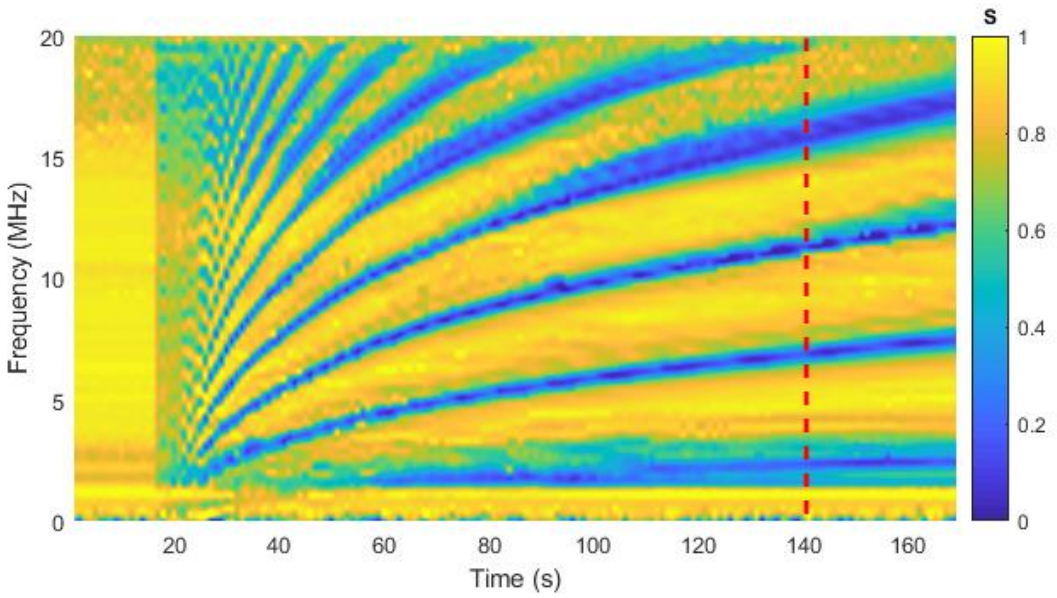

Figure 9-13. Colour plot showing intensity of the *S* values over the duration of the experiment for S3 oil sample. Resonant dip frequencies are observed as blue striations. The *S* profile at 140 second mark (red-dotted line) is shown in Figure 9-12.

During the first 15 seconds there was no oil on the surface and the *S* colour plot shows values approaching 1 across the frequency spectra. After 15 seconds the oil was deposited directly on the surface and was impinging at the region of sensitivity. It was observed that there was some distortion for around 5 seconds until around the 20 second mark in the S colour plot where the superimposed resonances had not been fully formed. This was because the sample was still being

deposited on the surface. The waviness of the oil-air interface during the impinging stage affected the ultrasonic measurements and it has been previously reported that ultrasound technique is not suited to wavy films [109]. After all the sample had been deposited, the resonant dips began to take form and were clearly visible as evidenced by the shades of the blue striations. The frequency difference between the individual striations showed an increase as the experiment progressed which signified a decrease in the localised film thickness. The frequency difference between adjacent resonant dips was averaged as shown in Figure 9-14.

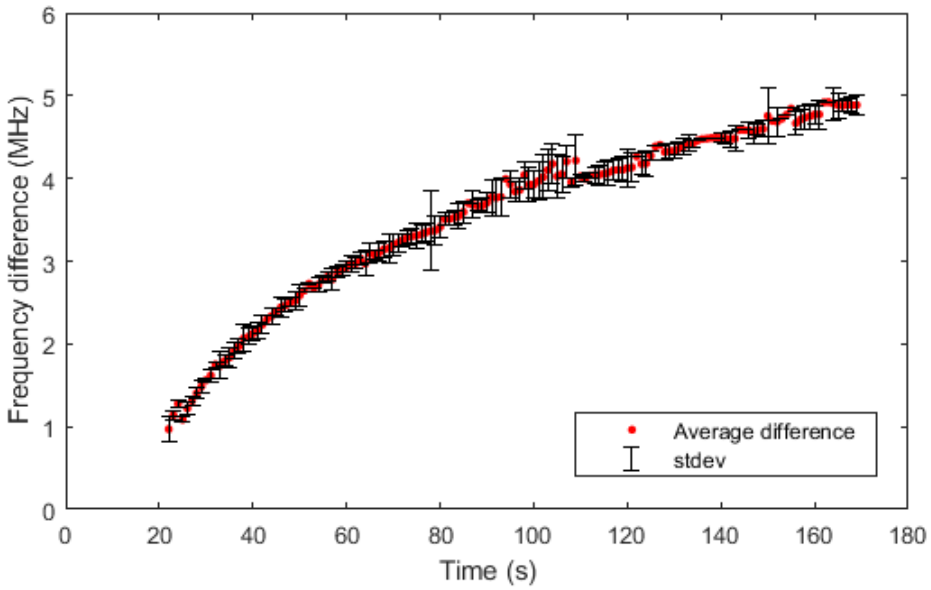

Figure 9-14. The average difference between the resonant dips for S3 sample the duration of the experiment.

The vertical error bars represent the standard deviation in the adjacent dips separation. It was observed that the average difference between the adjacent resonant dips increased as the sample spread across the surface. The averaged frequency difference between the peaks increased from 1MHz to 4.9MHz. The averaged frequency difference was halved to yield the fundamental frequency, f_0 and the oil film thickness, h was calculated using Equation 3-52 where the speed of sound in the oil sample, c was assumed as 1450 m/s. The oil film thickness was then plotted as shown in Figure 9-15.

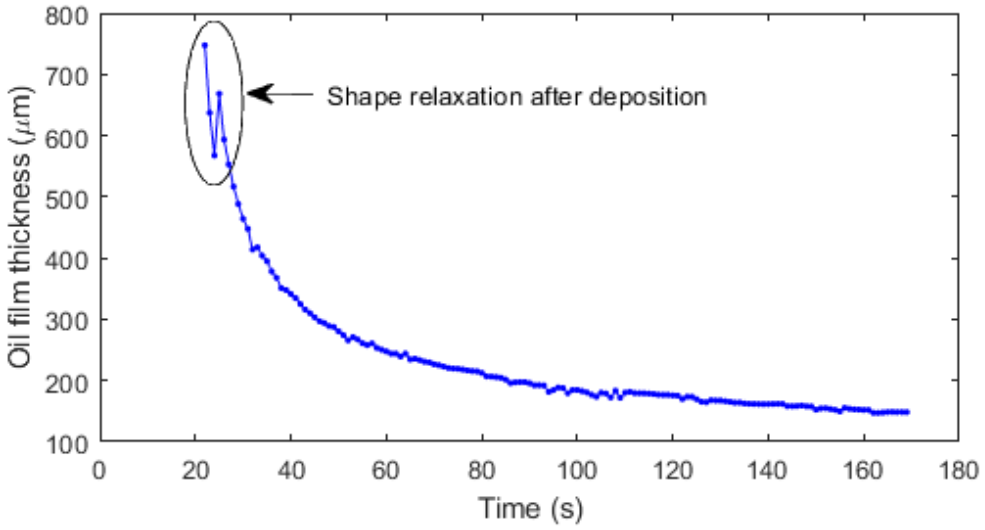

Figure 9-15. The change in oil film thickness of S3 oil sample during spreading conditions.

The initial detectable film thickness was calculated as 748µm. The calculated thickness then dropped to 567µm two seconds after this before rising to 668µm at the 25th second time stamp after which the thickness showed a gradual decrease to 148µm at 170 seconds. The thickness reduction and increase for a duration of 3 seconds between the 22nd and 25th second time stamps was thought to be caused by a shape relaxation of the sample after deposition on the surface due to viscoelasticity.

This relaxation of shape phenomenon has been reported by Jung et al. [110] where they investigated the evolution of a 30µm diameter drop of polystyrene solution impinging perpendicularly on a glass substrate that was coated with indium tin oxide. They captured sequential images to show the drop evolution during the impact and spreading stages. The images they acquired are shown in Figure 9-16.

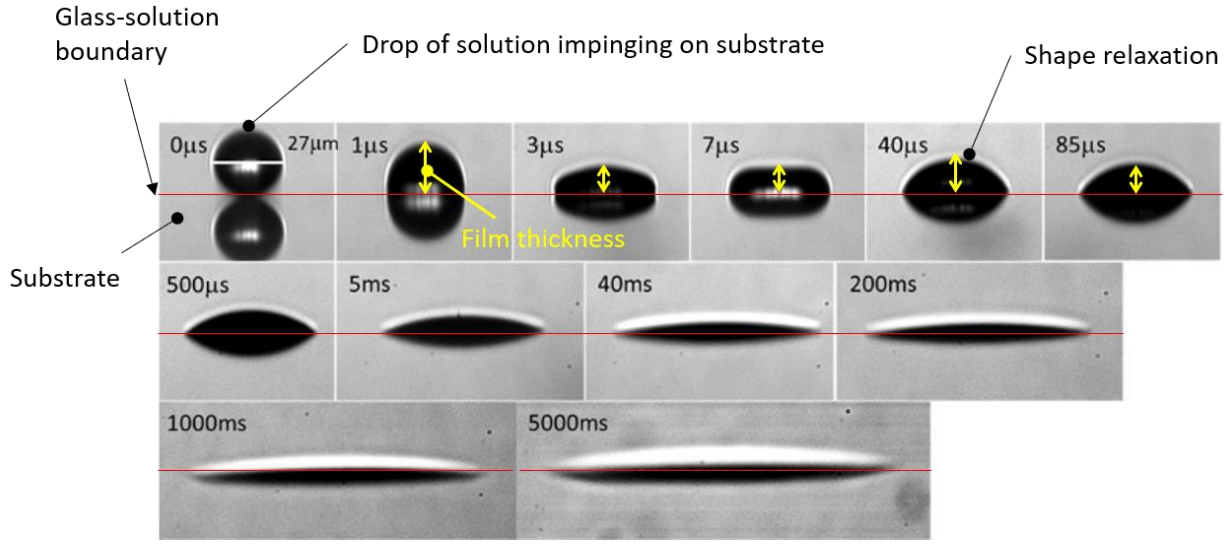

Figure 9-16. Annotated sequential single images that show the evolution of a drop of polystyrene solution impinging perpendicularly on a glass substrate that was coated with indium tin oxide for a duration of 5 seconds (Images extracted from [110]).

From Figure 9-16, it was observed that after the drop collided with the treated glass substrate the drop formed a film that assumed a dome shape as seen at 1μs. The film thickness then reduced as all the kinetic energy was used up and the sample had spread to form a flat disc shape as seen at 7μs. At this point the spreading had reached a maximum and paused briefly where the shape experienced a relaxation that made the film thickness to momentarily increase. This transition in the film thickness was evidenced in the images at 7μs and 40μs. The film thickness then continued to decrease steadily due to capillary effects until reaching an equilibrium after 5 seconds.

The findings from the polystyrene impinging on the treated glass substrate can therefore be used to explain the initial film thickness behaviour that was observed in Figure 9-15. Immediately upon deposition, the S3 oil sample bulk volume collided with the aluminium substrate. This kinematic phase lasted for around 5 seconds after which all the oil sample had been deposited on the surface. Afterwards, the oil-air interface was not wavy anymore and the oil sample was detectable as evidenced by the blue striations as shown in Figure 9-13. The sample was thought to assume a dome shape at the first measurable film thickness. The sample continued to spread after all the kinetic energy had been used for roughly 2 seconds and assumed the shape of a flat disc. The spreading was assumed to have stopped momentarily where the shape of the sample experienced a relaxation in shape and then underwent further spreading because of capillary effects.

The localised film thickness evolution of the Cannon™ oil samples is shown in Figure 9-17.

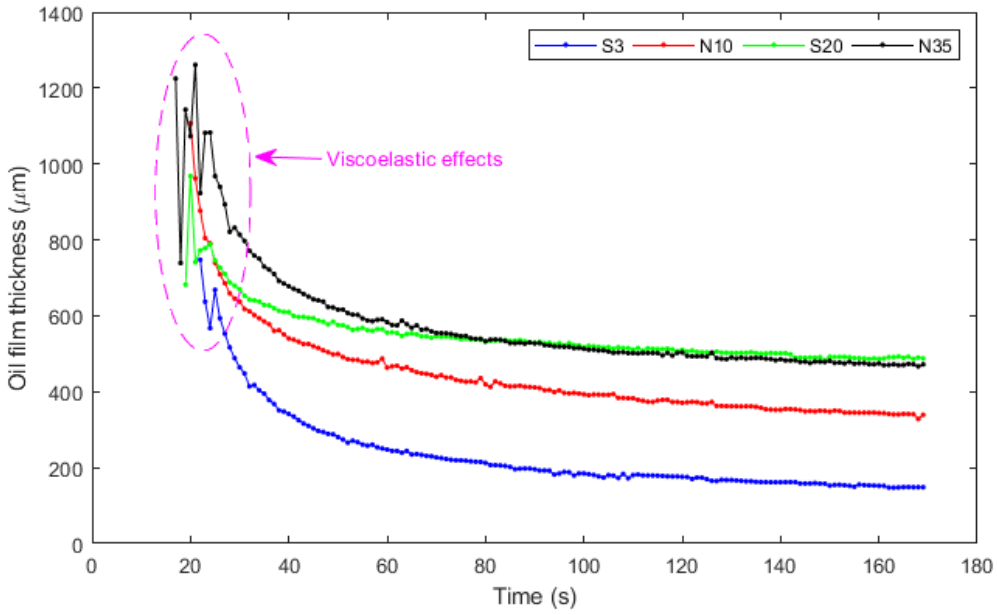

Figure 9-17. Cannon™ oil samples localised film thickness evolution during spreading conditions.

The shape relaxation effects due to elasticity were clearly observed for the rest of the samples as shown in Figure 9-17. The N35 sample showed the greatest effect of viscoelasticity where the phenomenon lasted for 6 seconds. It is thought that the shape underwent relaxation twice which would account for the film thickness behaviour at the initial stages during spreading. The N35 sample was the most viscous. The film thickness for N10 reduced from 1107μm to 339μm after

170 seconds. N35 sample reported the largest thickness measured upon deposition on the surface and the film thickness reduced from 1261µm to 472µm after 170 seconds whereas the S20 film thickness reduced from 968µm to 488µm after 170 seconds. These trends are summarised in Table 9-5.

Table 9-5. Mineral oil localised film thickness trend.

Sample	η at 25°C, mPa.s	Initial film thickness (µm)	Film thickness after 40 seconds (µm)	Film thickness at 170 seconds (µm)
S3	3.3	748	341	148
N10	16	1107	540	339
S20	29	968	610	488
N35	56	1261	678	472

The experimental data has shown that the viscoelastic properties of a liquid affect the localised film thickness measured immediately after impinging perpendicularly on a substrate. The experimental data also showed that viscosity affects the spreading of an oil sample on a surface and the more viscous an oil sample the less the sample spread on a free surface. This was evidenced by higher localised film thickness measured at the end of the experiment for the samples with higher viscosities.

9.7 Specialised Lubricants Performance

9.7.1 Measurement Procedure

The test block was placed on a flat surface and a spindle level was used to ensure a horizontal level. The top surface was cleaned using isopropanol solution and left to dry at ambient room temperature. For a solid-ML-air boundary condition, ultrasound responses were acquired for 30 seconds for both shear and longitudinal sensors. The liquid samples were weighed using an analytical balance and then deposited on the matching layer at a distance 10mm from location 1 (see Figure 9-1). The ultrasound signals were acquired simultaneously across the four locations as the fluids spread on the matching layer. A schematic of the fluid spreading across the matching layer is illustrated in Figure 9-18.

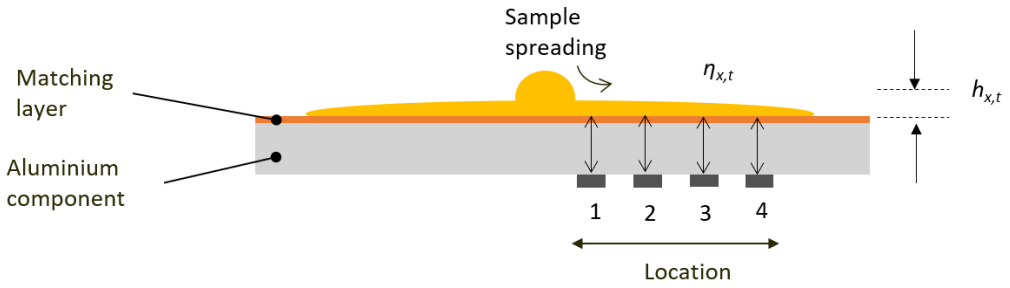

Figure 9-18. Schematic showing a side projection of instrumented aluminium component with fluid spreading on the matching layer.

Standing waves were generated at the four locations using the longitudinal sensor pairs. These were used for thin film thickness measurements. The generation parameters were such that the standing waves were centred at 10MHz with 16MHz frequency span and 2ms sweep time. On the other hand, 3MHz-7MHz 10 cycles chirp waves were pulsed using the shear sensors and the

responses recorded were used for ultrasonic viscometry. For solid-ML-oil boundary conditions, the measurements were recorded for the first 30 seconds of every minute, for 15 minutes at a capture rate of 1Hz. The measurements were performed at room temperature and the temperature of the component was monitored using k-type thermocouple.

9.7.2 Signal Processing

The signal processing steps for the chirp ultrasound responses in obtaining a *R* value to be used for viscosity calculation are demonstrated in Figure 9-19.

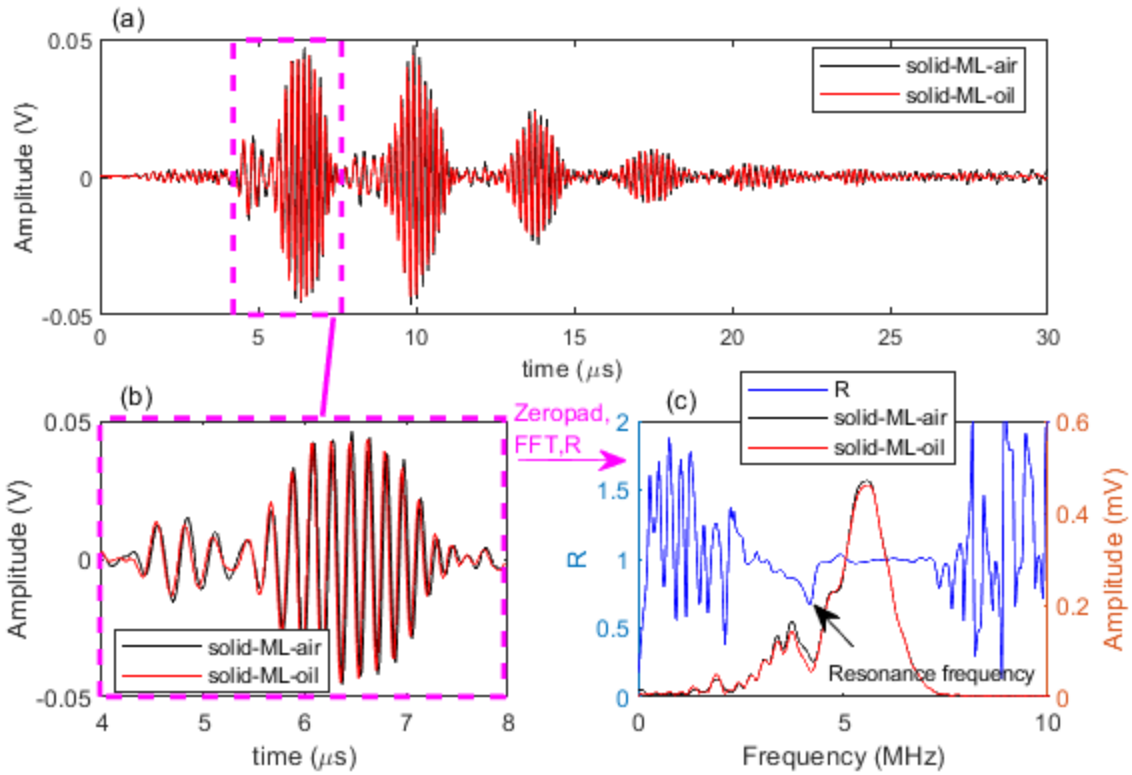

Figure 9-19. Signal processing steps for the viscosity measurements (a) the time domain of the solid-ML-air and solid-ML-oil boundary conditions for a base oil sample showing the reflected echoes at location 1 (b) the isolated echoes (c) the frequency responses of the isolated solid-ML-air and solid-ML-oil echoes after undergoing zero padding and FFT. The *R* spectra is also plotted, and it showed the resonance frequency region observed as a dip in the frequency spectrum.

The first reflected pulse was isolated in the time domain and then zero padded to increase the resolution. A FFT was performed to give the frequency response and a reflection coefficient, *R* (Equation 9-12) was calculated by dividing the solid-ML-oil with the solid-ML-air frequency responses. The magnitude of the resonance frequency observed as a dip was then extracted and used in a power fit model to calculate the viscosity.

The power fit model in Equation 9-14 was rearranged as shown in Equation 9-15:

$$\eta = \left(\frac{R-c}{a}\right)^{\frac{1}{b}} \qquad \text{Equation 9-15}$$

The coefficients *a*, *b*, and *c* from the power fit model for location 1 had the values given in Table 9-6:

Table 9-6. Coefficient values of the power fit model at location 1.

Coefficient	Value
a	-0.038
b	0.570
c	0.984

The *R* value at the resonance frequency region was identified as 0.6744. It was then converted to a η value using Equation 9-15 to give 38.9 mPa.s.

For the standing wave measurements, the solid-ML-air and solid-ML-oil time domain ultrasonic responses were converted to frequency domain by performing FFT. The reflection coefficient, *S* was calculated by dividing the solid-ML-oil with the solid-ML-air frequency responses. Figure 9-20 shows the *S* spectrum that identified the oil film resonant frequencies as dips.

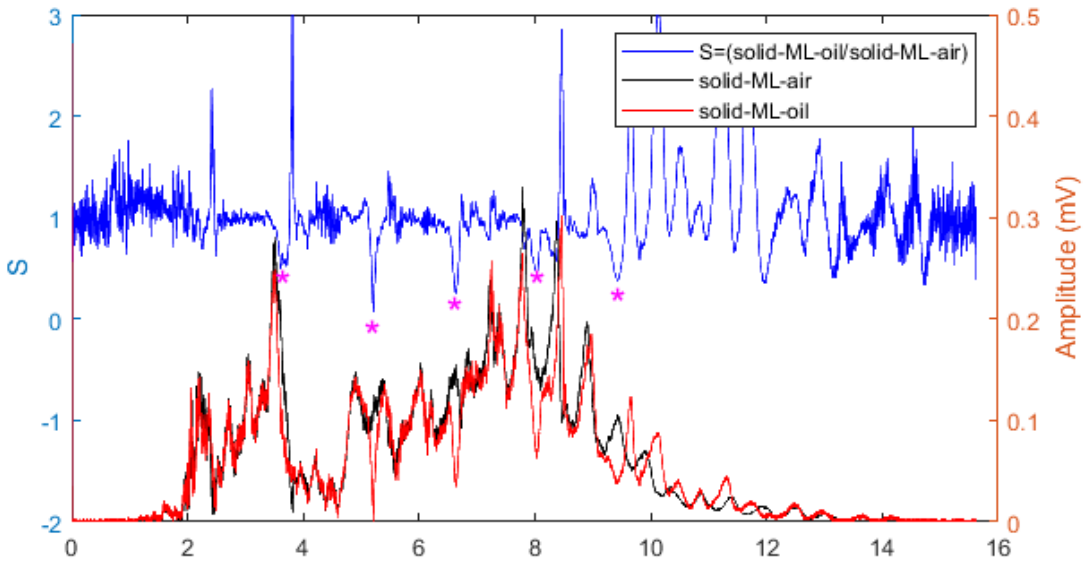

Figure 9-20. Standing wave frequency responses for solid-ML-air and solid-ML-oil boundary conditions with the associated *S* spectrum for base oil sample. The thin oil film resonant frequencies observed as dips in the S spectrum have been highlighted by *.

The differences between the adjacent resonant dips were calculated and then averaged. The fundamental frequency ,f_0 was then calculated by dividing this average by two. From Figure 9-20 f_0 was calculated as 0.73MHz. This was converted to a thickness measurement of 498.38µm using Equation 3-52 where the assumption for the speed of sound in the oil used was 1450 m/s.

9.7.3 Results

The viscosity and film thickness values for the samples during spreading condition were calculated by following the steps explained in the previous section (section 9.7.2). The results were then collated to show the evolution of the samples during spreading conditions.

The results for the solvents (D40, D60, D80, D95, and D110) are shown in Figure 9-21.

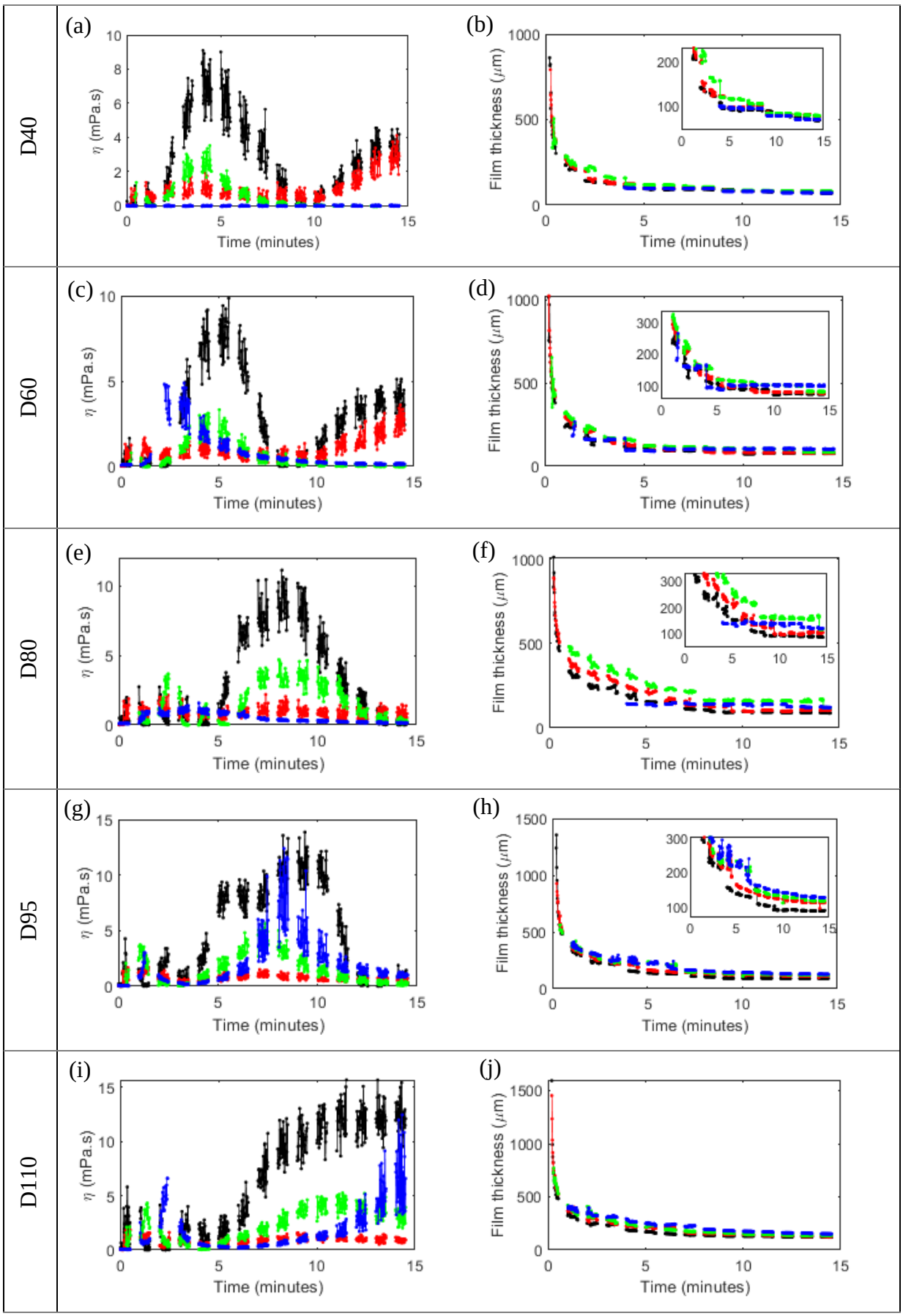

Figure 9-21. Solvents viscosity and film thickness evolution [colour scheme: **black**– Location 1, red-Location 2, green-Location 3, blue-Location 4].

The figures (a), (c), (e), (g), and (i) from Figure 9-21 show the viscosity results whereas the figures (b), (d), (f), (h), and (j) show the film thickness results. From the results shown in Figure 9-21, a trend was observed in the viscosity evolution profiles, particularly for location 1 data. This trend is visualised as shown in Figure 9-22.

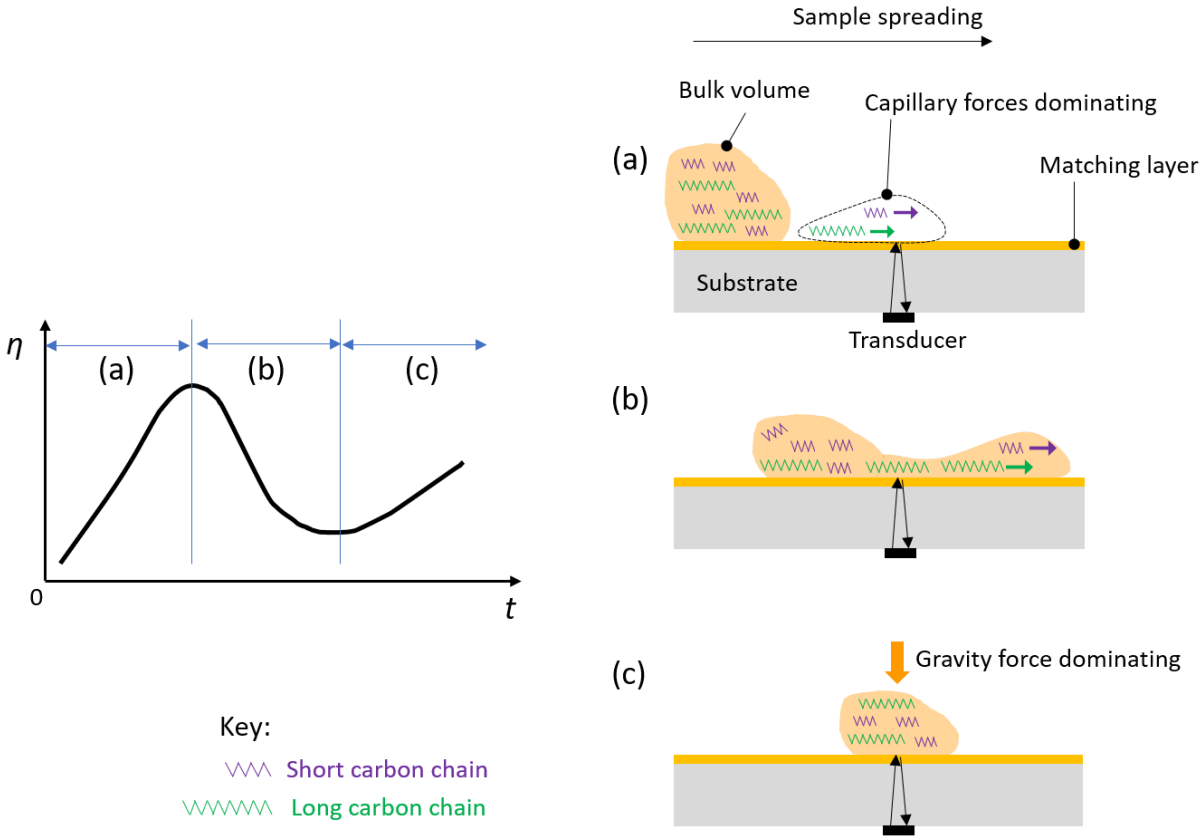

Figure 9-22. A visualisation to represent the viscosity evolution behaviour. (a) The capillary forces dominate over the viscous forces and the lighter components travel faster (b) The components are dragged to other sensors (c) Gravity force dominates and components settle on matching layer.

The viscosity profiles were visualised to have three distinct parts as illustrated in Figure 9-22. The first part represented as (a) from Figure 9-22 showed a gradual increase in the viscosity up to a maximum point. During this stage, it was hypothesised that the capillary forces dominated over the gravity forces [111]. This caused the lighter components that had short carbon chains to flow faster than the longer carbon chain components as the sample crossed over the matching layer at the region of ultrasound sensitivity which was at a position perpendicular to the shear sensors. Over time, the sample viscosity increased as more components within the penetration depth regime crossed over the sensor eventually reaching a maximum. The second part represented as (b) showed a gradual decrease in viscosity During this stage, it is thought that the some of the sample components within the penetration depth regime began to flow beyond location 1 causing the viscosity measured to decrease gradually up to a minimum. The third part represented as (c) showed that the viscosity began to gradually rise at a less steep incline compared to the first part (a). It is hypothesised that gravity was the dominating force at this stage and the rest of the components from the bulk volume were now settling on the matching layer.

Using the visualisation explained in Figure 9-22, the solvents viscosity experimental data shows that the transition point at the apex between part (a) to part (b), where the viscosity was at its maximum, was dependent on the carbon chain components. The longer the carbon chain content in the solvent the longer the time it took to reach this apex, particularly at location 1. This implies that the longer carbon chains flowed slower due to capillary effects than the shorter carbon chains. The D80 sample arrived at location 4 longitudinal sensors much later than at the shear sensors. It was visually observed that there was an uncovered area over the longitudinal sensors during the first three minutes as shown in Figure 9-23 after which the sample then spread to cover the area.

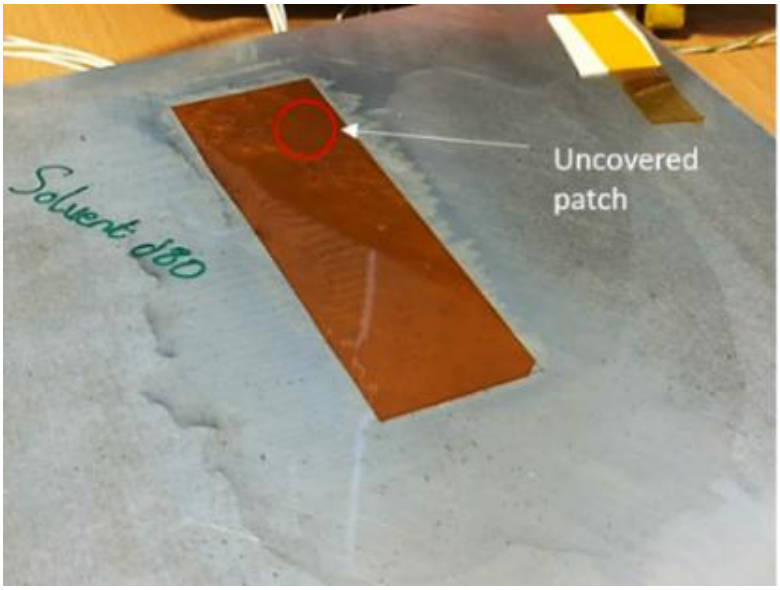

Figure 9-23. Photograph of D80 spreading on the surface at 3-minute mark showing uncovered patch (Photograph taken by author).

The film thicknesses measurements showed a gradual decrease with time. Interestingly however, a step change thickness reduction in the solvents film thickness data was further observed in the decreasing film thickness trend. For example, the film thickness for D40 sample showed a step change in the film thickness reduction at the 4^{th} minute mark for locations 1, 2 and 3. Another step-change decrease was also observed at the 9^{th} minute mark across all the locations. The magnified plot in the D40 film thickness plot from Figure 9-21b shows this trend. This step-change in the film thickness was thought to be caused by the evaporation of the lighter components at the liquid-air interface. This trend was visualised as illustrated in Figure 9-24.

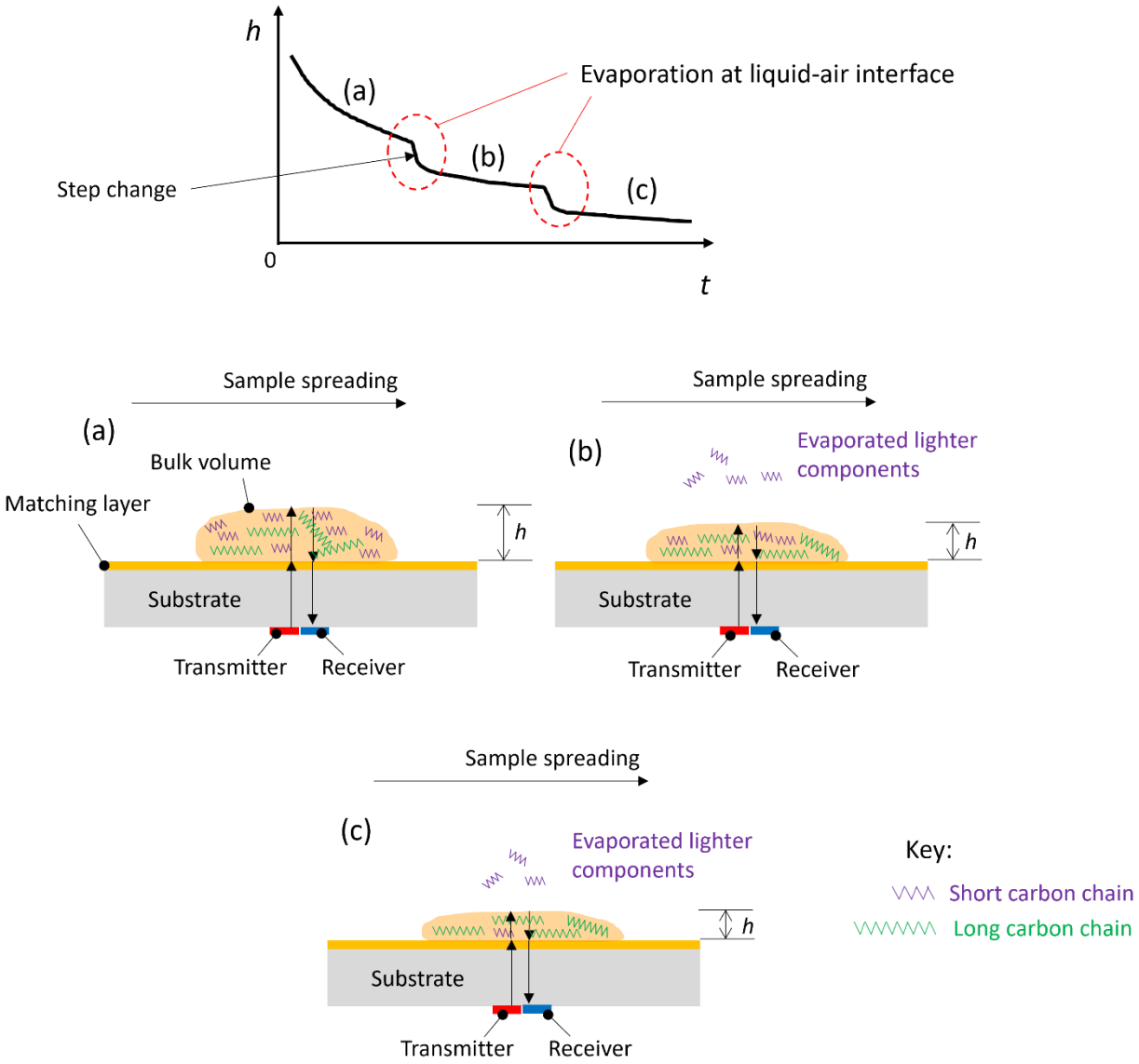

Figure 9-24. Visualisation of film thickness step-change reduction due to evaporation at the liquid-air interface. (a) The localised film thickness reduces due to spreading (b) the film thickness step change occurs due to evaporation of lighter components.

From Figure 9-24 it can be visualised that the film thickness reduction is caused by spreading and evaporation. For the first part (a) the film thickness gradually decreases as the sample is spreading across the surface. The transition between the first part and the second part (b) illustrates a relatively rapid step change reduction in the film thickness. This step change reduction is thought to be caused by the lighter components evaporating from the bulk volume at the liquid-air interface thereby reducing the sample film thickness. The heavier components are drawn to the surface due to gravity and as the lighter components are displaced to the top surface of the bulk volume, further evaporation occurs that was evidenced by a further step change reduction in the film thickness.

The base oil and concentrate results are shown in Figure 9-25.

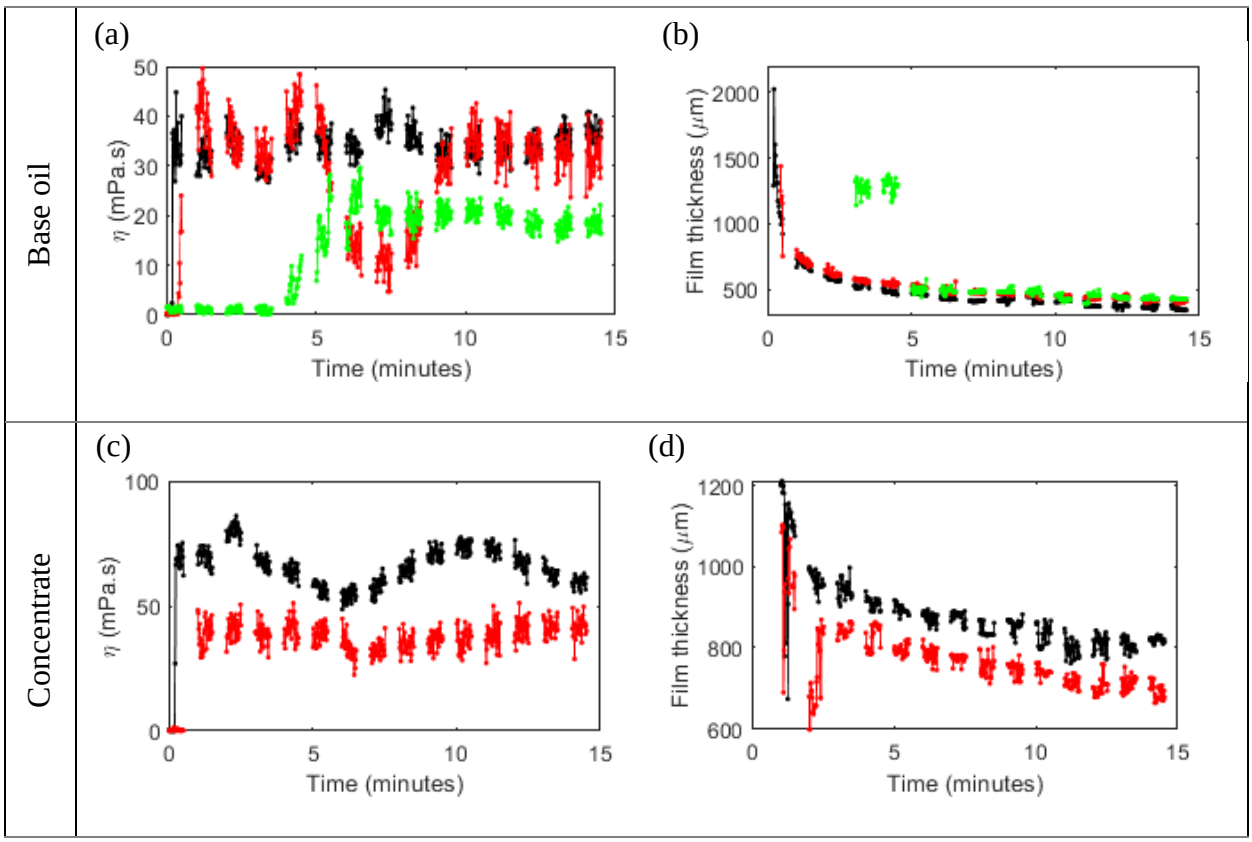

Figure 9-25. Base oil and concentrate viscosity and film thickness evolution [colour scheme: **black**– Location 1, red-Location 2, green-Location 3, blue-Location 4].

The figures (a) and (c) from Figure 9-25 show the viscosity results whereas the figures (b) and (d) show the film thickness results. The base oil viscosity and film thickness calculated earlier (section 9.7.2) as 38.9 mPa.s and 498.38μm respectively were calculated from experimental data at a time stamp of 4 minutes and 10 seconds for location 1.

It was also visually observed that the base oil sample spread laterally along the matching layer and that the radial spreading on the aluminium surface as a whole was negligible. A photograph to show base oil spread after 6 minutes is shown in Figure 9-26.

The temperature of the component during the experiments was monitored using a k-type thermocouple that was attached to a Cooper-Atkins 313 Series Digital Thermometer. The thermocouple was secured at a position on the surface of the component such that it would not disrupt the liquid spreading. A photograph to show this is given in Figure 9-26.

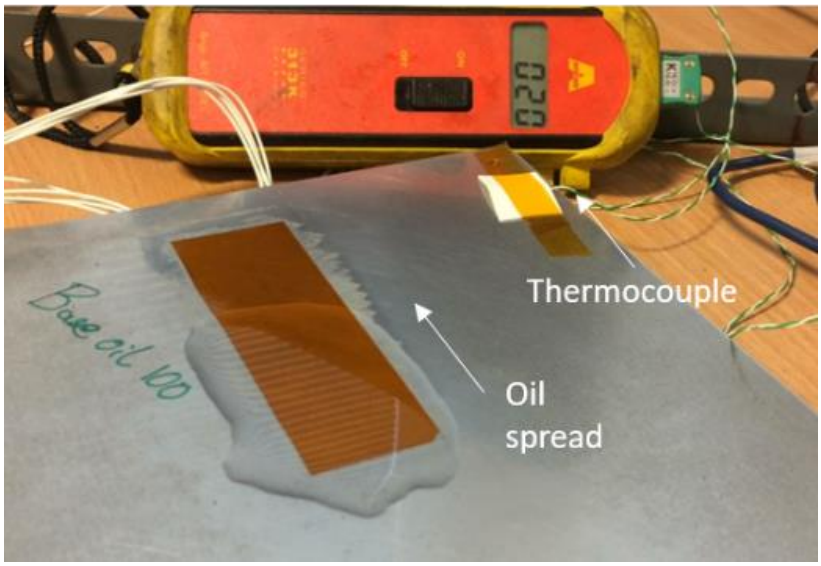

Figure 9-26. Photograph to show spreading of base oil sample on the surface and a k-type thermocouple secured on the component.

The temperature lay mostly in the range 19°C to 21°C during the experiment.

The base oil results show a steep increase in viscosity and oil film thickness when the oil sample reached locations 1 and 2 after 12 seconds and 30 seconds, respectively. However, the viscosity measurements at location 3 showed a gradual increase whereas the film thickness measurement at the same location was almost instantaneous. The base oil viscosity trends could also be explained using the visualisation shown in Figure 9-22. The gradual viscosity decrease observed at location 2 coincides with the gradual viscosity increase at location 3. It is thought that the components flowing from location 2 and on to location 3 at the penetration depth regime was a possible cause for this. The base oil and concentrate viscosity profiles at location 1 showed some similarities.

The concentrate thickness at location 2 reduced then increased in the time interval 1-3minutes. A possible cause of this could be the presence of air bubbles in the sample. These were observed in the sample and a photograph of the same is shown in Figure 9-27.

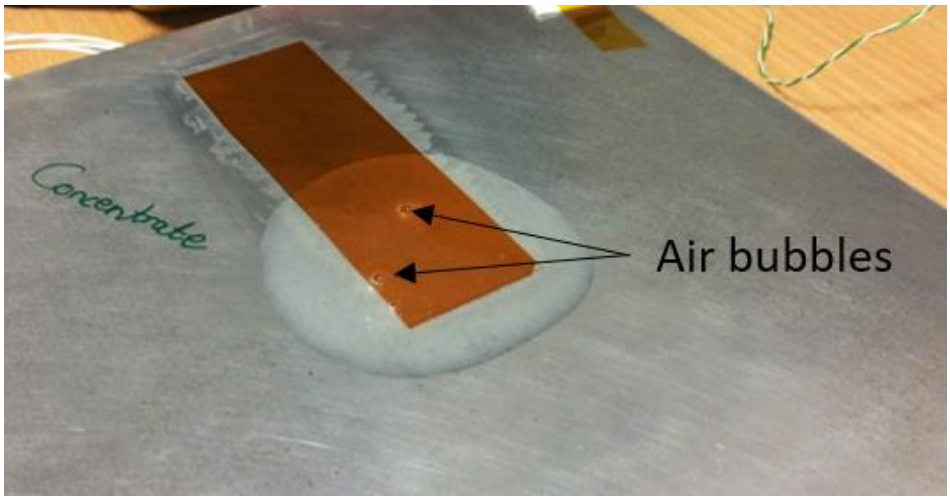

Figure 9-27. Photograph of the concentrate spreading on the surface.

Air bubbles were created by a sucking effect when the oil sample was being transferred from the concentrate-holding jar via a pipette and onto the weighing boat. The high viscosity and surface tension properties of the oil enabled the bubbles to remain in the sample. After deposition, an air bubble on the liquid surface began to flow towards location 2. A visualisation of an air bubble in a bulk volume and how it affects ultrasonic measurement is illustrated in Figure 9-28.

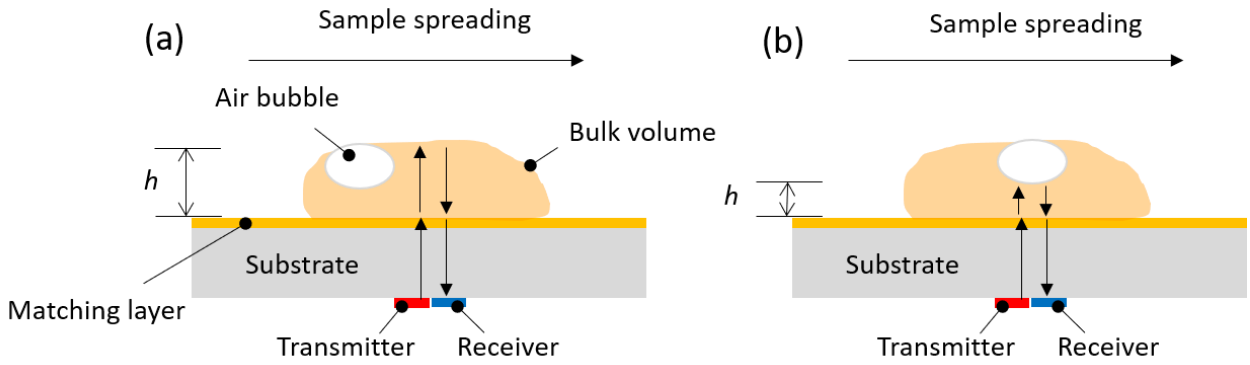

Figure 9-28. A visual representation of an air bubble in the bulk volume of a concentrate sample and how it affects ultrasonic measurement.

As the bulk volume is flowing across the matching layer, the air bubble that is trapped at the surface has not arrived at the ultrasonic sensitivity location. When the air bubble now arrives at the location as a result of the sample spreading as visualised in Figure 9-28, the air bubble causes ultrasound scattering [112]. This means that the frequencies that cause resonance within the layer between the air bubble and the liquid-substrate interface are changed. As a result the liquid fundamental frequency, f_0 is increased indicating a reduction in the film thickness. After the air bubble has crossed the location, the film thickness, h increases. It is thought that this phenomenon is what caused the concentration at location 2 to momentarily reduce then increase.

The viscosity and film thickness results for the WD40 formulation products are shown Figure 9-29 and Figure 9-30.

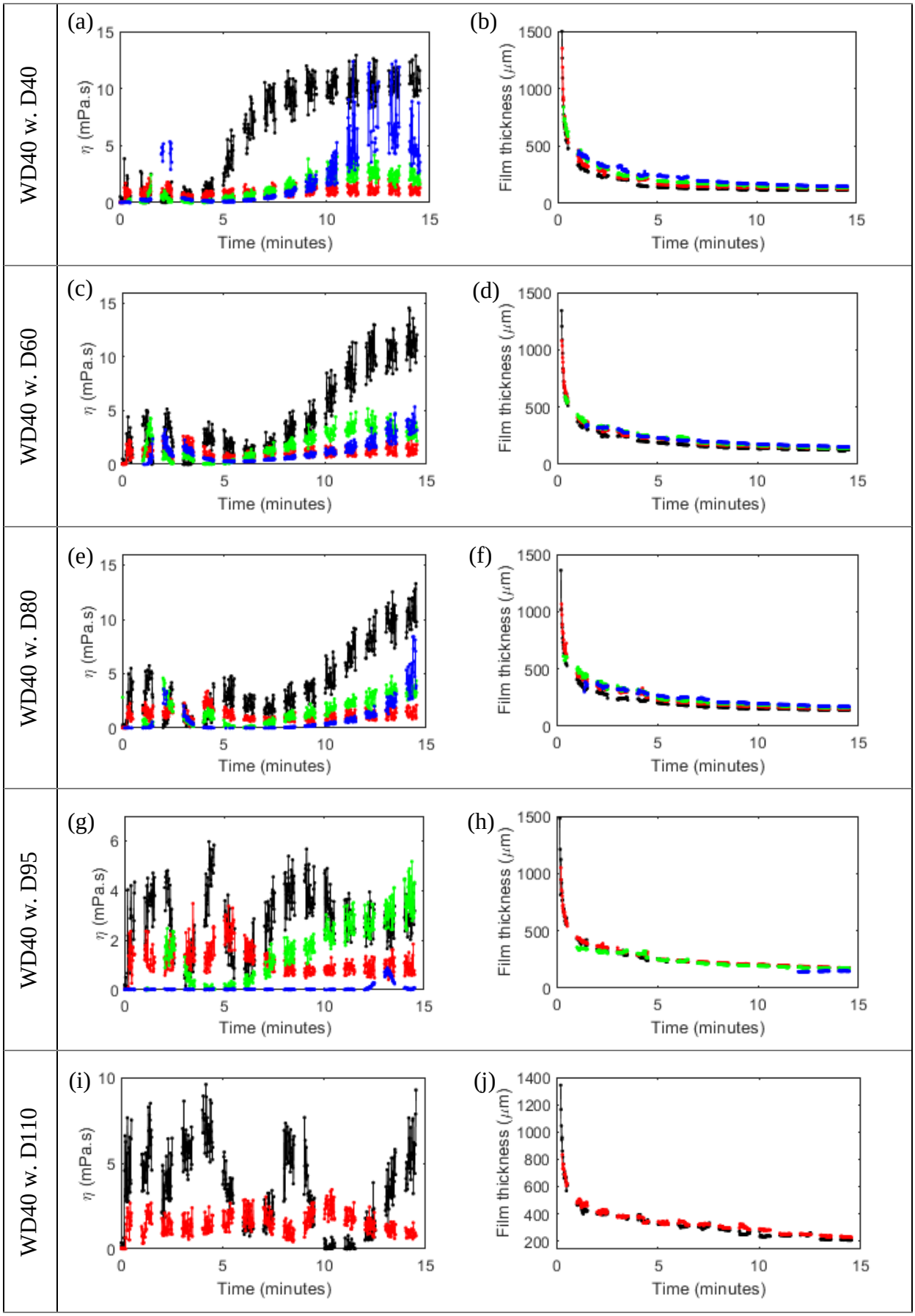

Figure 9-29. WD40™ formulated viscosity and film thickness evolution [colour scheme: **black**–Location 1, red-Location 2, green-Location 3, blue-Location 4].

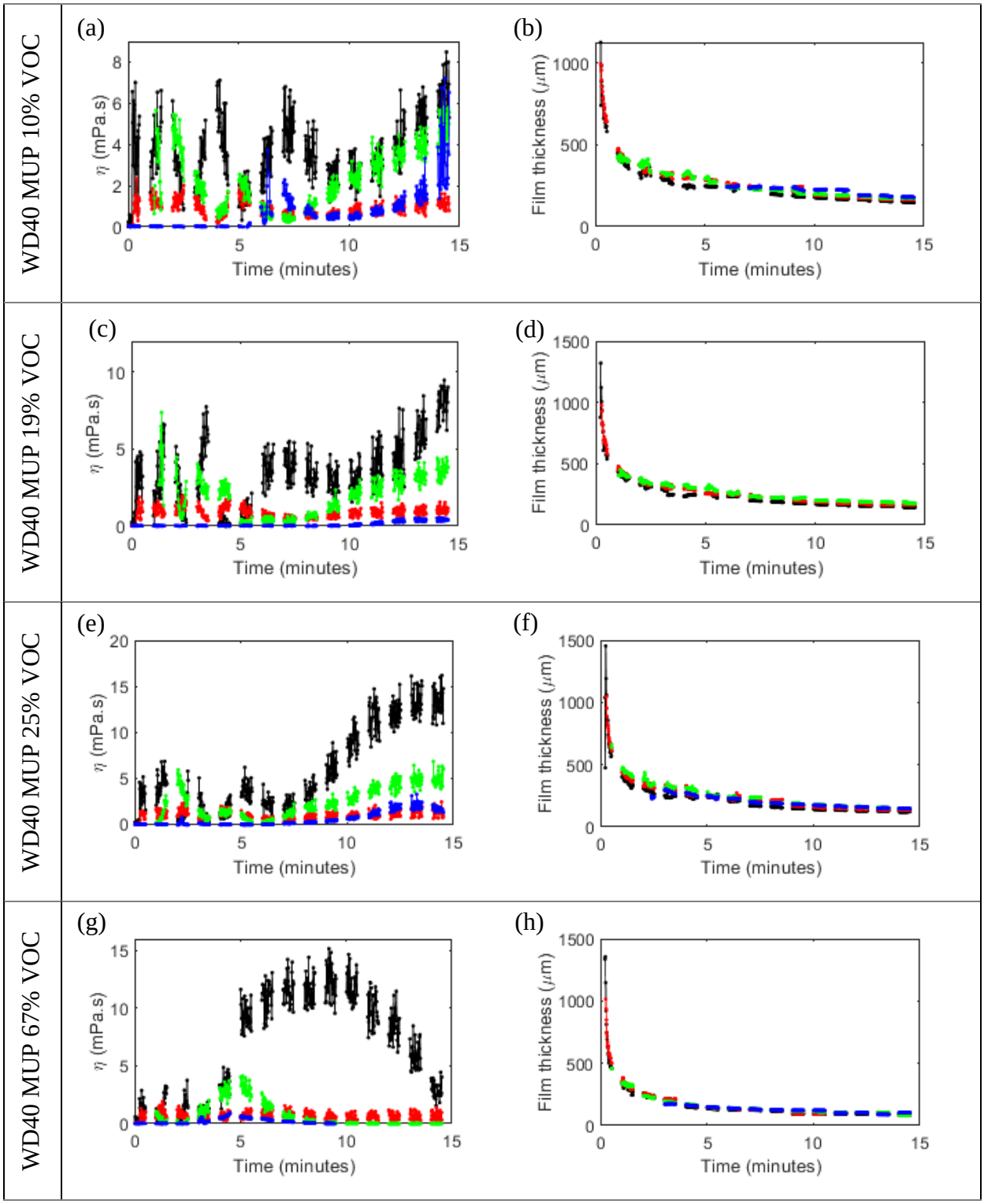

Figure 9-30. WD40™ formulated viscosity and film thickness evolution [colour scheme: **black**–Location 1, red-Location 2, green-Location 3, blue-Location 4].

The trend visualised in Figure 9-22 could also be used to explain the viscosity trends observed in the formulated products in Figure 9-29 and Figure 9-30. The greater the carbon chain length in the volatile content in the mixture the later the apex between parts (a) and (b) was arrived as visualised in Figure 9-22. However, some strange trends were observed particularly in the viscosity profiles at location 1 for some. For example, WD40 w. D95 sample showed that the viscosity experienced erratic behaviour for the first five minutes before assuming the shape of part (a) from the

illustration shown in Figure 9-22 where the viscosity gradually increased to its maximum. It is not entirely certain at this point what causes this. A possible explanation could be presence of impurities and degradation of the mixture. This erratic behaviour was also observed in WD40 w. D80, WD40 w. D110, WD40 MUP 10% VOC, WD40 MUP 19% VOC, and WD40 MUP 25% VOC samples.

9.8 Discussion

The results shown in the previous section report on the viscosity and film thickness evolution of various solvents and formulated products during spreading conditions. The results have been explained using capillary, evaporation, and gravity effects schools of thought. A summary of key results from the previous section are shown in Table 9-7.

Table 9-7. A summary of the key penetrant and solvent viscosity and film thickness results during spreading conditions.

Sample	Furthest location & (arrival time)	Viscosity (location 1)		Film thickness (location 1)	
		Min. η (mPa.s)	Max. η (mPa.s)	Initial. h (μm)	h at end of experiment (μm)
D40	4 (4 minutes)	0.25	9	862	70
D60	4 (1.5 minutes)	0.25	9.5	1016	77
D80	4 (2 minutes)	0.25	12	1014	88
D95	4 (2 minutes)	1	14	1355	91
D110	4 (2 minutes)	1	15	1593	123
Base Oil 100	3 (3 minutes)	24	50	2024	343
Concentrate	2 (2 minutes)	55	85	1212	821
WD40 w. D40	4 (1 minute)	1	13	1498	119
WD40 w. D60	4 (1.5 minutes)	2	15	1341	127
WD40 w. D80	4 (1.5 minutes)	1	12	1360	143
WD40 w. D95	4 (13 minutes)	1	6	1483	173
WD40 w. D110	2 (0.5 minutes)	0.25	9.5	1343	208
WD40 MUP 10% VOC	4 (5 minutes)	1	8	1125	152
WD40 MUP 19% VOC	4 (10 minutes)	0.5	9	1321	146
WD40 MUP 25% VOC	4 (2 minutes)	1	15	1453	127
WD40 MUP 67% VOC	4 (3 minutes)	1	15	1356	91

The results shown in Table 9-7 only report the viscosity and film thickness measurements at location 1. This location was chosen as a reference point because the viscosity and film thickness properties at the other locations were dependent on the events that occurred at location 1. That is to say, for example, a least film thickness at the end of the experiment (after 15 minutes) at location 1 would imply the least fluid motion resistance therefore the sample would spread further to the other locations. The viscosity calibration at location 1 also showed a better data fit with a power model as compared to the other locations.

The solvents (D40, D60, D80, D95, and D110) reported the lowest film thicknesses at the end of the experiment with D40 reporting the lowest film thickness of 70μm amongst the solvents. The maximum measured solvent viscosities were shown to increase with increasing carbon chain content in the mixture. The viscosities showed a correlation to the initial film thicknesses and the thicknesses at the end of the experiment where the least viscous sample showed the lowest measured film thickness.

The maximum solvents viscosities differed from those given by the manufacturer. The kinematic viscosities provided by the manufacturer are usually performed by measuring the time it takes for a liquid sample to flow, under gravity, in a calibrated glass capillary viscometer. These tests are performed very carefully and under strict laboratory conditions and ASTM D445 is the industry standard that is usually adhered to [113]. The manufacturer values only gave typical viscosity values, and these values were susceptible to change over time and do not usually constitute specification limits. However, the measured solvents viscosity range was shown to accommodate the manufacturer viscosity values and the discrepancies identified could have been caused by a degradation of the samples over time.

In most cases, where there had been a step-change reduction in the film thickness trends, a viscosity change was also reported. The film thickness measurements step change were thought to be caused by evaporation of lighter components at the liquid-air interface. This was thought to cause the change in the bulk viscosity.

Although the temperature monitored during the experiment did not change much, the measured temperature range was identified to affect the evaporation of the solvents from the surface. The solvents evaporation rate increased with decreasing viscosity therefore the high D40 evaporation rate indicated that the lighter components would evaporate faster at the solvent-air interface thereby causing a greater reduction in the film thickness during a spreading condition. The solvents evaporation rates could also account for the difference between the manufacturer viscosity values and those measured ultrasonically. Over time, the solvents in their storage containers could have evaporated when the caps were opened in order to retrieve the samples. Some humidity could also have been absorbed by the solvents during the process of opening the storage containers which would compromise the solvent viscosity.

From the results, it was observed that base oil and concentrate viscosity was proportional to the film thickness at the end of the experiment.

Also, the difference observed between the measured base oil viscosity and that obtained from the manufacturer could also be explained by base oil degradation. Nonetheless, the measured base oil viscosity range accommodated the manufacturer viscosity value.

The WD40 w. D40, WD40 w. D60, WD40 w. D80, WD40 w. D95, and WD40 w. D110 samples showed a general viscosity decrease from 13 mPa.s to 9.5 mPa.s with increasing number of carbon chain content in the constituent VOC that makes up the sample. The film thicknesses calculated at the end of the experiment showed an increase with increasing number of carbon chain content in the constituent VOC. The WD40 w. D40 sample had a film thickness of 119μm at the end of the experiment whereas WD40 w. D110 reported a film thickness of 208μm.

The WD40 MUP 10% VOC, WD40 MUP 19% VOC, WD40 MUP 25% VOC, and WD40 MUP 67% VOC results showed that the maximum viscosity increased with increasing D40 content in the sample. The film thickness measured at the end of the experiment decreased with increasing D40 content in the sample.

The furthest location where viscosity and film thickness measurements could be detected and monitored were proportional to the sample viscosity with the concentrate having only arrived at location 2 and base oil at location 3. The rest of the samples arrived at location 4 with the exception of WD40 w. D110 whose flow was affected. The times at which the samples arrived at the furthest locations could not be correlated with their viscosities because the spreading dynamics were not constant. The step-change between the top surface of the matching layer and the component surface (approximately 50μm) could also have interfered with the sample spreading. Although the surface of the matching layer and the component were made to be as visibly smooth as possible, there still could have been some portions on the surface that were not smooth and some particles that were not visible to the eye could have been embedded between the matching layer and the component during the bonding process. These could have affected the flow of the samples on the matching layer. Air currents could also have affected how far the samples reached. As a result, accurate spreading rates could not be calculated because of the many variables. It is suggested that future work should be focussed on making sure that the matching layer is embedded on the surface to form a flush finish. A dedicated trough could also be made to ensure a one direction lateral flow of the samples. Future measurements are also suggested to be performed in a fume chamber where there is no air current influence, and the temperature and humidity can be regulated.

The samples, apart from the base oil and the concentrate, showed that the time the measured viscosity achieved a maximum, especially at location 1, depended on the VOC content. The greater the carbon chain content in the VOC, the later the maximum viscosity was achieved. In some cases, especially for those samples with heavier carbon chain content, the viscosity trends indicated that the viscosity would continue to rise even after the end of the experiment. However, the viscosity of samples that contained D95 mixture showed erratic viscosity profiles and it is not entirely certain what caused this. The erratic viscosity profiles that were observed could have indicated the movement of molecules over the matching layer, or settling on the matching layer, or both. The molecules that were able to be excited depended on the ultrasound frequency with larger molecules being excited by low frequency and vice versa. Therefore, the viscosity profiles could have indicated the movement of molecules that were only excited by the frequencies in the chirp wave in the MHz range.

The results from a trapped oil sample film thickness measured using a standing wave method showed a good correlation with shim thickness. The difference between the ultrasonic measurements and shim thickness increased with increasing film thickness and it is hypothesised

that one cause of this is that the two metals that bound the oil samples were not entirely planar which would have caused uneven distribution of the oil sample. The shim thicknesses also had manufacturing tolerances that increased with increasing shim thickness and this could have affected the ultrasonic thickness measurement of the oil film in the gap. The speed of sound in the oil was assumed to be constant, however, this could also have changed with increasing film thickness. The presence of additives could also have affected the speed of sound estimation. The experiment was carried out at room temperature and therefore the temperature effects were assumed to be negligible. The pressure applied using the clamps was not entirely even and this could have caused some of the errors that were observed. Nonetheless, the standing wave method has shown great potential in measuring a trapped liquid film thickness with a good correlation observed with shim thickness and a standing wave method can be applied to measure a liquid film thickness on a free surface.

The results from the S3, N10, S20 and N35 localised film thickness measurements on a free surface showed that the film thickness spread was directly related to the sample viscosity. The experiment was carried out at ambient temperature and pressure and therefore the temperature effects were assumed to be negligible. The effect of a relaxation of shape was identifiable in the results. The film thickness spread was quantified by the measuring the film thickness at the end of the experiment. The S3 sample, which had the least viscosity, showed the least film thicknesses at the end of the experiment.

The viscosity measurements were limited by the viscosity of the standard mineral oils used during calibration. The actual temperature of the mineral oils when performing the calibration measurements could have differed from that of the room temperature which in turn could have affected the viscosity calculated using the Vogel equation. The viscosity measurements were also limited by the integrity of the mineral oils and with the assumption that the lubricants were Newtonian. The calibration measurements were measured when the mineral oil samples were stationary and therefore did not accommodate for a liquid in motion.

The speed of sound in the samples was assumed to be constant at 1450 m/s and at room temperature, although in practice this is not the case. Even though the component temperature was monitored, the actual temperature of the sample on the surface could have been different due to possible heat absorption from air. It was difficult to monitor the actual sample temperature on the surface without affecting the flow of the sample. A k-type thermocouple was used to monitor the component temperature, but at a location far away so as not to cause any flow disturbances. The individual samples speed of sound would have changed with a change in temperature especially for the solvents. As the solvents evaporated at the liquid-air interface, some heat was lost in the process as a result of conversion of the liquid from liquid phase to a gas phase. As a result, the temperature of the liquid decreased causing a reduction in the bulk temperature. This could have affected the speed of sound in the sample.

The lowest measurable film thickness of 23μm was limited by the upper frequency limit of 16MHz, with the assumption of good signal-to-noise ratio. There was no limit on the maximum measurable film thickness. The film thickness measurements were limited to the assumption of a constant speed of sound at constant temperature.

9.9 Conclusions

The viscosity and film thickness of specialised lubricants and solvents spreading on a surface were measured using ultrasonic methods. The viscosities lay in the range 0.25 mPa.s to 85 mPa.s whereas the film thicknesses lay in the range 70μm to 2024μm. It was observed that the liquid viscosity was proportional to the film thickness measured at the end with the most viscous sample having the greatest measured film thickness at the end of the experiment.

The measured viscosity values from the solvents and the base oil were different from those obtained from the manufacturer. It is thought that a cause for this was sample degradation over time. However, the measured viscosity range was found to have accommodated the manufacturer values. On the other hand, there was no reference point from which to compare the measured ultrasonic viscosity values for the formulated products that were comprised of a concentrate and solvent mixture. Nonetheless, because they were made up of base oil and solvents, the base oil and pure solvents viscosity profiles served as a reference point from which to draw comparisons.

The measurements were performed in open air and therefore the air currents in the room could have affected the evaporation of solvents at the liquid-air interface. It is suggested that the experiment should be carried out in a fume cabinet in order to control both the air temperature and air currents.

Despite the aforementioned disadvantages, the standing wave has shown potential that, when used alongside shear ultrasonic viscometry, it can be used to assess the performance properties of penetrants and solvents. As mentioned in the previous chapters, the standing wave method has been shown to increase measurement sensitivity compared to the conventional pulse echo method. It also has less signal processing times in the extraction of the liquid resonant frequencies. The measurement concept demonstrated could therefore be optimised and miniaturised in-house then later used to develop commercially viable instruments.

10 Conclusions and Future Work

10.1 Surface Coating Thickness Measurement Using A Standing Wave Method

The first aim of this research was to measure the thickness of an epoxy layer on an aluminium substrate using a standing wave method. A planar epoxy layer was cured on a 10mm thick aluminium component at room temperature and a surface profilometer was used to calculate an epoxy thickness of 138.2μm. A superimposed standing wave was formed by continuously sending a repeating chirp. Because of the multiple frequencies in the chirp, multiple peaks were formed in the substrate that correspond to the substrate harmonics. The multiple peaks are used as measurement points effectively increasing the usable bandwidth. A standing wave reflection coefficient *S* was calculated as the ratio of the solid-epoxy to solid-air standing wave frequency responses and the *S* spectrum was used to identify the epoxy resonant frequencies at f_0 = 4.58MHz and $3f_0$ = 13.93MHz that corresponded to a reversal in the phase when a phase difference spectrum was analysed. The phase difference spectrum was calculated by subtracting the solid-epoxy phase angle profile from the solid-air phase angle profile. The difference between the adjacent epoxy resonances was halved to give the epoxy fundamental frequency f_0 and the experimental thickness was calculated as 142.78μm using a quarter wavelength equation, where the acoustic velocity in epoxy was 2670 m/s.

The epoxy resonant frequencies obtained from the standing wave method showed a greater reduction in the resonant frequency mode magnitude than the resonances obtained from the pulse-echo method, signifying increased sensitivity due to the multiple reflections.

Further epoxy coatings in the range 70μm to 350μm were successfully measured using a standing wave method and a comparison between standalone profilometer measurements showed a good agreement. Experimental results showed that the lowest possible epoxy thickness of 35.1μm was limited by the upper frequency limit of the standing wave usable bandwidth. An increase in the epoxy thickness difference between ultrasonic measurements and standalone measurements was thought to be caused by speed of sound inaccuracies.

This chapter therefore presents a novel approach in measuring the thickness of surface coatings and films on substrates using a standing wave method. The standing wave method has demonstrated superiority over conventional pulsed wave method in the resonant frequency magnitude measurement sensitivity and by the extension of the usable bandwidth.

10.2 Development of An Analytical Model to Simulate Standing Wave Frequency Responses

A steady state mathematical model that incorporated a three-layered reflection coefficient was simulated using MATLAB software for a 138.2μm thick epoxy coating on a 10mm thick aluminium substrate. The model relies on fundamental principles of ultrasound standing waves and resonances. Ultrasonic frequencies were simulated for solid-air and solid-epoxy-air boundary conditions and a *S* spectrum was calculated to identify the epoxy resonant frequencies.

The factors that affect the mathematical model were investigated and thinner components were shown to report a reduced number of component resonances observed as peaks. The simulated responses for thinner components showed higher amplitudes due to less attenuation encountered

during wave propagation. The influence of the number of reflections within the component was shown to increase the wave amplitude up to a point where a peak value was attained and increasing the number of reflections beyond this had no significant impact on the wave amplitude. It was identified that the attenuation coefficient normalises out and the measurement of surface coating remains unaffected by the dependence of attenuation coefficient on frequency. The magnitude of the frequency responses, however, is dependent on the material acoustic properties and experimental results showed that the frequency response of an aluminium component had a greater amplitude than that of a similar steel substrate, as expected [45].

The modelled epoxy resonant frequencies and their magnitudes from the *S* spectrum showed a strong correlation with experimental values. A practical application of using the mathematical model would be in simulation scenarios to compare with real data from coatings inside closed vessels. The model could then be optimised to estimate a variety of previously unknown coating physical parameters.

10.3 Measurement Of A Surface Coating At Different Temperatures

The thickness of a steel substrate for a solid-air boundary at different temperatures (24°C to 120°C) was first investigated. The steel resonant frequency was shown to decrease with increasing temperature indicating an increase in thickness. The speed of sound in the steel at the different temperatures was calculated experimentally by considering the steel fundamental frequency and a steel thickness calculated using a linear thermal expansion model. The results were compared to a model that considered a temperature dependence of the speed of sound. A good correlation was observed in the results where the discrepancies were thought to be caused by impurities in the substrate.

Next, the thickness measurement of a cured epoxy coating on a metal substrate at the different temperatures was performed using a standing wave method. The results showed some promising results. The epoxy fundamental frequency showed a reduction with increasing temperature indicating an increase in the epoxy thickness. However, at high temperatures (>80°C), the solid epoxy entered a glass transition regime where the hardness decreased rapidly, and the attenuation increased. The glass transition temperature of epoxy is as low as 90°C. This caused difficulty in identifying the epoxy resonant frequencies at temperatures above 80°C. However, results between the polyimide thickness calculated using a standing wave and a linear thermal expansion showed a good correlation within the temperature range 24°C to 40°C.

Although this study neglected the acoustoelastic effects, it showed some promising results and is suggested that future work needs to be carried out that incorporates a comprehensive expansion model and the acoustoelastic effects. This endeavour could potentially benefit applications where thin coatings are subjected to varying temperatures such as the aviation or marine industry.

The standing wave method could also be improved by reducing the temperature steps during calibration process and increasing the wait times to ensure temperature stability. A calibration process could also be implemented where the substrate is heated first then measurements are recorded as the temperature is cooled.

10.4 Application of A Standing Wave Method for Surface Coating Thickness Monitoring

An investigation was carried out to determine the lowest measurable coating thickness possible using a standing wave. A polyimide layer that was bonded on a steel substrate was ground off to different thicknesses using an industrial grinding machine and the standing wave was used to measure the polyimide thickness during this process. The polyimide thickness was successfully measured as 529.94μm at the start of the experiment to a lowest measurable thickness of 42.49μm. The lowest measurable thickness was limited by the upper frequency limit of 14.24MHz. A comparison with independent micrometer measurements and ultrasonic steel thickness reduction measurements showed a good correlation. The standing wave method has no upper thickness limit.

The standing wave measurements showed greatest sensitivity in terms of the resonant mode magnitudes when compared with pulse-echo measurements. The multiple reflections that interfered within the substrate increased the measurement sensitivity at the interface of interest. This is particularly useful in improving the identification of the coating/film resonant modes.

The standing wave and pulsed wave polyimide thickness measurements showed excellent agreement when compared with a 1:1 exact fit line. Therefore, a standing wave method has shown capability in measuring a surface coating at different thicknesses.

Transducers with higher frequencies can be used to overcome the upper frequency limit. However, the higher the frequency used the more the ultrasound attenuation in the material making this impractical. Higher frequency sensors also have a thinner thickness, and this makes them very fragile. Nonetheless, contemporary technologies such as sputtering can be applied to manufacture thin film elements that have good signal strength and increased measurement resolutions. These can be used for future research work that would aim to extend the lowest measurable coating thickness.

10.5 Development of A Measurement Concept For Penetrants

A measurement concept was developed that was used to monitor the viscosity and film thickness of penetrants spreading on a surface simultaneously. The measurement concept involved a standing wave method to measure the film thickness and a pulse-echo method that measured the viscosity of the liquid. The ultrasonic viscometry method used an acoustic matching layer that increased the measurement sensitivity of the liquid. The measured viscosities lay in the range 0.25 mPa.s to 85 mPa.s whereas the film thicknesses lay in the range 70μm to 2024μm. It was observed that viscosity was proportional to the film thickness measured at the end with the most viscous sample having the greatest measured film thickness at the end of the experiment.

The ultrasonic viscometry results showed the length of carbon chain components in the sample affected the maximum measurable viscosity. The more the number of longer carbon chain components in the mixture the greater the viscosity and the longer it took to reach the maximum viscosity. However, it was difficult to justify some erratic behaviour in the viscosity evolution of some formulated products. Future work should be directed to investigate this.

The standing wave data showed that the evaporation of solvents at the solvent-air interface was detectable. This was evidenced by a step change reduction in the film thickness.

The instrumentation of the test component was rather difficult due to the number of sensors that were bonded as well as the matching layer. Clamping the sensors and particularly the matching layer in order to ensure a robust contact required multiple tries. A perfect contact between the sensors and the solid as well as the matching layer and the solid was practically impossible to achieve and it is thought that the thickness of the adhesive between these contacts could have compromised the measurements to some extent.

10.6 Future Work

The work presented in this research has investigated the fundamental principles of using a standing wave method to measure a surface coating and film thickness on a metal substrate. The experimental results show a good agreement with validation and modelling results and this is evidence that the standing wave method can be practically applied to overcome the sensing challenges that are usually encountered when using conventional pulse-echo methods on engineering surfaces.

The following, although not exhaustive, is a list of recommended future directions arising from this research work:

- Implementation of a high frequency sensor to extend the upper frequency limit of the transducer. Although it appears straightforward theoretically, this method presents setbacks such as high ultrasound attenuation at higher frequencies in most metals and increased fragility when handling high frequency piezoelectric transducers. Therefore the choice of transducer material and signal strength needs to be carefully evaluated. An alternative would be to apply the use of sputtering technology to manufacture these high frequency sensors.
- Development of a method that measures a thin surface coating thickness by analysing the maximum peak separation between solid-air and solid-epoxy frequency responses. It has been shown theoretically in this research work this separation occurs periodically. Therefore it is suggested that an experimental investigation should be carried out that uses the maximum peak separation instead of an amplitude change, or even a combination of both, to measure thin surface coating thicknesses. This could possibly extend the lowest measurable coating thickness without having to use high frequency transducers.
- Because most engineering surfaces are subjected to external stresses and vibrations that would otherwise affect the resonant frequencies of a standing wave within a solid, it is recommended that an investigation into the effect of an external stress and vibration on the formation of a standing wave should be carried out in future. To do this, an instrumented component could, for example, be clamped using a bench vice on the sides. Different forces could then be applied and investigated.
- Development of a method that measures the surface coating thickness and attenuation properties simultaneously using a standing wave. It has already been shown from previous research work [80] that a standing wave can be used to measure the speed of sound and attenuation of liquids inside closed chambers. This presents the possibility of performing a holistic analysis of a surface coating or film using a standing wave method alone by

measuring a variety of parameters. This investigation could potentially lead to the development of a commercially viable method.

- Implementation of a careful temperature calibration method for evaluation of coatings and films on metal substrates at different temperatures. A standing wave method could then be developed to investigate the onset of glass transition temperatures of solid coatings on metal substrates. This would be beneficial in applications where surface coatings on metal substrates are subjected to elevated temperatures. It has been shown from this research work that the coating resonant frequency reduces with increasing temperature. It has also been shown that the amplitude of the resonant frequency from a reflection coefficient plot increases with temperature. The method could then be optimised and implemented to measure both the changing attenuative properties and thicknesses of various coatings on metal substrates.
- In order to fully understand the evaporative effects on a solvent film thickness reduction, it is suggested that the film thickness of a static layer is first investigated. The work in this research has already shown that a step-change in the localised film thickness reduction occurs for solvents spreading on a free surface. Therefore, as a future progression of this work, a volatile sample film thickness in both open and closed chambers would first need to be measured in order to understand the influence of the vapour phase at the liquid-air interface and how this affects the film thickness reduction. Next, the influence of capillary forces on the spreading rates could be properly investigated where the volatile samples flow in one direction in a trough and a sensor array on the back face measures the film thickness using a standing wave method during spreading conditions. The sensors in the array could be bonded at set distances in such a way that the spreading rate of the volatile samples can be accurately quantified. The trough on the front face could be fabricated such that it is possible to have both an open and closed trough chambers. This would be aimed at investigating the effect of a vapour phase on the spreading dynamics of volatiles.
- Following from the above recommendation, a measurement concept could then be developed and optimised that first characterises the viscosity and film thickness of static lubricants and volatile samples on a free surface using ultrasonic methods. This would be aimed at eliminating the spreading conditions and to only investigate the gravity and evaporative effects at the liquid-air interface on the viscosity and film thickness evolution. This investigation could shed some insights on the viscosity and film thickness evolution results of spreading liquid samples that were observed in this research work. The natural progression of the research could then lead to the development of a miniaturised commercial product that can be retrofitted on to most engineering components for the investigation of a liquid viscosity and film thickness simultaneously.

References

[1] C. H. Wu and Y. T. Kung, “A parametric study on oil/air lubrication of a high-speed spindle,” *Precis. Eng.*, vol. 29, no. 2, pp. 162–167, 2005.

[2] B. R. Höhn, K. Michaelis, and H. P. Otto, “Minimised gear lubrication by a minimum oil/air flow rate,” *Wear*, vol. 266, no. 3–4, pp. 461–467, Feb. 2009.

[3] Marketsandmarkets.com, “Film Thickness Measurement Market by Technology, Film Type, Application (Aerospace & Aviation, Automotive, Food & Pharmaceutical Packaging, Industrial Manufacturing, Medical, Semiconductors), and Geography - Global Forecast to 2023,” 2018. https://www.marketsandmarkets.com/Market-Reports/film-thickness-measurement-market-207950545.html (accessed Jan. 25, 2020).

[4] T. Geng, Q. Meng, X. Xu, P. Wang, and X. Yuan, “An extended ultrasonic time-of-flight method for measuring lubricant film thickness,” *Proc. Inst. Mech. Eng. Part J J. Eng. Tribol.*, vol. 229, no. 7, pp. 861–869, 2015.

[5] B. Praher and G. Steinbichler, “Ultrasound-based measurement of liquid-layer thickness: A novel time-domain approach,” *Mech. Syst. Signal Process.*, vol. 82, pp. 166–177, Jan. 2017.

[6] J. T. Kimball, M. R. Bailey, and J. C. Hermanson, “Ultrasonic measurement of condensate film thickness,” *J. Acoust. Soc. Am.*, vol. 124, no. 4, pp. EL196–EL202, 2008.

[7] Z. Q. Chen, J. C. Hermanson, M. A. Shear, and P. C. Pedersen, “Ultrasonic monitoring of interfacial motion of condensing and non-condensing liquid films,” *Flow Meas. Instrum.*, vol. 16, no. 6, pp. 353–364, 2005.

[8] T. Pialucha and P. Cawley, “The detection of thin embedded layers using normal incidence ultrasound,” *Ultrasonics*, vol. 32, no. 6, pp. 431–440, 1994.

[9] R. S. Dwyer-Joyce, B. W. Drinkwater, and C. J. Donohoe, “The measurement of lubricant-film thickness using ultrasound,” *Proc.R.Soc.Lond.*, vol. 459, pp. 957–976, 2003.

[10] Elcometer, “Elcometer 456 Coating Thickness Gauge.” https://www.elcometer.com/en/coating-inspection/dry-film-thickness/dry-film-thickness-digital/elcometer-456-coating-thickness-gauge.html (accessed Aug. 16, 2021).

[11] DeFelsko, “Ultrasonic Coating Thickness Gage - PosiTector 200.” https://www.defelsko.com/positector-200 (accessed Aug. 17, 2021).

[12] W. B. Harding and G. A. Di Bari, *Testing of Metallic and Inorganic Coatings*. ASTM International, 1987.

[13] H.-J. Streitberger and A. Goldschmidt, *BASF Handbook Basics of Coating Technology*. 2007.

[14] “Paints and varnishes — Determination of film thickness,” ISO 2808, 2019.

[15] Cromwell, “Oxford 0-25mm/0.001mm EXTERNAL MICROMETER T106-01-000 | Cromwell Tools.” https://www.cromwell.co.uk/shop/measuring-and-test-equipment/analogue-external-micrometers/0-25mm-0-001mm-external-micrometer/p/OXD3355300K (accessed Aug. 11, 2021).

[16] “Standard Test Method for Measurement of Dry-Film Thickness of Organic Coatings Using Micrometers,” ASTM D1005-95, 2020.

[17] “Measurement of coating thicknesses - Measurement of the thickness of coatings by difference measurement using a stylus instrument,” DIN 50933, 2015.

[18] “Metallic and oxide coatings -- Measurement of coating thickness -- Microscopical method,” ISO 1463, 2004.

[19] “Paints and varnishes. Wedge-cut method for determination of film thickness (scribe and drill method),” ISO 19399, 2017.

[20] “Geometrical product specifications (GPS) — Surface texture : Areal Part 604 : Nominal characteristics of contact (coherence scanning interferometry) instruments,” ISO 25178-604, 2013.

[21] Elcometer, “Elcometer 112AL, 112 & 3236 Hexagonal Wet Film Combs.” https://www.elcometer.com/en/coating-inspection/wet-film-powder-thickness/wet-film-combs/elcometer-112al-112-3236-hexagonal-wet-film-combs.html (accessed Aug. 11, 2021).

[22] “Standard Practice for Measurement of Wet Film Thickness by Notch Gages,” ASTM D4414-95, 2020.

[23] Elcometer, “Elcometer 3230 Wet Film Wheels.” https://www.elcometer.com/en/coating-inspection/wet-film-powder-thickness/wet-film-wheels/elcometer-3230-wet-film-wheels.html (accessed Aug. 11, 2021).

[24] “Standard Test Methods for Measurement of Wet Film Thickness of Organic Coatings,” ASTM D1212-91, 2020.

[25] “Geometrical Product Specifications (GPS) — Dimensional measuring equipment — Design and metrological characteristics of mechanical dial gauges,” ISO 463, 2006.

[26] “Conversion coatings on metallic materials — Determination of coating mass per unit area — Gravimetric methods,” ISO 3892, 2000.

[27] BS 15042-2, “Thickness measurement of coatings and characterization of surfaces with surface waves. Guide to the thickness measurement of coatings by photothermic method,” 2006.

[28] “Non-magnetic coatings on magnetic substrates. Measurement of coating thickness. Magnetic method,” ISO 2178, 2016.

[29] “Non-conductive coatings on non-magnetic electrically conductive base metals — Measurement of coating thickness — Amplitude-sensitive eddy-current method,” ISO 2360, 2017.

[30] Tester, “Extech CG204 Coating Thickness Tester.” https://www.tester.co.uk/extech-cg204-coating-thickness-tester (accessed Aug. 11, 2021).

[31] “Metallic and non-metallic coatings. Measurement of thickness. Beta backscatter method,” ISO 3543, 2001.

[32] “Metallic coatings — Measurement of coating thickness — Scanning electron microscope method,” ISO 3497, 2001.

[33] K. Su, Y. C. Shen, and J. A. Zeitler, “Terahertz sensor for non-contact thickness and quality measurement of automobile paints of varying complexity,” *IEEE Trans. Terahertz Sci. Technol.*, vol. 4, no. 4, pp. 432–439, 2014.

[34] I. Ismail, J. C. Gamio, S. F. A. Bukhari, and W. Q. Yang, “Tomography for multi-phase flow measurement in the oil industry,” *Flow Meas. Instrum.*, vol. 16, no. 2–3, pp. 145–155, Apr. 2005.

[35] Y. Li, W. Yang, C. G. Xie, S. Huang, Z. Wu, D. Tsamakis, and C. Lenn, “Gas/oil/water flow measurement by electrical capacitance tomography,” *Meas. Sci. Technol.*, vol. 24, no. 7, p. 074001, 2013.

[36] Z. Cui, C. Yang, B. Sun, and H. Wang, “Liquid film thickness estimation using electrical capacitance tomography,” *Measurement Science Review*, vol. 14, no. 1. pp. 8–15, 2014.

[37] “Determination of the film thickness of coatings using an ultrasonic gage.,” ISO 19397, 2018.

[38] R. S. Dwyer-Joyce, D. A. Green, P. Harper, R. Lewis, S. Balakrishnan, P. D. King, H. Rahnejat, and S. Howell-Smith, “The measurement of liner - Piston skirt oil film thickness by an ultrasonic means,” in *SAE Technical Papers*, 2006.

[39] T. Reddyhoff, R. S. Dwyer-Joyce, J. Zhang, and B. W. Drinkwater, “Auto-calibration of ultrasonic lubricant-film thickness measurements,” *Meas. Sci. Technol.*, vol. 19, no. 4, 2008.

[40] R. S. Dwyer-Joyce, T. Reddyhoff, and B. Drinkwater, “Operating limits for acoustic measurement of rolling bearing oil film thickness,” *Tribol. Trans.*, vol. 47, no. 3, pp. 366–375, 2004.

[41] R. S. Dwyer-Joyce, P. Harper, and B. W. Drinkwater, “A method for the measurement of hydrodynamic oil films using ultrasonic reflection,” *Tribol. Lett.*, vol. 17, no. 2, pp. 337–348, 2004.

[42] R. Mills, E. Avan, and R. S. Dwyer-Joyce, “Piezoelectric sensors to monitor lubricant film thickness at piston–cylinder contacts in a fired engine,” *Proc. Inst. Mech. Eng. Part J J. Eng. Tribol.*, vol. 227, no. 2, pp. 100–111, 2012.

[43] R. S. Dwyer-Joyce, “The Application of Ultrasonic NDT Techniques in Tribology,” *Proc. Inst. Mech. Eng. Part J J. Eng. Tribol.*, vol. 219, no. 5, pp. 347–366, 2005.

[44] R. B. Lindsay, “The Story of Acoustics,” *J. Acoust. Soc. Am.*, vol. 39, no. 4, pp. 629–644, 1966.

[45] J. Krautkramer and H. Krautkramer, *Ultrasonic Testing of Materials*, 4th ed. Springer-Verlag Berlin Heidelberg GmbH, 1990.

[46] “Non-destructive testing — Ultrasonic testing — Vocabulary,” ISO 5577, 2017.

[47] L. E. Kinsler, A. R. Frey, A. B. Coppens, and J. V. Sanders, *Fundamentals of Acoustics*, 4th ed. John Wiley & Sons, Inc, 2000.

[48] A. D. Pierce, *Acoustics: An Introduction to Its Physical Principles and Applications*, Third. 1980.

[49] H. G. Tattersall, “The ultrasonic pulse-echo technique as applied to adhesion testing,” *J. Phys. D. Appl. Phys.*, vol. 6, no. 7, pp. 819–832, 1973.

[50] B. W. Drinkwater, J. Zhang, K. J. Kirk, J. Elgoyhen, and R. S. Dwyer-Joyce, “Ultrasonic measurement of rolling bearing lubrication using piezoelectric thin films,” *J. Tribol.*, vol. 131, no. 1, p. 011502, 2009.

[51] A. Migliori and J. L. Sarrao, *Resonant Ultrasound Spectroscopy: Applications to Physics, Material Measurements and Nondestructive Evaluation*. John Wiley, 1997.

[52] P. Dou, T. Wu, Z. Luo, Z. Peng, and T. Sarkodie-Gyan, "The application of the principle of wave superposition in ultrasonic measurement of lubricant film thickness," *Meas. J. Int. Meas. Confed.*, vol. 137, pp. 312–322, 2019.

[53] M. S. Greenwood and J. A. Bamberger, "Measurement of viscosity and shear wave velocity of a liquid or slurry for on-line process control," *Ultrasonics*, vol. 39, no. 9, pp. 623–630, Aug. 2002.

[54] A. Hunter, "Ultrasonic Measurements of the Strip Thickness, Lubricant Film Thickness, Roll Deflection and Roll Stress in the Roll Bite in the Cold Rolling of Steel," Doctoral Thesis, University of Sheffield, 2018.

[55] L. Svilainis and V. Dumbrava, "Analysis of the interpolation techniques for time-of-flight estimation," *Ultragarsas*, vol. 63, no. 4, pp. 25–29, 2008.

[56] R. Queirós, F. Corrêa Alegria, P. Silva Girão, and A. Cruz Serra, "Cross-correlation and sine-fitting techniques for high-resolution ultrasonic ranging," *IEEE Trans. Instrum. Meas.*, 2010.

[57] L. Angrisani, A. Baccigalupi, and R. Schiano Lo Moriello, "A measurement method based on Kalman filtering for ultrasonic time-of-flight estimation," *IEEE Trans. Instrum. Meas.*, vol. 55, no. 2, pp. 442–448, Apr. 2006.

[58] E. Mor, A. Azoulay, and M. Aladjem, "A matching pursuit method for approximating overlapping ultrasonic echoes," *IEEE Trans. Ultrason. Ferroelectr. Freq. Control*, 2010.

[59] J. Jiao, W. Liu, J. Zhang, Q. Zhang, C. He, and B. Wu, "Time-frequency analysis for ultrasonic measurement of liquid-layer thickness," *Mech. Syst. Signal Process.*, vol. 35, no. 1–2, pp. 69–83, Feb. 2013.

[60] F. Honarvar, H. Sheikhzadeh, M. Moles, and A. N. Sinclair, "Improving the time-resolution and signal-to-noise ratio of ultrasonic NDE signals," *Ultrasonics*, vol. 41, no. 9, pp. 755–763, Mar. 2004.

[61] P. C. Pedersen, Z. Cakareski, and J. C. Hermanson, "Ultrasonic monitoring of film condensation for applications in reduced gravity," *Ultrasonics*, vol. 38, no. 1, pp. 486–490, 2000.

[62] Lawrence C. Lynnworth, *Ultrasonic measurements for process control: Theory, techniques, applications*, vol. 29, no. 1. 1991.

[63] E. P. Papadakis and K. A. Fowler, "Broad-Band Transducers: Radiation Field and Selected Applications," *J. Acoust. Soc. Am.*, vol. 50, no. 3A, pp. 729–745, 1971.

[64] N. F. Haines, J. C. Bell, and P. J. McIntyre, "The application of broadband ultrasonic spectroscopy to the study of layered media," *J. Acoust. Soc. Am.*, vol. 64, no. 6, pp. 1645–1651, 1978.

[65] M. X. Li, X. M. Wang, and J. Mao, "Thickness measurement of a film on a substrate by low-frequency ultrasound," *Chinese Phys. Lett.*, vol. 21, no. 5, pp. 870–873, 2004.

[66] V. K. Kinra and C. Zhu, "Ultrasonic nondestructive evaluation of thin (subwavelength) coatings," *J. Acoust. Soc. Am.*, vol. 93, no. 5, pp. 2454–2467, 1993.

[67] A. I. Lavrentyev and S. I. Rokhlin, "Determination of elastic moduli, density, attenuation,

and thickness of a layer using ultrasonic spectroscopy at two angles," *J. Acoust. Soc. Am.*, vol. 102, no. 6, pp. 3467–3477, Dec. 1997.

[68] A. I. Lavrentyev and S. I. Rokhlin, "An ultrasonic method for determination of elastic moduli, density, attenuation and thickness of a polymer coating on a stiff plate," *Ultrasonics*, vol. 39, no. 3, pp. 211–221, 2001.

[69] A. Hunter, R. Dwyer-Joyce, and P. Harper, "Calibration and validation of ultrasonic reflection methods for thin-film measurement in tribology," *Meas. Sci. Technol.*, 2012.

[70] F. Lakestani, J. F. Coste, and R. Denis, "Application of ultrasonic Rayleigh waves to thickness measurement of metallic coatings," *NDT E Int.*, vol. 28, no. 3, pp. 171–178, Jan. 1995.

[71] G. Lindner, M. Schmitt, K. Schmidt, H. Faustmann, and S. Krempel, "Detection of coatings and measurement of coating thickness on technical substrates using surface acoustic waves in a waveguide configuration," in *Proceedings of the 14th International Conference on Sensors and Measurement Technology*, 2009, no. 1, pp. 35–40.

[72] V. V. Krylov, "Surface properties of solids and surface acoustic waves: Application to chemical sensors and layer characterization," *Appl. Phys. A Mater. Sci. Process.*, vol. 61, no. 3, pp. 229–236, 1995.

[73] A. G. Every, "Measurement of the near-surface elastic properties of solids and thin supported films," *Meas. Sci. Technol.*, vol. 13, no. R21, 2002.

[74] M. Thompson and D. C. Stone, *Surface-Launched Acoustic Wave Sensors: Chemical Sensing and Thin-Film Characterization*. 1997.

[75] J. Cirák, P. Koštial, J. Vajda, P. Tomčík, D. Barančok, and L. Keleši, "Surface acoustic wave propagation in Langmuir-Blodgett layers," *Appl. Surf. Sci.*, vol. 108, no. 1, pp. 53–57, 1997.

[76] A. J. Ricco, A. W. Staton, R. M. Crooks, and T. Kim, "Single-monolayer in situ modulus measurements using a SAW device: Photocrosslinking of a diacetylenic thiol-based monolayer," *Faraday Discuss.*, vol. 107, pp. 247–258, 1997.

[77] G. G. Roberts, B. Holcroft, A. Barraud, and J. Richard, "The properties of conducting tetracyanoquinodimethane Langmuir-Blodgett films: A study using acoustoelectric devices," *Thin Solid Films*, 1988.

[78] D. N. Sinha, "Acoustic Resonance Spectroscopy (ARS) Tracking those 'good vibrations' for non destructive evaluation," *IEEE Potentials*, vol. 11, no. 2, pp. 10–13, 1992.

[79] D. N. Sinha, K. Springer, W. Han, D. Lizon, and S. Kogan, "Applications of swept-frequency acoustic interferometer for nonintrusive detection and identification of chemical warfare compounds," Los Alamos, NM, Dec. 1997.

[80] D. N. Sinha and G. Kaduchak, "Noninvasive determination of sound speed and attenuation in liquids," in *Experimental Methods in the Physical Sciences*, vol. 39, 2001, pp. 307–333.

[81] B. T. Sturtevant, C. Pantea, and D. N. Sinha, "An acoustic resonance measurement cell for liquid property determinations up to 250 °C," *Rev. Sci. Instrum.*, vol. 83, no. 11, p. 115106, 2012.

[82] W. Wagner and H.-J. Kretzschmar, "IAPWS Industrial Formulation 1997 for the

Thermodynamic Properties of Water and Steam," in *International Steam Tables*, Springer Berlin Heidelberg, 2008, pp. 7–150.

[83] R. Mills, R. Dwyer-Joyce, and M. B. Marshall, "Continuous Wave Ultrasound For Analysis Of A Surface," Great Britain Patent WO 2017/109490 A1, 2018.

[84] T. Reddyhoff, S. Kasolang, R. S. Dwyer-Joyce, and B. W. Drinkwater, "The phase shift of an ultrasonic pulse at an oil layer and determination of film thickness," *Proc. Inst. Mech. Eng. Part J-Journal Eng. Tribol.*, vol. 219, no. J6, pp. 387–400, 2005.

[85] Y. A. Al-Aufi, B. N. Hewakandamby, G. Dimitrakis, M. Holmes, A. Hasan, and N. J. Watson, "Thin film thickness measurements in two phase annular flows using ultrasonic pulse echo techniques," *Flow Meas. Instrum.*, vol. 66, pp. 67–78, 2019.

[86] O. Manfredi, "The Development of an Ultrasonic Standing Wave Method to Measure Liquid Viscosity," Doctoral Thesis, University of Sheffield, 2019.

[87] D. Ensminger and L. J. Bond, *Ultrasonics: Fundamentals, Technologies, and Applications*, 3rd ed. CRC Press, 2011.

[88] Engineering ToolBox, "Thermal Conductivity of Metals, Metallic Elements and Alloys." https://www.engineeringtoolbox.com/thermal-conductivity-metals-d_858.html (accessed Aug. 15, 2021).

[89] P. Van Thanh, P. Thi Tuyet Nhung, L. Thi Minh Thuy, and N. Hoa Nhai, "Effect of Temperature on Ultrasonic Velocities, Attenuations, Reflection and Transmission Coefficients between Motor Oil and Carbon Steel Estimated by Pulse-echo Technique of Ultrasonic Testing Method," *VNU J. Sci. Math.*, vol. 31, no. 4, pp. 39–48, 2015.

[90] T. Wan, T. Naoe, T. Wakui, M. Futakawa, H. Obayashi, and T. Sasa, "Effects of grain size on ultrasonic attenuation in type 316L stainless steel," *Materials (Basel).*, vol. 10, no. 7, 2017.

[91] R. Gentle, P. Edwards, and B. Bolton, *Mechanical Engineering Systems*. Elsevier, 2001.

[92] J. C. Batista Abreu, L. M. C. Vieira, M. H. Abu-Hamd, and B. W. Schafer, "Review: development of performance-based fire design for cold-formed steel," *Fire Sci. Rev.*, vol. 3, no. 1, pp. 1–15, 2014.

[93] T. J. Eason and T. J. Eason, "Ultrasonic thickness structural health monitoring of steel pipe for internal corrosion," Doctoral Thesis, Iowa State University, 2017.

[94] E. Ginzel and R. Ginzel, "Approximate dV/dT values for some materials," *e-Journal of Nondestructive Testing (NDT) ISSN 1435-4934 (NDT.net Journal)*, 2017. https://www.ndt.net/search/docs.php3?id=21545 (accessed Aug. 20, 2021).

[95] J. Carvill, *Mechanical Engineer's Data Handbook*. Elsevier, 1993.

[96] K. Tezuka, M. Mori, S. Wada, M. Aritomi, and Y. Sakai, "Analysis of ultrasound propagation in high-temperature nuclear reactor feedwater to investigate a clamp-on ultrasonic pulse doppler flowmeter," *J. Nucl. Sci. Technol.*, vol. 45, no. 8, pp. 752–762, 2008.

[97] J. Feng and Z. Guo, "Temperature-frequency-dependent mechanical properties model of epoxy resin and its composites," *Compos. Part B Eng.*, vol. 85, pp. 161–169, 2016.

[98] Robnor Resinlab, "Robnor PX439XS Thermally Conductive Epoxy Resin." https://www.robnor-resinlab.com/product/px439xs/ (accessed Aug. 15, 2021).

[99] Robnor Resinlab, “Robnor PC590EF/NC Epoxy Foam.” https://www.robnor-resinlab.com/product/robnor-px590ef-nc/ (accessed Aug. 15, 2021).

[100] J. McHugh, J. Döring, W. Stark, and A. Erhard, “Characterisation of Epoxy Materials Used in the Development of Ultrasonic Arrays,” in *16th World Conference on NDT*, 2004.

[101] M. . Bessonov, M. M. Koton, V. . Kudryavtsev, and L. . Laius, *Polyimides: Thermally stable polymers*. Springer US, 1987.

[102] M. K. Ghosh and K. L. Mittal, *Polyimides: Fundamentals and applications*. CRC Press, 1996.

[103] M. Schirru, “Development of an Ultrasonic Sensing Technique to Measure Lubricant Viscosity in Engine Journal Bearing In-Situ,” Doctoral Thesis, University of Sheffield, 2017.

[104] J. R. Vail, R. S. Mills, J. T. Stephen, M. B. Marshall, and R. S. Dwyer-Joyce, “An ultrasonic method for measuring fluid penetration rate into threaded contacts,” *Tribol. Int.*, vol. 67, pp. 21–26, 2013.

[105] M. Schirru, R. Mills, R. Dwyer-Joyce, O. Smith, and M. Sutton, “Viscosity Measurement in a Lubricant Film Using an Ultrasonically Resonating Matching Layer,” *Tribol. Lett.*, vol. 60, no. 3, 2015.

[106] W. P. Mason, W. O. Baker, H. J. Mcskimin, and J. H. Heiss, “Measurement of shear elasticity and viscosity of liquids at ultrasonic frequencies,” *Phys. Rev.*, vol. 75, no. 6, pp. 936–946, 1949.

[107] E. E. Franco, J. C. Adamowski, and F. Buiochi, “Ultrasonic viscosity measurement using the shear-wave reflection coefficient with a novel signal processing technique,” *IEEE Trans. Ultrason. Ferroelectr. Freq. Control*, vol. 57, no. 5, pp. 1133–1139, 2010.

[108] G. W. Stachowiak and A. W. Batchelor, *Engineering Tribology*, 4th ed. Butterworth-Heinemann, 2013.

[109] Q. Lu, N. V. Suryanarayana, and C. Christodoulu, “Film thickness measurement with an ultrasonic transducer,” *Exp. Therm. Fluid Sci.*, vol. 7, no. 4, pp. 354–361, 1993.

[110] S. Jung, S. D. Hoath, and I. M. Hutchings, “The role of viscoelasticity in drop impact and spreading for inkjet printing of polymer solution on a wettable surface,” *Microfluid. Nanofluidics*, vol. 14, no. 1–2, pp. 163–169, 2013.

[111] D. Brutin and V. Starov, “Recent advances in droplet wetting and evaporation,” *Chem. Soc. Rev.*, vol. 47, no. 2, pp. 558–585, 2018.

[112] W. Wen, G. H. Zong, Y. Yu, and L. Sun, “The influence of bubbles on the performance of ultrasonic flow meter,” *Appl. Mech. Mater.*, vol. 678, pp. 285–289, 2014.

[113] “Standard Test Method for Kinematic Viscosity of Transparent and Opaque Liquids (and Calculation of Dynamic Viscosity),” ASTM D445, 2019.

Appendix A: MATLAB Mathematical Model Code

Model for superimposed standing wave based on multiple reflection summation

```
clearvars; clc; % clears variables in the workspace and clears the command window
```

Defining system variables

[Air | PZT | Component | Surface layer | Air] % schematic of layers

[z20 | z10 | z00 | z01 | z02] % acoustic impedances

```
% Component
L00 = 0.01;      % component thickness (metres)
a00 = -10;       % component attenuation coefficient (1/m)
c00 = 6211.8;      % component speed of sound (m/s)
p00 = 2700.0;      % component density (kg/m3)
z00 = c00*p00;     % component acoustic impedance

% Surface layer
th = 138.20e-6;   % surface layer thickness (m)
c01 = 2670;      % surface layer speed of sound (m/s)
p01 = 1180.0;       % surface layer density (kg/m3)
z01 = c01*p01;     % surface layer acoustic impedance

% air
c20 = 320.0;     % air speed of sound
p20 = 1.2;       % air density (kg/m3)
z20 = c20*p20;     % air acoustic impedance

% for reference situation
c02_ref = c20;
p02_ref = p20;
z02_ref = z20;

% when air is bounding a surface layer
c02 = c20;
p02 = p20;
z02 = z20;

% PZT
L10 = 0.0002;     % PZT thickness (m)
c10 = 4350.0;    % PZT speed of sound (m/s)
p10 = 7750;       % PZT density (kg/m3)
z10 = c10*p10;     % PZT acoustic impedance

% frequency settings
fs = 0e6;       % sweep start frequency (Hz)
fe = 20e6;      % sweep stop frequency (Hz)
df = 1e3;       % frequency increments
f = (fs:df:fe); % frequency range
w = 2*pi*f;     % angular frequency
N = 60;         % number of reflections
```

Main Calculations

```
Ref =  Sweep(w, N, a00, c00, c10, c01, L00, L10, 0.0, z00, z10, z01, z20, z02_ref);
Meas = Sweep(w, N, a00, c00, c10, c01, L00, L10, th, z00, z10, z01, z20, z02);
S = Meas./Ref;
[up,lo]=envelope(S,1000,'peak');

% Plotting the RMS waveforms
figure
subplot(2,1,1)
plot(f/1e6, Ref,'k',f/1e6, Meas,'r');
xlabel('Frequency (MHz)');
ylabel('Amplitude (arb.)');ylim([0 5]);xlim([0 20]);
legend('solid/air','solid/epoxy');
%Plotting S
subplot(2,1,2)
plot(f/1e6, S,'k');
ylim([-2 10]);xlim([0 20]);
xlabel('Frequency (MHz)');
ylabel('S');
```

Sweeping through multiple frequencies and then summing up the wave amplitudes

```
function Sw = Sweep ( w, N, a00, c00, c10, c01, L00, L10, L01, z00, z10, z01, z20, z02)
% Sweep response for 5 layer system ( --z20|z10|z00|z01|z02-- )
Sw=zeros(length(w),1);
for i = 1:length(w)
    wi = w(i);
    R_component_surfacelayer_interface = Reflection_coefficient(wi, z00, z01, z02, c01, L01);
    R_PZT_component_interface = Reflection_coefficient(wi, z00, z10, z20, c10, L10);
    Sw(i) = (Summation(wi, N, R_component_surfacelayer_interface, R_PZT_component_interface,
a00, c00, L00));
end
end
```

Reflection coefficient calculation

```
function RC = Reflection_coefficient ( w, z00, z01, z02, c01, L01)
% complex form (--z0|z1|z2-- )
RC = ((1-(z00/z02))*cos(w.*L01/c01) +1i* (z01/z02-z00/z01)* sin(w.*L01/c01))/ ((1+z00/z02)*
cos(w.*L01/c01) +1i* (z01/z02+z00/z01)* sin(w.*L01/c01));
end
```

Summing the wave amplitudes

```
function As = Summation (w, N, R_component_surfacelayer_interface, R_PZT_component_interface,
a00, c00, L00)
as=zeros(N,1);
for n=1:N % number of passes
    as(n) = exp(1i*w.*((2.*n*L00/c00))) * exp(2.*n*L00*a00) * (R_PZT_component_interface.^(n-
1))*(R_component_surfacelayer_interface.^n);
    %as(n) =
exp(1i*w.*(2*n*L00/c00))*(R_component_surfacelayer_interface^n)*(R_PZT_component_interface^(n-
1))*(exp(2*n*L00*a00));
```

```
    As=rms(sum(as)); % summation of wave amplitudes
end
end
```

Published with MATLAB® R2018a

Appendix B: Polyimide Thickness Measurement – Supplementary Data

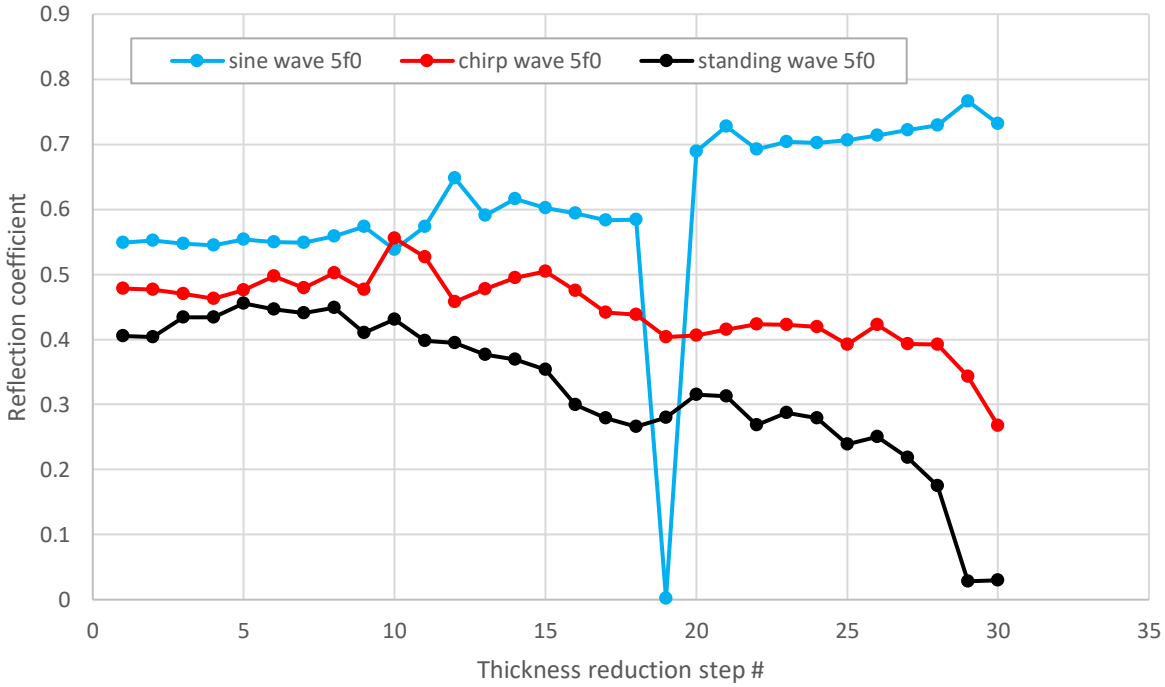

Figure 0-1. $5f_0$ magnitude comparison between pulsed wave and standing wave approaches.

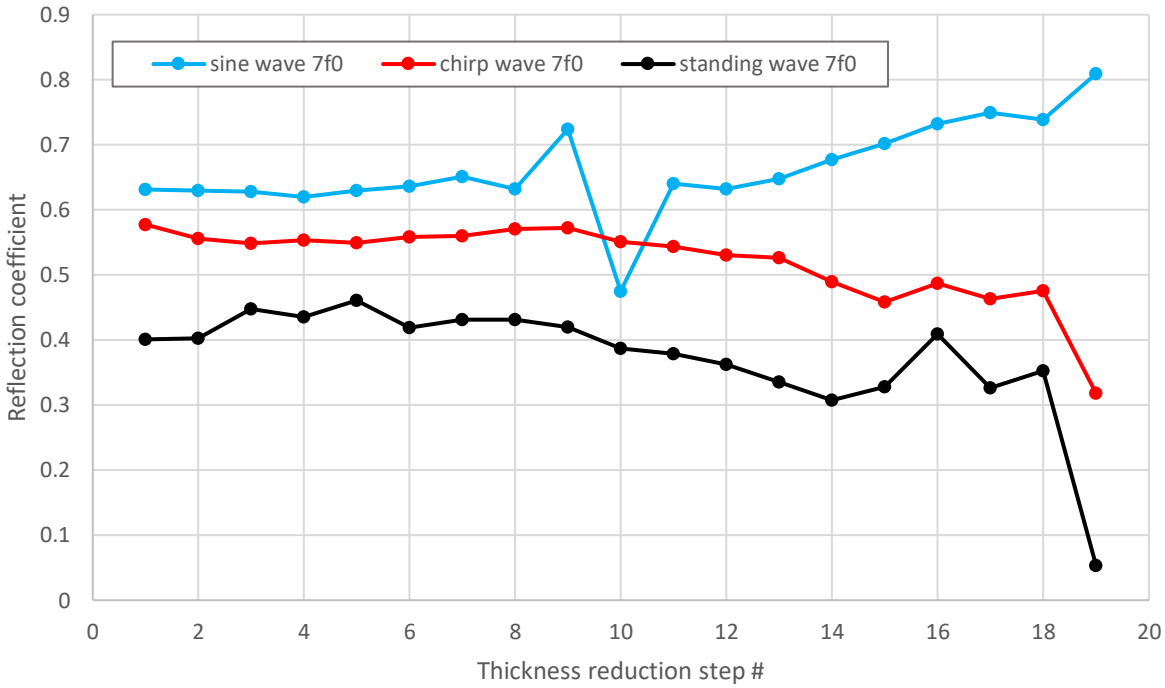

Figure 0-2. $7f_0$ magnitude comparison between pulsed wave and standing wave approaches.

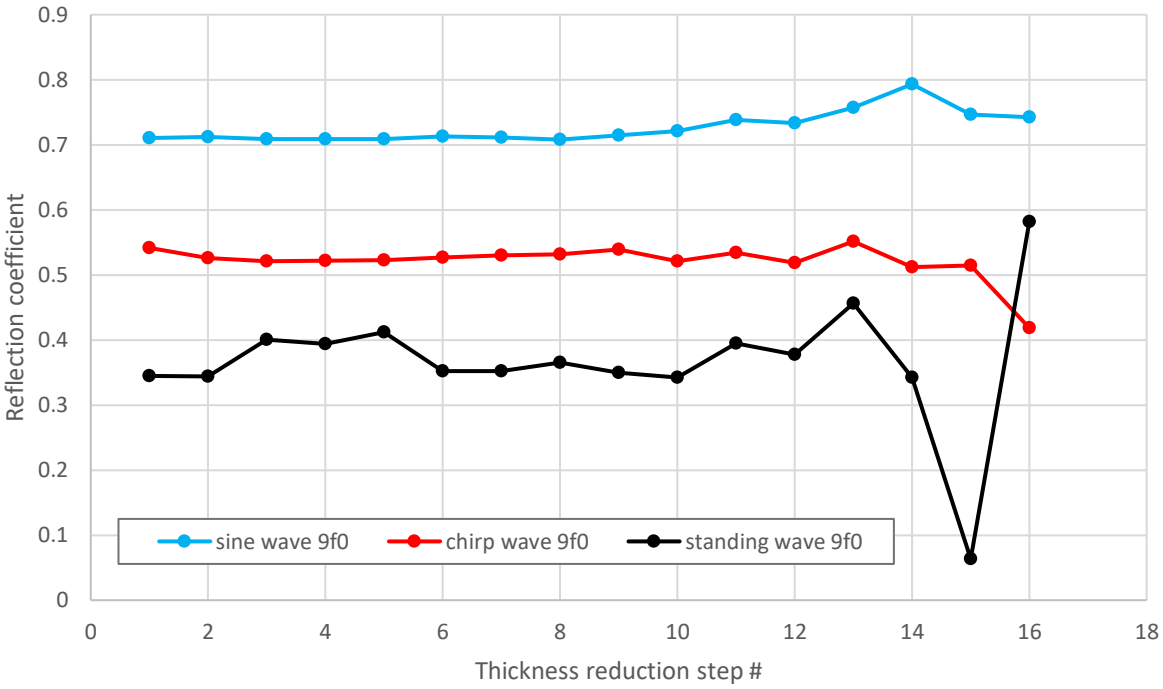

Figure 0-3. $9f_0$ magnitude comparison between pulsed wave and standing wave approaches.

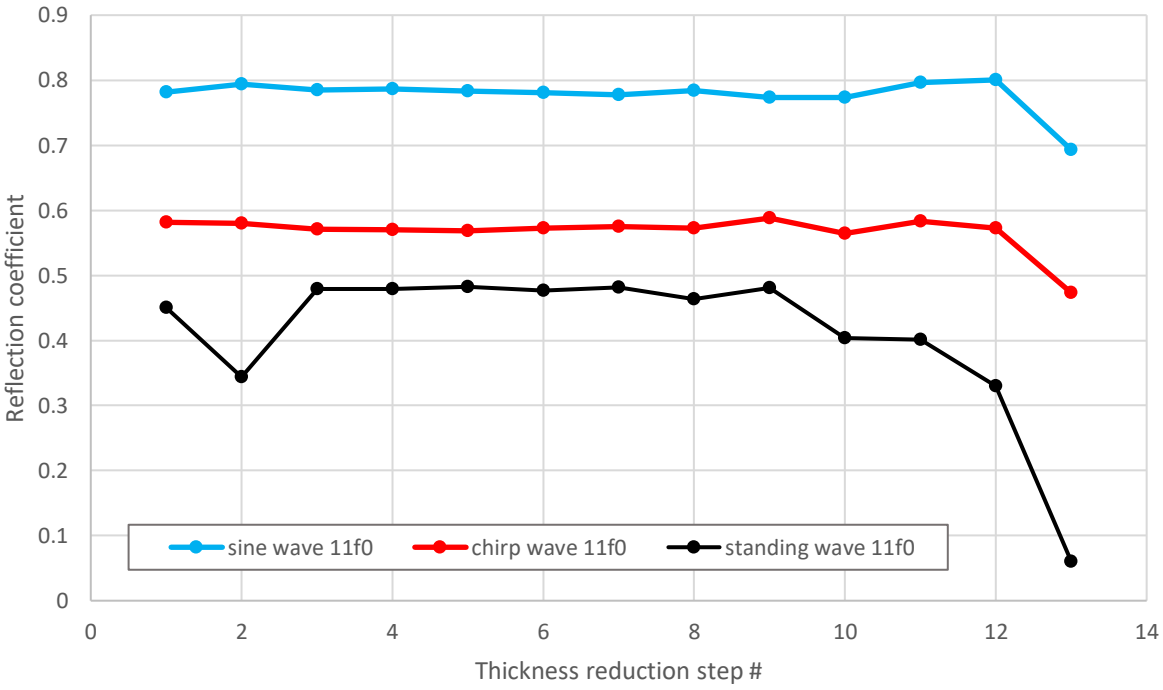

Figure 0-4. $11f_0$ magnitude comparison between pulsed wave and standing wave approaches.

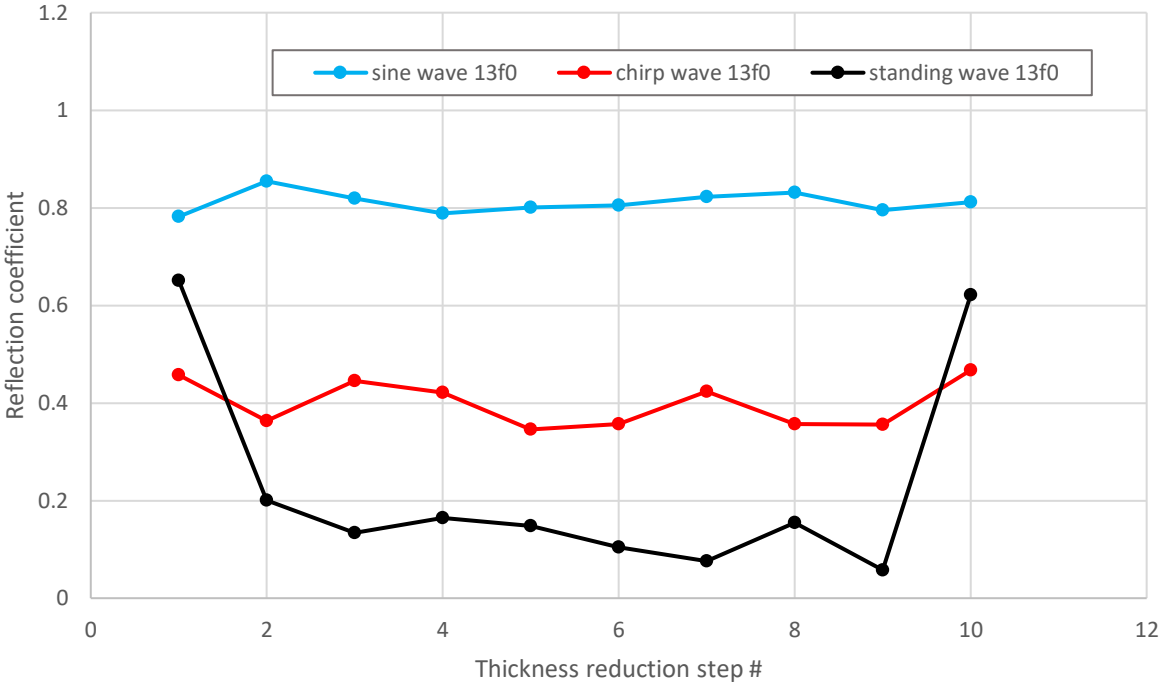

Figure 0-5. 13f_0 magnitude comparison between pulsed wave and standing wave approaches.

Appendix C: Associated Publications

Kanja, J., Mills, R., Li, X., Brunskill, H., Hunter, A. & Dwyer-Joyce, R., 2021. ‘Non-contact measurement of the thickness of a surface film using a superimposed ultrasonic standing wave’. *Ultrasonics*, 110, 106291.